Bioprocess development with *Clostridium ljungdahlii* based on metabolic modelling

DISSERTATION

Von der Fakultät Energie-, Verfahrens- und Biotechnik der Universität Stuttgart zur Erlangung der Würde eines Doktor-Ingenieurs (Dr.-Ing.) genehmigte Abhandlung

vorgelegt von

Maria Ankenbauer, geb. Hermann, M.Sc.

aus Oktjabrsk (RUS)

Hauptberichter: Prof. Dr.-Ing. Ralf Takors

Mitberichter: Prof. Dr.-Ing. Dirk Weuster-Botz

Tag der mündlichen Prüfung: 29. Juni 2023

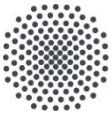

Universität Stuttgart

Institut für Bioverfahrenstechnik

2023

Titel in deutscher Sprache:

Bioprozessentwicklung mit *Clostridium ljungdahlii* auf der Basis metabolischer Stoffwechselmodellierung

Für Meine Familie

„Das Beste sollte nie hinter uns, sondern immer vor uns liegen.“

Bertrand Russel (18.05.1872 – 02.02.1970)

Acknowledgements

In the framework of this thesis, I was fortunate to be accompanied and supported by many great colleagues, wonderful friends, and my dear family. For all those I would like to express my gratitude and appreciation.

First and foremost, I want to thank Prof. Dr.–Ing. Ralf Takors for his trust and the opportunity to work on this interesting and challenging project within the IBVT team. His encouragement, the freedom he gave me, and numerous constructive discussions of experiments and results enabled me to grow beyond myself in successfully completing my scientific work and writing publications. I also want to thank Prof. Dr.– Ing. Dirk Weuster-Botz for his valuable feedback during several project meetings and his participation in the examination committee as co-examiner. Furthermore, I want to thank Prof. Dr. Ingrid Weiß for taking the chair of my defence, Jun. Prof. Dr. Michael Heymann, Prof. Dr.-Ing. Elias Klemm, and apl. Prof. Dr. habil. Martin Siemann-Herzberg for their participation in the circulation procedure.

Secondly, my special thanks go to Andreas Freund for installing the synthesis gas laboratory at IBVT and his tireless support in all technical challenges I had to face during my PhD; Alexander Nieß for his great modelling and IT support and especially for his friendship; and Attila Teleki for introducing me to the world of metabolomics and all the enlightening discussions far beyond the scientific work at IBVT. This thesis would have been hardly possible without your great support.

I also want to appreciate the technical help and guidance of Mira Lenfers-Lücker, Alexander Dietrich, Salaheddinne Laghrami, Martina Schweikert, and Andrea Seipel. Furthermore, I warmly thank my favourite secretary Silke Reu for her kind help in all administrative questions, even after my IBVT time.

A am grateful to my students Alex Akermann, Daniel Armbruster, Joshua Bär, and Moritz Amenitsch for contributing significantly to the results of this work in the framework of their student theses.

I would further like to acknowledge the funding of the synthesis gas project by the Federal Ministry of Education Research and this point deeply thank to all project partners of the University of Ulm and the Technical University of Munich for the fruitful collaboration as well as productive and pleasant project meetings.

I heartly want to thank all my former colleagues who became dear friends: Lisa, Max, Maike, Flora, Biggi, Richard, Michaela, Andi, Michi, Robert, Tobias und Anette. Many thanks to all other current and former IBVT members, too, for creating a very pleasant working atmosphere, not only during numerous nice lunch and coffee breaks.

Finally, my biggest thanks go to my friend Liana, my parents Olga und Vladimir, my sister Elena, my brother Robert, my nephew Fabian and my love and best friend Andi – thank you very much for the unconditional and unlimited support, your motivation, and your trust in my abilities that you give me in all situations.

Declaration of Authorship

I declare that the present work entitled:

"Bioprocess development with Clostridium ljungdahlii based on metabolic modelling"

has been written by me using only the sources and aids indicated. All passages and thoughts taken from external sources are marked as such. The thesis has not been submitted in the same or similar form to any other examination authority.

Ich versichere, dass die vorliegende Arbeit mit dem Titel:

„*Bioprozessentwicklung mit Clostridium ljungdahlii auf der Basis metabolischer Stoffwechselmodellierung*“

von mir selbstständig verfasst und nur unter Verwendung der angegebenen Quellen und Hilfsmittel angefertigt wurde. Alle aus fremden Quellen entnommene Passagen und Gedanken sind als solche kenntlich gemacht. Die Arbeit hat in gleicher oder ähnlicher Form noch keiner anderen Prüfungsbehörde vorgelegen.

Ulm, den

……

Maria Hermann

Table of Contents

List of Figures

List of Figures

List of Figures

List of tables

Nomenclature

Abbreviation	Description	Abbreviation	Description
2,3-BD	2,3-butanediol	HYD, Hyd	Bifurcating hydrogenase
A. woodii	*Acetobacterium woodii*	i.e.	*id est*, ‚that is'
ACS	Acetyl-CoA synthase	IlvC	Keto-acid reductoisomerase
Adh	Alcohol dehydrogenase	*ilvC*	Keto-acid reductoisomerase gene
adhA	Alcohol dehydrogenase gene	IlvD	Dihydroxyacid dehydratase
AdhE2	Bifunctional aldehyde / alcoholdehydrogenase	*ilvD*	Dihydroxyacid dehydratase gene
ADP	Adenosine diphosphate	*ilvE*	branched-chain amino acid aminotransferase gene
ack	Acetate kinase gene	KDPG	2-keto-3-deoxy- 6-phosphogluconate
aKG	2-ketoglutarate	KIV	ketoisovalerate
aldC	Acetolactate decarboxylase gene	KivD	Ketoisovalerate decarboxylase
alsS	Acetolactate synthase gene	*kivD*	Ketoisovalerate decarboxylase gene
AMP	Adenosine monophosphate	Kor	Ketoisovalerate ferredoxin oxidoreductase
AOR	Acetaldehyde:ferredoxin oxidoreductase	*kor*	Ketoisovalerate ferredoxin oxidoreductase gene
App./ approx.	Approximately	*L. lactis*	*Lactococcus lactis*

Nomenclature

Abbreviation	Description	Abbreviation	Description
ATP	Adenosine triphosphate	MTHFR	Methylene-tetrahydrofolate reductase
BSD	Bubble size distribution	MS	Mass Spectrometry
BCR	Bubble column reactor	*Moorella thermoacetica*	*M. thermoacetica*
C	Carbon	NAD^+	Nicotinamide adenine dinucleotide (oxidized)
C. acetobutylicum	*Clostridium acetobutylicum*	NADH	Nicotinamide adenine dinucleotide (reduced)
C. autoethanogenum	*Clostridium autoethanogenum*	$NADP^+$	Nicotinamide adenine dinucleotide phosphate (oxidized)
CDW	Cell dry weight	NADPH	Nicotinamide adenine dinucleotide phosphate (reduced)
CFD	Computational fluid dynamics	Nfn	NADH-dependent reduced ferredoxin:NADP+ oxidoreductase
C. glutamicum	*Corynebacterium glutamicum*	NGAM	Non-growth-associated maintenance
C. ljungdahlii, CLJU	*Clostridium ljungdahlii*	OAA	oxaloacetate
CODH	Carbon monoxide dehydrogenase	P	Promoter (with subscript indicating the respective gene)

Nomenclature

Abbreviation	Description	Abbreviation	Description
CSTR	Continous stirred tank reactor	PBM	Population balance model
C. thermocellum	*Clostridium thermocellum*	PCR	Polymerase chain reaction
D	Dilution rate	*pta*	Phosphate transacetylase
DRW	Discrete random walk	*R. eutropha*	*Ralstonia eutropha*
DNA	deoxyribonucleic acid	RANS	Reynolds-averaged Navier-Stokes equations
e, e^-	Electron	REF	Reference process
E. coli	*Escherichia coli*	rev	reverse
e.g.	*Exempli gratia,* ´for example´	Rnf	Ferredoxin:NAD^+ oxidoreductase
et al.	Et aliae (and others)	RNG	Re-Normalization Group
Etc.	*Et cetera,* ‘and so on’	RPLC	Reverse phase liquid chromatography
FDH	Formate dehydrogenase	rSMM	Reduced stoichiometric metabolic model
fwd	Forward	S. *cerevisiae*	*Saccharomyces cerevisiae*
FBA	Flux Balance Analysis	SMP	Sucrose – Magnesium - Phosphate
Fd_{ox}	Oxidized ferredoxin	SOB	Super Optimal Broth
Fd_{red}	Reduced ferredoxin	STR	Stirred tank reactor
GAM	Growth-associated maintenance	Syngas	Synthesis gas
GAPDH	Glyceraldehyde-3-phosphate dehydrogenase	THF	Tetrahydrofolate
GC	Gas chromatograph	*T. litoralis*	*Thermococcus litoralis*

Nomenclature

Abbreviation	Description	Abbreviation	Description
GEM	Genome-scale metabolic model	UDF	User defined function
Gxy	Glyoxylate	WLP	Wood-Ljungdahl-pathway
H^+	Proton	WT	Wild type
HPLC	High performance liquid chromatography	YE	Yeast Extract

Units:

Abbreviation	Description	Abbreviation	Description
°C	Degree Celsius	M	Molar (mol L^{-1})
F	Farad	µ	Micro
g	Gram	min	Minute
h	Hours	mol	Mol
K	Kelvin	Pa	Pascal
kg	Kilogram	rcf	Relative centrifugal force
L	Liter	s	second
m	Meter or milli (in combination with SI units)	Ω	Ohm
m^2	Square meter	V	Volt
m^3	Cubic meter		

Formula Symbols:

Abbreviation	Description	Abbreviation	Description
ε_G	Gas hold-up	H_R	Reactor height, m
η_L	Media viscosity, Pa s^{-1}	K_I	Inhibition constant, mmol g_{CDW}^{-1}

Nomenclature

Abbreviation	Description	Abbreviation	Description
μ	Growth rate, h^{-1}	k_L	Mass transfer coefficient, m s^{-1}
μ_{exp}	Exponential growth rate, h^{-1}	K_M	Monod constant, mmol g_{CDW}^{-1}
μ_{max}	Maximum growth rate, h^{-1}	K_S	Half-saturation constant, g L^{-1}
ρ_L	Liquid density, kg m^{-3}	$K_{Yp,x}$	Half-maximum yield, mmol g_{CDW}^{-1} h^{-1}
		lb	Lower bound
σ_L	Surface tension, N m^{-1}	q	Biomass specific consumption/ production rate, mmol g_{CDW}^{-1} h^{-1}
τ	Residence time, s	q_P	Biomass-specific product formation rate, g g^{-1} h^{-1}
A_R	Reactor cross section, m^2	q_S	Biomass-specific substrate consumption rate, g g^{-1} h^{-1}
a	Interfacial area concentration, m^{-1}	r	Volumetric consumption/ production rate, mmol L^{-1} h^{-1}
$c_{L,co}$	Dissolved CO concentration, mmol g_{CDW}^{-1}	R^2	Coefficient of determination
c_P	Product concentration, g L^{-1}	T	Temperature, K
c_S	Substrate concentration, g L^{-1}	ub	Upper bound
c_X	Biomass concentration, g L^{-1}	v_{rel}	Relative velocity, m s^{-1}

Nomenclature

Abbreviation	Description	Abbreviation	Description
d_B	Bubble diameter, m	$Y_{e^-(products)/e^-}$	Electron efficiency, mol mol^{-1}
D_R	Reactor diameter, m	$Y_{Products/e^-}$	Electron specific total product yield, C-mol mol^{-1}
D_L	Diffusion coefficient, m^2 s^{-1}	$Y_{X/S}$	Biomass substrate yield, g g^{-1}
ΔG_R	Gibbs reaction energy, kJ C-mol^{-1}	$Y_{X/P}$	Biomass product yield, g g^{-1}

Chemicals:

Abbreviation	Description	Abbreviation	Description
$CaCl_2$	Calcium dichloride	KH_2PO_4	Potassium dihydrogen phosphate
CO	Carbon monoxide	$MgCl_2$	Magnesium chloride
CO_2	Carbon dioxide	$MgSO_4$	Magnesium sulfate
$CoSO_4$	Cobalt sulfate	$MnSO_4$	Manganese sulfate
$CuSO_4$	Copper sulfate	N_2	Nitrogen
$FeSO_4$	Ferrous sulfate	NaCl	Sodium chloride
$Fe(SO_4)_2(NH_4)_2$	Ammonium ferrous sulfate	NaH_2PO_4	Sodium dihydrogen phosphate
		Na_2MoO_4	Sodium molybdate
H_2	Hydrogen	Na_2SeO_3	Sodium selenite
H_3BO_3	Boric acid	Na_2WO_4	Sodium tungstate
H_2O	Water	NH_3	Ammonia
H_2SO_4	Sulfuric acid	NH_4Cl	Ammonium chloride
HCl	Hydrochloric acid	$NiCl_2$	Nickel chloride
$KAl(SO_4)_2$	Aluminum potassium sulfate	Tris	Trometamol
KCl	Potassium chloride	$ZnSO_4$	Zinc sulfate
K_2HPO_4	Dipotassium hydrogen phosphate		

Abstract

Bacterial synthesis gas (syngas) fermentation offers a promising solution for the reduction of greenhouse gas emissions – the greatest challenge of today's society. The substrate gas, which mainly consists of CO_2, CO, and H_2, represents an inexpensive feedstock originating from agricultural, industrial, and municipal wastes. It can be metabolized to a multitude of valuable commodity chemicals and biofuels using different autotrophic bacteria. With syngas fermentation, fossil-based resources are replaced with the simultaneous diminution of the greenhouse gas CO_2 and usage of the waste gas CO. In this regard, *Clostridium ljungdahlii* (*C. ljungdahlii*) is a good representative of gas-fermenting acetogens, as it is natively endowed to convert syngas components into acetic acid, ethanol, 2,3-butanediol (2,3-BD) and lactate. In addition, *C. ljungdahlii* is genetically accessible and, therefore, a promising platform for the recombinant formation of high-value products like isobutanol. The autotrophic central metabolism of *C. ljungdahlii* refers to the Wood-Ljungdahl pathway (WLP), an ancient and energy-limited reductive pathway that relies on a proton gradient for ATP conservation. The conversion of reducing equivalents within this pathway is essential for the establishing of the proton gradient needed for ATP formation, and also for product formation based on several reductive steps starting from CO_2. The provision of crucial reducing equivalents depends on the oxidation of the electron source in the substrate gas - CO via carbon monoxide dehydrogenase (CODH) or H_2 by a bifurcating hydrogenase (HYD). Hence, for the optimized formation of natural and non-natural reduced products, it is decisive to thoroughly understand the cellular link between energy management, growth, by-product formation, and the electron availability in the substrate gas.

In the framework of this thesis, controlled bioreactor batch cultivations with continuous gas supply in 2 L scale were performed to study the growth and product formation of *C. ljungdahlii* in dependence on varying substrate compositions. These are CO, a mixture of CO_2 and H_2, and syngas. In addition, a stoichiometric metabolic model was manually reconstructed for subsequent analysis of intracellular carbon fluxes, redox and energy metabolism. Using flux balance analysis (FBA), it was demonstrated that

electron availability is the main influence factor for product formation. The product-per-electron yield in C-mol was roughly the same for all substrates despite clearly different growth and product profiles. CO was identified as the preferred carbon and energy source leading to doubled growth rates, the highest ATP formation rates, and the highest amounts of reduced products. Utilizing H_2 and CO_2, *C. ljungdahlii* produced acetate (approx. 9 g L^{-1}) almost exclusively. However, with CO mainly ethanol (approx. 5 g L^{-1}) and 2,3-BD (approx. 2 g L^{-1}) were produced. The autotrophic product spectrum is strongly influenced by the provision of reduced ferredoxin (Fd_{red}), the key intracellular control parameter of ATP synthesis, growth, and product formation in *C. ljungdahlii*. Fd_{red} provision by CODH or HYD is linked to the regeneration of NADH and NADPH, carried out by ATP synthesis via the Rnf complex, the methyl branch of the WLP, and a transhydrogenase-like Nfn complex. Using H_2, Fd_{red} provision yield NADH and NADPH formation that is fully regenerated by the methyl branch activity with final acetate and biomass production. In contrast, CO-induced Fd_{red} provision results in a surplus of reducing equivalents allowing higher ATP yields and increased formation of reduced by-products. By H_2-supplementation in CO-rich syngas, an even higher formation of the NADPH-dependent product 2,3-BD (approx. 4 g L^{-1}) was realized. Therefore, this substrate is very well suited to produce natural or even non-natural reduced alcohols with *C. ljungdahlii* during batch cultivations.

In close cooperation with the research group of Peter Dürre (Institute of Microbiology and Biotechnology, University of Ulm), we subsequently examined the heterologous syngas-based isobutanol production of *C. ljungdahlii,* applying a stepwise approach. First, a recombinant strain was engineered, that is characterized by an amplification of pyruvate-to-ketoisovalerate (KIV) conversion and subsequent metabolization of KIV to isobutanol via recombinant Ehrlich pathway (*C. ljungdahlii* [pKAIA]). Based on controlled batch cultivation studies in continuously gassed stirred bioreactors, this strain was physiologically characterized and thoroughly analysed via intracellular metabolomics. By doing this, pyruvate and KIV were identified as limiting key metabolites restricting isobutanol formation to a very low level. Additional blocking of valine biosynthesis in *C. ljungdahlii::ilvE* [pKAIA] resulted in a 6.5-fold increase in

isobutanol formation of 0.13 g L^{-1}. However, FBA revealed limited intracellular NADPH availability as a possible target for future metabolic engineering.

With regard to the scale-up of syngas fermentations to commercial scales, possible performance losses during CO-based cultivation of *C. ljungdhalii* in a 125 m^3 bubble column reactor were analysed using a kinetic correlation model, which was formulated based on substrate uptake and product formation rates derived from controlled bioreactor experiments at a 2 L scale. This was integrated into a 1-dimensional model of the bubble column reactor and combined with computational fluid dynamics (CFD) to perform statistical lifeline analysis. Bacterial motion patterns, circulation time, and metabolic short and long-term responses were analysed based on a pseudo-stationary CO gradient. It was shown, that 97% of bacterial cells faced severe CO limitations. 95% of the cells suffered substrate limitation long enough to probably show immediate metabolic responses and 84% were even likely to experience transcriptional modification due to an exposure time of at least 70 s.

In conclusion, the combination of experimental results with metabolic engineering strategies, metabolic modelling and mathematical simulation of large-scale bioreactors is a valuable tool for syngas-based bioprocess development to produce high-value bulk chemicals.

Zusammenfassung

Die bakterielle Synthesegasfermentation stellt eine vielversprechende Lösung für die Reduzierung von Treibhausgasemissionen dar - eine der bedeutendsten Herausforderungen der modernen Gesellschaft. Das Substratgas, welches vorwiegend aus CO_2, CO und H_2 besteht, lässt sich kostengünstig aus landwirtschaftlichen, industriellen und kommunalen Abfällen gewinnen. Mittels verschiedener autotropher Bakterien kann es in eine Vielzahl wertvoller chemischer Grundstoffe und Biokraftstoffe umgewandelt werden. Durch die Synthesegasfermentation können fossile Ressourcen bei gleichzeitiger Verringerung des Treibhausgases CO_2 und Nutzung des Abgases CO ersetzt werden. Ein hervorragender Vertreter der gasfermentierenden Acetogene ist *Clostridium ljungdahlii* (*C. ljungdahlii*), das von Natur aus die Fähigkeit besitzt, Synthesegasbestandteile in Essigsäure, Ethanol, 2,3-Butandiol (2,3-BD) und Laktat zu verstoffwechseln. *C. ljungdahlii* ist zudem genetisch gut zugänglich und bietet somit eine vielversprechende Ausgangsbasis für die rekombinante Produktion hochwertiger Produkte wie Isobutanol. Der autotrophe Zentralstoffwechsel von *C. ljungdahlii* basiert auf dem sogenannten Wood-Ljungdahl Weg (WLP), einem alten und energielimitierten Stoffwechselweg, der einen Protonengradienten zur ATP-Erhaltung nutzt. Bei diesem Stoffwechselweg spielt die Umwandlung von Reduktionsäquivalenten eine entscheidende Rolle, und zwar nicht nur beim Aufbau des für die ATP-Bildung notwendigen Protonengradienten, sondern auch bei der Produktbildung, die in mehreren reduktiven Schritten aus CO_2 gebildet werden. Die Versorgung mit den notwendigen Reduktionsäquivalenten basiert auf der Oxidation der Elektronenquelle im Substratgas - CO mittels Kohlenmonoxid-Dehydrogenase (CODH) oder H_2 durch die bifurkierende Hydrogenase (HYD). Für eine optimale Bildung natürlicher und nicht-natürlicher reduzierter Produkte ist es daher entscheidend, den zellulären Zusammenhang zwischen Energiemanagement, Wachstum, Nebenproduktbildung und der Elektronenverfügbarkeit im Substratgas genau zu verstehen.

In der vorliegenden Arbeit wurden kontrollierte Batch-Kultivierungen mit konstanter Gaszufuhr im 2-Liter-Maßstab durchgeführt, zur Untersuchung von Wachstum und

Produktbildung von *C. ljungdahlii* unter Berücksichtigung unterschiedlicher Substratzusammensetzungen. Als Substrate wurden CO, ein CO_2-H_2 Gemisch und Synthesegas untersucht. Für die anschließende Analyse der intrazellulären Kohlenstoffflüsse sowie des Redox- und Energiestoffwechsels wurde manuell ein stöchiometrisches Stoffwechselmodell rekonstruiert. Mit der Flux-Balance-Analyse (FBA) wurde nachgewiesen, dass die Verfügbarkeit von Elektronen der entscheidende Einflussfaktor für die Produktbildung ist. Die Ausbeute an Produkten je Elektron in C-mol blieb trotz der deutlich voneinander abweichenden Wachstums- und Produktprofile relativ gleich für alle Substrate. CO erwies sich als bevorzugte Kohlenstoff- und Energiequelle, was zu doppelten Wachstumsraten, höchsten ATP-Bildungsraten und den größten Mengen an reduzierten Produkten führte. Bei der Nutzung von H_2 and CO_2 erzeugte *C. ljungdahlii* nahezu ausschließlich Acetat (ca. 9 g L^{-1}), wohingegen bei CO hauptsächlich Ethanol (ca. 5 g L^{-1}) und 2,3-BD (ca. 2 g L^{-1}) gebildet wurde. Das autotrophe Produktspektrum wird maßgeblich von der Bereitstellung reduzierter Ferredoxine (Fd_{red}) bestimmt, dem wichtigsten intrazellulären Steuerungsparameter für ATP-Synthese, Wachstum und Produktbildung in *C. ljungdahlii*. Fd_{red} - Bereitstellung durch CODH oder HYD ist an die Regeneration von NADH und NAPDH gekoppelt, welche über die ATP-Synthese mittels des Rnf-Komplexes, den Methylzweig des WLP und einem Transhydrogenase-ähnlichen Nfn-Komplex abläuft. Beim Einsatz von H_2 entstehen bei der Fd_{red} - Bereitstellung NADH und NADPH, die vollständig durch die Aktivität des Methylzweigs mit abschließender Acetat - und Biomasseproduktion regeneriert werden. Eine CO-induzierte Versorgung mit FD_{red} führt hingegen zu einem Überangebot an Reduktionsäquivalenten, die höhere ATP-Erträge und eine vermehrte Erzeugung von reduzierten Nebenprodukten ermöglichen. Durch H_2-Anreicherung in CO-reichem Synthesegas wurde eine noch höhere Bildung des von NADPH abhängigen Produktes 2,3-BD (ca. 4 g L^{-1}) realisiert. Das Substrat eignet sich daher hervorragend, um mit *C. ljungdahlii* natürliche oder sogar nicht natürliche reduktive Alkohole in Batch-Kulturen zu produzieren.

In enger Zusammenarbeit mit der Arbeitsgruppe von Peter Dürre (Institut für Mikrobiologie und Biotechnologie, Universität Ulm) prüften wir nachfolgend die heterologe, Synthesegas-basierte Isobutanolproduktion von *C. ljungdahlii* in einem

stufenweisen Ansatz. Als erstes wurde ein rekombinanter Stamm entwickelt, der die Umwandlung von Pyruvat zu Ketoisovalerat (KIV) verstärkt und die anschließende Metabolisierung von KIV zu Isobutanol mittels eines rekombinanten Ehrlich-Wegs ermöglicht (*C. ljungdahlii [pKAIA]).* Durch kontrollierte Kultivierungsstudien in kontinuierlich begasten Rührkesselbioreaktoren konnte dieser Stamm physiologisch charakterisiert und mittels intrazellulärer Metabolomik eingehend analysiert werden. So konnten Pyruvat und KIV als limitierende Schlüsselmetabolite identifiziert werden, die die Bildung von Isobutanol auf ein äußerst niedriges Niveau beschränkten. Die zusätzliche Hemmung der Valin-Biosynthese in *C. ljungdahlii::ilvE [pKAIA]* bewirkte eine 6,5-fach erhöhte Isobutanolbildung von 0,13 g L^{-1}. Die FBA wies jedoch auf eine begrenzte intrazelluläre Bereitstellung von NADPH hin, einem möglichen Ziel für zukünftige Metabolic-Engineering-Ansätze.

Im Hinblick auf den Transfer von Synthesegasfermentationen von Labor zum Industriemaßstab wurde untersucht, welche Leistungsverluste während der Kultivierung von *C. ljungdhalii* mit CO in einem 125 m^3 Blasensäulenreaktor auftreten können. Ausgehend von Substrataufnahme- und Produktbildungsraten, die in kontrollierten Bioreaktorexperimenten im 2-Liter-Maßstab gewonnen wurden, wurde ein kinetisches Korrelationsmodell formuliert. Dieses Modell wurde dann in ein 1-dimensionales Modell eines Blasensäulenreaktors integriert und mit der numerischen Strömungsmechanik (CFD) kombiniert, um die statistische Analyse von Lebenslinien zu ermöglichen. Die Bewegungsmuster der Bakterien, die Zirkulationszeit sowie die kurz- und langfristigen Stoffwechselprozesse wurden ausgehend von einem pseudostationären CO-Gradienten analysiert. Es wurde nachgewiesen, dass 97% der Bakterienzellen mit starken CO-Limitationen konfrontiert waren. 95 % der Zellen waren so lange von der Substratbeschränkung betroffen, dass sie mit hoher Wahrscheinlichkeit unmittelbare Stoffwechselreaktionen zeigten. Bei 84 % der Zellen sind wahrscheinlich sogar Transkriptionsänderungen aufgetreten aufgrund einer Expositionszeit von mindestens 70 s.

Abschließend lässt sich festhalten, dass die Kombination von experimentellen Ergebnissen mit Metabolic-Engineering-Strategien, Stoffwechselmodellierung und einer mathematischen Simulation großtechnischer Bioreaktoren, ein nützliches

Instrument bei der Entwicklung Synthesegas-basierter Bioprozesse zur Erzeugung hochwertiger Basischemikalien darstellt.

1 Introduction

The rising global demand for energy, mainly based on fossil resources, brings the world to the edge of its capacity for regeneration. Climate change and environmental damages are the consequences (Benevenuti et al., 2021; Gunes, 2021; Sun et al., 2019). Increasing anthropogenic greenhouse gas emissions that mainly comprise CO_2, clearly exceed CO_2 removal by natural sinks yielding to an advancing global warming (Hepburn et al., 2019; Pavan, 2022). To limit the global average temperature increase to 1.5 °C, according to the Paris Climate Agreement of 2015, it is inevitable to reduce greenhouse gas emissions and explore sustainable non-fossil-based production routes for energy and chemicals (Bengelsdorf and Dürre, 2017; Takors et al., 2018). In this regard, a circular economy, that is characterized by the usage of biomass for the production of biofuels and fine chemicals, represents a promising strategy (Takors et al., 2018). Therefore, biofuel production as well as corresponding research and development is increasingly encouraged through worldwide policy (Daniell et al., 2012). For first-generation biofuels sugar-based food resources are used as substrates. Currently, they are mainly produced in the US, Brazil and the EU utilising corn, sugarcane as well as canola and sunflower, respectively. However, the sustainability of first-generation biofuels is considered to be limited from an environmental, social, and economic view. This is due to the food-versus-fuel debate affected by the intensive use of agricultural land and volatile sugar prices and the negative environmental impacts caused by a rising use of nitrogen fertilizers (Daniell et al., 2012). These disadvantages led to the development of second-generation biofuels that are based on non-food lignocellulosic feedstocks, which accumulates in large quantities as agricultural residues, energy crops, organic wastes, and woody by-products (Liew et al., 2016; Takors et al., 2018). As a result, either biochemical or thermochemical approaches are used for biomass conversion. Biochemical conversion comprises a pre-treatment step followed by hydrolysis and microbial fermentation to biofuels or value-added biocommodities. Pre-treatment of the lignocellulosic biomass is necessary to remove non-fermentable lignin polymers, which increases the accessibility of the cellulose and hemicellulose polymers to the subsequent enzymatic

hydrolysis step. By hydrolysis, sugar monomers are generated, serving as substrates for the successive microbial cultivation step. As the lignin fraction, which accounts for about 10 – 25 % of the biomass, cannot be enzymatically broken down to sugar monomers, a full conversion of the biomass cannot be achieved by the biochemical route. On the contrary, thermochemical conversion by, e.g., gasification or pyrolysis, yields a full conversion of the biomass to synthesis gas (syngas), bio-oils, or hydrocarbon fuels. In this context, syngas fermentation represents a hybrid approach of the two conversion processes characterized by the gasification of the whole lignocellulosic biomass to syngas, which is subsequently microbially fermented to second-generation fuels or value-added chemicals (Gunes, 2021).

1.1 Synthesis gas fermentation - chances and challenges

Syngas is produced by gasifying biomass, animal waste, municipal solid wastes, and coal. In addition, it may be derived from CO-rich off-gases from the steel, chemical, and oil-refining industries. It mainly consists of CO, CO_2, H_2 and N_2 with small amounts of CH_4 and other impurities such as H_2S, NH_3, tar, NO and HCN. Syngas composition strongly depends on the feedstock as well as the gasification approach (oxidizing agent, type of gasifier and operational conditions) (Sun et al., 2019; Takors et al., 2018). During syngas fermentation, mixtures of H_2, CO, and CO_2 are converted by various microorganisms to alcohol, organic acids and other chemicals via hydrogenesis, methanogenesis, or acetogenesis (Takors et al., 2018). Syngas fermentation offers a superior alternative to the thermochemical Fischer-Tropsch process, that converts syngas to liquid hydrocarbon fuels utilizing metal catalysts. This process operates at high temperatures and pressure and requires high H_2/CO ratios > 2. However, microbial syngas fermentation is characterized by near ambient temperature and pressure conditions and thus offers significant energy and expenditure savings. In addition, the biocatalysts possess higher flexibility to the H_2/CO ratios in the substrate gas and a higher tolerance to syngas impurities (Takors et al., 2018). Furthermore, by utilizing genetically modified microbes as well as mixed cultures a wider product spectrum can be achieved with syngas fermentation compared to the Fischer-Tropsch processes (Gunes, 2021; Sun et al., 2019).

However, one major challenge of syngas fermentation is the poor aqueous solubility of the substrate gases CO and H_2 creating gas-liquid mass transfer limitations (Sun et al., 2019; Takors et al., 2018). In addition, the autotrophic growth of acetogens is strongly energy-limited and therefore characterized by low volumetric productivities (Takors et al., 2018). Various reactor modifications and fermentation strategies were analysed to meet these challenges (Sun et al., 2019). Gas-liquid mass transfer can be improved by increasing the volumetric power input or applying increased partial pressures of the poorly soluble substrate gases. With regard to the commercialization and scale-up of syngas fermentation, bubble-column reactors (BCRs) represent a promising reactor system due to the high hydrostatic pressure at the bottom of the reactor based on the reactor height (Takors et al., 2018). In addition, unstirred BCRs are characterized by low energy costs and a simple design (Siebler, 2020). To implement industrial-scale syngas fermentation processes, several challenges must be faced: varying substrate composition and quality, mass-liquid limitations, and low productivity of the microbial conversions with possible performance losses in large-scale bioreactors due to the formations of gradients (Sun et al., 2019; Takors et al., 2018). Nevertheless, LanzaTech succeeded in realizing three commercial-scale plants in China converting steel mill emissions to ethanol. A further production facility is under construction at the ArcelorMittal in Ghent to produce 60.000 m^3 or ethanol based on the CO-rich exhaust gases emitted by the steel manufacturer (Takors et al., 2018).

1.2 Motivation and objectives of this thesis

Syngas fermentation holds great potential for replacing fossil-based production routes for biofuels and bulk chemicals with simultaneous reduction of climate-harmful greenhouse gas emissions. In this regard, *Clostridium ljungdahlii* represents a promising biocatalyst. This anaerobic acetogen can produce its natural products acetate, ethanol, lactate and 2,3-butanediol autotrophically based on syngas, CO solely or a mixture of CO_2 and H_2. In addition, *C. ljungdahlii* is genetically accessible allowing the optimized formation of natural and recombinant products via metabolic engineering (see chapter **2.1**). Therefore, the final goal of this thesis was the bioprocess development for the syngas-based formation of high-value reduced natural

and recombinant by-products with *C. ljungdahlii*. In this context, subsequent process scale-up on a commercial scale should also be considered.

In particular, 2,3-butanediol and isobutanol are very promising target products. 2,3-butanediol is an important chemical precurser for the production of a broad value of downstream products with a potential global market of around 43 billion dollars per year. Among other things, 2,3-butanediol is used in the manufacturing of rubbers, solvents and moisturizers (Köpke et al., 2011b; Siebler, 2020). Isobutanol is also an important platform chemical with rising global market size, that is mainly used as chemical intermediate, in coatings and solvents, and as a biofuel (Grand View Research, 2016; Karabektas and Hosoz, 2009; Ragsdale and Pierce, 2008). It is a promising second generation biofuel substitute because of its lower vapor pressure, volatility, and aqueous miscibility with simultaneously higher combustion power than bioethanol (Atsumi et al., 2010).

C. ljungdahlii uses the Wood-Ljungdahl pathway (WLP) for the fixation of CO_2 or CO to acetyl-CoA, the key precursor for biomass and by-products. This pathway is characterized by very limited ATP formation that is highly dependent on the conversion of reducing equivalents just like growth and by-product formation (see chapter **2.1**). Syngas-based production of value-added by-products with *C. ljungdahlii* can only be realized within an equilibrated redox and ATP balance. This challenging necessity demands a comprehensive understanding of the intracellular link between energy management, product formation and electron availability in the substrate gas. To fulfill this requirement and achieve the main objective of this thesis, the following sub-goals were defined:

I. Manually reconstruction of a genome-scale metabolic model and the conduction of flux balance analysis for the characterization of intracellular carbon fluxes, redox metabolism and energy management.
II. Performance of bioreactor cultivations under controlled cultivation conditions in 2 L scale for the analysis of growth and product formation based on different substrate gas compositions.

III. The thoroughly investigation of recombinant isobutanol formation applying batch cultivations in gassed stirred bioreactors, intracellular metabolomics, and flux balance analysis.

IV. Provision of appropriate experimental data for mathematical modelling of large-scale bioreactors for syngas-based product formation with *C. ljungdahlli.*

2 Theoretical background

2.1 *Clostridium ljungdahlii*

Clostridium ljungdahlii (*C. ljungdahlii*) was first isolated from chicken yard waste for its ability to utilize synthesis gas for acetate and ethanol production (Barik et al., 1988). The bacterium was further characterized as an anaerobic, rod-shaped, gram-positive, motile, and spore-forming acetogen (Tanner et al., 1993). It grows autotrophically on CO, H_2 and CO_2 as well as heterotrophically on a variety of organic compounds (Köpke et al., 2010; Tanner et al., 1993). The pH and temperature for optimal growth are 6.0 and 37°, respectively (Tanner et al., 1993). Its natural product spectrum during autotrophic growth comprises acetate, ethanol, lactate and 2,3-butanediol (2,3-BD) (Köpke et al., 2011b; Köpke et al., 2010; Tanner et al., 1993).

2.1.1 Autotrophic metabolism

Acetogenic bacteria, including *C. jungdahlii*, use the WLP to convert CO_2 and CO into acetyl-CoA, which then serves as the key-precursor for anabolic reactions (Köpke et al., 2010; Ljungdahl, 1986; Wood, 1991). The WLP, also called reductive acetyl-CoA pathway, was first described by Ljungdahl (1986) and Wood (1991) and was further summarized in several outstanding reviews (Drake et al., 2008; Ragsdale and Pierce, 2008; Schuchmann and Müller, 2014). It is a linear pathway that consists of two branches: the methyl branch and the carbonyl branch. In the methyl branch CO_2 undergoes a stepwise six-electron reduction to a methyl group via several one-carbon intermediates that are linked to tetrahydrofolate. In this reaction cascade, one mole of ATP is consumed. In the carbonyl branch the bound methyl group is combined with CO and coenzyme A (CoA) to synthesize acetyl-CoA. A schematic overview of the WLP is shown in **Figure 3.13**. In detail, CO_2 is first reduced to formate by an electron-bifurcating formate dehydrogenase using NADPH and reduced ferredoxin (Fd_{red}) as electron donors (Mock et al., 2015; Wang et al., 2013). Formate is subsequently condensed with tetrahydrofolate (THF) by an ATP-dependent formyl-THF synthetase yielding formyl-THF. In the following steps one water molecule is split off by a methenyl-THF cyclohydrolase forming methenyl-THF, which is then reduced to

methylene-THF via methylene-THF dehydrogenase using NADPH as electron donor (Mock et al., 2015). Methylene-THF is finally reduced to methyl-THF by methylene-THF reductase (MTHFR). The nature of the electrons donors of this reaction is still uncertain. First, it has been postulated that the MTHFR of *C. ljungdahlii* is an NADH and ferredoxin-dependent electron-bifurcating enzyme (Köpke et al., 2010; Mock et al., 2015). Subsequently, it was demonstrated that MTHFR of *C. ljungdahlii* grown on CO is a non-electron-bifurcating enzyme that probably uses reduced ferredoxin as electron carrier, whereas NADPH and NADH are not used. However, this does not allow for a positive ATP gain during autotrophic growth on H_2 + CO_2. Therefore, further research is needed to resolve this enigma (Öppinger et al., 2021; Yi et al., 2021). Finally, the methyl group of methyl-THF is transferred via a methyltransferase and a corrinoid iron-sulfur protein to a subunit of the bifunctional carbon monoxide dehydrogenase (CODH)/ acetyl-CoA synthase (ACS) – the dominating enzyme of the carbonyl branch. For one thing, CODH/ACS catalyses the reversible reduction of CO_2 to CO (the carbonyl group of acetyl – CoA) using ferredoxin as electron carrier (Mock et al., 2015). Secondly the enzyme catalyses the assembly of acetyl-CoA from CO, the methyl-group and CoA.

Acetyl-CoA is converted to pyruvate by pyruvate ferredoxin oxidoreductase (PFOR) using ferredoxin as the electron donor (Mock et al., 2015). This reaction couples the WLP to the anabolic biosynthesis of cellular carbon and the formation of the pyruvate-derived products 2,3-butanediol and lactate (Furdui and Ragsdale, 2000; Köpke et al., 2011b). For lactate formation, one further reaction is needed that is catalysed by lactate dehydrogenase using NADH as the cofactor. 2,3-butanediol formation involves three enzymes (acetolactate synthase, acetolactate decarboxylase and 2,3-butanediol dehydrogenase) and is characterized by the generation of one CO_2 molecule and the use of NADH or NADPH as the electron carrier (Köpke et al., 2014; Köpke et al., 2011a). In addition, acetyl-CoA can be metabolized to acetate via acetyl phosphate by the two enzymes phosphotransacetylase and acetate kinase. In this way, one mole of ATP is generated via substrate-level phosphorylation by the acetate kinase reaction (Köpke et al., 2010). Another acetyl-CoA-derived product is ethanol. On the one hand, acetyl-CoA can be directly converted to ethanol via acetaldehyde using the bifunctional

NAD^+-dependent acetaldehyde/ethanol dehydrogenase. On the other hand, ethanol production can proceed through acetate using the enzyme aldehyde ferredoxin oxidoreductase (AOR). AOR catalyses the ferredoxin-based reduction of acetate to acetaldehyde which again is reduced by the above mentioned ethanol dehydrogenase (Köpke et al., 2010). It has been shown, that the AOR pathway is exclusively used for ethanol production by *C. ljungdahlii* grown on syngas (Richter et al., 2016).

2.1.2 Energy conservation during autotrophic growth

Figure 3.13 shows a schematic overview of the link between ATP synthesis and the WLP. Two mechanisms for energy conservation can be used: substrate-level phosphorylation and ATP synthesis driven by a transmembrane electrochemical ion gradient (Hess et al., 2016; Schuchmann and Müller, 2014). In the WLP, no net ATP is generated via substrate-level phosphorylation, as one mole ATP is consumed during formate activation, which is subsequently regenerated via the acetate phosphate reaction (Drake et al., 2008; Ragsdale and Pierce, 2008; Schuchmann and Müller, 2014). Therefore, for energy conservation during autotrophic growth, *C. ljungdahlii* exclusively refers to an H^+-translocating membrane-bound ATPase driven by a proton gradient. The Rnf complex – a ferredoxin:NAD^+ oxidoreductase (Liang et al., 2019; Mock et al., 2015; Wang et al., 2013) – generates the proton gradient by coupling the electron flow from reduced ferredoxin to NAD^+ with proton translocation across the membrane (Hess et al., 2016; Köpke et al., 2010; Tremblay et al., 2012).

C. ljungdahlii can utilize CO and H_2 to provide reducing equivalents required for both CO_2 reduction and energy conservation (Köpke et al., 2010). Although, the genome of *C. ljungdahlii* contains several hydrogenases, it is assumed that only one electron-bifurcating ferredoxin and $NADP^+$-dependent hydrogenase is used during autotrophic growth. This enzyme supplies the cells with Fd_{red} and NADPH and is also involved in converting CO_2 to formate by forming a complex with formate dehydrogenase of the WLP (Köpke et al., 2010; Mock et al., 2015; Wang et al., 2013). Using CO as substrate, reducing equivalents are provided by the CODH reaction described in **Figure 3.13.**

Besides the WLP, the NADH-dependent reduced ferredoxin:$NADP^+$ oxidoreductase (Nfn) is also decisively involved in energy conservation via chemiosmotic

phosphorylation by exchanging electrons among different electron carriers. This enzyme is an electron bifurcating transhydrogenase that catalyses the endergonic reduction of $NADP^+$ with NADH coupled to the exergonic reduction of $NADP^+$ with Fd_{red} in a reversible reaction (Liang et al., 2019; Mock et al., 2015; Wang et al., 2013).

2.1.3 Gas fermentation

C. ljungdahlii is able to utilize syngas, solely CO or mixtures of H_2 and CO_2, H_2 and CO as well as CO and CO_2 as energy and carbon source (Köpke et al., 2010; Tanner et al., 1993). Gas fermentation approaches with *C. ljungdahlii* applying different cultivation modes and conditions are described in several publications. **Table 2.1** gives a comparative summarize of the main results of various gas fermentation studies with *C. ljungdahlii*. The experimental results of the different studies are difficult to compare due to inconsistent cultivation conditions between the research groups (e.g., cultivation mode, reactor type, substrate gas composition, medium composition, pH, pressure, preculture conditions etc.). Nevertheless, the results indicate that acetate and ethanol are the main products during autotrophic cultivation. Small amounts of 2,3-BD were produced by applying batch cultivation approaches with CO-rich substrate gases (Köpke 2011, Jack 2019). A clearly higher 2,3-BD concentration was achieved with a pH and pressure-controlled batch cultivation in a stirred tank reactor (STR) with a continous supply of a CO-rich substrate gas (Zhu et al., 2020). Using controlled continuous cultivation modes especially with cell recycling, high product concentrations of up to 50 g L^{-1} can be achieved (Martin et al., 2016; Phillips et al., 1993; Richter et al., 2016; Richter et al., 2013). In addition, growth and product formation can be affected by the substrate composition and the pH of the growth medium. Higher CO concentration favors the production of more reduced products (Jack et al., 2019; Phillips et al., 1994; Zhu et al., 2020). Applying two-stage processes, ethanol selectivity can also be increased by a lower pH value in the second solventogenic stage (Martin et al., 2016; Perez et al., 2013). However, a lower initial pH value may have a negatively affect growth and, therefore, yield lower final ethanol concentrations (Cotter et al., 2009). Furthermore, it can be assumed that ATP generation via the Rnf-ATPase system is affected by the pH value of the growth medium (Tremblay et al., 2012). Therefore, a constant optimal pH value during the whole fermentation may favor ATP

production and strongly influence growth and product formation, respectively (Zhu et al., 2020).

Table 2.1: Comparative summary of different autotrophic cultivation studies with *C. ljungdahlii.*

Cultivation mode	**Substrate composition**	**Temperature**	**pH**	**Biomass formation**	**Product formation**	**Reference**
Continous cultivation in a stirred tank reactor (CSTR) with cell recycle	55% CO, 20% H_2, and 10% CO_2	36 °C	pH = 4.5 (controlled)	Cell dry weight (CDW) = 4.0 g L^{-1}	3 g L^{-1} acetate 48 g L^{-1} ethanol	(Phillips et al., 1993)
Batch cultivation in serum bottles with batchwise replenishment of the substrate gas	75% H_2 and 25% CO_2	37 °C	pH = 4.5 (maintained by batchwise base addition)	μ_{exp} = 0.03 h^{-1}*	Ethanol to acetate ratio:0.30	(Phillips et al., 1994)
	80% CO and 20% CO_2			μ_{exp} = 0.06 h^{-1}*	Ethanol to acetate ratio:0.66	
Batch cultivation in serum bottles with one-time feeding of the substrate gas prior inoculation	55% CO, 20% H_2, and 10% CO_2	37 °C	Not indicated	CDW = 1.2 g L^{-1}	1.3 g L^{-1} acetate 0.55 g L^{-1} ethanol	(Younesi et al., 2005)
Batch cultivation in a flask with continuous gas supply	20% CO, 10% H_2, and 20% CO_2	37 °C	Initial pH = 5.5 (not controlled)	CDW = 0.4 g L^{-1}	2.1 g L^{-1} acetate 0.08 g L^{-1} ethanol	(Cotter et al., 2009)
			Initial pH = 6.8 (not controlled)	CDW = 0.6 g L^{-1}	2.1 g L^{-1} acetate 0.18 g L^{-1} ethanol	

Cultivation mode	Substrate composition	Temperature	pH	Biomass formation	Product formation	Reference
Batch cultivation in serum bottles with one-time feeding of the substrate gas prior inoculation	44% CO, 2% H_2, and 22% CO_2	37 °C	Initial pH = 5.9* (not controlled)	OD_{600nm} ~ 1.0	1.68 g L^{-1} acetate* 1.01 g L^{-1} ethanol* 0.14 g L^{-1} 2,3-BD*	(Köpke et al., 2011b)
Two-stage CSTR system (STR + bubble column reactor with cell recycle); Stage 1: Dilution rate (D) = 0.04h^{-1} Stage 2: D = 0.01 h^{-1}	60% CO, 35% H_2, and 5% CO_2	35 °C	Stage 1: pH = 5.5 (controlled) Stage 2: pH = 4.4 - 4.8 (controlled)	CDW = 9.3 g L^{-1}	8.6 g L^{-1} acetate 19.7 g L^{-1} ethanol	(Richter et al., 2013)
Two-stage CSTR system (STR + bubble column reactor with cell recycle); Stage 1: D = 0.04 h^{-1} Stage 2: D = 0.01 h^{-1}	60% CO, 35% H_2, and 5% CO_2	35 °C	Stage 1: pH = 5.5 (controlled) Stage 2: pH = 5.5 - 4.5 (controlled)**	CDW = 5.0 g L^{-1}	4.5 g L^{-1} acetate 19.0 g L^{-1} ethanol	(Martin et al., 2016)
Batch cultivation in a STR with continuous gas supply	80% CO, and 20% CO_2	37 °C	Initial pH = 5.9* (not controlled)	OD_{600nm} ~ 1.5	5.0 g L^{-1} acetate 0.8 g L^{-1} ethanol	(Xie et al., 2015)

Cultivation mode	Substrate composition	Temperature	pH	Biomass formation	Product formation	Reference
Batch cultivation in a STR with continuous gas supply	32.5% CO, 32.5% H_2, and 16% CO_2	37 °C	pH = 5.9 (controlled)	CDW = 0.3 g L^{-1}	15.9 g L^{-1} acetate 2.0 g L^{-1} ethanol	(Oswald et al., 2016)
Batch cultivation in a STR with continuous gas supply	53.3% H_2, and 26.7% CO_2	37 °C	pH = 5.9* (controlled)	Not indicated	9.3 g L^{-1} acetate 2.8 g L^{-1} ethanol	(Oswald et al., 2018)
Batch cultivation in serum bottles with one-time feeding of the substrate gas prior inoculation	40% CO, 20% H_2, and 10% CO_2*	37 °C	Initial pH = 7.0 (not controlled)	OD_{600nm} ~ 0.45	1.4 g L^{-1} acetate* 0.25 g L^{-1} ethanol* 0.47 g L^{-1} 2,3-BD*	(Jack et al., 2019)
	20% CO, 40% H_2, and 10% CO_2*			OD_{600nm} ~ 0.45	2.1 g L^{-1} acetate* 0.34 g L^{-1} ethanol*	
Batch cultivation in a STR with continuous gas supply and a constant pressure of 0.1 MPa	80% CO, and 20% CO_2	37 °C	pH = 6.0 (controlled)	OD_{600nm} = 8.4	3.1 g L^{-1} acetate* 15.5 g L^{-1} ethanol* 2.1 g L^{-1} 2,3-BD*	Zhu et al. (2020)
	60% H_2, and 20% CO_2			OD_{600nm} = 1.6	8.5 g L^{-1} acetate*	

* Calculated/derived on the basis of literature data

** pH value was gradually decreased from OD_{600nm} of 10

2.1.4 Metabolic engineering and recombinant product formation

C. ljungdahlii represents an important gas-fermenting chassis for the recombinant formation of biocommodities and fuels. Various DNA transfer and gene expression methods were applied to either improve substrate utilisation and native product formation or to realize recombinant production of non-native biochemicals (Jin et al., 2020). It was demonstrated that the carbon and electron flow in *C. ljungdahlii* can be redirected from acetate to ethanol by gene deletion via homologous recombination as well as the utilization of a lactose-inducible plasmid-based gene expression system (Banerjee et al., 2014; Leang et al., 2013). Köpke et al. (2010) first engineered a recombinant butanol-producing *C. ljungdahlii* strain with syngas as substrate using a plasmid for gene expression. In addition, it was demonstrated that *C. ljungdahlii* is natively endowed to metabolize butanol to butyrate in the presence of another substrate (Köpke et al., 2010). Effective autotrophic heterologous butyrate formation with carbon and electron yields up to 73% in butyrate was also achieved by chromosomal insertion of plasmids (Ueki et al., 2014). Using plasmid-based gene expression systems, further autotrophically grown *C. ljungdahlii* strains were engineered for the recombinant formation of acetone and 2-propanol (Banerjee et al., 2014; Bengelsdorf et al., 2016), 3-hydroxybutyrate (Woolston et al., 2018), poly(3-hydroxybutyrate) (Flüchter et al., 2019), as well as mevalonate and isoprene (Diner et al., 2018). Furthermore, transfer and genomic integration of an entire heterologous acetone biosynthesis pathway resulting in acetone and isopropanol formation was achieved by transposon mutagenesis (Philipps et al., 2019). Employing ClosTron™ and CRISPR-Cas systems for strain engineering, the genetic toolbox for *C. ljungdahlii* was further expanded (Bengelsdorf et al., 2016; Huang et al., 2016; Woolston et al., 2018; Zhao et al., 2019).

2.1.5 Systems biology and omics data

Systems biology aims at the holistic and quantitative understanding of the function of cellular systems by analysing the cellular phenotype at different control levels as well as the interaction between these control layers (Fiehn, 2001; Takors et al., 2007). Therefore, datasets on the genome, transcriptome, proteome, metabolome, and

fluxome level of a cell are measured by applying corresponding ‘omics’ techniques. Genomics enabled the sequencing and characterization of the complete *C. ljungdahlii* genome (Köpke et al., 2010). Furthermore, transcriptome analysis was employed to analyse genome-wide gene expression levels of gas-fermenting *C. ljungdahlii*. In this way, genes were identified, that are important for autotrophic carbon fixation and energy metabolism as well as ethanol formation, and therefore represent possible metabolic engineering targets (Aklujkar et al., 2017; Tan et al., 2013; Whitham et al., 2015). In addition, *C. ljungdahlii’s* response to different energy sources at the transcriptional level was analysed (Zhu et al., 2020). By linking transcriptomics to ribosome profiling, Al-Bassam et al. (2018) were also able to investigate the translational efficiency of critical pathways related to carbon and energy metabolism of *C. ljungdahlii* fermenting different energy sources. Both studies identified CODH and AOR to play an important role in CO utilisation and alcohol formation. Finally, a combined approach of proteomics and metabolomics revealed that nutrient limitation result in ethanol production that is regulated by thermodynamics rather than different enzyme expression (Richter et al., 2016).

2.2 Genome-scale metabolic modelling

Genome-scale metabolic models (GEMs) are powerful tools for the system-level analysis of microbial metabolism. GEMs are generated based on multi-omics data and represent a mathematical description of an organism's metabolism. Using genome-scale reconstruction of microbial biochemical networks, the relationship between all known metabolic reactions and the corresponding metabolic genes of an organism can be depicted. The resulting reaction networks, in turn, can be used to computationally predict different cellular behavior based on specific genotypes. In this way, microbial growth and product formation in dependence on various substrates as well as new metabolic engineered strains can be studied in silico prior to performing respective lab experiments (Daniell et al., 2016; O'Brien et al., 2015).

The stepwise generation of GEMs was described by Thiele and Palsson (2010) and vividly reviewed by Hamilton and Reed (2014) and O'Brien et al. (2015). In short, the reconstruction process is divided into four stages: draft reconstruction, manual curation, mathematically representation and evaluation. First, a collection of biochemical reactions is generated based on the annotated genome of an organism in consideration of gene-protein-reaction relationships. Then, the network draft is thoroughly curated based on organism-specific expert knowledge, primary literature, and experimental data. Besides the verification of gene-protein-reaction associations, this stage focuses on the revision of the directionality, stoichiometry, as well as substrates, products, and cofactors of the reactions with their physiological charges. Prior to the conversion to a GEM that can be used for computational predictions, additional reactions have to be added to the network assembly to describe biomass formation, cellular maintenance costs, and the transport of metabolites and media components. Afterwards, the network reconstruction can be transferred to a mathematical format using a numerical matrix to describe the stoichiometric coefficients of each metabolic reaction. In the final stage, for model evaluation, mathematical simulations are applied to identify metabolic dead ends, and gaps and to check for blocked reactions, and stoichiometric imbalances. Finally, the GEM is validated against experimentally derived data.

2.2.1 Genome-scale metabolic models of acetogens

For the comprehensive characterization of acetogenic metabolism, several GEMs for different gas-fermenting acetogens were published, as summarized in **Table 2.2** Nagarajan et al. (2013) published the first GEM of an acetogen, named iNH637, that was able to predict the phenotype of *C. ljungdahlii* in dependence of different hetero- and autotrophic substrate conditions. In addition, it was demonstrated that electron bifurcation and the activity of the Rnf complex are crucial for *C. ljungdahlii*'s autotrophic energy metabolism. Moreover, a novel nitrate reduction pathway for ammonia assimilation was identified and validated. Secondly, a GEM of *Moorella thermoacetica (M. thermoacetica)*, named *i*AI558, was generated (Islam et al., 2015). This model was able to simulate the growth and ATP production of *M. thermoacetica* with different heterotrophic and autotrophic substrates. In addition, it was revealed, that the degenerative TCA cycle of acetogens only provides precursors for biosynthesis and catabolic reaction without contributing to catabolic ATP formation. Furthermore, a feasible energy conservation process of autotrophically grown *M. thermoacetica* was postulated based on modelling results. Moreover, Marcellin et al. (2016) generated a GEM for the acetogenic microorganism *C. autoethanogenum*, named iCLAU786, to evaluate experimentally derived omics data. By comparative simulation of growth and by-product formation on fructose and syngas they demonstrated the importance of the Rnf and Nfn complex in redox balancing during autotrophic growth. Moreover, a new glyceraldehyde-3-phosphate dehydrogenase (GAPDH) was identified, that leads to a potential reduction of ATP consumption during gluconeogenesis. This GEM was further refined and extended by Valgepea et al. (2017a) and used in several subsequent publications for the system-level analysis of *C. autoethanogenums'* autotrophic metabolism. In this way, among other simulative findings, arginine could be identified as a growth-boosting supplement, a Fd_{red} – dependence of the methylene THF reductase reaction was predicted, and the direct reduction of CO_2 to formate through a formate-H_2 lyase activity was revealed (Heffernan et al., 2020; Valgepea et al., 2018; Valgepea et al., 2017a; Valgepea et al., 2017b). Moreover, another GEM for *C. autoethanogenum* was generated, named MetaCLAU (Norman et al., 2019). In contrast to the previously published iCLAU786, this model was complemented with

species-specific parameters describing ATP maintenance costs and biomass formation. Subsequent model-simulations revealed a considerable increase in 2,3-BD formation under non-carbon-limited culture conditions.

Table 2.2: Comparative summary of published acetogenic GEMs

Organism	Meta-bolites	Reactions	Main simulative results	Reference
C. ljungdahlii	698	785	• Growth prediction in dependence of different substrate conditions • Identification and validation of a novel nitrate reduction pathway	Nagarajan et al. (2013)
M. thermoacetica	698	705	• Characterization of heterotrophic and autotrophic metabolic phenotypes • Analysis of autotrophic energy conservation process	Islam et al. (2015)
C. auto-ethanogenum	1075	1002	• Simulation of hetero- and autotrophic growth and by-product formation • Identification of a novel gluconeogenic GAPDH	Marcellin et al. (2016)
C. auto-ethanogenum	1097	1109	• In silico identification of an alternative ATP-generating pathway and growth-enhancing nutrients	Valgepea et al. (2017a)
C. auto-ethanogenum	772	775	• Considerable 2,3-BD production under non-carbon-limited conditions	Norman et al. (2019)

2.2.2 Flux Balance Analysis

Most simulations performed on a GEM use flux-balance-analysis (FBA), a constraint-based algorithm, to calculate the flow of metabolites through a metabolic network. In this way, the prediction of different phenotypes of an organism based on various culture conditions is made possible (Hamilton and Reed, 2014; Orth et al., 2010).

The first step of the FBA is the mathematical representation of the metabolic reactions. Therefore, a numerical matrix of the stoichiometric coefficients of each reaction with rows corresponding to the metabolites and columns representing the reactions is used. The rates at which every metabolite is consumed or produced by every reaction is constrained by the coefficients of each reactions, the mass balance constraint at steady state, and the upper and lower bounds of every reaction. This defines the space of the allowable flux distributions in a system (Orth et al., 2010).

At the next step of the FBA, a phenotype of interest e.g., maximum biomass formation, is defined in the form of an objective function. Then, a system of linear equations is generated that can be solved by linear programming. The resulting solution represents one optimal point within a constrained space (Orth et al., 2010).

In this way, the FBA can be used to solve a mathematical system with more variables than equations. This applies to most GEMs that are characterized by more reactions than metabolites. In addition, FBA can be calculated very quickly even for large reaction networks as it does not rely on kinetic parameters. However, this also leads to the fact, that no metabolite concentrations can be predicted. Furthermore, FBA in its original form does not consider cellular regulatory effects and is only applicable for steady-state analysis (Orth et al., 2010). Nevertheless, to enable an accurate reflection of the real physiological state of an organism the solution space can be restricted by experimentally derived knowledge (O'Brien et al., 2015).

2.3 Microbial cultivation in batch processes

Microbial cultivation processes can be performed in batch, fed-batch, and continuous mode. Batch processes are characterized by an initial unlimited substrate supply and a fixed cultivation volume during the course of the cultivation. The growth curve - increase in biomass over time - is usually used to describe microbial cultivation processes. After inoculation of a sterile medium that contains all the nutrients for growth with suitable cultivation conditions (e.g., temperature and pH) the microorganisms show typically a six-phase growth behaviour (see **Figure 2.1**), as described by Monod (1949). First, the microorganisms may have to adapt their metabolism to the potential new cultivation conditions showing no growth during the initial lag-phase. Subsequently, the cells accelerate their growth until they enter the exponential growth phase, which is characterized by a constant unlimited growth rate μ_{max}. As substrate consumption and product formation are also assumed to be constant during this period, the exponential growth phase is also referred to the “pseudo metabolic steady state” of the cells. As soon as the cultivation conditions no longer allow for unlimited growth, for example, due to a limitation of at least one nutrient or accumulation of an inhibiting product, a reduction in growth is observed. This deceleration phase is followed by the stationary phase, in which the growth and death rate are in equilibrium. In the phase of decline, cell lysis finally predominates.

Assuming mass balance in a closed system and only one growth-limiting substrate, the specific growth rate μ (in h^{-1}) is mathematically described by the Monod-equation (Monod, 1949) **(18)**

$$\mu = \mu_{max} * \frac{c_S}{K_S + c_S} \tag{1}$$

where μ_{max} (in h^{-1}) represents the maximum growth rate for the installed cultivation conditions. The maximum growth rate μ_{max} can theoretically be achieved if the substrate concentration c_S (in g L^{-1}) is much greater than the half-saturation constant K_S (in g L^{-1}). K_S is equal to the substrate concentration that leads to the half maximum

growth rate. This assumption is considered true during the exponential growth phase of a batch culture.

The growth rate μ is coupled to the biomass-specific substrate consumption rate q_s (in g g^{-1} h^{-1}) via the biomass substrate yield $Y_{X/S}$ according to the following equation **(2)**

$$Y_{X/S} = \frac{dc_X}{dc_S} = \frac{\mu}{q_S} \tag{2}$$

where $Y_{X/S}$ (in g g^{-1}) represents the ratio between the amount of produced biomass and the amount of consumed substrate.

In the same manner, the biomass-specific substrate rate is related to the biomass-specific product formation rate q_P via the biomass product yield $Y_{X/P}$ according to the following equation **(3)**

$$Y_{X/P} = \frac{dc_X}{dc_P} = \frac{\mu}{q_P} \tag{3}$$

where $Y_{P/S}$(in g g^{-1}) represents the ratio between the amount of produced biomass and the amount of formed product.

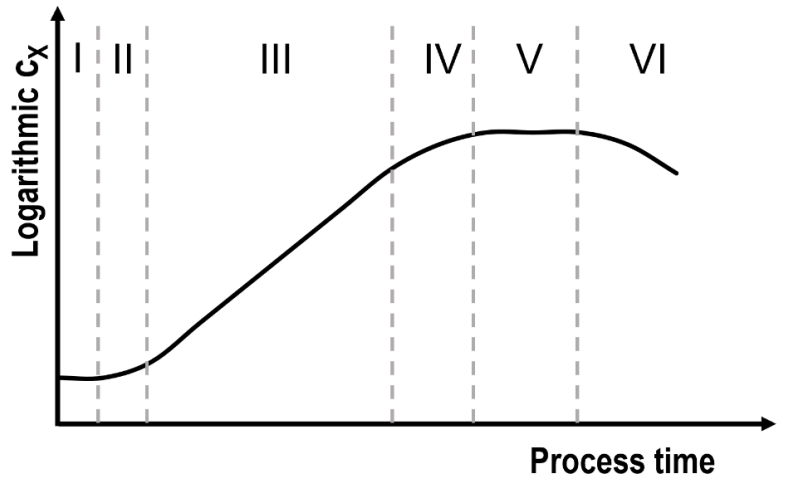

Figure 2.1: Illustration of idealised microbial growth during a batch cultivation by means of a semilogarithmic plot of the biomass concentration (C_X) over the process time. (I) Lag phase; (II) acceleration phase; (III) exponential phase; (IV) retardation phase; (V) stationary phase; (VI) phase of decline.

3 Results: Publications

This doctoral thesis contributed to four peer-reviewed publications, that are presented below:

I. Electron availability in CO_2, CO and H_2 mixtures constrains flux distribution, energy management and product formation in *Clostridium ljungdahlii* (Hermann et al., 2020)
II. Isobutanol production by autotrophic acetogenic bacteria (Weitz et al., 2021)
III. Identifying and engineering bottlenecks of autotrophic isobutanol formation in recombinant *C. ljungdahlii* by systemic analysis (Hermann et al., 2021)
IV. The impact of CO gradients on *C. ljungdahlii* in a 125 m^3 bubble column: Mass transfer, circulation time and lifeline analysis (Siebler et al., 2019)

The main part of this thesis is covered in manuscripts I – III due to thematic proximity. In addition, a proof of concept is shown in manuscript IV for the combination of experimental data with large-scale simulation to predict possible performance losses within process transfer into commercial scales.

To improve readability of this thesis some formatting changes were performed to the original published manuscripts. In addition, references of every publication were combined in the overall reference section of this dissertation. Content, tables and illustrations have not been changed.

3.1 Authors contribution

All publications have been prepared in close cooperation with other researchers and colleagues of the Institute of Biochemical Engineering of the University of Stuttgart led by Prof. Takors and the Institute of Microbiology and Biotechnology of the Ulm University of Ulm headed by Prof. Dürre. The detailed contributions of the individual authors to the respective publications are summarized in Table 3.1.

Manuscript	Author contribution
I	Maria Hermann (MH) and Ralf Takors (RT) conceived the study. MH performed the bioreactor experiments, reconstructed the stoichiometric model, performed flux balance analyses, and supported the laboratory conversion. Attila Teleki (AT) and MH designed and performed the metabolomics analysis. Andreas Freund (AF) designed and set up the laboratory for the performance of synthesis gas bioreactor studies. Alexander Niess (AN) and RT advised the network reconstruction and flux balance analysis. MH, Sandra Weitz (SW), Frank R. Bengelsdorf (FB), and RT analysed the datasets and wrote the manuscript. All authors contributed to the article and approved the submitted version.
II	SW, FB, MH, RT, and Peter Dürre (PD) conceived and designed the experiments. SW and Sonja Linder (SL) performed the experiments. SW, MH, SL, FB, RT, and PD analysed and discussed the data. MH, SL, FB, RT, and PD wrote the manuscript. All authors contributed to the article and approved the submitted version.
III	MH and RT conceived the study. MH performed the bioreactor experiments, reconstructed the stoichiometric model, performed flux balance analyses, and supported the laboratory conversion. AT and MH designed and performed the metabolomics analysis. AF designed and set up the laboratory for the performance of synthesis gas bioreactor studies. AN and RT advised the network reconstruction and flux balance analysis. SW constructed the recombinant strains CLJU[KAIA] and CLJU[KAIA]:ilvE. FB and PD supervised the strain reconstruction and advised the study. MH, SW, FB, PD and RT analysed the datasets and wrote the manuscript. All authors contributed to the article and approved the submitted version.
IV	Flora Siebler (FS) conducted the simulation, evaluation and writing of the manuscript. MH provided the experimental uptake and production rates. RT and Alexei Lapin (AL) advised the study.

3.2 Manuscript I: Electron availability in CO_2, CO and H_2 mixtures constrains flux distribution, energy management and product formation in *Clostridium ljungdahlii*

Maria Hermann, [1] Attila Teleki, [1] Sandra Weitz, [2] Alexander Niess, [1] Andreas Freund, [1] Fank R. Bengelsdorf [2] and Ralf Takors [1,*]

[1]Institute of Biochemical Engineering, University of Stuttgart, Allmandring 31, 70569 Stuttgart, Germany

[2] Institute of Microbiology and Biotechnology, Ulm University, Albert-Einstein-Allee 11, 89069 Ulm, Germany

*Corresponding author. Prof. Dr.-Ing. Ralf Takors

takors@ibvt.uni-stuttgart.de

SUMMARY

Acetogens such as *Clostridium ljungdahlii* can play a crucial role reducing the human CO_2 footprint by converting industrial emissions containing CO_2, CO and H_2 into valuable products such as organic acids or alcohols. The quantitative understanding of cellular metabolism is a prerequisite to exploit the bacterial endowments and to finetune the cells by applying metabolic engineering tools. Studying the three gas mixtures CO_2+H_2, CO and CO+CO_2+H_2 (syngas) by continuously gassed batch cultivation experiments and applying flux balance analysis, we identified CO as the preferred carbon and electron source for growth and producing alcohols. However, the total yield of moles of carbon (mol-C) per electrons consumed was almost identical in all setups which underlines electron availability as the main factor influencing product formation. The Wood-Ljungdahl pathway (WLP) showed high flexibility by serving as the key NAD^+ provider for CO_2+H_2 whereas this function was strongly compensated by the transhydrogenase-like Nfn complex when CO was metabolized. Availability of reduced ferredoxin (Fd_{red}) can be considered as a key determinant of metabolic control. Oxidation of CO via carbon monoxide dehydrogenase (CODH) is the main route of Fd_{red} formation when CO is used as substrate, whereas Fd_{red} is mainly regenerated via the methyl branch of WLP and the Nfn complex utilizing CO_2+H_2. Consequently, doubled growth rates, highest ATP formation rates, and highest amounts of reduced products (ethanol, 2,3-butanediol) were observed when CO was the sole carbon and electron source.

INTRODUCTION

Climate protection and sustainability are two of the greatest challenges for today's society and for decision-makers in politics and in industry. In this context, bacterial synthesis gas (syngas) fermentation represents a promising technology for the sustainable production of commodity chemicals and biofuels. It offers a possibility to replace fossil-based resources while reducing the Greenhouse Gas carbon dioxide (CO_2) and utilizing the waste gas carbon monoxide (CO) (Bengelsdorf and Dürre, 2017; Takors et al., 2018). For instance, this was already achieved by using exhaust

gas of the steel industry as a carbon source (LanzaTech Press release, 2018). Alternately, syngas, a mixture mainly comprising CO, CO_2 and hydrogen (H_2), may be utilized as an inexpensive feedstock because it is derived from agricultural, industrial and municipal wastes (Bengelsdorf and Dürre, 2017; Takors et al., 2018). Syngas could be metabolized via hydrogenesis, methanogenesis or acetogenesis by a multitude of anaerobic bacteria thereby accessing a wide range of products (Diender et al., 2015; Latif et al., 2014; Takors et al., 2018). One popular representative of gas-fermenting acetogenic bacteria is *C. ljungdahlii*. The strain was isolated in 1993 from chicken yard waste (Tanner et al., 1993). Characteristically, this bacterium shows a wide substrate spectrum. Beside different sugars, it can metabolize syngas autotrophically, CO solely and a mixture of CO_2 and H_2 to form the natural products acetate, ethanol, 2,3-butanediol, and lactate (Köpke et al., 2011b; Köpke et al., 2010; Tanner et al., 1993). In addition, *C. ljungdahlii* is genetically accessible enabling metabolic engineering for the optimized formation of natural and non-natural products (Huang et al., 2019; Molitor et al., 2017; Woolston et al., 2018).

As a prerequisite of further strain application, it is crucial to understand energy and redox management in acetogens, as they are known to live at the thermodynamic edge of life (Schuchmann and Müller, 2014). *C. ljungdahlii* uses the WLP for the fixation of CO_2 and CO (Köpke et al., 2010). The pathway consists of two branches and is characterized by the stepwise reduction of CO_2 to a methyl group that is combined with CO and CoA to generate acetyl-CoA, consuming one ATP. The conversion of acetyl-CoA to acetate provides *C. ljungdahlii* one possibility to gain one ATP via substrate-level phosphorylation (Drake et al., 2008; Ragsdale, 2008; Schuchmann and Müller, 2014). Consequently, no net ATP is produced via central metabolism which is why *C. ljungdahlii* relies on a proton gradient coupled to an H^+- translocating ATPase to obtain additional ATP. To establish the proton gradient, the membrane ferredoxin:NAD^+ oxidoreductase (Rnf complex) catalyzes the oxidation of Fd_{red} while transferring electrons to NAD^+. For providing crucial reducing equivalents either oxidation of CO via CODH or of H_2 by a bifurcating hydrogenase (HYD) is used (Köpke et al., 2010; Müller et al., 2008; Tremblay et al., 2012; Wang et al., 2013). Reducing equivalents are not only needed to enhance ATP formation, they are electron donors

for native products such as ethanol and 2,3-butanediol, too (Köpke et al., 2011b; Köpke et al., 2010). Therefore *C. ljungdahlii* can regulate its ATP availability by redirecting the reducing equivalents in different by-products (Mock et al., 2015; Molitor et al., 2017; Norman et al., 2019; Richter et al., 2016; Valgepea et al., 2017b). Apparently, this links cellular energy formation, growth, and by-product formation with the electron availability in the gas mixture, the core topic of this study. We investigated growth kinetics and by-product formation of *C. ljungdahlii* as a function of varying substrate compositions. Hence, bioreactor cultivations were performed installing controlled cultivation conditions in 2 L scale using the three different substrates CO, a mixture of CO_2 and H_2 and syngas. Intracellular carbon fluxes, redox metabolism and energy management was further characterized using flux balance analysis by coupling the experimentally observed uptake and production rates with a manually reconstructed genome-scale metabolic model.

RESULTS

Comparative autotrophic batch cultivation of *C. ljungdahlii* with different substrate conditions

Growth kinetics: To gain a better understanding of the carbon and energy metabolism of *C. ljungdahlii* we compared growth, product formation and substrate uptake for different substrates (**Figure 3.1** and **Figure 3.2**). The respective total substrate-to-biomass and substrate-to-product yields are summarized in **Table 3.2**. Batch cultivations were performed in steadily gassed 2 L bioreactors using the compositions **CO**, **CO_2+H_2**, and **syngas** in duplicates. Detailed gas compositions are described in the Experimental procedures section. In the presence of CO two growth phases occurred with an exponential growth rate of μ_{exp} = 0.06 ± 0.004 h^{-1} [average ± standard deviation] on CO and μ_{exp} = 0.04 ± 0.007 h^{-1} on syngas during the first, and lowered growth with μ_{exp} = 0.01 ± 0.002 h^{-1} on CO and μ_{exp} = 0.01 ± 0.001 h^{-1} on syngas during the following period. On contrary, *C. ljungdahlii* showed steady exponential growth with μ_{exp} = 0.024 ± 0.003 h^{-1} utilizing CO_2+H_2. After approximately 140 h the maximum cell dry weight (CDW) of 0.93 ± 0.08 g L^{-1} and CDW = 0.76 ± 0.06 g L^{-1} was achieved

representing 6.8 ± 0.7 % and 2.7 ± 0.1 % of totally captured CO and syngas, respectively. The CO_2+H_2 approach fixed 3.1 ± 0.1 % of captured carbon as biomass reaching maximum CDW = 0.26 ± 0.001 g L^{-1} already after 120 h.

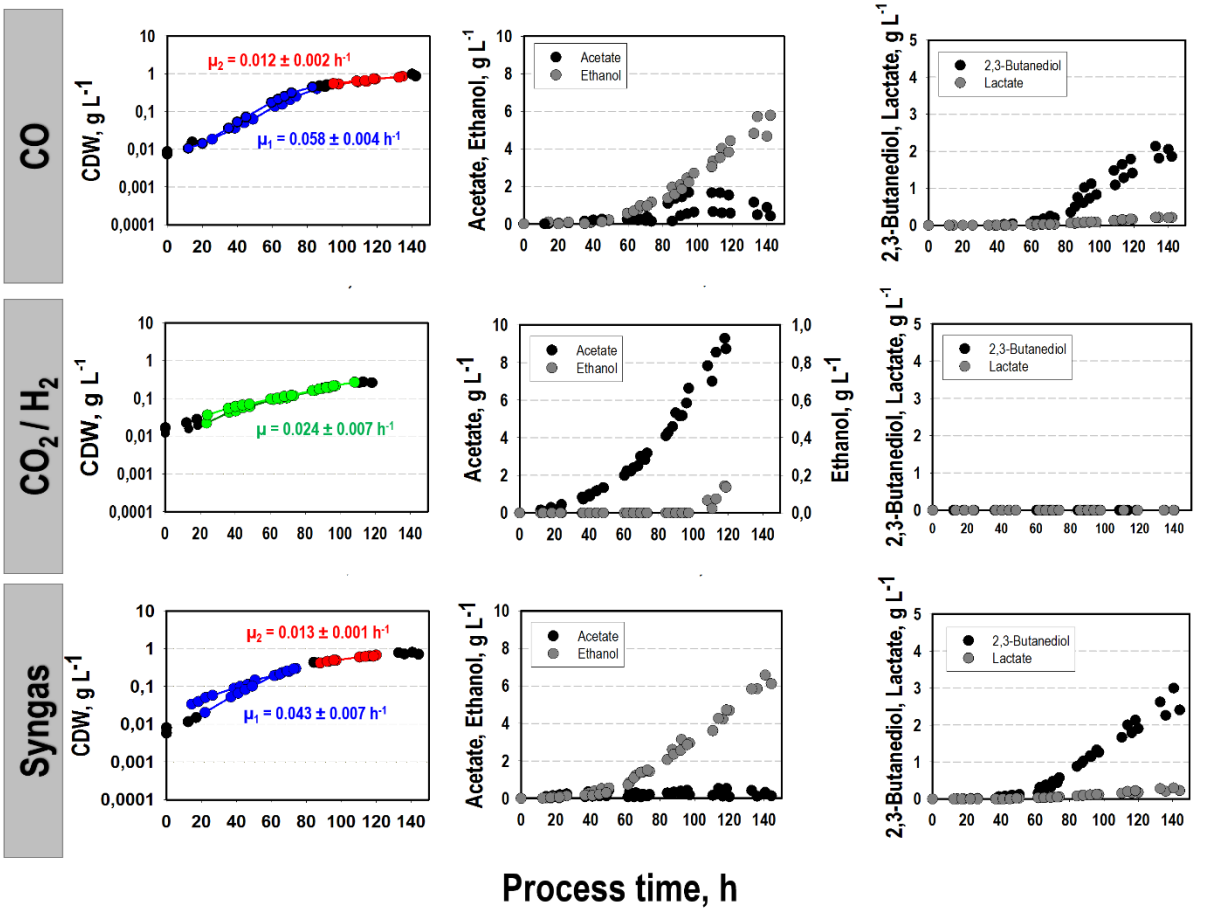

Figure 3.1: Comparative analysis of growth and product formation of *C. ljungdahlii* based on the conversion of CO, CO_2 + H_2 or syngas in steadily gassed batch cultivations using stirred-tank bioreactor. For each substrate condition, two independent experiments were performed that are demonstrated by individual graphs (T= 37 °C; pH = 5.9; V_R = 3 L; 500 rpm). To determine the respective growth rate, we performed regression fitting for each data set. Growth rates μ and coefficients of determination R^2 are given in the Supplementary Material (**Table 7.5**).

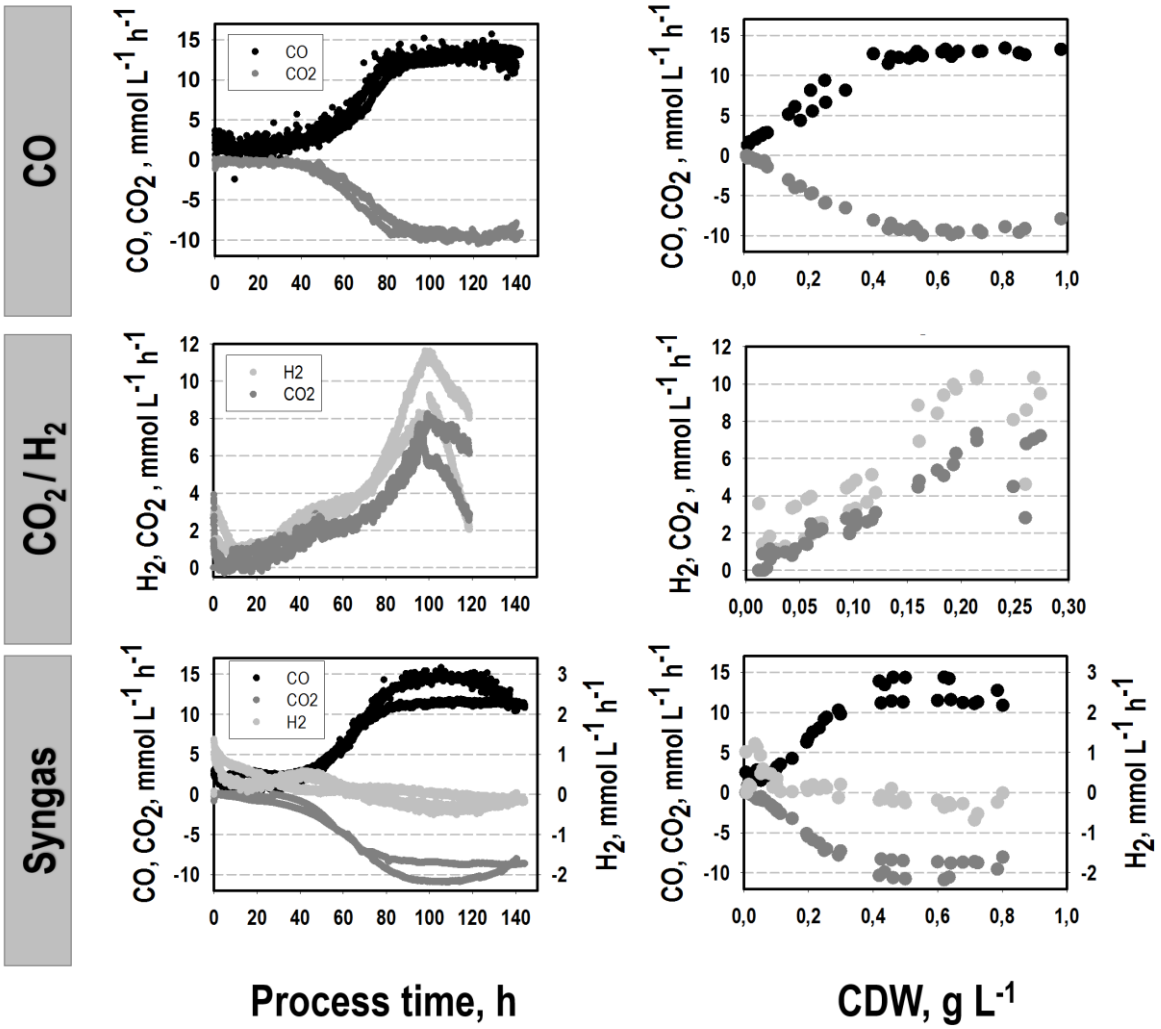

Figure 3.2: Comparative analysis of the gas uptake of *C. ljungdahlii* based on the conversion of CO, CO_2+H_2 or syngas in steadily gassed batch cultivations using stirred-tank bioreactor. For each substrate condition two independent experiments were performed that are demonstrated by individual graphs plotted against the process time and the respective CDW (T = 37°C; pH = 5.9; V_R = 3 L; 500 rpm).

In agreement with the growth phenotype, two phases of gas uptake were observed when CO was present. Proportional to the growth, the preferred substrate CO was consumed exponentially yielding a maximum volumetric uptake rate of 12.7 ± 0.4 mmol $(L\ h)^{-1}$ i.e. q_{CO} = 23.8 ± 1.3 mmol $(g\ h)^{-1}$, both in the CO and the syngas approach. CO uptake was accompanied by a proportional CO_2 formation achieving a maximum formation rate of 9.6 ± 0.5 mmol $(L\ h)^{-1}$ i.e. q_{CO2} = 17.9 ± 0.4 mmol $(g\ h)^{-1}$. In the following growth phase both volumetric rates remained almost constant. The values are in good accordance with previously described CO uptake and CO_2 production rates of *Clostridium autoethanogenum* and

C. ljungdahlii cultivated on syngas in chemostat mode with a dilution rate of 0.04 h^{-1}. The authors determined CO uptake rates of 18.4 – 30 mmol $(g\ h)^{-1}$ and CO_2 formation rates of 4 – 20 mmol $(g\ h)^{-1}$ with different biomass concentrations and H_2 proportions in the substrate gas cultivating *C. autoethanogenum*. For *C. ljungdahlii* CO uptake rates of 16.6 – 32.7 mmol $(L\ h)^{-1}$ and CO_2 production rates of 2.1 – 16.6 mmol $(L\ h)^{-1}$ were reported (Martin et al., 2016; Richter et al., 2016; Valgepea et al., 2018; Valgepea et al., 2017b). Remarkably, only a low mean H_2 uptake of 0.29 ± 0.05 mmol $(L\ h)^{-1}$ was observed in our syngas studies during the first growth period which even turned into H_2 formation of about 0.30 ± 0.06 mmol $(L\ h)^{-1}$ in the subsequent phase. Whereas, a simultaneous utilization of H_2 and CO is shown in several previous studies describing continuous cultivations performed in a chemostat mode (Martin et al., 2016; Richter et al., 2013; Valgepea et al., 2018). In CO_2+H_2 mixtures, both substrates were taken up simultaneously during the exponential growth with the maximum H_2 uptake rate of 10.35 ± 0.10 mmol $(L\ h)^{-1}$ i.e. q_{H2} = 50.8 ± 0.1 mmol $(g\ h)^{-1}$ and the maximum CO_2 uptake rate of 7.16 ± 0.27 mmol $(L\ h)^{-1}$ i.e. q_{CO2} = 35.0 ± 1.2 mmol $(g\ h)^{-1}$ after about 100 h. Subsequently, a decrease of both uptake rates was observed.

Product formation: Depending on the carbon source, different by-product formation patterns were observed (**Table 3.1**). Utilizing CO, acetate, ethanol, 2,3-butanediol and lactate were produced. Ethanol formation occurred steadily whereas acetate was only formed during exponential growth and was consumed afterwards leaving 0.68 ± 0.27 g L^{-1}. 2,3-butanediol production started in the second growth phase together with lactate. Final 2,3-butanediol and lactate titers were 1.96 ± 0.14 g L^{-1} and 0.21 ± 0.01 g L^{-1}, respectively. Related final substrate-to-product conversion yields were 0.020 ± 0.01 C-mole $mole_{CO}^{-1}$ for acetate, 0.205 ± 0.01 C-mole $mole_{CO}^{-1}$ for ethanol, 0.078 ± 0.007 C-mole $mole_{CO}^{-1}$ for 2,3-butanediol and 0.008 ± 3.5*10^{-5} C-mole $mole_{CO}^{-1}$ lactate.

Table 3.1: Maximal growth rates of *C. ljungdahlii* and final by-product concentrations using CO, CO_2+H_2 or syngas. 2,3-butanediol is abbreviated by 2,3-BD. Gas compositions are described in the Experimental procedures section. Rates reflect exponential growth during batch cultivation in steadily gassed stirred-tank bioreactor. Values indicated mean of duplicates.

Substrate	μ_{max}, h^{-1}	c_{CDW}, g L^{-1}	$c_{Acetate}$, g L^{-1}
CO	0.058 ± 0.004	0.93 ± 0.08	0.68 ± 0.27
CO_2+H_2	0.024 ± 0.003	0.26 ± 0.001	9.02 ± 0.39
Syngas	0.043 ± 0.007	0.76 ± 0.06	0.38 ± 0.08

Substrate	$c_{Ethanol}$, g L^{-1}	$c_{2,3\text{-}BD}$, g L^{-1}	$C_{Lactate}$, g L^{-1}
CO	5.23 ± 0.79	1.96 ± 0.14	0.21 ± 0.01
CO_2+H_2	0.14 ± 0.01	-	-
Syngas	5.91 ± 0.95	4.45 ± 0.64	0.26 ± 0.06

Table 3.2: Final biomass and product yields using CO, CO_2+H_2 or syngas as substrates. 2,3-butanediol is abbreviated by 2,3-BD. Gas compositions are described in the 'Experimental procedures' the section. Values indicate mean of duplicates.

Substrate	$Y_{CDW, CO/CO2,}$ C-mole $mole^{-1}$	$Y_{Acetate, CO/CO2,}$ C-mole $mole^{-1}$	$Y_{Ethanol, CO/CO2,}$ C-mole $mole^{-1}$
CO	0.068 ± 0.007	0.020 ± 0.01	0.205 ± 0.026
CO_2+H_2	0.031 ± 0.001	0.93 ± 0.001	0.019 ± 2.0*10^{-5}
Syngas	0.027 ± 0.001	0.007 ± 0.004	0.24 ± 0.004

Substrate	$Y_{2,3\text{-}BD, CO/CO2,}$ C-mole $mole^{-1}$	$Y_{Lactate,CO/CO2,}$ C-mole $mole^{-1}$	$Y_{CO2,CO/CO2,}$ C-mole $mole^{-1}$
CO	0.078 ± 0.007	0.008 ± 3.5*10^{-5}	0.667 ± 0.050
CO_2+H_2	-	-	-
Syngas	0.11 ± 0.026	0.008 ± 0.001	0.714 ± 0.003

By contrast, CO_2+H_2 consumption mainly caused the growth-coupled production of acetate and ethanol, the latter in the aftermath of exponential growth. Maximum titers of acetate and ethanol were observed as 9.02 ± 0.39 g L^{-1} and 0.14 ± 0.01 g L^{-1},

respectively. Related substrate-to-product conversion yields were 0.93 ± 0.001 C-mole $mole_{CO2}^{-1}$ for acetate and 0.02 ± 2.0*10^{-5}C-mole $mole_{CO2}^{-1}$ for ethanol. No formation of 2,3-butanediol and lactate was found. Product formation using syngas resembled the CO phenotype although acetate formation was less pronounced. The final substrate-specific product yields were 0.007 ± 0.004 C-mole $mole_{CO}^{-1}$ for acetate, 0.24 ± 0.004 C-mole $mole_{CO}^{-1}$ for ethanol, 0.11 ± 0.026 C-mole $mole_{CO}^{-1}$ for 2,3-butanediol and 0.008 ± 0.001 C-mole $mole_{CO}^{-1}$ for lactate.

The determined total consumption and production yields were applied to formulate cellular reduction balances for each experiment (see Supplementary Material, **Figure 7.1**). Estimated free Gibbs reaction energies ΔG_R and electron specific total product yields are shown in **Table 3.3**. While the total product yields remained similar for each substrate condition with around 0.25 C-mol normalized to the provided electrons, clearly, a larger proportion of electrons was drained into products utilizing CO and syngas compared to CO_2+H_2. The first fixed 62-60 % electrons in products whereas the latter only achieved 50%. In addition, the highest ΔG_R were calculated when CO was consumed, underpinning the advantage of preferring CO compared to CO_2+H_2 during batch cultivations.

Table 3.3: Carbon and electron balances, Gibb's free reaction energies and electron specific overall product yields during growth of *C. ljungdahlii* using CO, CO_2+H_2 or syngas. For gas compositions see the Experimental procedures section. Rates reflect exponential growth during batch cultivation in steadily gassed stirred-tank bioreactor. Values indicated mean of duplicates.

Substrate	C – Balance, %	e – Balance, %	$Y_{Products, e^-}$, C-mole $mole^{-1}$	$Y_{e^-(Products), e^-}$, mole $mole^{-1}$	ΔG_R, kJ C-$mole^{-1}$
CO	103.29 ± 2.67	104.54 ± 3.77	0.24 ± 0.03	0.62 ± 0.02	-47.57 ± 1.17
CO_2+H_2	99.97 ± 0.16	106.33 ± 0.30	0.27 ± 0.002	0.53 ± 0.001	-32.30 ± 3.33
Syngas	109.74 ± 2.92	101.62 ± 7.16	0.24 ± 0.02	0.60 ± 0.04	-38.86 ± 8.70

Moreover, intracellular ATP pools were measured and depicted in **Figure 3.1**. For each substrate condition the ATP levels of one independent representative run were determined in order to qualitatively compare the three substrate conditions. All courses showed reducing trends leading to similar mean values of about 0.04 µmol g_{CDW}^{-1}.

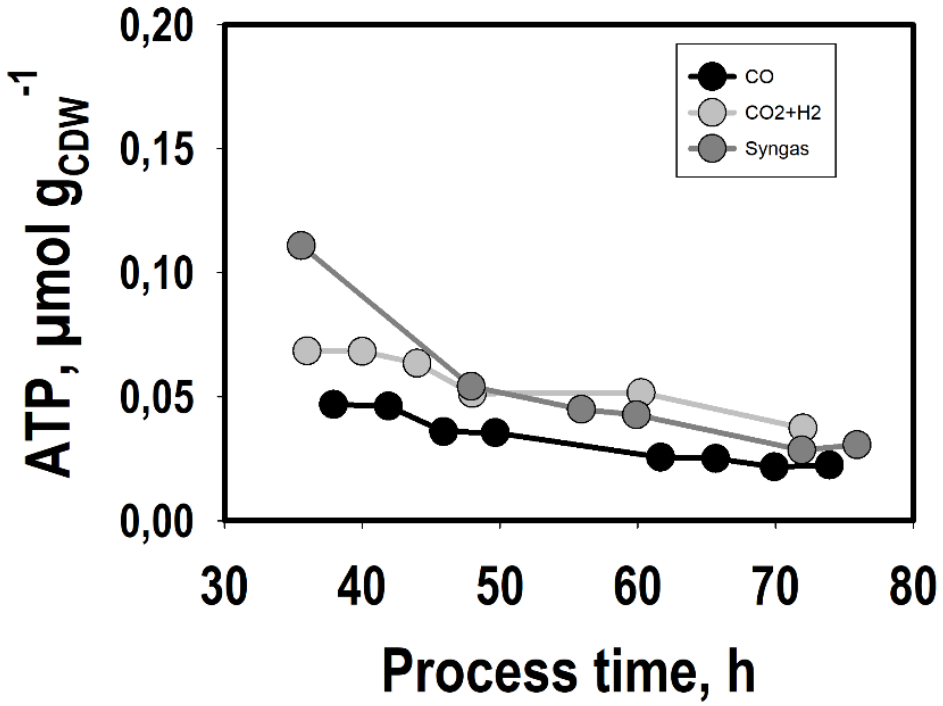

Figure 3.3: Intracellular ATP levels during exponential growth of *C. ljungdahlii* based on the conversion of CO, CO_2+H_2 or syngas during batch cultivations in steadily gassed stirred-tank bioreactors (T = 37°C; pH = 5.9; V_R = 3 L; 500 rpm). ATP levels were determined for one representative experiment of each substrate condition.

Simulation of intracellular flux distribution for different substrates

To investigate the links between intracellular carbon distribution, redox metabolism and energy conservation of *C. ljungdahlii*, flux balance analysis was performed. Accordingly, we studied intracellular flux patterns during the 'pseudo-steady states' of the batch cultivations. To restrict the solution space assuring that FBA results reflect real physiological state, we constrained our model with all experimentally determined rates (O'Brien et al., 2015). We have reconstructed a small-scale stoichiometric metabolic model (rSMM) comprising 117 intracellular and 46 transport reactions thereby balancing 180 metabolites (inner degree of freedom: 12, outer degree of freedom: 22). Mean values of the uptake and secretion fluxes for each substrate condition and growth phase detected (summarized in the Supplementary material, **Table 7.6** and **Table 7.7**), served as constraints which outlines the importance of accurate measurements. Carbon balances were closed by 103.29 ± 2.67%,

99.97 ± 0.16% and 109.74 ± 2.92% using CO, CO_2 + H_2 and syngas respectively. In addition, it was important to validate whether the simulation quality of our modelling approach basically allows a reliable comparison of metabolic fluxes using data of the three different substrate conditions we tested. This quality was checked by plotting simulated growth rates μ_{sim} versus experimental observations μ_{exp} (**Figure 3.4**) applying growth maximization as objective function. High correlation coefficients $R^2 \geq 0.9944$ indicated satisfying quality of the simulated results.

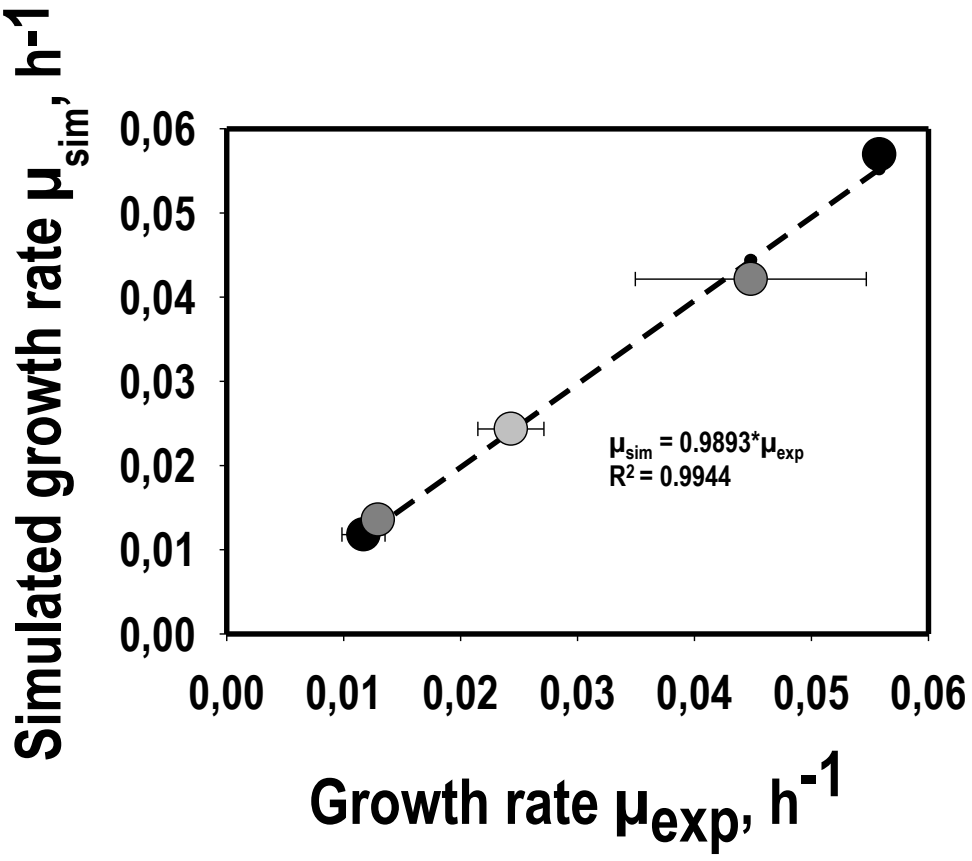

Figure 3.4: Simulated versus measured growth rates of *C. ljungdahlii* converting CO (●), CO_2+H_2 (○) or syngas (◉) in steadily gassed batch cultivations in stirred-tank bioreactors. For each substrate condition two independent experiments were performed (T = 37°C; pH = 5.9; V_R = 3 L; 500 rpm).

Intracellular metabolic flux distributions of each growth phase are given in **Figure 3.5**, **Figure 3.6** and **Figure 3.7**. To assess the variability of the model calculation, FBA for each cultivation was performed. The results are demonstrated in the Supplementary Material (**Table 7.4)**. In addition, a condensed figure showing the fluxes of reducing

equivalents and ATP formation normalized to the uptake rate of the respective energy source can be found in the Supplementary Material (**Figure 7.2**). In case of sole CO use, the gas served as carbon and energy (electron) source. Remarkably, about 83% of consumed CO was converted intracellularly to CO_2 thereby stoichiometrically producing Fd_{red} via CODH. 78% of the produced CO_2 left the cell which equals 61% of total CO consumed. Accordingly, the function of electron capturing dominated as 83% of CO was capitalized for Fd_{red} formation and only 39% were captured inside serving as carbon source.

The provision of Fd_{red} is the key determinant for the autotrophic metabolism of *C. ljungdhalii*, as it couples ATP synthesis to growth and product formation. First, Fd_{red} is required for reducing NAD^+ to NADH via the Rnf complex and $NADP^+$ to NADPH via the Nfn complex (Mock et al., 2015; Wang et al., 2013). In turn, cells need NADH and NADPH to reduce CO_2 to acetyl-CoA in the methyl branch of WLP, the latter serving as main precursor for growth and product formation in *C. ljungdahlii* (Köpke et al., 2011b; Köpke et al., 2010). In addition, ATP synthesis is coupled to the Rnf complex. Accordingly, the cellular energy management of *C. ljungdahlii* represents a concerted interplay of Nfn and Rnf complex, the CODH reaction, growth and product formation.

Sixty-one percent of consumed CO were converted to CO_2 during the first exponential growth phase. The ratio of the product rates was 0.075: 1: 0.15: 0.01 for acetate, ethanol, 2,3-butanediol and lactate resulting in the ATP yield of 0.34 mole $mole_{(CO)}^{-1}$ and the formation yields of 0.77 mole $mole_{(CO)}^{-1}$ for Fd_{red}, 0.49 mole $mole_{(CO)}^{-1}$ for NAD^+ and 0.02 mole $mole_{(CO)}^{-1}$ for NADPH (**Table 3.4**). In the subsequent growth phase, the portion of Fd_{red} formation from CO uptake almost remained similar. In addition, the produced acetate was incorporated again which lead to product formation ratios of 1: 0.2: 0.02 for ethanol, 2,3 butanediol and lactate respectively.

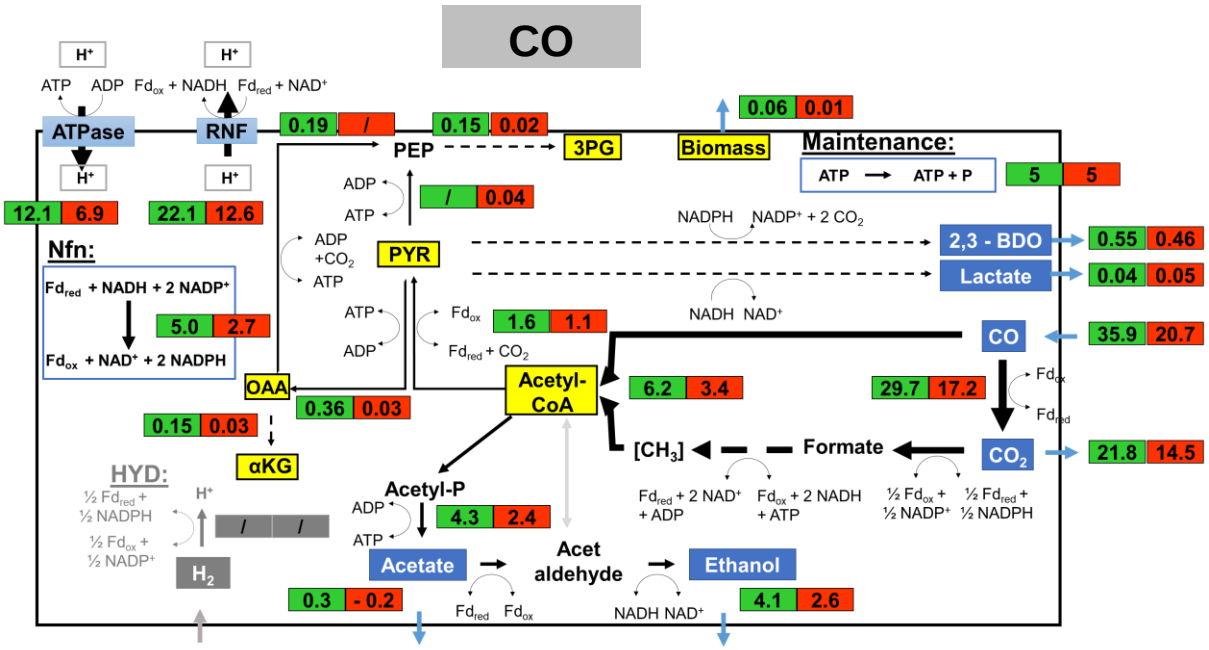

Figure 3.5: Metabolic flux distributions of *C. ljungdahlii* based on the conversion of CO in steadily gassed batch cultivations in stirred-tank bioreactors, performed in duplicates. Illustrated are the simulated fluxes in mmol $(g_{CDW}*h)^{-1}$ for the first (■) and second (■) growth phase.

Table 3.4: ATP, Fd_{red} and NAD^+ yields derived from flux balance analysis considering exponentially growing *C. ljungdahlii* using CO, CO_2+H_2 or syngas as substrates. The illustrated ATP yields refer to the ATPase activity coupled to the Rnf complex.

Sub-strate	ATP, mole $mole_{(CO+H2)}$ $^{-1}$	Fd_{red}, mole $mole_{(CO+H2)}$ $^{-1}$	NAD^+, mole $mole_{(CO+H2)}$ $^{-1}$	NADPH, mole $mole_{(CO+H2)}$ $^{-1}$
CO	0.34	0.77	0.49	0.02
CO_2+H_2	0.24	0.44	0.43	0.008
Syngas	0.32	0.72	0.47	0.014

In case of CO_2 + H_2 consumption, the formation of Fd_{red} is ensured by the HYD reaction that is accompanied by the regeneration of $NADP^+$ to NADPH (Buckel and Thauer, 2013; Schuchmann and Müller, 2012; Wang et al., 2013). Additionally, the Nfn reaction is needed to refill the NADP+ pool. Remarkably, the Nfn encoded transhydrogenase runs opposite to the CO case, i.e., NADPH is oxidized creating $NADP^+$ and NADH. By taking up the substrate gases H_2 and CO_2 with a ratio of 2:1, *C. ljungdahlii* can balance

the energy and redox metabolism simply by producing acetate. Thereby ATP was formed with the yield of 0.24 mole mole$_{(H2)}$ $^{-1}$ and the formation yields of 0.44 mole mole$_{(H2)}$ $^{-1}$ for Fd$_{red}$, 0.43 mole mole$_{(H2)}$ $^{-1}$ for NAD$^+$ and 0.008 mole mole$_{(H2)}$ $^{-1}$ for NADPH were achieved.

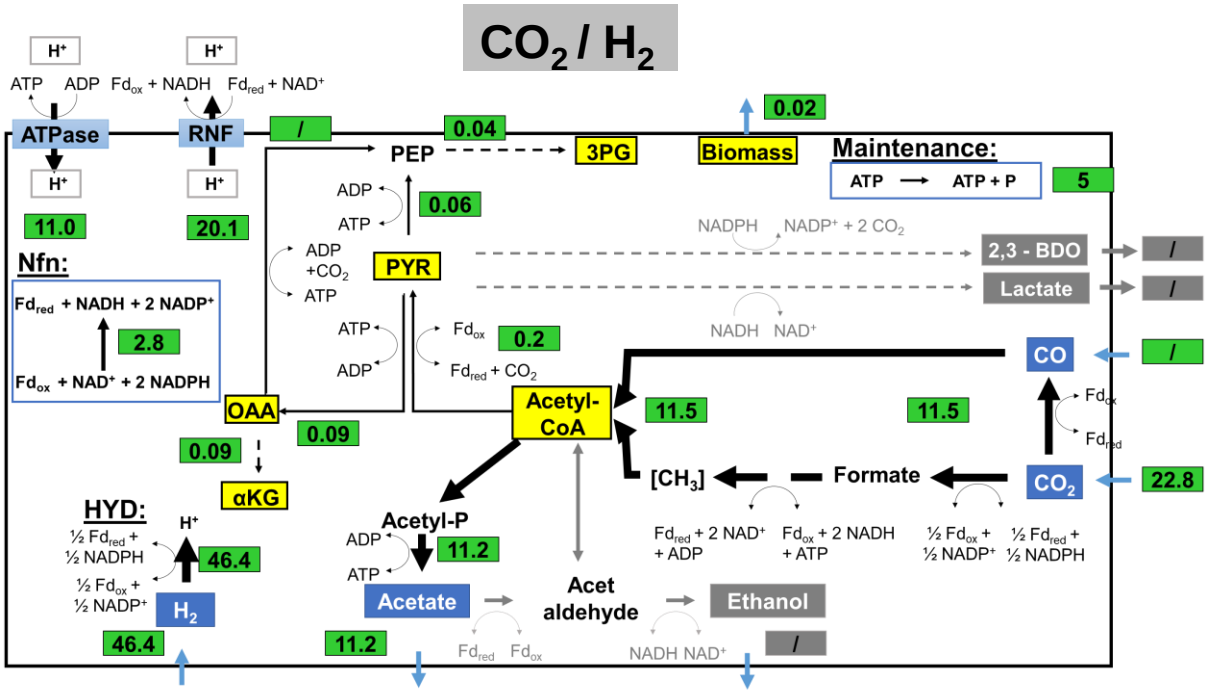

Figure 3.6: Metabolic flux distributions of *C. ljungdahlii* based on the conversion of CO_2+H_2 in steadily gassed batch cultivations in stirred-tank bioreactors, performed in duplicates. Illustrated are the simulated fluxes in mmol $(g_{CDW}*h)^{-1}$ for the exponential growth phase

Utilizing syngas *C. ljungdahlii* makes use of the CODH and the HYD reaction to generate Fd$_{red}$. However, oxidation of H_2 crucially relies on the availability of NADP$^+$. The latter is solely provided by the formate dehydrogenase reaction of the WLP and the 2,3-butanediol dehydrogenase. In parallel, Nfn and Rnf complexes are used to regenerate the redox metabolites oxidized ferredoxin (Fd$_{ox}$), NADH and NADPH. Growing on syngas 64% of CO is converted to CO_2 during the first exponential growth phase when the by-product ratios were 0.4: 1: 0.15: 0.03 for acetate, ethanol, 2,3-butanediol and lactate respectively. The ATP yield of 0.32 mole mole$_{(CO+H2)}$ $^{-1}$ was achieved with the formation yields of 0.72 mole mole$_{(CO+H2)}$ $^{-1}$ for Fd$_{red}$, 0.47 mole mole$_{(CO+H2)}$ $^{-1}$ for NAD+ and 0.014 mole mole$_{(CO+H2)}$ $^{-1}$ for NADPH. In the

second growth phase, the HYD direction changed. Acetate was taken up, and the proportion of CO converted to CO_2 increased to 74%. This led to a product formation rate ratio of 1: 0.18: 0.02 for ethanol, 2,3-butanediol and lactate.

Summarizing, the consumption of CO enabled highest Fd_{red}, ATP and NADPH formation yields with respect to the electrons provided (see **Table 3.4**). Furthermore, the formation of reduced by-products was highest, too (see **Table 3.1**).

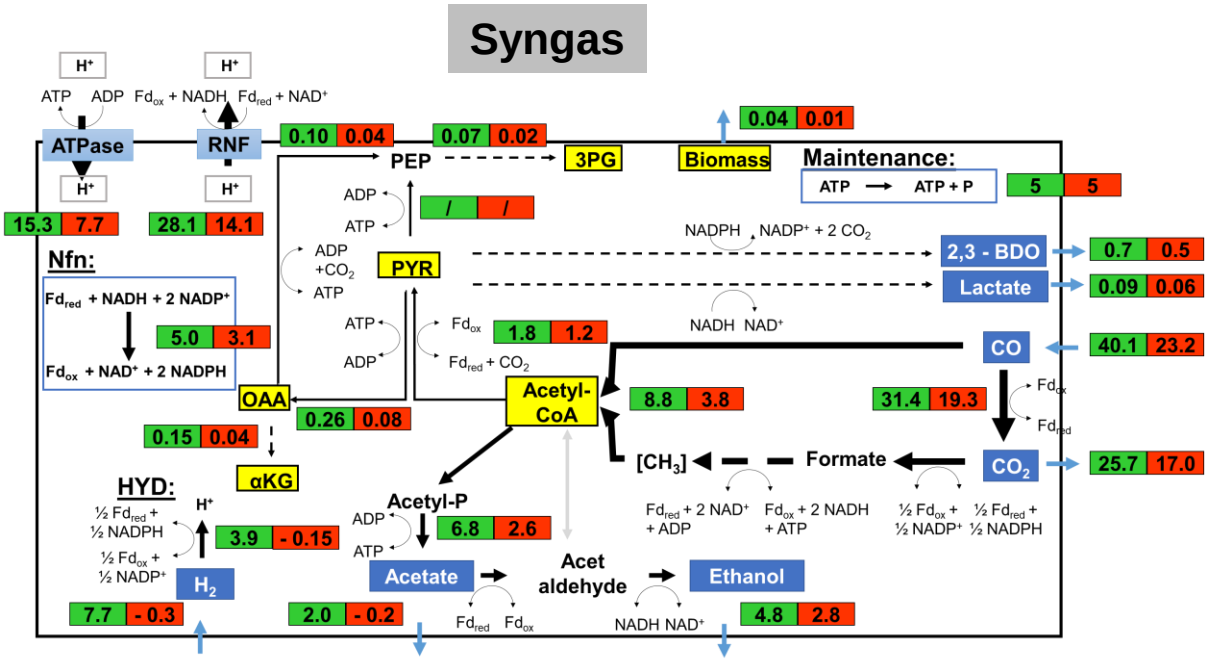

Figure 3.7: Metabolic flux distributions of *C. ljungdahlii* based on the conversion of syngas in steadily gassed batch cultivations in stirred-tank bioreactors, performed in duplicates. Illustrated are the simulated fluxes in mmol $(g_{CDW}*h)^{-1}$ for the first (■) and second (■) growth phase.

DISCUSSION

Growth phenotypes

During autotrophic cultivations, the composition of energy and carbon sources severely influences the growth phenotype and the product spectrum of *C. ljungdahlii*. Our results outline that CO consumption enabled faster growth rates than using gas mixtures of $CO_2 + H_2$. During the first period, growth rates of CO cultures with $\mu_{exp} = 0.06 \pm 0.004\ h^{-1}$ more than doubled the rates of $CO_2 + H_2$ with

μ_{exp} = 0.024 ± 0.003 h $^{-1}$ and were even faster than syngas tests characterized by μ_{exp} = 0.04 ± 0.007 h $^{-1}$. The observation reflects that putative CO-growth inhibition, as outlined by Mohammadi et al. (2014), was not active. Apparently, dissolved CO levels were lower than the half-saturation constant K_S of 6.33 mmol L $^{-1}$ and the inhibition constant K_I of 4.44 mmol L $^{-1}$ identified by Mohammadi et al. (2014). Furthermore, CDW values were almost four times higher. The findings are comparable to the observation of Mayer and Weuster-Botz (2017). They showed that *Clostridium aceticum* yielded almost doubled exponential growth rate and higher CDW concentration using CO instead of CO_2 + H_2. By analogy, *C. ljungdahlii* prefers CO because 0.34 mole ATP per mole CO were generated and 7% of captured carbon was used for biomass formation and maintenance needs. On contrary, only 3% of the captured carbon were fixed in biomass and only 0.24 mole ATP per mole H_2 were gained when utilizing CO_2 + H_2. Furthermore, rising acetate concentrations are known to inhibit growth yielding higher cellular maintenance costs by decoupling proton import and ATP synthesis (Jones and Woods, 1986; Valgepea et al., 2017b). As less ATP is available, utilizing CO_2 + H_2 cells are likely to run in ATP shortage (Valgepea et al., 2017b) finally causing growth collapse. Noteworthy, the final acetate concentration of 9.02 ± 0.39 g L $^{-1}$ reached with the CO_2 + H_2 approach is close to the inhibitory concentration of 12 g L $^{-1}$ postulated by Yang and Tsao (1994) for *Clostridium acetobutylicum*.

The link between ATP formation and redox balance

The findings anticipate that the consumption of CO led to a higher energy availability than the use of H_2 as electron source, as already described before (Jack et al., 2019). In agreement with this hypothesis, highest ΔG_R was calculated when CO was consumed compared to the substrate CO_2 + H_2. Interestingly, the intracellular biomass-specific ATP pools did not differ, indicating that *C. ljungdahlii* is able to balance its energy requirement via a tight link between the energy and redox metabolism. A similar characteristic was also postulated for *C. autoethanogenum* before (Marcellin et al., 2016). Under balanced growth conditions, formate activation

requires ATP which is equilibrated by the formation of acetate. Theoretically, ATP can be further generated via oxaloacetate decarboxylation, but this reaction plays only a minor role. Most important, autotrophic ATP production relies on the ATPase activity coupled to the Rnf complex. The respiratory enzyme utilizes Fd_{red} in order to reduce NAD^+ irrespective of the carbon and electron source used (Müller et al., 2008; Tremblay et al., 2012). However, the formation of Fd_{red} is dependent on the electron source and differs for CO and H_2. In case of CO, CODH is applied predominately, whereas the HYD reaction is the key for generating Fd_{red} from H_2. In addition, Fd_{red} is needed to reduce $NADP^+$ to NADPH. The latter greatly influences growth and the by-product spectrum, as acetogens crucially need to balance NADPH formation with anabolic consumption (Fuhrer and Sauer, 2009). Accordingly, Fd_{red} may be regarded as the key player providing electrons for proper distribution in ATP and products. Besides, the product spectrum has also an important influence on the efficiency of intracellular ATP availability. With increasing acetate formation during growth, the cellular ATP maintenance costs are likely to increase caused by the decoupling of the proton motive force and ATP synthesis (Jones and Woods, 1986; Valgepea et al., 2017b). The trend of falling intracellular ATP levels consuming CO_2 + H_2 (**Figure 3.3**) may reflect the hypothesis. However, even CO consuming cells show similar ATP decline although they may counteract the inhibitory effect of acetate by producing ethanol. Noteworthy, the latter is chaotropic which may cause additional stress per se (Valgepea et al., 2017b). Schatschneider et al. (2018) determined intracellular ATP concentration of 0.095 µM $gCDW^{-1}$ in *C. autoethanogenum* grown on CO in continuous culture. The value fits well to ATP levels determined in our study. Nevertheless, intracellular ATP levels for heterotrophically cultivated *Clostridium beijerinckii* and *Clostridium acetobutylicum* are higher by 1–2 orders of magnitude (0.55 – 5.1 µmol $gCDW^{-1}$; Liu et al., 2016; Meyer and Papoutsakis, 1989). Apparently, this reflects the way of better ATP supply consuming sugars.

Fd_{red} formation using different gases

The flux balance analysis revealed that with CO the provision of Fd_{red} was ensured by the CODH reaction leading to the stoichiometric regeneration of NAD^+ to NADH via the Rnf complex. Driven by the H^+ export via the Rnf complex, ATP was formed while

importing H^+ (Tremblay et al., 2012). Concomitantly, NADPH was produced via the Nfn complex, driven by NADH formed via the Rnf complex (Mock et al., 2015). These findings reflect well the results summarized for *C. autoethanogenum* by Norman et al. (2019). Balancing the regeneration of reducing equivalents via the WLP 0.77 mole Fd_{red}, 0.49 mole NAD^+ and 0.02 mole NADPH per mole CO was net provided. In essence, these values represent the reducing power and energy equivalents for serving maintenance needs, cellular growth, and product formation.

Using $CO_2 + H_2$ as substrate, Fd_{red} was formed by the HYD reaction that is accompanied by the regeneration of $NADP^+$ to NADPH. To refill the high need of $NADP^+$, the Nfn complex runs opposite to the CO case by oxidizing NADPH transferring electrons to NAD^+. The latter was fuelled from the conversion of CO_2 to acetyl-CoA via the WLP. Summarizing, 0.44 mole Fd_{red}, 0.43 mole NAD^+ and 0.008 mole NADPH per mole H_2 were net provided balancing the Nfn complex, the HYD reaction and the WLP. Obviously, the use of $CO_2 + H_2$ provides fewer reducing equivalents and ATP than the consumption of CO.

These results show the importance of the methyl branch of WLP strongly depended on substrate and electron needs thereby shifting the main purpose: Consuming CO, the branch mainly served as acetyl-CoA provider and contributed less to Fd_{red} and NAD^+ formation. The latter was mainly provided by the Nfn complex. In particular, only 8.7% of Fd_{red} and 56.0% of NAD^+ were drained from the methyl branch (**Table 3.5**). On contrast, when $H_2 + CO_2$ was used, the methyl branch supported Fd_{red} formation by 16.5% and gained more importance as NAD^+ provider: The total NAD^+ formation relied on this source which clearly illustrates the dual function of the pathway that adapts to current substrate conditions.

When syngas was used, the CO and $CO_2 + H_2$ scenarios somehow overlapped. The activity of the methyl branch was less than the $CO_2 + H_2$ metabolism but higher compared to the CO-only case. This was due to the combined provision of Fd_{red} by HYD and CODH yielding more reducing power for the reduction of CO_2. Increasing fluxes through WLP with increased H_2 supply were also observed by Valgepea et al. (2018) investigating continuously cultivated *C. autoethanogenum* on syngas. They predicted direct reduction of CO_2 with H_2 to formate by formate-H_2 lyase enabling high

methyl branch activity with less redox consumption. However, said reaction is not considered in our model, as the *C. ljungdahlii* genome lacks the annotated gene (Köpke et al., 2010). Nevertheless, we performed additional model simulations including a formate-H_2 lyase for the three different substrate conditions to further assess our findings. The results are summarized in the Supplementary Material (**Figure 7.3**, **Table 7.8** and **Table 7.9**). The simulations show a partly changed flux pattern for syngas and CO_2 + H_2 but they support our hypotheses even more. Including formate-H_2 lyase activity, the methyl branch supports the Fd_{red} formation by 39.6% on H_2 + CO_2 and by 20.5% on syngas. Besides, similar overlapping flux scenarios were also found for the HYD reaction, the Nfn complex and the Rnf complex. Consequently, the output of redox and energy equivalents was better than utilizing CO_2 + H_2 but slightly less than using CO as sole electron and substrate donor.

Table 3.5: Percentage provision of NAD^+ and Fd_{red} and consumption of NADH and NADPH in the methyl branch derived from flux balance analysis considering exponentially growing cells of *C. ljungdahlii* using CO, CO_2+H_2 or syngas as substrates.

Substrate	NAD^+, %	Fd_{red}, %	NADH, %	NADPH, %
CO	56.10	8.66	56.10	92.16
CO_2/H_2	100	16.54	100	74.16
Syngas	62.70	9.95	62.70	95.09

Product formation

The product-per-electron yield in mol-C was fairly the same in all studies (about 0.25 C moles per electron). The observation outlines the fundamental restriction of acetogens offering a maximum product formation that is limited by electron availability (**Table 3.2**). However, the product portfolio differed depending on the carbon and electron source. To illustrate the spectrum, the electron efficiency Y_{e^-,e^-} was calculated, i.e. the fraction of ‘free electrons’ found in the product versus consumed electrons in the substrates. Utilizing CO solely, about 62% of substrate electrons were found in the products mirroring that the reduction degree of all products was the highest when using CO. The utilization of syngas still showed the same trend, but the changing flux distributions (see above) finally lowered the reduction degree of the products. When the mixture of

CO_2 and H_2 was applied, Y_{e^-,e^-} was found to be the lowest, again mirroring the changed intracellular flux distribution.

Acetate turned out to be the dominating product when CO_2 + H_2 mixtures were used. The finding coincided with the complete equilibration of ATP use in the methyl branch versus ATP formation via acetate formation. The exclusive role of the methyl branch as NAD^+ provider using H_2 + CO_2 finally lead to minimal NADH excess to produce reduced products such as ethanol. Furthermore, the ATP gain was the lowest (**Table 3.4**). When CO was applied, the methyl branch activities only halved those of H_2 + CO_2 and related ATP use was no longer covered by acetate formation. For compensation, NAD^+ pushed the Rnf complex activity which finally provided strong ATP formation. Interestingly, the net NADH formation using CO outnumbered the needs of the low activity methyl branch which lead to the production of reduced products such as ethanol or 2,3 butanediol (**Table 3.5**). The latter represents the highest 2,3-butanediol production of a batch process with *C. ljungdahlii* described so far (Köpke et al., 2011b) and reflects well the hypothesis of Norman et al. (2019). They predicted high 2,3-butandiol production under ample carbon but restricted H_2 supply.

CONCLUSION

The metabolism of *C. ljungdahlii* showed high flexibility and adaption for optimum use of CO, CO_2 + H_2 and syngas. Clearly, the application of CO as substrate and electron donor is favoured with respect to growth rate, ATP supply and the formation of reduced products. The yield of electrons bound in products compared to electrons used in substrates is the highest for CO. This mirrors the dual role of the methyl branch of the WLP which showed comparably low activity under CO consumption thereby providing excess NADH to produce alcohols. Thereof, the conclusion could be drawn that CO should be the preferred substrate for the production of natural or even non-natural alcohols with *C. ljungdahlii*. Accordingly, CO-rich off-gases of the steel industry should be ideal substrates for the production of alcohols (Sun et al., 2019).

EXPERIMENTAL PROCEDURES

Bacterial strain, growth medium and preculture preparation

C. ljungdahlii (DSM 13528) was obtained from the German Collection of Microorganisms and Cell Culture (DSMZ). All experiments were performed under strict anaerobic conditions (Hungate, 1976) using the Tanner mod. PETC medium (ATCC medium 1754) with 15 g L^{-1} MES buffer and 0.5 g L^{-1} yeast extract (Tanner et al., 1993). The redox indicator resazurin was solely used for the preculture steps prior to the controlled cultivation in the bioreactor. The preculture seed train contained heterotrophic as well as autotrophic cultivation steps. A frozen cell stock was used to inoculate 5 mL of a heterotrophic medium with 10 g L^{-1} fructose in an unshaken 10 mL anaerobic hungate tube (Glasgerätebau Ochs, Bovenden/Lenglern, Germany) which was incubated for 48 h at 37 °C. Next, 4% (vv^{-1}) cell suspension of the preculture was transferred into 50 mL of a heterotrophic medium with 10 g L^{-1} fructose into an anaerobic cultivation bottle with total a volume of 100 mL (Duran protect, Duran group GmbH, Mainz, Germany). The culture was incubated for 48 h at 37 °C and 100 rpm on an orbital shaker (New Brunswick Scientific, Connecticut, USA). In order to adapt the cells to the fructose-free medium in the bioreactor, an additional preculture step was performed comprising anaerobic cultivation in 500 mL bottles filled with 100 mL fructose-free medium. Before inoculating the medium with 4 mL preculture, the headspace of the bottles was exchanged three times with the filter sterilized gas mixture. Then, 2 bar overpressure was installed and the culture was incubated at 37 °C and 100 rpm. Exponentially growing cells of this seed step were used to inoculate the bioreactor.

Batch cultivation studies in a stirred-tank reactor with different substrates

Anaerobic autotrophic batch cultivations with different substrate gas compositions were performed in a fully controlled 3 L stirred-tank bioreactor (Bioengineering, Wald,

Switzerland) with an operational volume of 1.5 L. The bioreactor was equipped with sensors for pH (Mettler Toledo, Columbus, OH, USA), redox potential (Mettler Toledo, Columbus, OH, USA), pressure (Keller AG für Druckmesstechnik, Winterthur,

Switzerland) and temperature. LabVieW was used to track process parameters. Temperature was set at 37 °C, and pH was kept constant at 5.9 using 2 M NaOH for titration. Four mass flow controllers (Bronkhorst High-Tech B.V., Ruurlo, Netherlands) were used to apply different gas mixtures and flows. In the baffled bioreactor, an L-tube sparger and a six-blade Rushton impeller stirring with an agitation speed of 500 rpm ensured gas dispersion. The mass spectrometer (Prima Pro, Thermo Fischer Scientific, Waltham, USA) allowed the online measurement of the reactor off-gas. To avoid foam formation during the batch processes, the antifoam Struktol 674 (Still und Seilacher) was added manually using sterile single-use syringes and cannulas via a septum (Carl Roth GmbH + Co. KG, Karlsruhe, Germany). Three gas compositions were tested in duplicates: (i) **CO** (39% CO; 4% CO_2; 57% Ar) with a constant gassing rate of 18.9 L h^{-1}, (ii) **CO_2 + H_2** (47.5% H_2; 47.5% CO_2; 5% Ar) with a constant gassing rate of 13.2 L h^{-1} and (iii) **syngas** (55% CO; 30% H_2; 5%CO_2; 10% Ar) with a constant gassing rate of 13.2 L h^{-1}. As we only had a limited number of gas flow controllers (two at the beginning of our study and three at the end), we partly had to work with predefined gas mixtures. Therefore, it was not possible to establish identical gassing rates and partial pressures of the substrate components for all conditions. We assumed equal supply conditions for all tests, given that average residence time of gas was 11 s in the stirred bioreactor. The latter was estimated considering the reactor diameter and a turbulence factor for the rise velocity of bubbles (Alves et al., 2004). To ensure anaerobic conditions, the medium containing bioreactor was sparged with nitrogen with a gassing rate of 60 L h^{-1} applied for 2 h. Off-gas measurements ensured that oxygen concentrations were always below 0.01% (vv^{-1}). Afterwards, the medium was equilibrated with one of the gas compositions (i)–(iii) for 5 h. Two hours prior to inoculation of the bioreactor, sterile reducing agent was added (Tanner et al., 1993). During the cultivations, samples were taken frequently to determine the CDW, the extracellular product formation and the intracellular ATP pools.

Analytical methods

Biomass concentration analysis. The optical density was measured offline via a UV/Visible spectrophotometer (Ultrospec 1100 pro, Amersham Bioscience GmbH, Freiburg, Germany) at 600 nm. Thereof, the CDW concentration in [g_{CDW} L^{-1}] was

correlated with CDW-to-OD_{600nm} as 0.25. CDW measurements were based on twice washed (mineralized water) pellets of three 4 mL samples of the cell suspension, centrifuged at 6900 rcf and 4 °C for 5 min (5430 R, Eppendorf, Hamburg, Germany), which were transferred to preweighed glass vials with a total volume of 1.5 mL and dried at 105 °C. for at least 24 h in a convection oven (Heraeus, Hanau, Germany). Empty glass vials and the cell pellets were stored in a desiccator (Duran vacuum desiccator, DWK Life Sciences GmbH, Mainz, Germany) for several hours before weighting.

Analysis of extracellular products. The detection of the by-products ethanol, acetate, 2,3-butanediol and lactate was carried out by an isocratic high-performance liquid chromatography (HPLC), equipped with a RI detector (1200 Series, Agilent, Santa Clara, CA, USA) and a Rezex ROA-Organic Acid H^+ column, at a temperature of 55 °C. A 5 mM H_2SO_4 was used as effluent with a flow rate of 0.4 mL min^{-1}. Cell-free samples were generated by centrifugation (5430 R, Eppendorf, Hamburg, Germany) of the cell suspension at 18,000 rcf and 4 °C for 2 min. Subsequently, samples were pretreated consecutively with 4 M NH_3 and 1.2 M $MgSO_4$ solutions to precipitate phosphate and were finally incubated with 0.1 M H_2SO_4.

Analysis of the intracellular ATP concentrations. Intracellular ATP pool concentrations in [µmol g_{CDW}^{-1}] were quantified using an HPLC system (1200 Series, Agilent, Santa Clara, CA, USA) coupled to a triple quadrupole tandem mass spectrometer (QQQ-MS/MS) equipped with an electrospray ion source (Agilent 6410B, Agilent Technologies, Waldbronn, Germany). The method based on a bicratic zwitterionic hydrophilic interaction chromatography (ZIC-pHILIC) with alkaline (pH 9.2) mobile phase conditions (Teleki et al., 2015). The detection was carried out in negative (ESI-) ionization mode and multiple reaction monitoring (MRM) mode with

preoptimized precursor-to-product ion transitions (Teleki et al., 2015). The ATP standard was obtained from Sigma-Aldrich (Schnelldorf, Germany). MS-grade water, methanol, chloroform and acetonitrile were purchased from Carl Roth (Karlsruhe, Germany). Standard stock solutions of ATP were prepared in MS-grade water and stored at −70 °C. Sample preparation was based on an adapted sequential protocol

via fast centrifugation treatment (FCT; Plassmeier et al., 2007) and a subsequent cold methanol-chloroform extraction (CME; Koning and van Dam, 1992). During the exponential growth phase of batch cultures, 5 mL cell suspension was taken periodically as triplicates. The samples were centrifuged at 6900 rcf and −11 °C for 2 min (5430 R, Eppendorf, Hamburg, Germany) and subsequently washed with 5 mL ice-cold isotonic 0.9% (vv^{-1}) sodium chloride solution. Resulting cell pellets and cultivation supernatants (analogues extracellular samples) were immediately quenched by liquid nitrogen and temporarily stored at −70 °C.

Defined cell amounts were resuspended in 200 µL of a precooled 50% (vv^{-1}) methanol solution by pulse vortexing (20 s) and merged with 200 µL of precooled chloroform. These extraction solutions were shaken for 1.5 h at −20 °C and subsequently for 1 h at room temperature using a cellmixer (CMV, Labortechnik Fröbel GmbH, Lindau, Germany). After a centrifugation step at 18,000 rcf at −11 °C for 15 min (5430 R, Eppendorf, Hamburg, Germany), the upper aqueous methanol phase (ATP extracts) was removed and temporarily stored at −70 °C. ATP concentrations were absolutely quantified by a standard-based external calibration using isotope dilution mass spectrometry (IDMS) as quantification strategy. Prior to analysis, samples and standard mixtures were prepared by constant addition of 10 mM ammonium acetate, 60% (vv^{-1}) acetonitrile, 2.5 mM 2-keto-3-deoxy- 6-phosphogluconate (KDPG) and 8% (vv^{-1}) uniformly labelled (U-^{13}C) *Corynebacterium glutamicum* metabolite extracts (Feith et al., 2019). The external calibration range (2.5 nM to 40 µM) with 19 levels was adapted based on previous measurements. Calibration curves were prepared by linear regression of ratios of non-labelled ATP peak areas and U-^{13}C-labelled analogues as internal standard against the respective concentration levels.

KDPG was considered for monitoring of instrumental fluctuations but not for normalization of obtained peak areas.

Online analysis of the exhaust gas. The exhaust gas was monitored online by mass spectrometry (Prima Pro,Thermo Fischer Scientific, Waltham, USA). The molar CO, CO_2 and H_2 concentrations produced or consumed by *C. ljungdahlii* in the course of the different cultivations were determined by taking into account the adjusted inlet flow

rates of the individual gases as well as the measured gas concentrations in the inlet and outlet gas streams **(4)**. In each case, Argon was used as inert gas.

$$r_i(t) = \frac{p}{R \cdot T} \cdot \frac{V_{g,in}}{V_R} \cdot \left(\frac{c_{i,\,in}}{100} - \frac{c_{Ar,\,in}}{c_{Ar,\,out}} \cdot \frac{c_{i,\,out}}{100} \right) \quad (4)$$

$R_i\,(t)$ represents the volumetric uptake rate of the respective gas at one time point of the cultivation process. For the values of the pressure p, the temperature T and the gas constant R normal conditions are assumed. $V_{g,inlet}$ reflects the aeration rate and V_R is the working volume of the reactor. To account for dissolved CO_2, total inorganic carbon in cell-free filtrates was measured using a TC analyzer (Multi N/C 2100s, Analytik Jena, Jena, Germany) as described in Graf et al. (2018). To calculate the molar concentrations of the gases produced or consumed by the cells as function of the process time the volumetric rates were integrated.

Determination of cell specific rates

The biomass-specific substrate uptake and product formation rates were calculated by dividing the exponential growth rate μ by the biomass substrate yield $Y_{X/S}$ or the biomass product yield $Y_{X/P}$ respectively (**formula (**5 **and (**6). In prior, the exponential growth rate μ was determined graphically by a linear fit of the semilogarithmic plot of the calculated CDW as function of the process time. To deduce graphically the biomass substrate yields as well as the biomass product yields, a linear regression of the substrate or product concentration curves as function of the biomass concentration was applied.

$$q_S = \frac{\mu}{Y_{X/S}} \quad (5)$$

$$q_P = \frac{\mu}{Y_{X/P}} \quad (6)$$

In addition, electron specific overall product yields were calculated (**(7 (8**) by assuming that one mole CO_2 produced and/or one mole H_2 incorporated yield two electrons that can be transferred to reducing equivalents (Müller, 2003).

$$Y_{products,e^-,} = \frac{\sum c_{Pi}}{(c_{co2} + c_{H2}) * 2} \quad (7)$$

$$Y_{e^-(Products),e^-,} = \frac{\sum c_{Pi} * k_i^*}{(c_{co2} + c_{H2}) * 2} \quad (8)$$

C_{Pi} represents the molar concentration of the respective product, c_{CO2} and c_{H2} are the molar concentrations of CO_2 produced and H_2 consumed at the end of the respective cultivation and κ_i* reflects the degree of reduction per carbon of the respective product.

Determination of the Gibbs free energy changes ΔG_R

In order to evaluate the energy yield of the different analyzed substrate conditions the Gibbs free reaction energy change ΔG_R was determined as described by (Villadsen et al., 2011) (**formula**(**9**) and (**formula** (**10**)).

$$\Delta G_R = (\sum_i Y_{Pi/S} * \Delta G_{c,i})_{products} - (\sum_i Y_{Si/S} * \Delta G_{c,i})_{substrates} \quad (9)$$

$$\Delta G_{Ci} = -94.4\kappa_i^* + 86.6\ kJ(C-mole)^{-1} \quad (10)$$

ΔG_{ci} is the free energy of combustion of the reactant *i*, that is dependent on the respective degree of reduction κ_i^*. The experimental coefficients $Y_{Pi/S}$ and $Y_{Si/S}$ reflect the yields of products and substrates in mol-C. The respective coefficients for H_2O, NH_3 and H^+ were estimated assuming elemental balances. The biomass composition was assumed according to Alberty (1998). A detailed description is attached in the Supplementary Material (**Figure 7.1**).

Stoichiometric metabolic modelling

Stoichiometric network reconstruction. Based on the genome annotation of *C. ljungdahlii* (Köpke et al., 2010), the genome-scale models of *C. ljungdahlii* (Nagarajan et al., 2013) and of the related clostridial strain *C. acetobutylicum* (Senger and Papoutsakis, 2008), we manually reconstructed a reduced stoichiometric metabolic model (rSMM) using the combined information from the databases KEGG and MetaCyc, literature and own experimental results. In addition, we compared our model with the metabolic model of *C. autoethanogenum* (Marcellin et al., 2016). The network was reconstructed, checked for consistency and topologically investigated by means of the Insilico Discovery™ platform (Insilico Biotechnology AG, Stuttgart, Germany). For the sake of simplicity, biosynthetic pathways of glycerophospholipids, cell wall, DNA and nucleotides were lumped. To cover maintenance demands, the growth-associated value (GAM) of 46.7 mmol ATP per g CDW was installed (Nagarajan et al., 2013), whereas non-growth-associated maintenance (NGAM) was set to 5 mmol $(g_{CDW}*h)^{-1}$. This value corresponds to the mean maintenance cost identified for the closely related acetogen *C. autoethanogenum* on CO, syngas and CO_2 + H_2 (Heffernan et al., 2020; Valgepea et al., 2018). In addition, we made the following assumptions: (i) The ATP synthase reaction is characterized by a conservative stoichiometry of 3.66 H^+ per 1 ATP (Mock et al., 2015); (ii) the HYD is an electron-bifurcating, $NADP^+$ and ferredoxin-dependent enzyme that uses 2 H_2 for the reversible reduction of $NADP^+$ and Fd_{ox} (Mock et al., 2015); (iii) the formate dehydrogenase reaction is based on NADPH and Fd_{red} as electron donor (Schuchmann and Müller, 2014); (iv) the membrane-bound Rnf complex translocates 2 protons via the Fd_{red}:NAD^+ oxidoreductase reaction (Perez et al., 2013); and (v) the methylene-H_4F reductase reaction catalyses the reduction of methylene-H_4 presumably coupled to the reduction of ferredoxin Fd_{ox} with NADH (Köpke et al., 2010; Mock et al., 2015). Accordingly, Fd_{ox}, ATP and 2 NADH are converted to Fd_{red}, ADP and 2 NAD^+. The direct reduction of *CO_2 with H_2 to formate by formate-H_2 lyase was not considered in our model, as the C. ljungdahlii* genome lacks the annotated gene (Köpke et al., 2010). However, formate-H_2 lyase activity was identified for CO consuming *C. autoethanogenum* (Wang et al., 2013). Therefore, an additional model containing the aforementioned reaction (modified rSMM) was used to further assess

our simulative results. Both models are attached in the Supplementary Material (**Table 7.1**, **Table 7.2** and **Table 7.3**).

Flux balance analysis. Flux balance analysis (FBA) was performed to investigate the intracellular carbon, redox and energy balances of *C ljungdahlii* as a function of varying substrate conditions (Orth et al., 2010; Schilling et al., 2000). This was necessary as the degree of freedom of the model exceeds the maximal number of quantifiable fluxes. For simulations, the Insilico Discovery™ platform was used. Maximization of biomass production was set as objective function, while all experimentally determined extracellular substrate uptake and product formation rates were used as constraints. YE was not considered for modelling, as only 0.5 g L^{-1} YE was provided in the batch medium accounting for < 5% of the incorporated carbon during all cultivations we described. This is reflected by well-closed balances for measured carbon without YE consideration. Total organic carbon content in YE was measured using a TC analyser (Graf et al., 2018). We normalized the sum of the product fluxes to the sum of substrate fluxes (set to 100%) and analysed the relative distributions. Due to the reversibility of the phosphotransacetylase, the acetate kinase, aldehyde oxidoreductase and the acetaldehyde/ alcohol dehydrogenase reactions, non-realistic futile cycling may occur biasing ATP formation. To prevent non-wanted ATP futile cycles via acetate and ethanol formation, the following constraint was additionally set: We limited the acetyl-CoA synthase flux (r_{ACCOAS}) by the simulated maximum using experimentally observed substrate uptake rates. Consequently, this maximum also limited the phosphotransacetylase reaction (r_{PTA}) which, again, served as upper limit for the acetate kinase reaction (r_{ACK}). Accordingly, a two-step simulation was performed preventing non-wanted futile cycling.

ACKNOWLEDGEMENTS

The authors thank Salaheddine Laghrami for excellent support with bioreactor fermentations and Mira Lenfers-Lücker for assistance with the HPLC analyses. Moreover, we thank Alexander Akermann for his great help with the reconstruction of the stoichiometric model and laboratory contribution. We also thank Flora Siebler for

her support and advice during this study. Furthermore, we thank all members of the project ‘Gase als neue Kohlenstoffquelle für biotechnologische Fermentationen (Gas-Fermentation)’ for a great cooperation. The authors further gratefully acknowledge the funding of this work by the Federal Ministry of Education and Research (BMBF).

CONFLICT OF INTEREST

None declared.

REFERENCES

See 6 references.

SUPPLEMENTARY MATERIAL

The Supplementary Material for this article can be found online at: https://sfamjournals.onlinelibrary.wiley.com/doi/full/10.1111/1751-7915.13625 and in chapter **7.1** of this document.

3.3 Manuscript II: Isobutanol production by autotrophic acetogenic bacteria

Sandra Weitz[1], Maria Hermann[2], Sonja Linder[1], Frank R. Bengelsdorf[1], Ralf Takors[2], Peter Dürre[1,*]

[1]Institut für Mikrobiologie und Biotechnologie, Universität Ulm, Ulm, Germany

[2]Institut für Bioverfahrenstechnik, Universität Stuttgart, Stuttgart, Germany

*Corresponding Author: Prof. Dr. Peter Dürre;

Email: peter.duerre@uni-ulm.de

Reproduced with permission from Weitz et al. (2021)

KEYWORDS

Acetobacterium woodii, acetogens, *Clostridium ljungdahlii*, gas fermentation, isobutanol production, syngas

ABSTRACT

Two different isobutanol synthesis pathways were cloned into and expressed in the two model acetogenic bacteria *Acetobacterium woodii* and *Clostridium ljungdahlii*. *A. woodii* is specialized on using CO_2 + H_2 gas mixtures for growth and depends on sodium ions for ATP generation by a respective ATPase and Rnf system. On the other hand, *C. ljungdahlii* grows well on syngas (CO + H_2 + CO_2 mixture) and depends on protons for energy conservation. The first pathway consisted of ketoisovalerate ferredoxin oxidoreductase (Kor) from *Clostridium thermocellum* and bifunctional aldehyde/alcoholdehydrogenase (AdhE2) from *Clostridium acetobutylicum*. Three different *kor* gene clusters are annotated in *C. thermocellum* and were all tested. Only in recombinant *A. woodii* strains, traces of isobutanol could be detected. Additional feeding of ketoisovalerate increased isobutanol production to 2.9 mM under heterotrophic conditions using *kor*3 and to 1.8 mM under autotrophic conditions using *kor*2. In *C. ljungdahlii*, isobutanol could only be detected upon additional ketoisovalerate feeding under autotrophic conditions. *Kor*3 proved to be the best suited gene cluster. The second pathway consisted of ketoisovalerate decarboxylase from *Lactococcus lactis* and alcohol dehydrogenase from *Corynebacterium glutamicum*. For increasing the carbon flux to ketoisovalerate, genes encoding ketol-acid reductoisomerase, dihydroxy-acid dehydratase, and acetolactate synthase from *C. ljungdahlii* were subcloned downstream of *adhA*. Under heterotrophic conditions, *A. woodii* produced 0.2 mM isobutanol and 0.4 mM upon additional ketoisovalerate feeding. Under autotrophic conditions, no isobutanol formation could be detected. Only upon additional ketoisovalerate feeding, recombinant *A. woodii* produced 1.5 mM isobutanol. With *C. ljungdahlii*, no isobutanol was formed under heterotrophic conditions and only 0.1 mM under autotrophic conditions. Additional feeding of ketoisovalerate increased these values to 1.5 mM and 0.6 mM, respectively. A further

increase to 2.4 mM and 1 mM, respectively, could be achieved upon inactivation of the *ilvE* gene in the recombinant *C. ljungdahlii* strain. Engineering the coenzyme specificity of IlvC of *C. ljungdahlii* from NADPH to NADH did not result in improved isobutanol production.

INTRODUCTION

Isobutanol is an important platform chemical, representing an app. one billion US $ market in 2019. The compound is mainly used in solvents and coatings, as a chemical intermediate, or as a biofuel (gasoline additive). Synthesis is chemically achieved by hydroformylation of propylene, followed by hydrogenation of the formed aldehyde, but bio-based processes have been developed by companies Gevo Inc. (Douglas County, CO) and Butamax Advanced Biofuels LLC (Wilmington, DE; joint venture of BP and DuPont). The share of bio-based isobutanol is expected to rise in the near future significantly compared to the synthetic compound. A number of microorganisms have been engineered for isobutanol production, including aerobic and anaerobic bacteria as well as *Saccharomyces cerevisiae* (Chen and Liao, 2016). Gevo is using a recombinant yeast for its corn-based process, but details have not yet been disclosed. A landmark publication reported genetically engineered isobutanol formation by modification of amino acid synthesis pathways (Atsumi et al., 2008). 2-Ketoisovalerate, an intermediate in valine and isoleucine biosynthesis, was first decarboxylated by e.g., KivD from *Lactococcus lactis* and then the formed aldehyde was reduced to isobutanol by an alcohol dehydrogenase (e.g., Adh2 from *Saccharomyces cerevisiae*) **(Figure 3.8).**

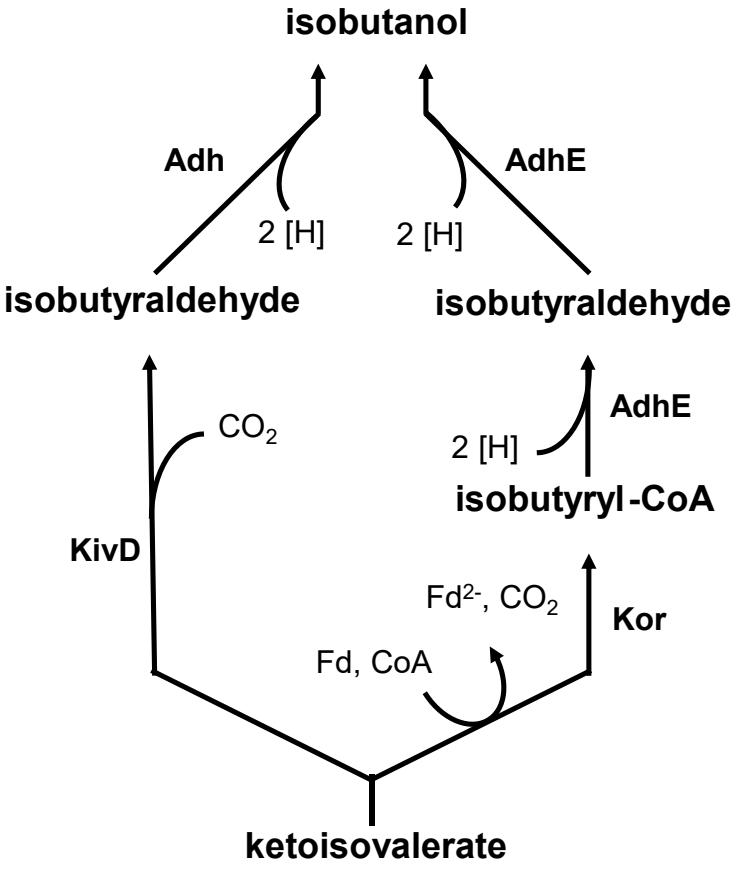

Figure 3.8 Formation of isobutanol by the enzymes KivD (ketoisovalerate decarboxylase) and Adh (alcohol dehydrogenase) or Kor (ketoisovalerate ferredoxin oxidoreductase) and AdhE (bifunctional aldehyde/alcohol dehydrogenase) from ketoisovalerate, the precursor of valine.

A natural pathway for production is based on the enzyme ketoisovalerate ferredoxin oxidoreductase (Kor), which was first found and characterized in hyperthermophilic archaea, where it is involved in branched-chain amino acid degradation and biosynthesis (Heider et al., 1996). This isobutanol synthesis pathway (**Figure 3.8**) was shown to be active in e.g., *C. thermocellum* (Lin et al., 2015).

Using biological production with recombinant strains, high isobutanol titers in typical fermentation setups were obtained with e.g., *E. coli* (22 g L^{-1}; (Atsumi et al., 2008)), *Corynebacterium glutamicum* (13 g L^{-1}; (Blombach et al., 2011)), *C. thermocellum* (5.4 g L^{-1}; (Lin et al., 2015)), *Geobacillus thermoglucosidasius* (3.3 g L^{-1}; (Lin et al., 2014)), *S. cerevisiae* (2.1 g L^{-1}; (Wess et al., 2019)), and *Ralstonia eutropha* (0.03 g L^{-1}; (Black et al., 2018)). All these processes used sugar or cellulose as a carbon source. Cheaper substrates would be CO_2 (in combination with a reductant) or

CO, which are also waste and greenhouse gases. A photosynthetic isobutanol production of up to 0.9 g L^{-1} from CO_2 and solar energy has been reported for *Synechocystis* PCC 6803 (Miao et al., 2018). The electrochemical conversion of CO_2 and water to formate was coupled with formate-dependent growth of recombinant cells of the aerobic "Knallgas" bacterium *R. eutropha*, yielding up to 0.85 g isobutanol/L (Li et al., 2012). However, some challenges still remain for CO_2-based biological isobutanol formation compared to the non-biological production (Brigham, 2019). Here, we report an approach to isobutanol synthesis using two anaerobic bacteria, which became model organisms of the so-called acetogens: *A. woodii*, growing on CO_2/H_2, and *C. ljungdahlii*, growing on syngas (a mixture of mostly CO and H_2).

MATERIALS AND METHODS

A. woodii (DSM 1030) and *C. ljungdahlii* (DSM13583) were obtained from the DSMZ (Deutsche Sammlung von Mikroorganismen und Zellkulturen GmbH, Brunswick, Germany). *E. coli* XL1-Blue MRF'[1(mcrA)1831(mcrCB-hsdSMR-mrr)173 endA1 supE44 thi-1] stemmed from Stratagene (La Jolla, CA). All plasmids used in this study are listed in **Table 3.6**.

Table 3.6: Plasmids used in this study.

Plasmid	Relevant features	Reference
pJUL34	*kivD from L. lactis, Ptuf from L. lactis, adhA from Corynebacterium glutamicum; aph3; sacB, replicon repBL1 for Corynebacterium*	Gift from Bastian Blombach (Technical University of Munich, Germany) and Bernhard Eikmanns (University of Ulm, Germany)
pMTL007-E2_ilvE	ColE1 ori$^-$, pCB102 ori$^+$, *catP*, *lacZ*, *ltrA*, *oriT*, Pfdx, *ermB*, *traJ,* ClosTron™plasmid to inactive *ilvE* in the genome of *C. ljungdahlii*	This study, ATUM, Newark, CA, USA
pMTL83151	*catP*, ColE1 ori$^-$, *lacZ*, pCB102 ori$^+$, *traJ*	Heap et al., 2009
pMTL83151_ ptaack_aacht_cac	pMTL83151, $P_{pta\text{-}ack}$ from *C. ljungdahlii, adhE2* from *C. acetobutylicum*; *abfD* from *C. scatologenes*, *crt* from	This study

Plasmid	Relevant features	Reference
	C. acetobutylicum; *hbd* from *C. acetobutylicum*, *thlA* from *C. acetobutylicum*	
pKAIA	pMTL83151, $P_{pta\text{-}ack}$ from *C. ljungdahlii, kivD* from *L. lactis*, *adhA* from *Corynebacterium glutamicum*, *ilvC*, *ilvD*, and *alsS* from *C. ljungdahlii*	This study
$pKAI_{NADH}A$	pMTL83151 $P_{pta\text{-}ack}$ from *C. ljungdahlii*, *kivD* from *L. lactis, adhA* from *C. glutamicum*, *ilvD* and *alsS* from *C. ljungdahlii*, $ilvC^{P2D1\text{-}A1}$ from *E. coli*, codon optimized for clostridia	This study, Thermo Fisher Scientific GENEART GmbH, Regensburg, Germany, (Brinkmann-Chen et al., 2013)
pKOR2	pMTL83151, $P_{pta\text{-}ack}$ from *C. ljungdahlii*, *adhE2* from *C. acetobutylicum*, *kor2* from *C. thermocellum*	This study

Media and growth conditions

E. coli was cultivated aerobically in LB (Luria-Bertani) medium (per L: tryptone 10 g, yeast extract 5 g, NaCl 10 g) (Green and Sambrook, 2012) at 37°C on a rotary shaker (175 rpm). For generation of competent cells, *E. coli* was grown in modified SOB (Super Optimal Broth; per L: tryptone 20 g, yeast extract 5 g, NaCl 0.5 g, KCl 1.92 g, $MgCl_2 \times 6\ H_2O$ 2.03 g) (Green and Sambrook, 2012).

Basal medium for *A. woodii* was modified from Balch et al. (1977) and contained per L: KH_2PO_4 0.33 g, K_2HPO_4 0.45 g, $MgSO_4 \times 7\ H_2O$ 0.33 g, NH_4Cl 1 g, yeast extract 2 g, L-cysteine-HCl × H_2O 0.5 g, resazurin 1 mg. To this solution, 20 mL of trace element solution (per L: nitrilotriacetic acid 1.5 g, $MgSO_4 \times 7\ H_2O$ 3 g, $MnSO_4 \times H2O$ 0.5 g, NaCl 1 g, $FeSO_4 \times 7\ H_2O$ 0.1 g, $CoSO_4 \times 7\ H_2O$ 0.18 g, $CaCl_2 \times 2\ H_2O$ 0.1 g, $ZnSO_4 \times 7\ H_2O$ 0.18 g, $CuSO_4 \times 5\ H_2O$ 0.01 g, $Kal(SO_4)_2 \times 12\ H_2O$ 0.02 g, H_3BO_3 0.01 g, $Na_2MoO_4 \times 2\ H_2O$ 0.01 g, $NiCl_2 \times 6\ H_2O$ 0.03 g, $Na_2SeO_3 \times 5\ H_2O$ 0.3 mg, $Na_2WO_4 \times 2\ H_2O$ 0.4 mg) and 20 mL vitamin solution (per L: biotin 2 mg, folic acid 2 mg, pyridoxine-HCl 10 mg, thiamine-HCl 5 mg, riboflavin 5 mg, nicotinic acid 5 mg, D-Ca-pantothenate 5 mg, vitamin B12 0.1 mg, p-aminobenzoic acid 5 mg, lipoic acid

5 mg (DSMZ_Medium141-1.pdf,[1]) were added. Media were prepared under strictly anaerobic conditions. Heterotrophic growth was performed with 40 mM fructose as a carbon source under an atmosphere consisting of N_2 (80%) and CO_2 (20%), autotrophic growth with a CO_2 + H_2 gas mixture (33% + 67%), both at 30°C.

C. ljungdahlii was cultivated in a modified medium described by Tanner et al. (1993). It contained per L: 2-(*N*-morpholino) ethanesulfonic acid 20 g, yeast extract 0.5 g, L-cysteine-HCl × H_2O 1 g, resazurin 1 mg. To this solution, 25 mL of mineral salts solution (per L: $CaCl_2$ × 2 H_2O 4 g, KCl 10 g, KH_2PO_4 10 g, $MgSO_4$ × 7 H_2O 20 g, NaCl 80 g, NH_4Cl 100 g), 10 mL of modified trace element solution (American Type Culture Collection (ATCC)[2]; 1754 PETC medium) (per L: nitrilotriacetic acid 2 g, $MnSO_4$ × H_2O 0.5 g, $Fe(SO_4)_2(NH_4)_2$ × 6 H_2O 0.8 g, $CoCl_2$ × 6 H_2O 0.2 g, $ZnSO_4$ × 7 H_2O 1 mg, $CuCl_2$ × 2 H_2O 20 mg, $NiCl_2$ × 6 H_2O 20 mg, Na_2MoO_4 × 2 H_2O 20 mg, Na_2SeO_3 × 5 H_2O 20 mg, Na_2WO_4 × 2 H_2O 20 mg), and 10 mL vitamin solution (per L: biotin 2 mg, folic acid 2 mg, pyridoxine-HCl 10 mg, thiamine-HCl 5 mg, riboflavin 5 mg, nicotinic acid 5 mg, D-Ca-pantothenate 5 mg, vitamin B12 5 mg, p-aminobenzoic acid 5 mg, and lipoic acid 5 mg) were added. Media were prepared under strictly anaerobic conditions. Heterotrophic growth was performed with 40 mM fructose as a carbon source under an atmosphere consisting of N_2 (80%) and CO_2 (20%), autotrophic growth with a syngas mixture (50% CO, 45% H_2, and 5% CO_2), both at 37°C.

For cultivation of *A. woodii* and *C. ljungdahlii* on solid media, a modified version of yeast tryptone fructose medium (Leang et al., 2013) was used (per L: yeast extract 10 g, tryptone 16 g, fructose 5 g, NaCl 4 g, L-cysteine-HCl × H_2O 1 g, resazurin 1 mg, agar 15 g). Agar plates were poured using anaerobic water in an anaerobic cabinet containing a N_2:H_2 (95:5%) gas atmosphere. Cell suspensions were dripped on plates and spread using glass beads. *A. woodii* cells were incubated at 30°C and *C. ljungdahlii* cells at 37°C in an incubator located in the anaerobic cabinet. For selection of antibiotic-resistant strains, the following concentrations were used per mL: ampicillin 100 mg, clarithromycin 2.5 mg, chloramphenicol 30 mg, kanamycin 50 mg, thiamphenicol 7.5 mg.

[1] https://www.dsmz.de/collection/catalog/details/culture/DSM-4553

[2] https://www.lgcstandards-atcc.org/products/all/55383.aspx#culturemethod

Analytical methods

Cell growth was monitored offline by measuring the optical density at 600 nm (Ultrospec 3100, Amersham Bioscience Europe GmbH, Freiburg, Germany) in 1 mL cuvettes (width 1 cm).

Ethanol, isobutanol, and isoamyl alcohol were determined using gas chromatograph (GC) “Clarus 680” (PerkinElmer, PerkinElmer, Waltham, MA, United States). GC was equipped with an Elite-FFAP column (i ∅ 0.32 mm x 30 m). H_2 was the carrier gas (2.25 mL min^{-1}, 100°C), injector temperature was 225°C, split 1:20, and flame ionization detector temperature was 300°C. Detector gases were synthetic air (450 mL min^{-1}) and H_2 (45 ml min^{-1}). A temperature profile was predefined: 90°C for 2 min, 40°C min^{-1} increasing steps to 250 C (constant for 1 min). Supernatant (0.48 mL) was acidified with 0.02 mL of 2 M HCl. 1 mL was injected into the GC. Calibration was performed using defined standards of the individual components.

Acetate, 2,3-butanediol, fructose, and ketoisovalerate were determined using high performance liquid chromatography (Agilent 1260 Infinity Series HPLC, Agilent Technologies, Santa Clara, CA) equipped with a refractive index detector (for 2,3-butanediol, fructose, ketoisovalerate) operating at 35 C and a diode array detector (for acetate) at room temperature. The “CS-Chromatographie organic acid column” (CS-Chromatographie Service GmbH, Langerwehe, Germany) was kept at 40 C. 5 mM H_2SO_4 was used as mobile phase with a flow rate of 0.7 mL min^{-1}. 20 mL of supernatant were injected into the HPLC system for determination of compounds.

DNA isolation

Bacterial genomic DNA was isolated using the “MasterPureTM Gram-Positive DNA Purification Kit” (Epicentre, Madison, WI, United States). 2 mL samples of late exponential cultures were centrifuged (18,000 g, 30 min, 4°C) and further processed according to the manufacturer’s instructions. Isolation of plasmid DNA from *E. coli* strains was performed with the “ZyppyTM Plasmid Miniprep Kit” (ZYMO Research Europe GmbH, Freiburg, Germany). 4 mL samples of overnight cultures were centrifuged (18,000 g, 1 min) and further processed according to the manufacturer’s instructions. In case of *A. woodii* and *C. ljungdahlii*, 2 mL were sampled and

centrifuged (18,000 g, 30 min, 4°C). The cell pellet was suspended in 600 mL Tris-HCl (20 mM, pH 7). For effective lysis, 60 mL lysozyme (20 mg mL^{-1}) were added, and the solution was incubated for 1 h at 37°C before proceeding according to the manufacturer's instructions. DNA from *C. thermocellum* DSM 1313 was purchased from the DSMZ (Deutsche Sammlung von Mikroorganismen und Zellkulturen GmbH, Brunswick, Germany). Sequencing of DNA was performed by GATC Biotech AG (Constance, Germany).

Plasmid construction

Standard molecular cloning techniques were performed according to established protocols (Green and Sambrook, 2012). In *C. thermocellum*, three gene clusters encoding a putative ketoisovalerate ferredoxin oxidoreductase (Kor) are annotated [*kor1* (Clo1313_0020-0023), *kor2* (Clo1313_0382- 0385), *kor3* (Clo1313_1353-1356)]. *Kor1* was PCR-amplified using primers clo0020T_fwd and clo0020T_rev, *kor2* was PCR-amplified using primers clo0382T_fwd and clo0382T_rev, and *kor3* was PCR-amplified using primers clo1353T_fwd and clo1353T_rev. Then, each fragment was subcloned into the pMTL83151 backbone (Heap et al., 2009), together (upstream) with the also PCR-amplified $P_{pta\text{-}ack}$ promoter from *C. ljungdahlii* (primers: Ptaack_fwd and Ptaack_rev) and the gene encoding bifunctional butyraldehyde/butanol dehydrogenase AdhE2 from *C. acetobutylicum* [primers: adhE2_pka_fwd and adhE2_pka_rev; plasmid pMTL83151_ptaack_aacht_cac (Supplementary **Figure 7.4**)]. All primers used are listed in Table 3.7. Subcloning was performed by in-fusion cloning using the NEBuilder Assembly Tool (New England Biolabs Inc.,Ipswich, MA, United States[3]). The resulting plasmids pKOR1, pKOR2, and pKOR3 are shown in Supplementary **Figure 7.5.** pMTL83151 was kindly provided by Nigel Minton (University of Nottingham, United Kingdom).

The plasmids constructed for elucidation of the ketoisovalerate decarboxylase pathway were also based on the pMTL83151 backbone. The *kivD* gene from *L. lactis* was PCR-amplified using primers kivd_fwd_XhoI and kivd_rev_Eco81I (making use of the inserted restriction sites for subcloning), *adhA* from *C. glutamicum* was PCR-amplified

[3] https://international.neb.com/products/e5520-nebuilder-hifi-dna-assemblycloning-kit#ProductInformation

using primers adhA_fwd_XhoI and adhA_rev_NheI (making use of the inserted restriction sites for subcloning). DNA source for amplification was plasmid pJUL34 (Supplementary **Figure 7.6**), which was kindly provided by Bastian Blombach (Technical University of Munich, Germany) and Bernhard Eikmanns (University of Ulm, Germany) **(Table 3.7**). Both fragments were subcloned together in several steps into pMTL83151. Upstream of *kivD*, the PCR-amplified $P_{pta\text{-}ack}$ promoter fragment from *C. ljungdahlii* (primers: Ptaack_fwd and Ptaack_rev) was inserted. The genes *ilvC* (encoding ketol-acid reductoisomerase) (primers ilvC_fwd and ilvC_rev), *ilvD* (encoding dihydroxyacid dehydratase) (primers ilvD_fwd and ilvD_rev), and *alsS* (encoding acetolactate synthase) (primers alsS_fwd and alsS_rev), all from *C. ljungdahlii*, were PCR-amplified (**Table 3.7**). Subcloning downstream of *adhA* was performed by in-fusion cloning using the NEBuilder Assembly Tool (New England Biolabs inc., Ipswich, MA, United States; see text footnote 3). The resulting plasmid was designated pKAIA (Supplementary **Figure 7.7**).

For changing the coenzyme specificity of IlvC (ketol-acid reductoisomerase) of *C. ljungdahlii* from NADPH to NADH, the $ilvC^{NADH}$ gene of *E. coli* was commercially synthesized according to Brinkmann-Chen et al. (2013), with appropriate overlaps for in-fusion cloning. Codon optimization for clostridia was suggested by the commercial supplier Thermo Fisher Scientific GENEART GmbH (Regensburg, Germany). The sequence of the codon-optimized, synthesized gene is provided in Supplementary **Figure 7.8**.

The *ilvC* gene was cut out of pKAIA and the codonoptimized, synthesized gene was subcloned into the linearized vector using in-fusion cloning, resulting in plasmid $pKAI_{NADH}A$ (Supplementary **Figure 7.9**).

The ClosTron plasmid pMTL007-E2_ilvE (**Table 3.6**) was synthesized by the company DNA 2.0 (now ATUM, Newark, CA, United States) (see below).

Table 3.7: Primer used for cloning procedures.

Name	Sequence	Amplification
clo0020T_fwd	GATATCTATATAAAATCATTTTAACCTCG AGAGGAGGATTACCACATGGGCAA	KOR1 Clo1313_0020-0023
clo0020T_rev	CAAATGCAGGCTTCTTATTTTTATGGCTA GCCAATAATATTTTCTCATTTTAAAAAAT	
clo0382T_fwd	GATATCTATATAAAATCATTTTAACCTCG AGAGGGAGCGATGGAGATGACAGA	KOR2 Clo1313_0382-0385
clo0382T_rev	CAAATGCAGGCTTCTTATTTTTATGGCTA GCCTCCTTTTTTCAAAAAAAGTCCATGTT CC	
clo1353T_fwd	GATATCTATATAAAATCATTTTAACCTCG AGGGGGGATTTACATGGCTAAGGT	KOR3 Clo1313_1353-1356
clo1353T_rev	CAAATGCAGGCTTCTTATTTTTATGGCTA GCCGTATAAGAATTAAAAATAAGAATTA AAAATCAAAACAATCAAAAAAAG	
Ptaack_fwd	ACAGCGGCCGCGTCGACGTTACCACTCAT	$P_{pta\text{-}ack}$
Ptaack_rev	ACAACCGGTCCTCAGGTCCTCCCTTTA	
adhE2_pka_fwd	TTAAATTTAAAGGGAGGACCTGAGGATG AAAGTTACAAATCAAAAAGAAC	*adhE2*
adhE2_pka_rev	CTTGGGGTGCAGCAGTGGTCATCCTCGAG TTAAAATGATTTTATATAGATATCCTTAA GTTC	
kivd_fwd_XhoI	CTCGAGGTCCTCCTATTTATAAATTATG	*kivD*
kivd_rev_Eco81I	ACACCTGAGGATGTATACAGTAGGAG	
adhA_fwd_XhoI	CTCGAGATGACCACTGCTGCACCC	*adhA*
adhA_rev_NheI	ACAGCTAGCGCGAGTCGAACAGATGTG	
ilvC_fwd	TGTGGCGATTCGTTTCTAACGACGTCAAA ATAGTATAAATAAATTATTCAGGAGG	*ilvC*
ilvC_rev	TGTAAAAAAATACTAGTTTACTCATTATC AGGATTTTCATTG	
ilvD_fwd	TAATGAGTAAACTAGTATTTTTTTACAAA AAATTTCCAG	*ilvD*
ilvD_rev	GATCTTTATACCATGGTTATTTAAGAACT GCACCTGTATTTG	
alsS_fwd	TTCTTAAATAACCATGGTATAAAGATCAG AGGAAGTTTTATATG	*alsS*
alsS_rev	CAAAGTAGCTTCAGAGCAGTTCTAGATTA CATATTTTCATAAACTTCTTTTAAATG	

Underlined nucleotides are vector overlapping fragments used for In-Fusion® cloning.

Transformation

In case of *E. coli*, competent cells (Inoue et al., 1990) were obtained by inoculating 250 mL SOB medium with a 5-mL overnight culture grown in the same medium. Incubation was performed in a 2-L Erlenmeyer flask at 18 C under aerobic conditions and shaking (60 rpm), until an optical density (600 nm) of 0.6 – 0.8 was reached. Then, cells were put on ice for 30 min and afterward centrifuged (4,500 g, 4 C, 10 min). The pellet was suspended in 40 mL buffer (per 125 mL: piperazine-N,N'–bis(2-ethanesulfonic acid) 0.756 g, $CaCl_2$ 0.42 g, pH 6.7; mixed with 125 mL containing 4.66 g KCl and 1.72 g $MnCl_2$ x 4 H_2O), incubated on ice for 10 min, and again centrifuged (4,500 g, 4 C, 10 min). The pellet was suspended in 10 mL of the same buffer. 1.5 mL sterile dimethyl sulfoxide were added, and the solution was split into 200 µL aliquots and stored at – 80 C. For transformation, such aliquots were thawed on ice, mixed with 10 µl of a DNA solution (in-fusion reaction mix or plasmid), incubated on ice for 10 min, and then at 42 C for 1 min. After an incubation period of 10 min again on ice, 800 µL LB medium were added, and the solution was incubated aerobically for 1 h at 37 C with shaking (160 rpm). Then, cells were centrifuged (4,000 g, room temperature, 3 min), and 800 µl of the supernatant discarded. The pellet was resuspended in the remaining liquid, which was used for plating on solid media with respective selection.

Electroporation of *A. woodii* and *C ljungdahlii* was performed using a modified protocol of Leang et al. (2013). All plastic materials were stored in an anaerobic cabinet at least 1 day before transformation to eliminate any remaining traces of oxygen. For preparation of competent cells, 100 ml medium were supplemented with 40 mM fructose and 40 mM DL-threonine, inoculated with an early exponential culture, and grown at the appropriate temperature to an optical density (600 nm) of 0.3 – 0.7. Cultures were centrifuged anaerobically (6,000 g, 4 C, 10 min), and the pellet was washed twice with 50 mL cool, anaerobic SMP buffer (per L: sucrose 92.4 g, $MgCl_2$ 6 H_2O 0.2 g, NaH_2PO_4 0.84 g; pH 6) and suspended in 0.6 mL SMP buffer. 120 µL cool anti-freezing buffer (mix of 20 mL SMP buffer and 30 mL dimethylformamide) were added, and aliquots stored at – 80 C.

Electroporation was carried out in an anaerobic cabinet. 25 µL of electrocompetent cells were mixed with 3 – 5 µg of plasmid DNA, cooled, and transferred to a pre-cooled 1-mm gap electroporation cuvette (Biozym Scientific GmbH, Hessisch Oldendorf, Germany). Electric pulse was performed with 625 V, resistance of 600 Ω, and a capacitance of 25 µF using a "Gene- Pulser XcellTM" pulse generator (Bio-Rad Laboratories GmbH, Munich, Germany). Afterward, cells were recovered using 5 mL of the respective medium without antibiotic in a Hungate tube and incubated until the optical density (600 nm) doubled. Then, the appropriate antibiotic was added and growth monitored. If growth was detectable, cells were inoculated into fresh medium with antibiotic and, after reaching the early exponential growth phase, plated onto solid media. Single colonies of obtained transformants were picked, and successful transformation was confirmed by isolating genomic or plasmid DNA and PCR amplification of respective sequences for verification.

Gene Inactivation by ClosTron

The ClosTron method was performed according to Heap et al; Heap et al. (2007). The aim was to create an insertion mutant in *ilvE* of *C. ljungdahlii*, which blocked the last step of valine biosynthesis. Target region for integration was determined using the respective algorithm (Perutka et al., 2004)[4] and the respective ClosTron plasmid (pMTL007-E2_ilvE) (**Table 3.6**) was synthesized by the company DNA 2.0 (now ATUM, Newark, CA). After transformation into *C. jungdahlii*, recombinant strains were verified by PCR amplification and sequencing of the respective gene region.

RESULTS

Isobutanol Production via Ketoisovalerate Ferredoxin Oxidoreductase (Kor)

In the genome of *C. thermocellum* three gene clusters are annotated that encode a putative ketoisovalerate ferredoxin oxidoreductase (Kor), i.e., *kor1* (Clo1313_0020-0023), *kor2* (Clo1313_0382-0385), and *kor3* (Clo1313_1353-1356). *Kor3* differs

[4] www.clostron.com

significantly from the other two clusters with respect to length (smaller) and gene arrangement (Supplementary **Figure 7.10**). However, all clusters consist of four genes, encoding the α, β, γ, and δ subunits of Kor. The α subunit carries the core domain of pyruvate-ferredoxin oxidoreductase, β a C-terminal thiamine pyrophosphate-binding domain, γ a catalytic domain of pyruvate/ketoisovalerate oxidoreductase, and δ a binding domain for 4Fe-4S ferredoxin. All clusters were PCR-amplified and subcloned each into the pMTL83151 backbone, together (upstream) with the $P_{pta\text{-}ack}$ promoter from *C. ljungdahlii* and the gene encoding bifunctional butyraldehyde/butanol dehydrogenase AdhE2 from *C. acetobutylicum*. The resulting plasmids (pKOR1, pKOR2, and pKOR3) were transformed into *A. woodii* and *C. ljungdahlii*. Recombinant strains were then tested under heterotrophic conditions with fructose as a carbon source as well as with and without addition of ketoisovalerate (15 mM). Both, *A. woodii* and *C. ljungdahlii* did not grow with ketoisovalerate as sole carbon and energy source and also did not show an increase in optical density when fructose and ketoisovalerate were supplied together, compared to fructose alone. Wild type strains and empty plasmid-carrying strains [*A. woodii* (pM83) and *C. ljungdahlii* (pM83)] were used as controls. Without ketoisovalerate addition, recombinant *A. woodii* strains only formed traces of isobutanol (0.1 mM). However, all pKOR-carrying strains produced increased amounts of ethanol. With addition of ketoisovalerate, *A. woodii* [pKOR1] produced 0.2 mM isobutanol, *A. woodii* [pKOR2] 0.3 mM, and *A. woodii* [pKOR3] 2.9 mM (**Figure 3.9**). Some isoamyl alcohol (up to 0.3 mM) was formed in addition. The respective data for *C. ljungdahlii* are shown in Supplementary **Figure 7.11**. With and without ketoisovalerate addition, no isobutanol was formed. pKOR-carrying strains produced increased amounts of ethanol with addition of ketoisovalerate.

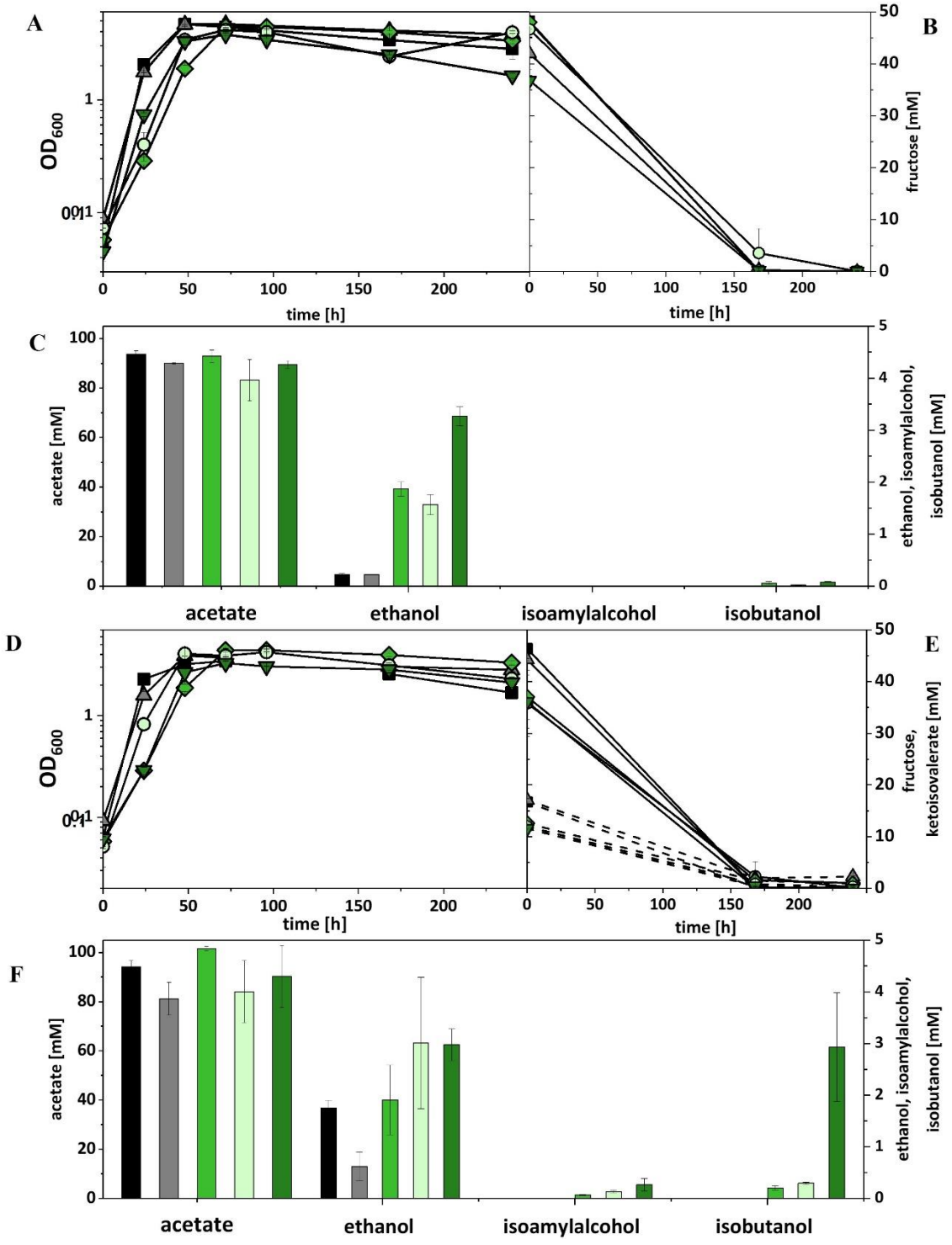

Figure 3.9: Heterotrophic isobutanol production with recombinant *A. woodii* strains by the Kor pathway. Growth behavior (**A,D**); fructose consumption (**B,E**); ketoisovalerate consumption; product pattern (**C,F**). *A. woodii* [WT], black, squares; *A. woodii* [pM83], gray, triangles; *A. woodii* [pKOR1], green, diamonds; *A. woodii* [pKOR2], light green, circles; *A. woodii* [pKOR3], dark green, triangle pointing downward. Panels (**A–C**) without ketoisovalerate supplementation; Panels (**D–F**) with ketoisovalerate supplementation. Each strain was analyzed in biological triplicates (n = 3).

For autotrophic growth, *A. woodii* was cultivated under a CO_2 + H_2 atmosphere, *C. ljungdahlii* under syngas. Without ketoisovalerate addition, recombinant *A. woodii* strains formed no isobutanol. With addition, *A. woodii* [pKOR1] produced 0.3 mM, *A. woodii* [pKOR2] 1.8 mM, and *A. woodii* [pKOR3] 1.1 mM (**Figure 3.10**). *A. woodii* [pKOR1] and *A. woodii* [pKOR2] produced also increased amounts of ethanol. Some isoamyl alcohol (up to 0.4 mM) was formed in addition. The respective data for *C. ljungdahlii* are shown in Supplementary **Figure 7.12**. Without ketoisovalerate addition, no isobutanol was formed and even with addition only trace amounts [*C. ljungdahlii* (pKOR2) 0.1 mM; *C. ljungdahlii* (pKOR3) 0.2 mM]. However, *C. ljungdahlii* [pKOR3] showed a significant increase in ethanol formation without ketoisovalerate addition as well as *C. ljungdahlii* [pKOR2] with addition.

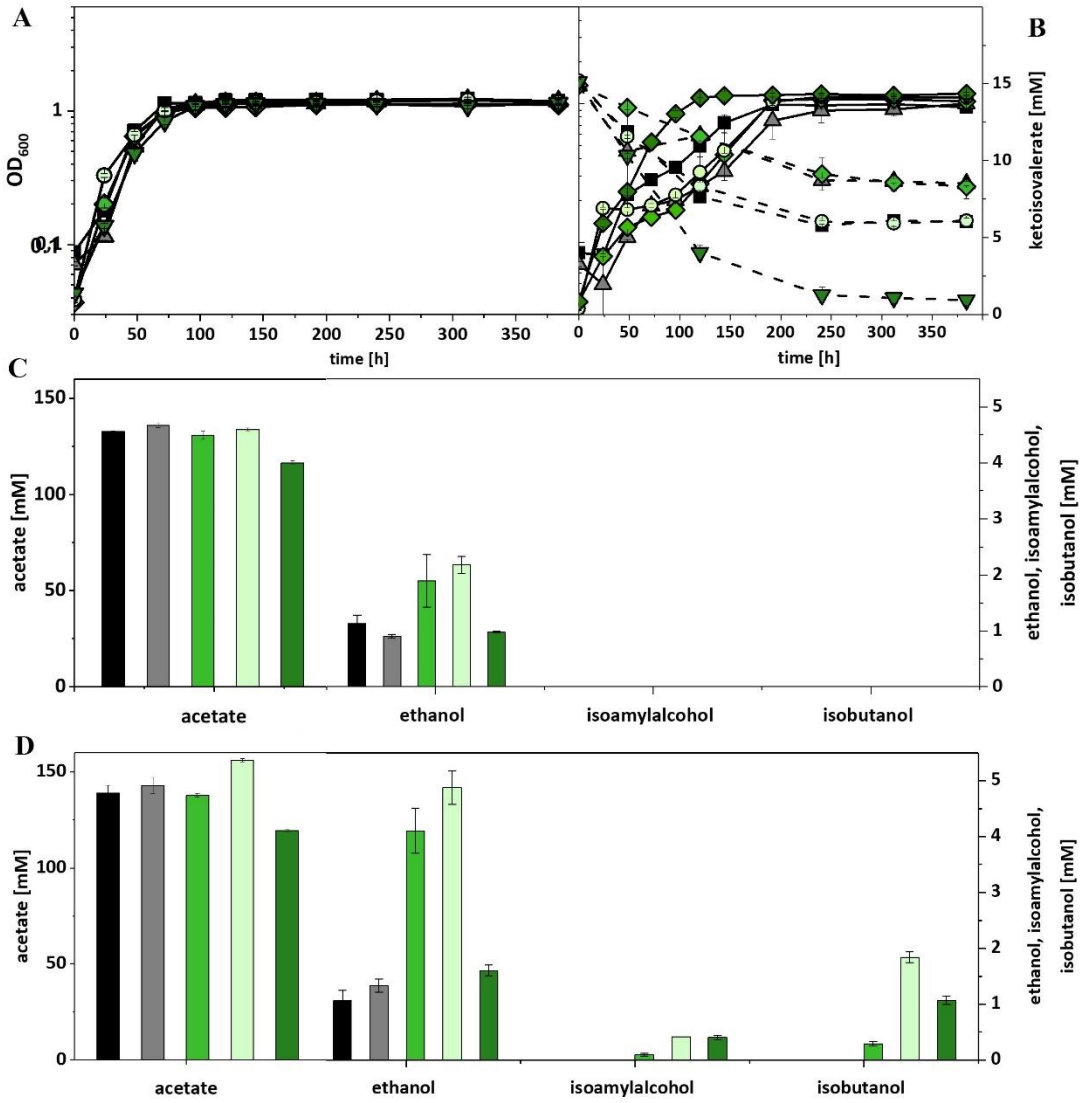

Figure 3.10: Autotrophic isobutanol production with recombinant *A. woodii* strains by the Kor pathway. Growth behavior (**A,B**); ketoisovalerate consumption (**B**); product pattern (**C,D**). *A. woodii* [WT], black, squares; *A. woodii* [pM83], gray, triangles; *A. woodii* [pKOR1], green, diamonds; *A. woodii* [pKOR2], light green, circles; *A. woodii* [pKOR3], dark green, triangle pointing downward. Panels (**A,C**) without ketoisovalerate supplementation; Panels (**B,D**) with ketoisovalerate supplementation. Each strain was analyzed in biological triplicates (n = 3).

Isobutanol Production via Ketoisovalerate Decarboxylase (KivD)

Next, the isobutanol synthesis pathway via ketoisovalerate decarboxylase and alcohol dehydrogenase in acetogens was elucidated. The *kivD* gene from *L. lactis* and *adhA* from *C. glutamicum* were PCR-amplified and subcloned together into the pMTL83151 backbone, controlled by the also PCR-amplified $P_{pta\text{-}ack}$ promoter from *C. ljungdahlii*. In

order to increase the carbon flux from pyruvate to ketoisovalerate, genes *ilvC* (encoding ketol-acid reductoisomerase), *ilvD* (encoding dihydroxy-acid dehydratase), and *alsS* (encoding acetolactate synthase), all from *C. ljungdahlii*, were PCR-amplified and subcloned downstream of *adhA*. The resulting plasmid pKAIA was transformed into *A. woodii* and *C. ljungdahlii.* In case of *C. ljungdahlii*, it was also possible to construct an insertion mutant in *ilvE* (encoding an aminotransferase), which blocked the last step of valine biosynthesis. This strain, *C. ljungdahlii:ilvE* was also transformed with pKAIA. Recombinant strains were then tested under heterotrophic conditions with fructose as a carbon source as well as with and without addition of ketoisovalerate (15 mM). Wild type strains and empty plasmid-carrying strains were used as controls.

Without ketoisovalerate addition, only *A. woodii* [pKAIA] formed some isobutanol (0.2 mM). With addition, the same strain produced 0.4 mM (Supplementary **Figure 7.13**). Some isoamyl alcohol (up to 0.2 mM) was formed in addition. The respective data for *C. ljungdahlii* are shown in Supplementary **Figure 7.14**. Without ketoisovalerate addition, no isobutanol was formed. With addition, *C. ljungdahlii* [pKAIA] and C*. ljungdahlii:ilvE* [pKAIA] produced up to 2.4 mM isobutanol during the exponential growth phase.

Under autotrophic growth conditions, recombinant *A. woodii* strains formed no isobutanol. With addition of 15 mM isovalerate, *A. woodii* [pKAIA] produced 1.7 mM isobutanol and 0.8 mM isoamyl alcohol (**Figure 3.11**). The respective data for *C. ljungdahlii* are shown in **Figure 3.12**. Only *C. ljungdahlii* [pKAIA] and *C. ljungdahlii:ilvE* [pKAIA] formed isobutanol (and isoamyl alcohol) without ketoisovalerate addition. The latter strain formed three times more alcohols (up to 0.4 mM isobutanol). Addition of ketoisovalerate increased production of both alcohols in the pKAIA-carrying strains (up to 1 mM in *C. ljungdahlii:ilvE* [pKAIA]).

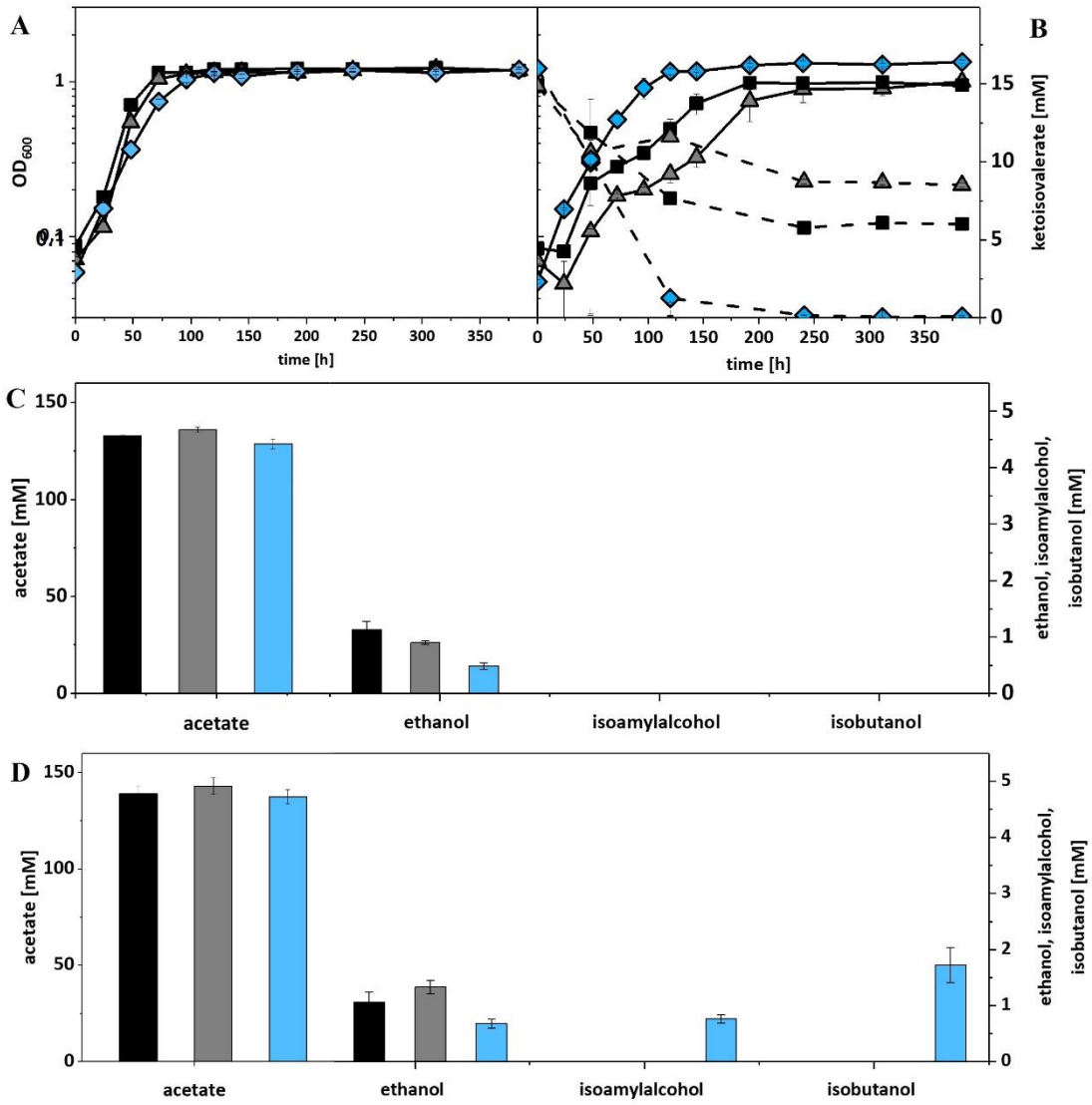

Figure 3.11: Autotrophic isobutanol production with recombinant *A. woodii* strains by the KivD pathway. Growth behavior (**A,B**); ketoisovalerate consumption (**B**); product pattern (**C,D**). *A. woodii* [WT], black, squares; *A. woodii* [pM83], gray, triangles*; A. woodii* [pKAIA], blue, diamonds. Panels (**A,C**) without ketoisovalerate supplementation; Panels (**B,D**) with ketoisovalerate supplementation. Each strain was analyzed in biological triplicates (n = 3).

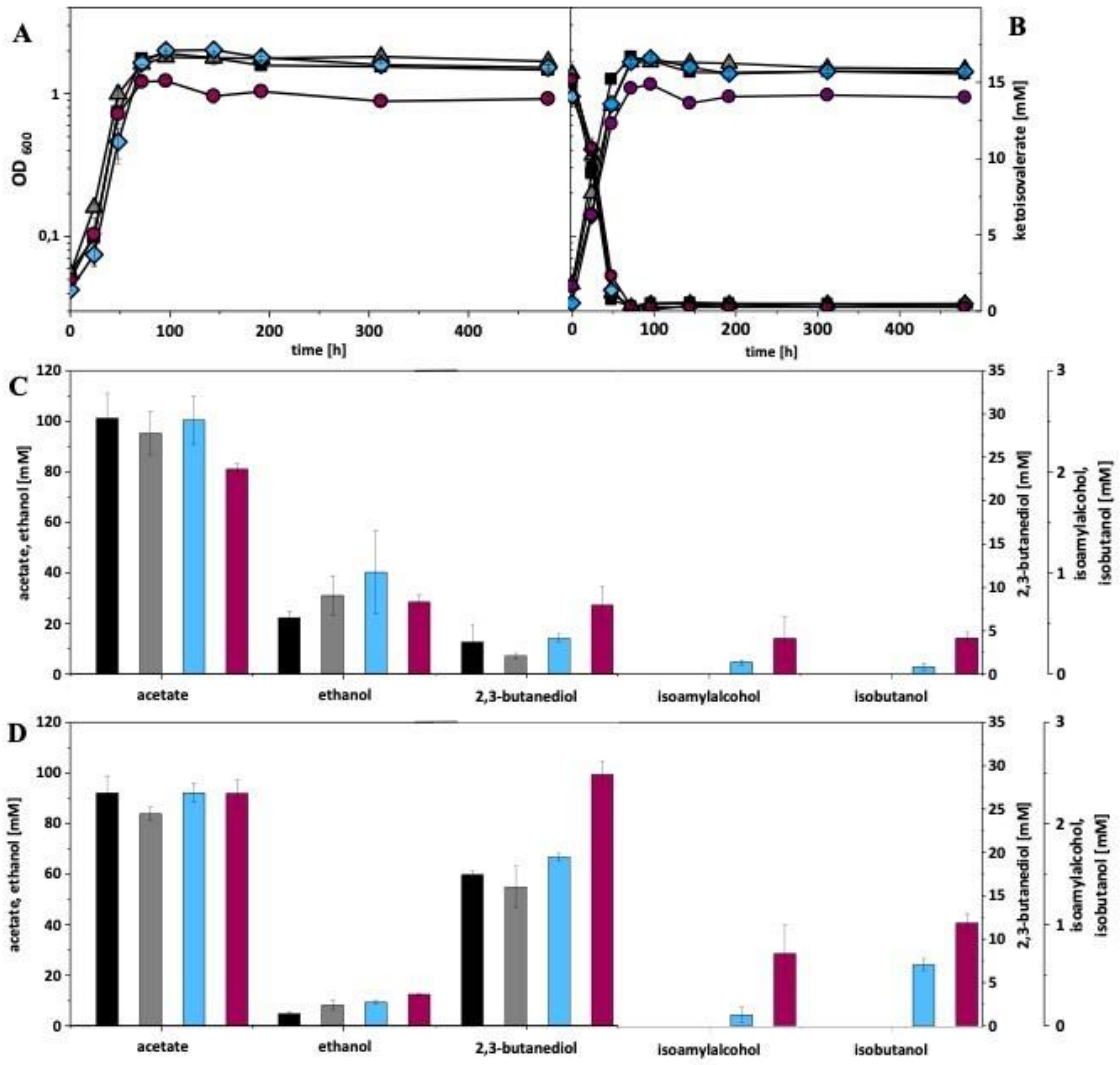

Figure 3.12: Autotrophic isobutanol production with recombinant *C. ljungdahlii* strains by the KivD pathway. Growth behavior (**A,B**); ketoisovalerate consumption (**B**); product pattern (**C,D**). *C. ljungdahlii* [WT], black, squares; *C. ljungdahlii* [pM83], gray, triangles; *C. ljungdahlii* [pKAIA], blue, diamonds; *C. ljungdahlii:ilvE* [pKAIA], purple, circles; Panels (**A,C**) without ketoisovalerate supplementation; Panels (**B,D**) with ketoisovalerate supplementation. Each strain was analyzed in biological triplicates (n = 3).

Coenzyme Dependency of Isobutanol Production via Ketoisovalerate Decarboxylase (KivD)

The *ilvC* gene product of *C. ljungdahlii*, the ketol-acid reductoisomerase, uses NADPH for reduction of acetolactate to 2,3-dihydroxyisovalerate. However, NADPH might be a limiting factor in a catabolic pathway with high amounts of products. Therefore, this

gene in pKAIA was replaced by a similar gene encoding a NADH-dependent IlvC enzyme from *E. coli* (Brinkmann-Chen et al., 2013). The nucleotide sequence of Ec_IlvC$^{P2D1\text{-}A1}$ was codon-optimized for clostridia, PCR-amplified, and subcloned into pKAIA by replacing the *C. ljungdahlii* ilvC gene. The resulting plasmid was designated pKAI$_{NADH}$A (**Supplementary Figure 6**). This plasmid was transformed into *C. ljungdahlii::ilvE*, and the recombinant tested in heterotrophic and autotrophic fermentations. With fructose as a carbon source, *C. ljungdahlii::ilvE*[pKAI$_{NADH}$A] produced isobutanol only upon addition of ketoisovalerate. The production was slightly higher than with the corresponding pKAIA-carrying strain (1.6 mM vs. 1.4 mM). Under autotrophic conditions without isovalerate supplementation, *C. ljungdahlii::ilvE*[pKAI$_{NADH}$A] formed only trace amounts of isobutanol (0.1 mM). Even with isovalerate addition, lower amounts were produced than by *C. ljungdahlii::ilvE*[pKAIA] (0.8 mM compared to 1 mM).

DISCUSSION

The data presented clearly demonstrate that subcloning of both, the KivD as well as the Kor pathway lead to heterologous expression of isobutanol formation in acetogenic bacteria. Both key enzymes, ketoisovalerate decarboxylase and ketoisovalerate ferredoxin oxidoreductase, belong to the group of pyruvate decarboxylases/pyruvate oxidoreductases and are dependent on thiamine pyrophosphate (de la Plaza et al., 2004; Heider et al., 1996). The active forms are homo- or heterotetramers, respectively. KivD from *L. lactis* decarboxylates preferentially ketoisovalerate, but also showed specific activity towards other keto compounds, from ketoisocaproate (23 % relative activity) to pyruvate (0.6 % relative activity) (de la Plaza et al., 2004). The temperature optimum is 45 °C, but more than 74 % relative activity is found between 30 and 50 °C (de la Plaza et al., 2004). The pH optimum is more pronounced, with a peak at pH 6.5 and app. 90 % relative activity between pH 6 and 7 (de la Plaza et al., 2004). Kor has been purified from *Pyrococcus* and *Thermococcus* strains, which are proteolytic and hyperthermophilic archaea. Highest activity was observed with ketoisovalerate, lowest activity with phenylpyruvate, pyruvate, and glyoxylate (Heider

et al., 1996). Based on the back reaction of acetyl-CoA + CO_2 + reduced ferredoxin to pyruvate, Xiong et al. (2016) characterized the kor gene clusters of *C. thermocellum* as reversed pyruvate ferredoxin oxidoreductases. *T. litoralis* Kor exhibits a sharp pH optimum at 7, with less than 50 % relative activity of pH 6 and 25 % at pH 8 (Heider et al., 1996). The temperature optimum of enzymes from the different archaea varies between 90 and 98 °C (Heider et al., 1996).

Our results demonstrate that the *kor3* and *kor2* gene clusters are the best suited candidates for further improvement of isobutanol production in acetogens by the Kor pathway, especially in *A. woodii*. Interestingly, the relatively low similarity between the respective gene products (Supplementary **Figure 7.10**) does not show a massive effect on product formation. Although the titers are still low (0.1 mM without and up to 2.9 mM with ketoisovalerate addition), it must be kept in mind that in other reported production organisms such as *E. coli* and *C. glutamicum* only numerous additional gene inactivations finally led to promising strains (Atsumi et al., 2008; Blombach et al., 2011). The formation of isoamylalcohol (3-methyl-1-butanol) is most probably due to the relatively broad substrate spectrum of ketoisovalerate ferredoxin oxidoreductase (and also ketoisovalerate decarboxylase) (Atsumi et al., 2008; Heider et al., 1996). Ketoisocaproate would be the precursor and is metabolized by both enzymes. This substance is formed naturally during leucine biosynthesis. Interestingly, the introduction of the *kor1* and *kor2* gene clusters led in both, *A. woodii* and *C. ljungdahlii* to an app. doubling of the ethanol formation, but only under autotrophic conditions upon addition of ketoisovalerate. *Kor2* in *A. woodii* under heterotrophic conditions resulted in the same phenomenon, whereas in *C. ljungdahlii* rather a decrease in ethanol formation in kor-carrying strains under heterotrophic conditions could be observed. The reason for this phenomenon is not obvious, as especially in *A. woodii* the stoichiometry of added ketoisovalerate and formed ethanol does not match. On the other hand, the increase of 2,3-butanediol production in all *C. ljungdahlii* strains upon addition of ketoisovalerate can be easily explained. Obviously, ketoisovalerate was converted to acetolactate, which was then decarboxylated and reduced to yield 2,3-butanediol.

The KivD pathway also allowed formation of trace amounts of isobutanol in *A. woodii* (heterotrophic conditions) and *C. ljungdahlii* (autotrophic conditions). Addition of ketoisovalerate clearly stimulated isobutanol production in both organisms under all tested growth conditions. The inactivation of *ilvE* in *C. ljungdahlii* (blocking the last step of valine biosynthesis) led to a significant increase in isobutanol production. This stresses again the necessity of further tailored metabolic mutations for optimizing the isobutanol fermentation. Unfortunately, an attempt during this project to inactivate the *aldC* gene of *C. ljungdahlii* (encoding the acetolactate decarboxylase, which catalyzes the first step of 2,3-butanediol synthesis) failed. Such a mutant would have prevented the carbon flow towards 2,3-butanediol. It was also disappointing that changing the coenzyme specificity of IlvC, the ketol-acid reductoisomerase, of *C. ljungdahlii* from NADPH to NADH did not result in an increase in isobutanol formation. However, as already stressed before, most probably only a combination of a series of metabolic alterations will result in a suitable production strain, as was the case with other heterotrophic bacteria.

What targets for such mutations can be imagined? Of course, reduction of other products will be the primary goal. Acetate formation is of vital importance for acetogens regarding ATP formation, but it can be further converted to ethanol using aldehyde ferredoxin oxidoreductase and alcohol dehydrogenase. The required reducing equivalents (reduced ferredoxin and NADH) can be easily generated from hydrogen under autotrophic conditions. Thus, 2,3-butanediol is the prime candidate for a product to be eliminated. If the ClosTron technology does not work (as mentioned, our attempt to inactivate the *ilvC* gene failed), CRISPR/Cas9-based genome editing will be an alternative that has recently been developed for *C. ljungdahlii* (Huang et al., 2016; Jin et al., 2020). The optimal temperatures for both key enzymes, ketoisovalerate decarboxylase (45 °C) and ketoisovalerate ferredoxin oxidoreductase (growth temperature of *C. thermocellum* is 60 °C), significantly exceed the range of mesophilic fermentations. The same applies to the pH optimum of both enzymes. Acetogenic bacteria generate a low pH, which results in reduced enzyme activity. Also, the broad enzyme substrate range is a disadvantage, as is obvious from the formation of isoamylalcohol by *A. woodii*. Thus, mutational adaptation of the key enzymes with

respect to pH and temperature tolerance as well as increase of substrate specificity will be another prime target in future. The change of coenzyme specificity from NADPH to NADH has already been achieved for IlvC from *C. ljungdahlii* and can thus easily be combined with the aforementioned alterations. Finally, growing the strains in gassed and stirred bioreactors will certainly improve the fermentation outcome. In fact, a *C. ljungdahlii::ilvE* strain carrying pKAIA showed under such conditions an increased isobutanol production by factor 6.5 (Hermann et al., 2021).

Further metabolic engineering will focus on the *kor3* gene cluster in case of *A. woodii* and the KivD pathway in *C. ljungdahlii::ilvE* [pKAIA], which so far allowed highest product formation. Strains suitably improved as described above might then become a viable option for commercial isobutanol synthesis from waste and greenhouse gases such as CO and CO_2.

DATA AVAILABILITY STATEMENT

The original contributions presented in the study are included in the article/**Supplementary Material**, further inquiries can be directed to the corresponding author/s.

AUTHOR CONTRIBUTIONS

SW, FB, MH, RT, and PD conceived and designed the experiments. SW and SL performed the experiments. SW, MH, SL, FB, RT, and PD analyzed the data. MH, SL, FB, RT, and PD wrote the manuscript. All authors contributed to the article and approved the submitted version.

FUNDING

This work was supported by the Bundesministerium für Bildung und Forschung (BMBF) in its program “Gase als neue Kohlenstoffquelle für biotechnologische Fermentationen,” project gas fermentation (031A468A).

ACKNOWLEDGMENTS

We thank Nigel Minton (University of Nottingham, United Kingdom) for providing plasmid pMTL83151 and Bastian Blombach (Technical University of Munich, Germany) as well as Bernhard Eikmanns (University of Ulm, Germany) for providing plasmid pJUL34.

SUPPLEMENTARY MATERIAL

The Supplementary Material for this article can be found online at: https://www.frontiersin.org/articles/10.3389/fbioe.2021.657253/full#supplementary-material and in chapter **7.2** of this document.

Figure 7.4: Schematic representation of plasmid pMTL83151_ptaack_aacht_cac. *adhE2*, bifunctional aldehyde/alcohol dehydrogenase gene (*C. acetobutylicum*); *abfD*, 4-hydroxybutyryl-CoA dehydratase gene (*Clostridium scatologenes*); *crt*, crotonase gene (*C. acetobutylicum*); *hbd*, 3-hydroxybutyryl-CoA dehydrogenase gene (*C. acetobutylicum*); *thlA*, acetyl-CoA acetyltransferase gene (*C. acetobutylicum*); *catP*, chloramphenicol resistance gene; ColE1, origin of replication for Gram-negative bacteria; *repH*, origin of replication for Gram-positive bacteria; *lacZ* alpha, truncated b-galactosidase gene (*E. coli*); *traJ*, gene for DNA transfer by conjugation.

Figure 7.5: Schematic representation of plasmids pKOR1, pKOR2 and pKOR3. *Kor1*, *kor2*, *kor3*, potential ketoisovalerate ferredoxin oxidoreductases gene clusters (*C. thermocellum*); *adhE2* bifunctional aldehyde/alcohol dehydrogenase gene (*C. acetobutylicum*); $P_{pta\text{-}ack}$, promoter upstream of *pta-ack* genes *(C. ljungdahlii*); *catP*, chloramphenicol resistance gene; ColE1, origin of replication for Gram-negative bacteria; *repH*, origin of replication for Gram-positive bacteria; *traJ*, gene for DNA transfer by conjugation.

Figure 7.6: Schematic representation of plasmid pJUL34. P_{tuf}, promoter upstream of EF-Tu gene (*L. lactis*); *kivD*, ketoisovalerate decarboxylase gene (*L. lactis*); *adhA*, alcohol dehydrogenase gene (*Corynebacterium glutamicum*); *lacZ alpha*, truncated b-galacosidase gene (*E. coli*); *aph3,* kanamycin resistance gene; *sacB,* levansucrase gene; repBL1, origin of replication for *Corynebacterium*.

Figure 7.7: Schematic representation of plasmid pKAIA. *kivD*, ketoisovalerate decarboxylase gene (*L. lactis*); *adhA*, alcohol dehydrogenase gene (*C. glutamicum*); *ilvC*, ketol-acid reductoisomerase gene (*C. ljungdahlii*); *ilvD*, dihydroxy-acid dehydratase gene (*C. ljungdahlii*); *alsS*, acetolactate synthase gene (*C. ljungdahlii*); $P_{pta\text{-}ack}$, promoter upstream of *pta-ack* genes (*C. ljungdahlii*); *catP*, chloramphenicol resistance gene; ColE1, origin of replication for Gram-negative bacteria; *repH*, origin of replication for Gram-positive bacteria; *traJ*, gene for DNA transfer by conjugation.

Figure 7.8: Sequence of the commercially synthesized and codon-optimized $ilvC^{NADH}$ gene.

Figure 7.9: Schematic representation of plasmid $pKAI_{NADH}A$. *kivD*, ketoisovalerate decarboxylase gene (*L. lactis*); *adhA*, alcohol dehydrogenase gene (*Corynebacterium glutamicum*); *ilvC*, ketol-acid reductoisomerase gene (*C. ljungdahlii*); $ilvC^{NADH}$, NADH-dependent ketol-acid reductoisomerase gene (Ec_IlvCP2D1-A1 from *E. coli*, codon-optimized for clostridia); *ilvD*, dihydroxy-acid dehydratase gene (*C. ljungdahlii*); *alsS*, acetolactate synthase gene (*C. ljungdahlii*); $P_{pta\text{-}ack}$, promoter upstream of *pta-ack* genes (*C. ljungdahlii*); *catP*, chloramphenicol resistance gene; ColE1, origin of replication for Gram-negative bacteria; *repH*, origin of replication for Gram-positive bacteria; *traJ*, gene for DNA transfer by conjugation.

Figure 7.10: tBLASTx comparison of gene clusters Clo1313_0020-0023 [*kor1*], Clo1313_0382-0385 [*kor2*], and Clo1313_1353-1356 [*kor3*] from *C. thermocellum*.

Figure 7.11: Heterotrophic isobutanol production with recombinant *C. ljungdahlii* strains by the Kor pathway. Growth behavior (**A,D**); fructose consumption (**B,E**); ketoisovalerate consumption €; product pattern (**C,F**). *C. ljungdahlii* [WT], black, squares; *C. ljungdahlii* [pM83], gray, triangles; *C. ljungdahlii* [pKOR1], green, diamonds; *C. ljungdahlii* [pKOR2], light green, circles; C. ljungdahlii [pKOR3], dark green, triangle pointing downward. Panels (**A–C**) without ketoisovalerate supplementation; Panels (**D–F**) with ketoisovalerate supplementation. Each strain was analyzed in biological triplicates (*n = 3*).

Figure 7.12: Autotrophic isobutanol production with recombinant *C. ljungdahlii* strains by the Kor pathway. Growth behavior (**A,B**); ketoisovalerate consumption (**B**); product pattern (**C,D**). *C. ljungdahlii* [WT], black, squares; *C. ljungdahlii* [pM83], gray, triangles; *C. ljungdahlii* [pKOR1], green, diamonds; *C. ljungdahlii* [pKOR2], light green, circles; *C. ljungdahlii* [pKOR3], dark green, triangle pointing downward. Panels (**A,C**) without ketoisovalerate supplementation;

Panels (**B,D**) with ketoisovalerate supplementation. Each strain was analyzed in biological triplicates (*n = 3*).

Figure 7.13: Heterotrophic isobutanol production with recombinant *A. woodii* strains by the KivD pathway. Growth behavior (**A,D**); fructose consumption (**B,E**); ketoisovalerate consumption €; product pattern (**C,F**). *A. woodii* [WT], black, squares; *A. woodii* [pM83], gray, triangles; *A. woodii* [pKAIA], blue, diamonds. Panels (**A–C**) without ketoisovalerate supplementation; Panels (**D–F**), with ketoisovalerate supplementation. Each strain was analyzed in biological triplicates (*n = 3*).

Figure 7.14: Heterotrophic isobutanol production with recombinant *C. ljungdahlii* strains by the KivD pathway. Growth behavior (**A,D**); fructose consumption (**B,E**); ketoisovalerate consumption €; product range (**C,F**). *C. ljungdahlii* [WT], black, squares; *C. ljungdahlii* [pKAIA], blue, diamonds; *C. ljungdahlii:ilvE* [pKAIA], purple, circles. Panels (**A–C**) without ketoisovalerate supplementation; Panels (**D–F**) with ketoisovalerate supplementation. Each strain was analyzed in biological triplicates (*n = 3*).

REFERENCES

See 6 references.

Conflict of Interest: The authors declare that the research was conducted in the absence of any commercial or financial relationships that could be construed as a potential conflict of interest.

3.4 Manuscript III: Identifying and engineering bottlenecks of autotrophic isobutanol formation in recombinant *C. ljungdahlii* by systemic analysis

Maria Hermann, [1] Attila Teleki, [1] Sandra Weitz, [2] Alexander Niess, [1] Andreas Freund, [1] Fank R. Bengelsdorf [2], Peter Dürre[2] and Ralf Takors [1,*]

[1]Institute of Biochemical Engineering, University of Stuttgart, Allmandring 31, 70569 Stuttgart, Germany

[2] Institute of Microbiology and Biotechnology, Ulm University, Albert-Einstein-Allee 11, 89069 Ulm, Germany

*Corresponding author. Prof. Dr.-Ing. Ralf Takors

takors@ibvt.uni-stuttgart.de

KEYWORDS

Clostridium ljungdahlii, intracellular metabolite pools, recombinant product formation, isobutanol, synthesis gas fermentation

ABSTRACT

Clostridium ljungdahlii (*C. ljungdahlii*, CLJU) is natively endowed producing acetic acid, 2,3 butanediol, and ethanol consuming gas mixtures of CO_2, CO, and H_2 (syngas). Here, we present the syngas-based isobutanol formation using *C. ljungdahlii* harbouring the recombinant amplification of the 'Ehrlich' pathway that converts intracellular KIV to isobutanol. Autotrophic isobutanol production was studied analyzing two different strains in 3-L gassed and stirred bioreactors. Physiological characterization was thoroughly applied together with metabolic profiling and flux balance analysis. Thereof, KIV and pyruvate supply were identified as key 'bottlenecking' precursors limiting preliminary isobutanol formation in CLJU[KAIA] to 0.02 g L^{-1}. Additional blocking of valine synthesis in CLJU[KAIA]::*ilvE* increased isobutanol production by factor 6.5 finally reaching 0.13 g L^{-1}. Future metabolic engineering should focus on debottlenecking NADPH availability, whereas NADH supply is already equilibrated in the current generation of strains.

INTRODUCTION

Isobutanol is an important commodity in the chemical, food, and pharmaceutical industries with rising global market size (Grand View Research, 2016; Karabektas and Hosoz, 2009; Ragsdale and Pierce, 2008). Furthermore, it is a promising fuel substitute showing lower vapor pressure, volatility, and hygroscopicity and higher energy density than bioethanol (Atsumi et al., 2010). Currently, the production of isobutanol is mainly based on petroleum resources. In addition, there are already several biotechnological approaches mainly based on sugars (Chen and Liao, 2016). Synthesis gas (syngas) represents a further promising substrate for biotechnological production of isobutanol as it can replace fossil-based resources and simultaneously prevent a competition with

the availability of food. Syngas is a mixture mainly composed of carbon monoxide (CO), carbon dioxide (CO_2), and hydrogen (H_2) derived from agricultural, industrial, and municipal wastes and thus representing an inexpensive feedstock (Bengelsdorf and Dürre, 2017; Takors et al., 2018). Several anaerobic bacteria are able to metabolize syngas components via hydrogenesis, methanogenesis, or acetogenesis to a wide range of products (Diender et al., 2015; Latif et al., 2014; Takors et al., 2018). Thereof, *C. ljungdahlii* is a promising biocatalyst as it can convert autotrophically syngas, solely CO, and mixtures of CO_2 and H_2 to its natural products acetate, ethanol, 2,3-butanediol, and lactate (Köpke et al., 2011b; Köpke et al., 2010; Tanner et al., 1993). Its ability to fix CO and CO_2 relies on the Wood-Ljungdahl-Pathway (WLP) that is described in detail in several excellent review articles (Drake et al., 2008; Ragsdale and Pierce, 2008; Schuchmann and Müller, 2014). **Figure 3.13** shows a scheme of the basic metabolic pathways of syngas-fermenting *C. ljungdahlii*. In short, the WLP is a two-branched reductive pathway characterized by a stepwise reduction of CO_2 to a methyl group (methyl branch) which subsequently is combined with CO (carbonyl branch) to acetyl-CoA, the key-precursor for biomass and products. The WLP is energy-limited as only one ATP may be generated by the conversion of acetyl-CoA to acetate. This, in turn, is needed to reduce CO_2 in the methyl branch, leaving no net ATP formation via substrate-level phosphorylation. Hence, a proton gradient coupled to an H^+-translocating ATPase is decisive for the energy provision in *C. ljungdahlii*. In this context, the membrane-bound ferredoxin:NAD oxidoreductase (Rnf complex) plays a crucial role as it couples the electron transfer from reduced ferredoxin (Fd_{red}) to NAD^+ to a simultaneous translocation of protons through the cell membrane (Buckel and Thauer, 2013; Müller et al., 2008; Tremblay et al., 2012; Wang et al., 2013). The required reducing equivalents are provided by the oxidation of CO via carbon monoxide dehydrogenase (CODH) or H_2 using a bifurcating hydrogenase (Hyd) reaction (Buckel and Thauer, 2013; Köpke et al., 2010; Schuchmann and Müller, 2012; Wang et al., 2013). An electron bifurcating transhydrogenase (Nfn) reaction is also involved in the energy conservation of *C. ljungdahlii.* It catalyses the endergonic reduction of $NADP^+$ with NADH coupled to the exergonic reduction of $NADP^+$ with Fd_{red} (Aklujkar et al., 2017; Liang et al., 2019; Mock et al., 2015).

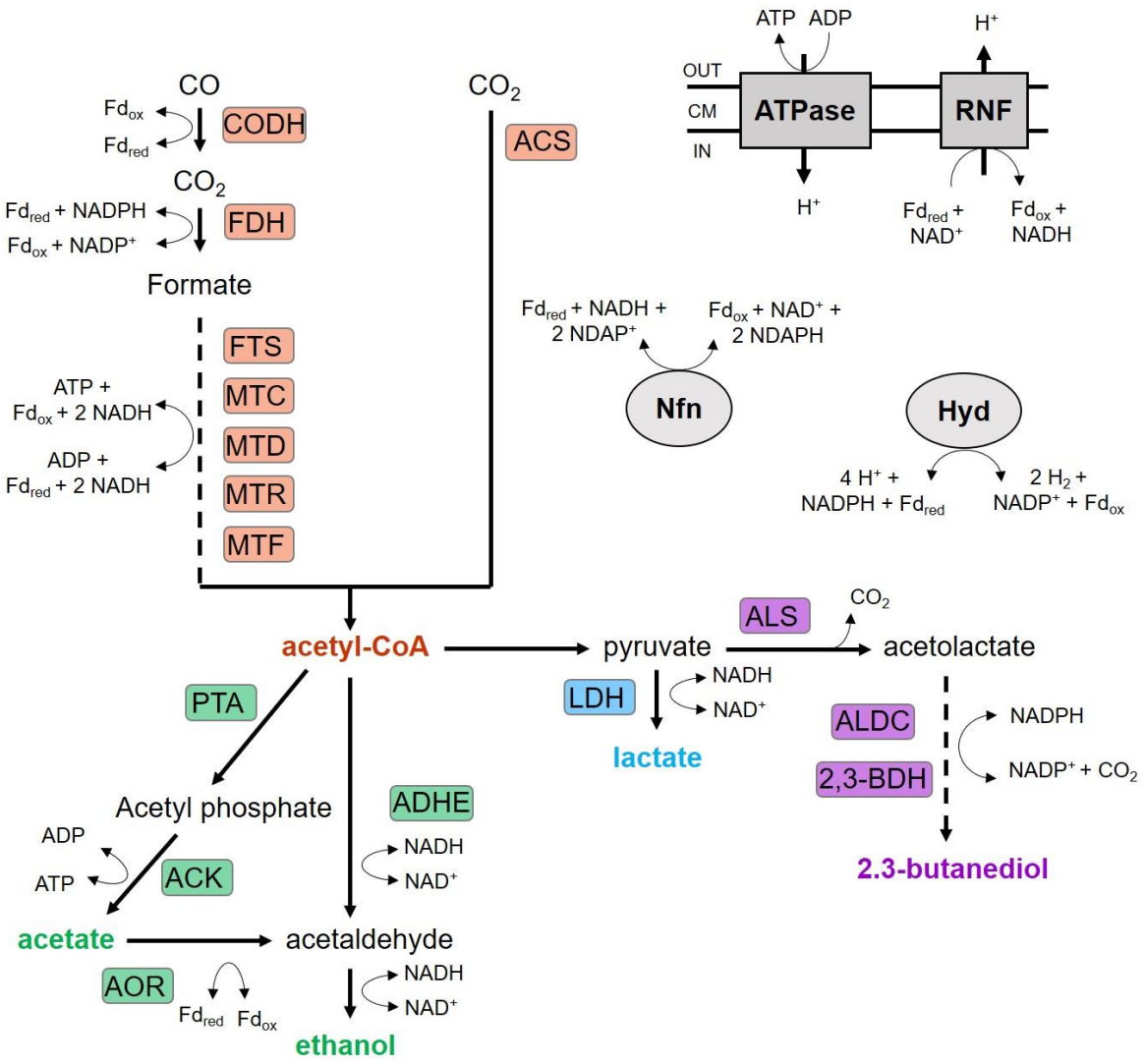

Figure 3.13: Wood-Ljungdahl pathway and product formation of *C. ljungdahlii*. ACK, acetate kinase; ACS, acetyl-CoA synthase; ADHE, aldehyde/alcohol dehydrogenase; ALDC. Acetolactate decarboxylase; ALS, acetolactate synthase; AOR; aldehyde:ferredoxin oxidoreductase; CODH, CO dehydrogenase; FDH, formate dehydrogenase; FTS, Formyl-THF synthetase; Hyd, electron-bifurcation hydrogenase, LDH, lactate dehydrogenase; MTC, methenyl-THF cyclohydrolase; MTD, methylene-THF dehydrogenase; MTF, methyltransferase; MTR, methylene-THF reductase; Nfn, electron-bifurcating and ferredoxin-dependent transhydrogenase; PFOR, pyruvate:ferredoxin oxidoreductase; PTA, phosphotransacetylase; PTF, phosphotransferase; RNF, Rnf complex; THF, tetrahydrofolate 2,3-BDH: 2,3-butanediol dehydrogenase.

Consequently, Fd_{red} availability tightly links energy management, substrate composition, and product formation in *C. ljungdahlii*. In this context, we identified syngas as a suitable substrate to produce reduced alcohols, presenting the highest 2,3-butanediol formation using a batch process with *C. ljungdahlii* described so far (Hermann et al., 2020). Furthermore, *C. ljungdahlii* is genetically accessible enabling

the optimized formation of natural and recombinant products via metabolic engineering (Huang et al., 2019; Molitor et al., 2017; Woolston et al., 2018). Weitz et al. (2021) engineered several *C. ljungdahlii* strains and successfully demonstrated isobutanol formation analyzing heterotrophic and autotrophic growth conditions by lab scale batch fermentation experiments. This study builds on the findings of Weitz et al. (2021) by investigating autotrophic syngas-based isobutanol formation applying the two recombinant strains CLJU[KAIA] and CLJU[KAIA]::*ilvE*. Based on 3 L batch cultivations in gassed stirred bioreactors, strains were physiologically characterized, thoroughly investigated via intracellular metabolomics, and quantified via flux balance analysis. Thereof, promising metabolic engineering targets were derived finally yielding CLJU[KAIA]::*ilvE* which achieved 130 mg of isobutanol/L.

MATERIALS AND METHODS

A complete description of all methods below can be found in chapter's **3.2** experimental procedures and online at: https://www.frontiersin.org/articles/10.3389/fbioe.2021.647853/full#supplementary-material

Bacterial strains, growth medium and pre-culture preparation

C. ljungdahlii DSM 13528 (Tanner et al., 1993) was obtained from the German Collection of Microorganisms and Cell Cultures (DSMZ). The recombinant *C. ljungdahlii* strains CLJU[KAIA] and CLJU[KAIA]::*ilvE* were kindly provided by the group of Peter Dürre (Institute of Microbiology and Biotechnology, University of Ulm). Details of strain construction are described elsewhere (Weitz et al., 2021). Medium and preculture seed train was described earlier (Hermann et al., 2020). The last pre-culture step was based on syngas, characterized by the same gas composition as the bioreactor substrate.

Batch cultivation studies in a stirred-tank reactor

Anaerobic syngas-based batch cultivations were performed in a fully controlled 3-L stirred-tank bioreactor (Bioengineering, Wald, Switzerland) with an operational volume of 1.5 L. The detailed reactor equipment was previously described in Hermann et al. (2020). Temperature and pH were kept constant at 37 °C and 5.9 respectively. The agitation speed of the impeller was 500 rpm during the whole cultivation process. The substrate gas was fed continuously into the reactor using one mass flow controller (Bronkhorst High-Tech B.V., Ruurlo, Netherlands) and a predefined gas mixture with a constant gassing rate of 13.2 L h^{-1}. The gas composition was 55% CO, 30% H_2, 5% CO_2, and 10% Ar. To set anaerobic conditions, the medium-containing bioreactor was sparged with nitrogen with a gassing rate of 60 L h^{-1} applied for 2 h. Off-gas measurements guaranteed that oxygen concentrations were always below 0.01% (vv^{-1}). Afterwards, the medium was equilibrated with the substrate gas for 5 h. Two hours prior to inoculation of the bioreactor, sterile reducing agent was added (Tanner et al., 1993). To observe growth, extracellular product formation, and intracellular metabolite pools, samples were taken frequently during the cultivations.
All fermentations showed very similar growth and substrate uptake kinetics. Only product formation differed with respect to isobutanol production.

Analytical methods

Biomass concentration analysis. Cell density was determined offline via a UV/Visible spectrophotometer at 600 nm. A detailed description is found in Hermann et al. (2020).

Analysis of extracellular products. The extracellular formation of ethanol, acetate, 2,3-butanediol, lactate, and isobutanol was observed using an isocratic high-performance liquid chromatography (HPLC) equipped with a RI detector and a Rezex ROA-Organic Acid H^+ column. Measuring parameters and sample preparation are described in Hermann et al. (2020).

LC-MS based analysis of intracellular metabolites' concentrations. Intracellular metabolites' concentrations in [µmol g_{CDW}^{-1}] were quantified using an HPLC system

coupled to a triple quadrupole tandem mass spectrometer (QQQ-MS/MS) equipped with an electrospray ion source. Therefore, 5 mL cell suspension each were taken periodically as triplicates in the course of the exponential growth phases of the batch cultures. Extraction and quantification of non-derivatized polar metabolites was described earlier (Hermann et al., 2020; Teleki et al., 2015). Due to their high reactivity, the analysis of α-keto acids (aKG, pyruvate, and OAA) required a preceding derivatization treatment based on the condensation of aldehyde and keto groups by phenylhydrazine (Zimmermann et al., 2014). In addition, a quantification method based on bicratic reverse phase chromatography (RPLC) with acidic mobile phase conditions was applied. For this purpose, an adapted derivatization strategy as well as the respective LC-MS/MS protocol was developed and described by Junghans et al. (2019). Therefore, for determination of the intracellular pools of pyruvate, KIV, aKG, and OAA 2.5 µL of a freshly prepared 50 mM phenylhydrazine stock solution were added to 24 µL of the metabolite extracts. Additionally, the samples were spiked with 4 µL of a defined standard mix or water and mixed with 1 µL of a 2.2 mM glyoxylate (Gxy) solution. After an incubation at room temperature for 1 h the samples were quenched with 0.5 µL of a 10%(vv^{-1}) formic acid stock solution and 18 µL of acetonitrile. Gxy was considered to monitor instrumental fluctuations and the standard mix was needed for the absolute quantification of the respective α-keto acids. Based on previous measurements, the composition of the standard mix was set to 12 µM pyruvate, 1.6 µM OAA, 2 µM KIV, and 6 µM aKG. By means of different water to standard mix ratios during sample preparation internal calibration curves with four levels for each metabolite were achieved. Thus, internal calibration curves resulted from a standard quadruple addition of defined amounts of the respective metabolite standards directly to the sample.

Online analysis of the exhaust gas: Exhaust gas measurement was performed online by mass spectrometry to determine gas uptake and production as described in Hermann et al. (2020).

Determination of cell specific rates: For each growth phase biomass-specific substrate uptake and product formation rates were calculated by considering the

exponential growth rate μ, the biomass substrate yield $Y_{X/S}$, or the biomass product yield $Y_{X/P}$ respectively. A detailed description is found in Hermann et al. (2020).

Determination of the Gibbs free energy changes ΔG_R: Gibbs free reaction energy changes ΔG_R were calculated to compare the individual processes at the energetic level as described by Villadsen et al. (2011). Corresponding calculations for the individual processes are attached in the appendix.

Flux Balance Analysis (FBA)

Model simulations were performed based on the Insilico Discovery™ platform using the previously reconstructed and described model rSMM (Hermann et al., 2020), which was supplemented by a formate-H_2 lyase like reaction (Wang et al., 2013) and recombinant isobutanol formation. This model is characterized by a constant growth-associated maintenance (GAM) value of 46.7 mmol ATP g_{CDW}^{-1} (Nagarajan et al., 2013) and the invariable non-growth-associated maintenance value (NGAM) of 5 mmol $(g_{CDW}*h)^{-1}$. For NGAM estimation the mean maintenance cost identified for the closely related acetogen *C. autoethanogenum* growing on different gaseous substrates was considered (Heffernan et al., 2020; Valgepea et al., 2018). Further assumption and characteristics of the model are described in Hermann et al. (2020). As the degree of freedom exceeds the maximal number of quantifiable fluxes, flux balance analysis was used to investigate the intracellular flux distribution (Orth et al., 2010; Schilling et al., 2000). Maximization of biomass production was set as objective function, while all experimentally determined product formation and substrate uptake rates were used to constrain the solution space (O'Brien et al., 2015). Further details of the applied FBA method are found in Hermann et al. (2020).

RESULTS

Syngas-based batch cultivation of CLJU[WT]

Growth, product formation and substrate uptake: Before investigating a recombinant isobutanol formation based on syngas, a reference process (REF) was used to analyze growth, product formation, and substrate uptake of the *C. ljungdahlii*

wildtype strain (CLJU[WT]) (**Figure 3.14**). Therefore, a syngas-based batch cultivation in a steadily gassed 3-L bioreactor was performed in duplicates. The detailed composition of the substrate gas is described in the Experimental procedures section. The growth phases, final product concentrations, and substrate-to-product yields of the process are summarized in **Table 3.8** and **Table 3.9**.

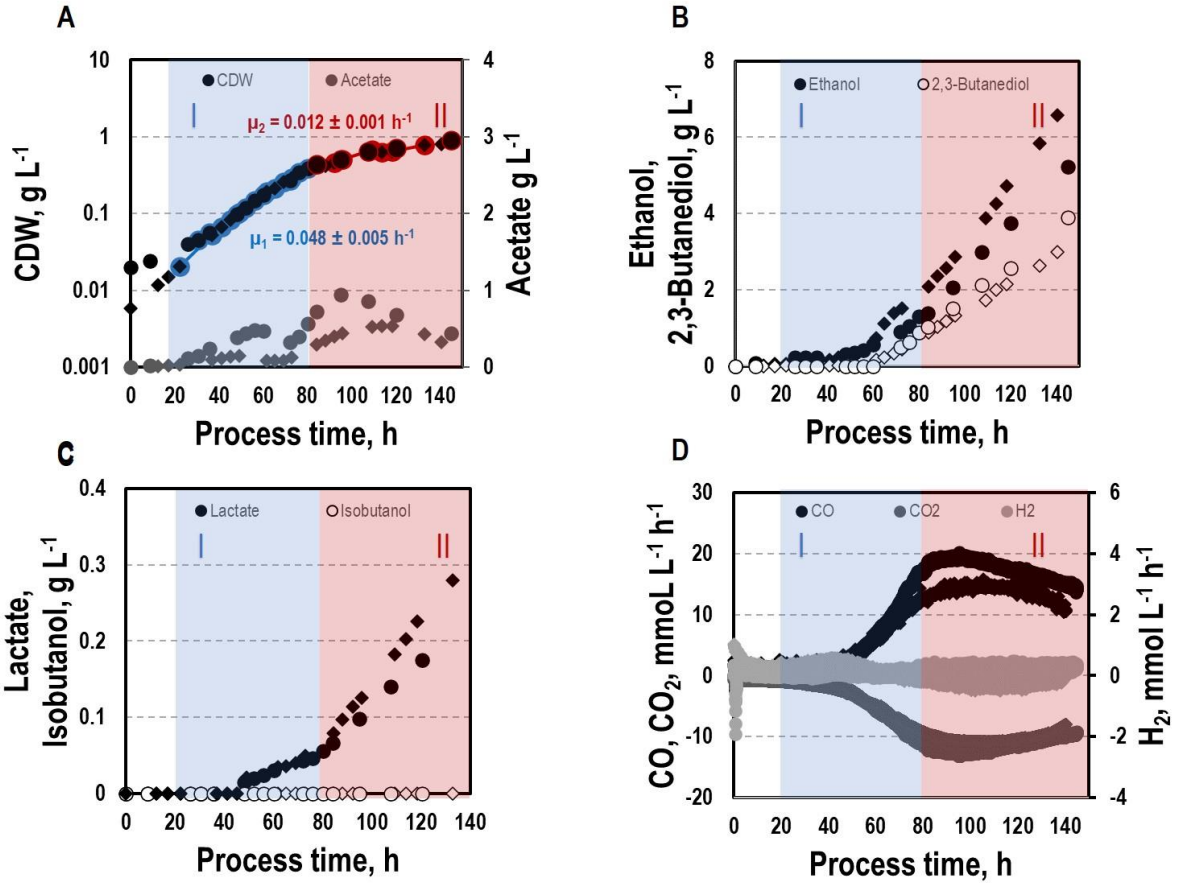

Figure 3.14: Syngas batch cultivation of CLJU[WT] in a stirred bioreactor with continuous gas supply. Depicted are concentrations of cell dry weight and acetate (**A**), ethanol and 2,3-butanediol (**B**), lactate and isobutanol (**C**), and gas uptake (**D**) of two independent experiments (circles and diamonds). Two growth phases I (blue) and II (red) were identified. Statistical details are given in the Supplementary Material (**Table 7.10**).

We identified two growth phases with μ_{exp} = 0.05 ± 0.005 h^{-1} [average ± standard deviation] in the first (approximately 20 – 80 h) and μ_{exp} = 0.01 ± 0.001 h^{-1} in the following period (approximately 90 – 120 h). After approximately 140 h, the final CDW = 0.85 ± 0.06 g L^{-1} was reached representing 2.3 ± 0.6% of totally captured carbon. Furthermore, the two growth periods were characterized by different substrate

uptake patterns. During the first phase, CO uptake accompanied by proportional CO_2 formation occurred. Maximum volumetric and biomass specific rates were r_{CO} = 16.3 ± 4.1 mmol $(L*h)^{-1}$ *i.e.* q_{CO} = 38.8 ± 4.1 mmol $(g_{CDW}*h)^{-1}$ and r_{CO2} = 11.3 ± 1.4 mmol $(L*h)^{-1}$ *i.e.* q_{CO2} = 27.4 ± 3.4 mmol $(g_{CDW}*h)^{-1}$, respectively. Subsequently, both rates decreased to r_{CO} = 12.8 ± 2.7 mmol $(L*h)^{-1}$ *i.e.,* q_{CO} = 16.1 ± 3.4 mmol $(g_{CDW}*h)^{-1}$ and r_{CO2} = 8.7 mmol ± 1.0 $(L*h)^{-1}$ *i.e.,* q_{CO2} = 11.00 mmol ± 1.3 $(g_{CDW}*h)^{-1}$. Only very low H_2 uptake even revealing large deviations between the two biological replicates was observed. On average, r_{H2} = 0.2 ± 0.03 mmol $(L*h)^{-1}$ and r_{H2} = - 0.01 ± 0.4 mmol $(L*h)^{-1}$ were measured for the first and second period, respectively. Acetate patterns showed similar trends in biological duplicates with acetate formation during early first phase, reaching a maximum until the beginning of the second period when consumption started. The residual of 0.38 ± 0.08 g L^{-1} represented only 0.9 ± 0.02% of totally captured carbon. On the contrary, the formation of the reduced products ethanol, 2.3-butanediol, and lactate started after the initiation of acetate formation showing a steady rise with final concentrations of 5.9 ± 0.9 g L^{-1} for ethanol, 3.5 ± 0.6 g L^{-1} for 2.3-butanediol, and 0.01 ± 0.03 g L^{-1} for lactate. Accordingly, *C ljungdahlii* converted approximately 30% of consumed carbon into reduced products. The total free Gibbs reaction energy ΔG_R of the process was - 33.55 ± 1.92 kJ C-$mole^{-1}$ (**Table 3.10**).

Table 3.8: Maximal growth rates and final by-product concentrations of the syngas-based batch cultivations of the different *C. ljungdahlii* strains in a steadily gassed stirred bioreactor. Rates reflect exponential growth. Values of the wildtype cultivation indicate mean of duplicates.

Strain	**μ_{max}, h^{-1}**	**c_{CDW}, g L^{-1}**	**$c_{Acetate}$, g L^{-1}**	**$c_{Ethanol}$, g L^{-1}**	**$c_{2,3\text{-}BD}$, g L^{-1}**	**$c_{Lactate}$, g L^{-1}**	**$c_{Isobutanol}$, g L^{-1}**
CLJU[WT]	0.048 ± 0.005	0.85 ± 0.06	0.38 ± 0.08	5.90 ± 0.95	3.45 ± 0.64	0.26 ± 0.05	-
CLJU[KAIA]	0.071	0.73	0.22	5.25	2.38	0.25	0.02
CLJU[KAIA]::*ilvE*	0.055	0.89	0.83	5.90	3.42	0.09	0.13

Table 3.9: Final biomass and product yields of the syngas-based batch cultivations of the different *C. ljungdahlii* strains in steadily gassed stirred-tank bioreactor (T = 37°C; pH = 5.9; V_R = 3 L; 500 rpm. Values of the wildtype cultivation indicate mean of duplicates.

Strain	Y_{CDW}	$Y_{Acetate}$	$Y_{Ethanol}$	$Y_{2,3\text{-}BD}$	$Y_{Lactate}$	$Y_{Isobutanol}$	Y_{CO2}
	C-mole $_{(Product)}$ mole^{-1} $_{(CO)}$						
CLJU[WT]	0.023 ± 0.006	0.009± $2.3*10^{-5}$	0.19 ± 0.07	0.12 ± 0.002	0.007 ± 0.003	-	0.71 ± 0.005
CLJU[KAIA]	0.026	0.006	0.20	0.09	0.009	0.001	0.70
CLJU [KAIA]::*ilvE*	0.027	0.024	0.17	0.09	0.002	0.003	0.65

Table 3.10: Carbon balances and Gibb's free reaction energies of the syngas-based batch cultivations of the different *C. ljungdahlii* strains in steadily gassed stirred-tank bioreactor (T = 37°C; pH = 5.9; V_R = 3 L; 500 rpm. Values of the wildtype cultivation indicate mean of duplicates.

Strain	C - Balance, %	ΔG_R, kJ C-mole^{-1}
CLJU[WT]	106.1 ± 7.6	-33.6 ± 1.9
CLJU[KAIA]	102.3	-36.2
CLJU[KAIA]::*ilvE*	96.6	-37.9

Intracellular metabolites pattern: To further characterize the physiological state of the cells 32 intracellular metabolite pools were analyzed (**Figure 3.15**) at representative sampling times. Pool sizes differed individually ranging from about 0.001 µmol g_{CDW}^{-1} for KIV, oxaloacetate (OAA), and 2-ketoglutarate (αKG) to 8 µmol g_{CDW}^{-1} for alanine. Whereas most pool sizes remained constant throughout the process, pyruvate and serine depleted during the second growth phase. In contrast, remarkably large pool sizes were found for valine, glutamate, aspartate, alanine, and lysine.

Intracellular patterns of ATP, ADP, AMP, and the respective adenylate energy charge (AEC) were studied to evaluate whether or not non-wanted energy shortage might exist growing on syngas (**Figure 3.16**). ATP pools dropped until they levelled out at

0.08 $\mu molg_{CDW}^{-1}$ during the second period. A similar trend was found for AEC starting at 0.46 and ending at 0.28. On contrary, AMP and ADP rather remained at about 0.25 $\mu molg_{CDW}^{-1}$.

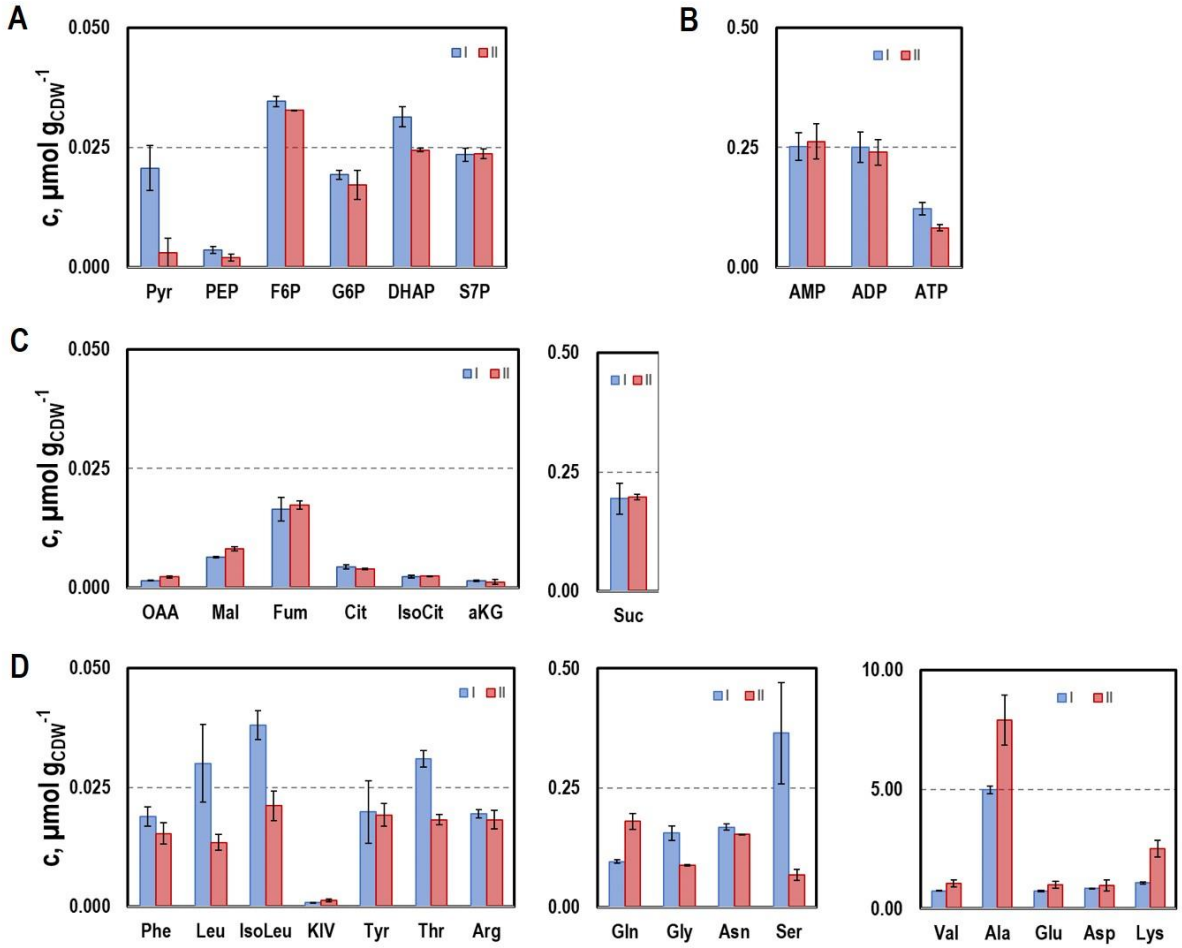

Figure 3.15: Selected intracellular pools representing Emden-Meyerhof-Parnas and the pentose-phosphate pathway (**A**), energy metabolism (**B**), citrate cycle (**C**), and amino acids (**D**). Samples were taken during growth phases I and II cultivating CLJU[WT] on syngas in a stirred tank. Error bars are derived from technical replicates.

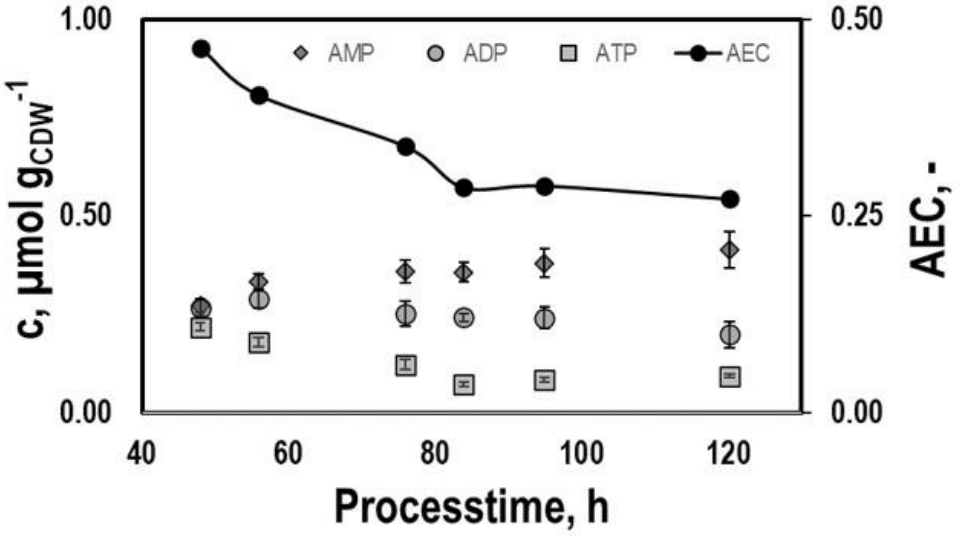

Figure 3.16: Intracellular pools of AMP, ADP, and ATP and the respective AEC values. Samples were taken during growth phases I and II cultivating CLJU[WT] on syngas in a stirred tank. Error bars are derived from technical replicates.

Batch cultivations of the recombinant strains CLJU[KAIA] and CLJU[KAIA]::*ilvE* using syngas

CLJU[KAIA]: Recombinant isobutanol production from syngas was studied using the strain CLJU[KAIA] which possesses plasmid-encoded amplification of pyruvate-to-KIV conversion followed by the conversion of KIV via recombinant Ehrlich pathway (**Figure 3.17**). Process parameters of the batch equaled those of the reference process leading to kinetics and process values indicated in **Figure 3.18** and in **Table 3.8** and **Table 3.9**.

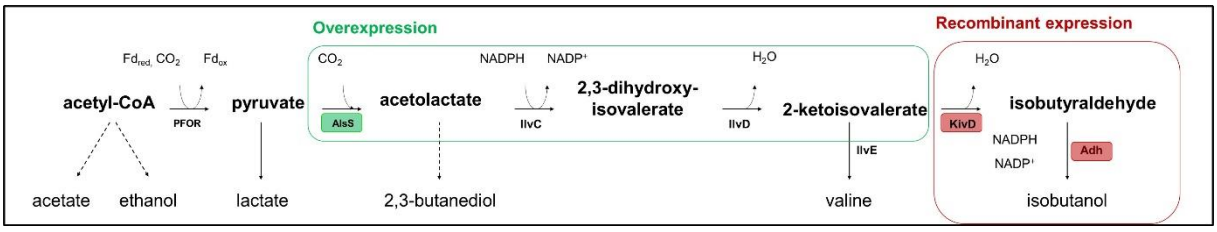

Figure 3.17: Recombinant isobutanol pathway in CLJU[KAIA] characterized by plasmid-encoded amplification of pyruvate-to-KIV conversion followed by the conversion of KIV via recombinant Ehrlich pathway. PFOR: pyruvate:ferredoxin-oxidoreductase; AlsS: acetolactate synthase; IlvC: ketol-acid reductoisomerase, IlvD: dihydroxy-acid dehydratase; Ilve: amino acid aminotransferase; KivD: ketoisovalerate decarboxylase; Adh: alcohol dehydrogenase

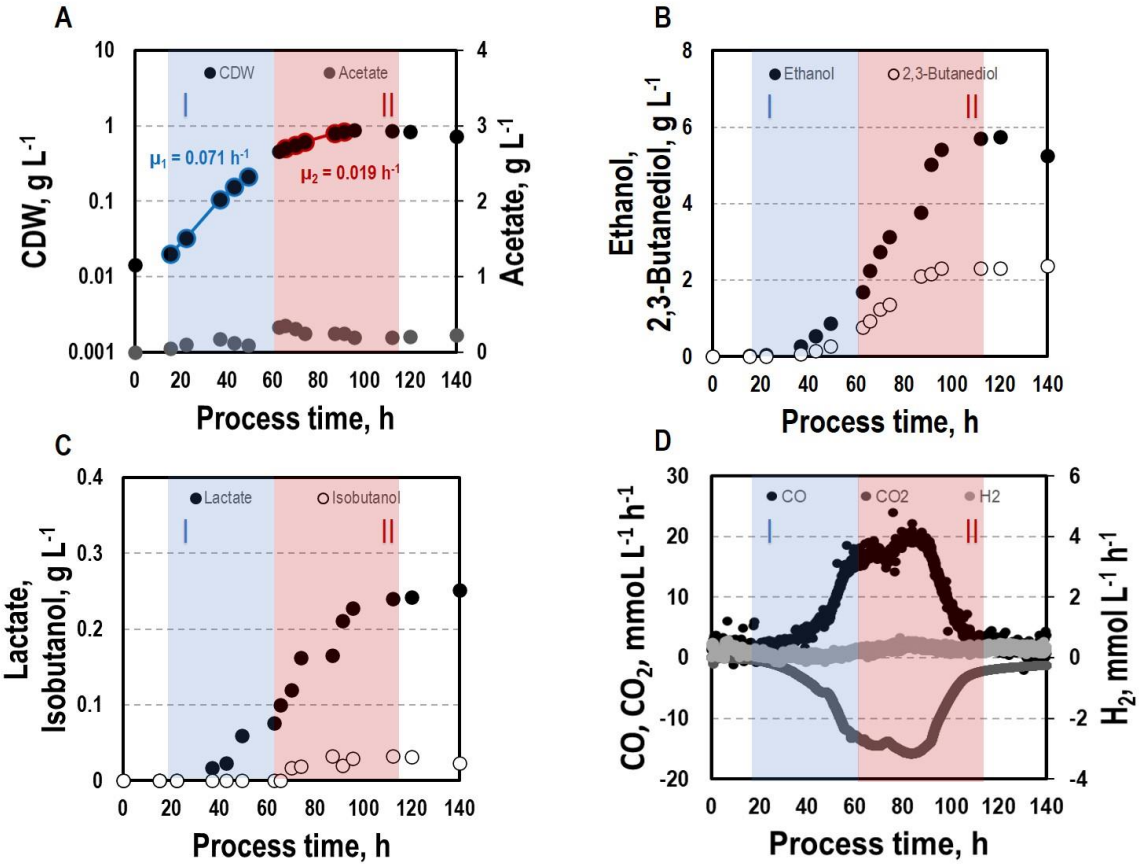

Figure 3.18: Syngas-based batch cultivation of CLJU[KAIA] in a stirred tank bioreactor with a continuous gas supply. Shown are the concentrations of cell dry weight and acetate (**A**), ethanol and 2,3-butanediol (**B**), lactate and isobutanol (**C**), and the gas uptake (**D**) (T = 37°C; pH = 5.9; V_R = 3 L; 500 rpm). Two growth phases I (marked blue) and II (marked red) were identified. Statistical details are given in the Supplementary Material (**Table 7.10**).

Again, biphasic growth occurred revealing μ_{exp} = 0.07 h^{-1} between 20 – 60 h and μ_{exp} = 0.02 h^{-1} between 60 – 120 h. The final CDW was 0.73 g L^{-1} which equals 2.6% of the entire carbon capture in biomass. Compared to REF, CLJU[KAIA] grew 50% faster during phase I disclosing similar CO-to-CDW yield. Also, substrate uptake kinetics resembled REF showing CO_2 formation accompanying CO uptake during phase I. Maximum volumetric and specific rates were r_{CO} = 17.6 mmol $(L*h)^{-1}$ *i.e.* q_{CO} = 34.6 mmol $(g_{CDW}*h)^{-1}$ and r_{CO2} = 13.8 mmol $(L*h)^{-1}$ *i.e.* q_{CO2} = 27.0 mmol $(g_{CDW}*h)^{-1}$. During growth period II, biomass specific rates for CO uptake q_{CO} = 25.2 mmol $(g_{CDW}*h)^{-1}$ and CO_2 formation q_{CO2} = 18.9 mmol $(g_{CDW}*h)^{-1}$ decreased. Low H_2 uptake was observed in each phase with $r_{H2,I}$ = 0.2 mmol $(L*h)^{-1}$ followed by $r_{H2,II}$ = 0.4 mmol $(L*h)^{-1}$. The product spectrum was similar to the reference

process with the final concentrations of 0.22 g L^{-1} of acetate, 5.25 g L^{-1} of ethanol, 2.38 g L^{-1} of 2.3-butanediol, 0.25 g L^{-1} of lactate, and 0.02 g L^{-1} of isobutanol. The total free Gibbs reaction energy ΔG_R of the process was - 36.15 kJ C-$mole^{-1}$ (**Table 3.10**).

In order to identify possible metabolic engineering targets for optimizing isobutanol production, we compared the patterns of the intracellular metabolites pyruvate, KIV, and valine with those of the reference process (**Figure 3.19**). KIV courses were almost identical, notably revealing the lowest pool sizes of all. Pyruvate levels in CLJU[KAIA] were higher than in REF which might be explained by the elevated growth rate. In addition, substantially higher levels of valine were measured in CLJU[KAIA] compared to REF throughout the entire batch culture.

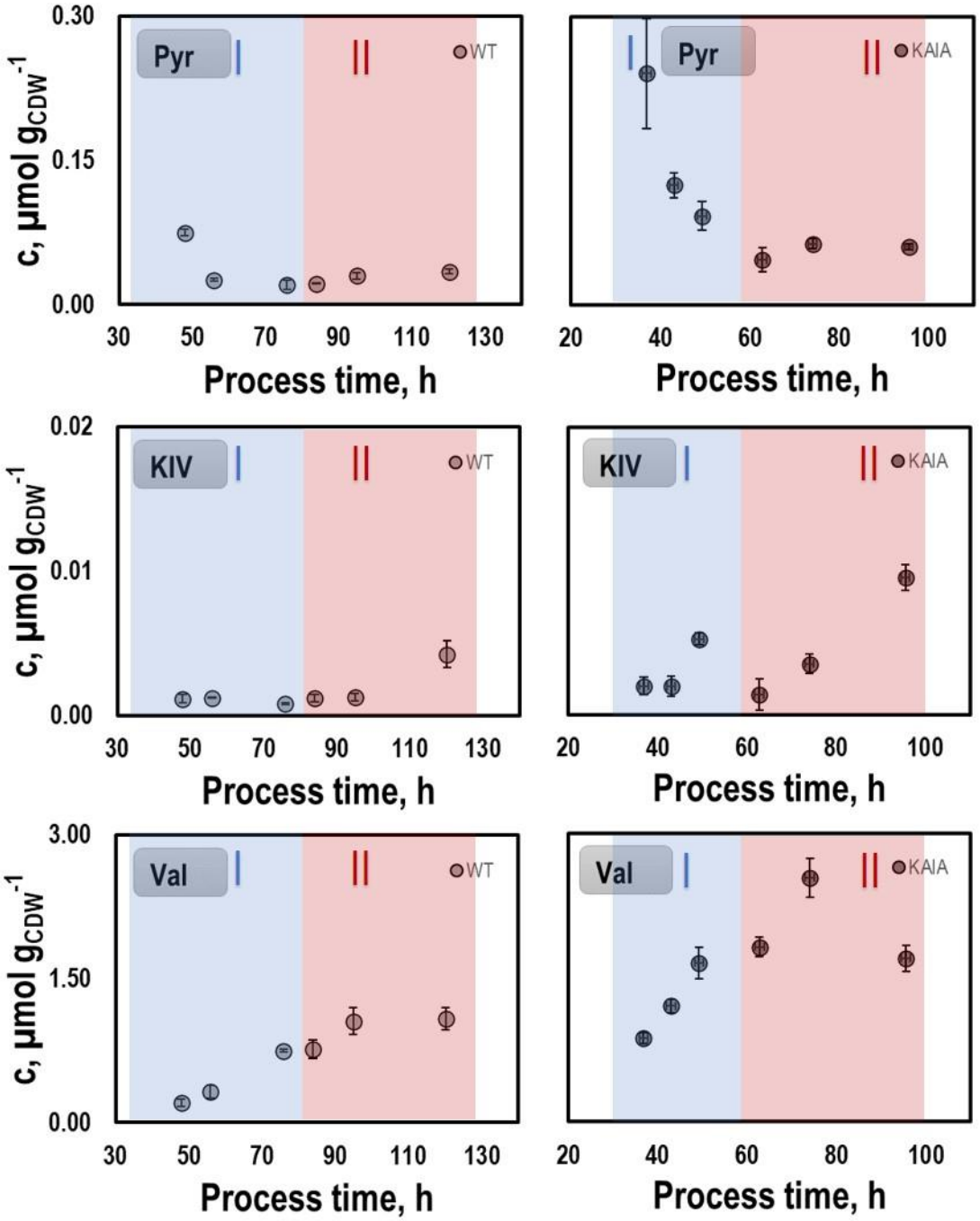

Figure 3.19: Pyruvate (PYR), ketoisovalerate (KIV), and valine (VAL) pools in autotrophic batch cultivations of CLJU[WT, REF] and CLJU[KAIA] using syngas. Error bars are derived from technical replicates.

CLJU[KAIA]::ilvE: By interrupting *ilvE* encoding valine amino transferase a block of valine synthesis was achieved. The resulting strain CLJU[KAIA]::*ilvE* was cultivated under reference conditions revealing kinetics as indicated in **Figure 3.20** and in **Table 3.8** and **Table 3.9**.

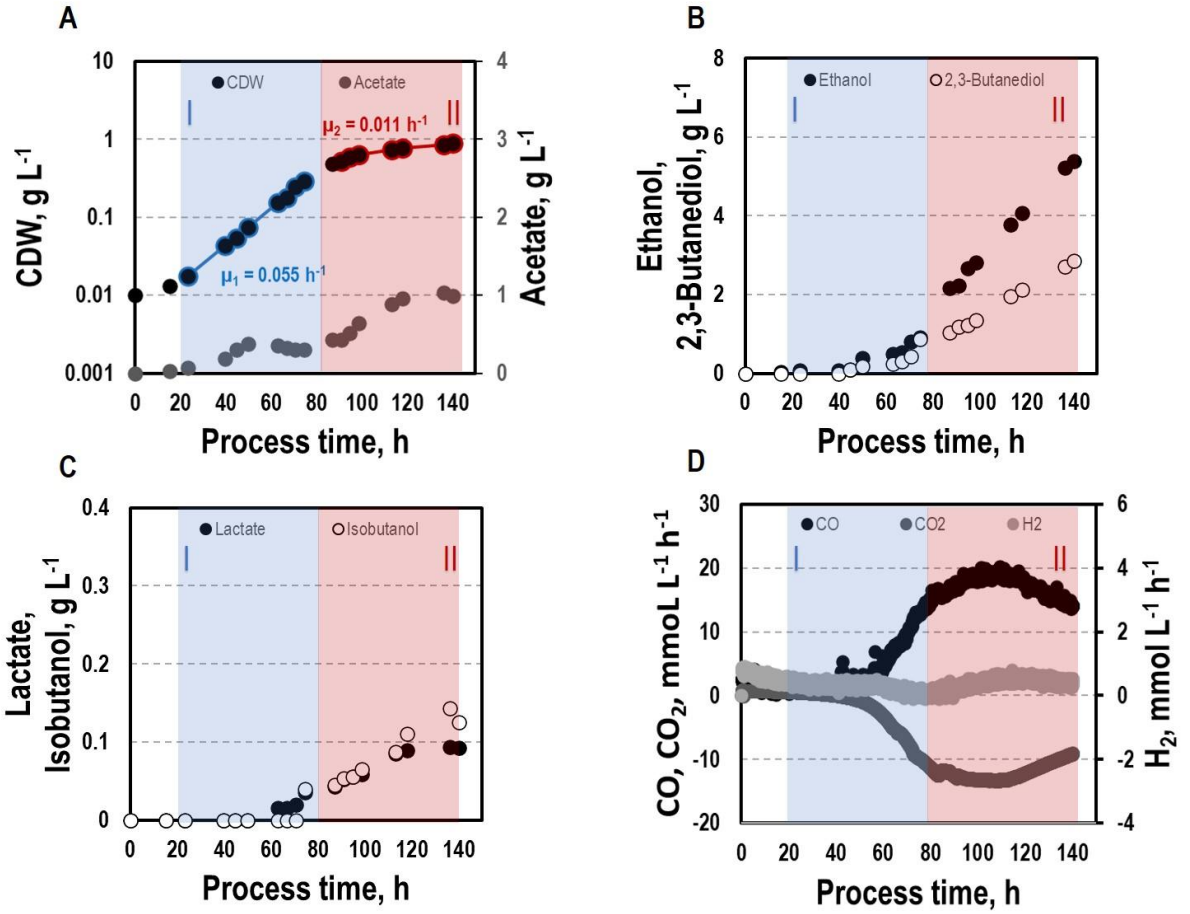

Figure 3.20: Syngas-based batch cultivation of CLJU[KAIA]::ilvE in a stirred tank bioreactor with a continuous gas supply. Shown are the concentrations of the cell dry weight and acetate (A), ethanol and 2,3-butanediol (B), lactate and isobutanol (C), and the gas uptake (D) (T = 37°C; pH = 5.9; VR = 3 L; 500 rpm). Two growth phases I (marked blue) and II (marked red) were identified. Statistical details are given in the Supplementary Material (**Table 7.10**).

Growth, substrate uptake, and product formation (except for isobutanol) resemble the wildtype. Again, we identified biphasic growth with $\mu_{exp,I}$ = 0.055 h^{-1} (20 – 80 h) and $\mu_{exp,II}$ = 0.011 h^{-1} (90 – 140 h) reaching CDW = 0.89 g L^{-1} which represents 2.7% of CO captured in biomass. Despite a suspected valine auxotrophy of CLJU[KAIA]::*ilvE* there was no reduction of growth compared to the wildtype. This indicates that the valine concentration provided by the 0.5 g L yeast extract in the medium is sufficient.

During phase I, maximum volumetric and specific rates were r_{CO} = 16.2 mmol $(L*h)^{-1}$ *i.e.,* q_{CO} = 33.8 mmol $(g_{CDW}*h)^{-1}$ and r_{CO2} = 11.9 mmol $(L*h)^{-1}$ *i.e.,* q_{CO2} = 24.9 mmol $(g_{CDW}*h)^{-1}$. The mean volumetric H_2 uptake rate was 0.2 mmol $(L*h)^{-1}$. In phase II, biomass specific CO uptake and CO_2 formation rates decreased to q_{CO} = 23.5 mmol $(g_{CDW}*h)^{-1}$ and q_{CO2} = 16.1 mmol $(g_{CDW}*h)^{-1}$. Volumetric H_2 uptake rate slightly increased to 0.3 mmol $(L*h)^{-1}$. At the end of the process, 0.83 g L^{-1} acetate, 5.90 g L^{-1} ethanol, 3.42 g L^{-1} 2.3-butanediol, 0.09 g L^{-1} lactate, and 0.13 g L^{-1} isobutanol were determined. The total free Gibbs reaction energy ΔG_R of the process was - 37.89 kJ C-mole^{-1} (Table 3).

Both, isobutanol and 2,3 butanediol formation depend on NADPH which is why internal supply was worth investigating.

Simulation of intracellular flux distribution

For determination of NADH and NADPH availabilities in the strains, flux balance analysis (FBA) were performed. Intracellular flux patterns of the 'pseudo-steady states' in phases I and II were studied using the stoichiometric metabolic model 'modified rSMM' (Hermann et al., 2020), that was extended by recombinant isobutanol formation (see appendix, **7.1** and **7.3**). We applied FBA as the number of the unknown intracellular fluxes exceeded the total number of measured extracellular fluxes. Since growth was exponential in both phases, we chose the maximization of biomass production as objective function in each case. Measured uptake and consumption rates further constrained the solution space. As already shown in Hermann et al. (2020) the approach allowed very well to predict real growth rates further elucidating intracellular flux patterns. Alternate application of determined metabolic flux analysis was not possible as additional measurements e.g. using ^{13}C labeling were not accessible. Since we could not resort to this method, we restricted the solution space by using all experimentally determined uptake and secretion rates as constraints to assure that FBA results reflect real physiological states (O'Brien et al., 2015). As a prerequisite, we qualified the achieved experimental carbon closures of 106.10 ± 7.59%, 100.02%, and 96.55% as 'sufficient' analyzing cultivations of the wild-type (REF), CLJU[KAIA], and CLJU[KAIA]::*ilvE*, respectively (**Table 3.10**). The

overview of all flux patterns is given in **Figure 3.21**. Furthermore, NADH and NADPH formation related to the consumption of electron donors CO and H_2 are listed in **Table 3.11**. Yields were derived from the WLP and from the Nfn reaction. In *C. ljungdahlii*, regeneration of NADH and NADPH are strongly intertwined and controlled by the provision of Fd_{red} (Hermann et al., 2020). Utilizing syngas, NADH supply is ensured via WLP and via the Rnf complex. The transhydrogenase Nfn consumes NADH providing NADPH. In turn, the reduction of CO_2 to formate by the formate dehydrogenase activity represents a NADPH sink. Also, *C. ljungdahlii* directly reduces CO_2 to formate utilizing H_2 through the formate-hydrogen lyase reaction which is carried out by a complex composed of the electron-bifurcating $NADP^+$- and ferredoxin-dependent [FeFe]-hydrogenase and formate dehydrogenase (Wang et al., 2013). Our simulation results show simultaneous activity of both reactions in each cultivation. However, the share of the formate-hydrogen lyase-like reaction strongly decreases due to limited H_2 uptake during phase II. This finding is remarkable as the explicit use of this formate-hydrogen lyase-like reaction for CO_2 reduction was found in continuously cultivated *C. autoethanogenum* (Valgepea et al., 2017b). Apparently, *C. ljungdahlii* adapts CO_2 reduction to current needs via flexible enzyme activities of said reductive route. Interestingly enough, NADPH yields were up to 30% higher in isobutanol producers than in the wildtype. Higher activities of transhydrogenase (Nfn) and of the formate-hydrogen reaction rate enable this phenotype. Nevertheless, strongly decreasing NADPH yields of 65 – 70% were determined in the second growth phase for each cultivation. On the contrary, NADH availabilities almost remained constant during phases I and II, only showing a slight 20% decrease for CLJU[KAIA]::*ilvE*.

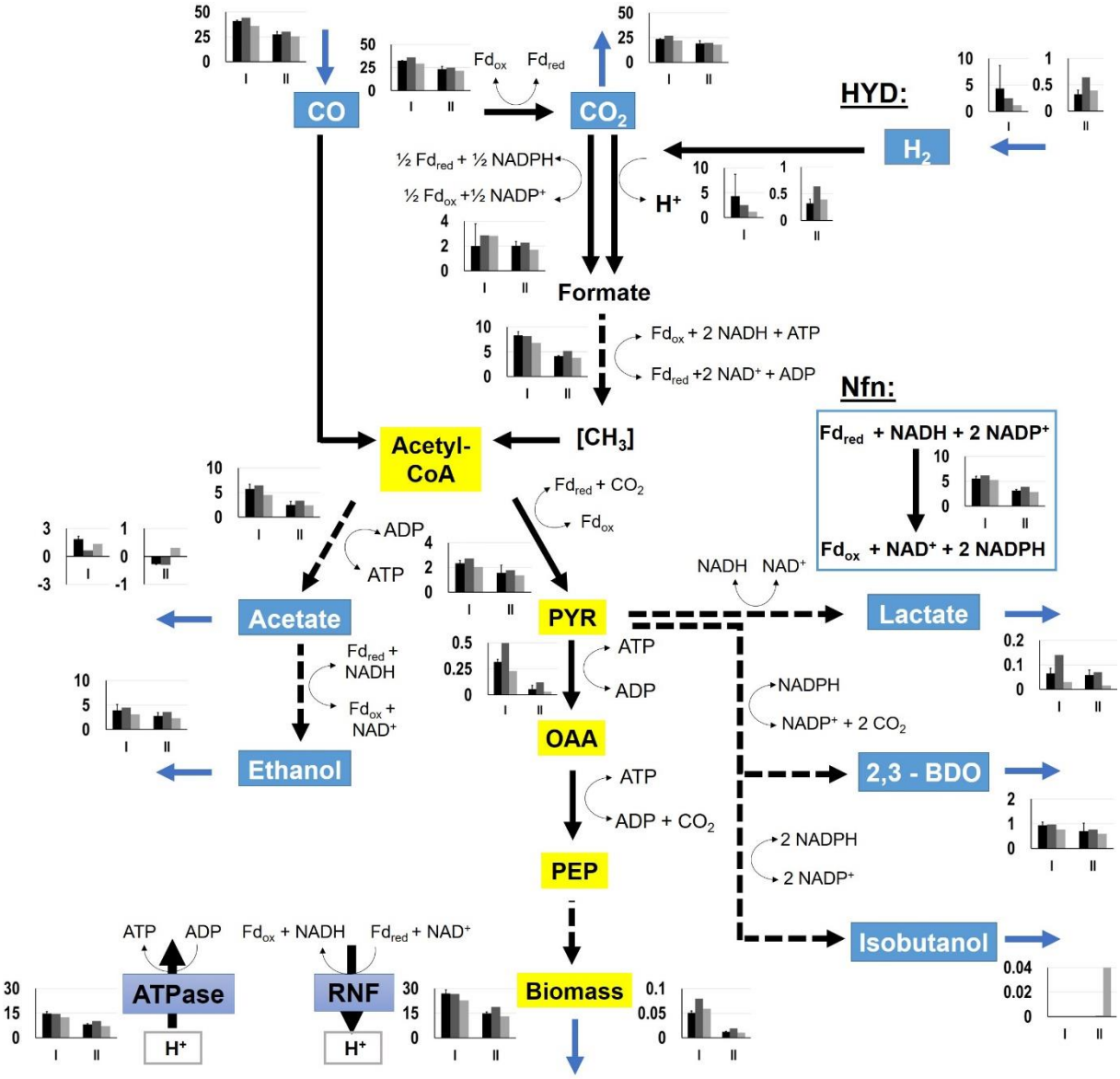

Figure 3.21: Metabolic flux distributions of CLJU[WT, REF] (black) CLJU[KAIA] (dark grey), and CLJU[KAIA]::ilvE (light grey) based on the conversion of syngas in steadily gassed batch cultivations in stirred-tank bioreactors. Illustrated are the simulated fluxes in mmol (gCDW*h)-1 for the first (I) and second (II) growth phase. Values of the wildtype cultivation indicate mean of duplicates.

Table 3.11: NADH and NADPH yields derived from flux balance analysis for the first (I) and second (II) growth phase considering the WLP and the Nfn reaction. Values of the wildtype cultivation indicate mean of duplicates.

Strain	Phase I		Phase II	
	NADH, mole $mole_{CO+H2}^{-1}$	NADPH, mole $mole_{CO+H2}^{-1}$	NADH, mole $mole_{CO+H2}^{-1}$	NADPH, mole $mole_{CO+H2}^{-1}$
CLJU[WT]	0.119 ± 0.026	0.020 ± 0.001	0.131 ± 0.028	0.006 ± 0.001
CLJU[KAIA]	0.095	0.029	0.147	0.01
CLJU[KAIA] ::*ilvE*	0.109	0.027	0.086	0.009

DISCUSSION

Syngas-based reference process

Metabolizing syngas during a batch cultivation *C. ljungdahlii* shows a biphasic growth behavior, that is characterized by growth reduction with simultaneously increased formation of reduced products. This coincidence was also observed in a two-stage process cultivating *C. ljungdahlii* on syngas (Richter et al., 2016). Previous studies have shown that shifts from acetogenesis to solventogenesis in syngas-fermenting *C. ljungdahlli* are accompanied by growth reduction. Metabolic rearrangements may be induced by pH shifts, nutrient limitation or addition of reducing agents into the growth medium (Richter et al., 2016). In this context, Valgepea et al. (2017b) demonstrated that solvent formation in *Clostridium autoethanogenum* may be promoted by simply increasing biomass concentrations. This can be explained by the metabolic link between energy conservation and redox management in acetogens. Shifting to solventogenic alcohol production improves ATP availability via the Rnf-ATPase-system (Hermann et al., 2020; Richter et al., 2016; Valgepea et al., 2017b). Further evidence was given by Oswald et al. (2016). They measured CO uptake rates of 33 – 100 mmol $(g_{CDW}*h)^{-1}$ and CO_2 production rates of 13 – 40 mmol $(g_{CDW}*h)^{-1}$ during a batch-cultivation of *C. ljungdahlii* with continuous gas supply. These values fit fairly well to our study. In contrast to our process, however, they identified a

simultaneous and equivalent uptake of CO and H_2. The simultaneous utilization of these gases is also shown in further studies describing continuous cultivations performed in chemostat mode installing 0.04 h^{-1} dilution rate (Martin et al., 2016; Richter et al., 2013; Valgepea et al., 2018; Valgepea et al., 2017b). Our observations did not reveal proportionality between CO and H_2 uptake which might be explained by the different syngas composition used (32.5 % H_2, 32.5 % CO, 16 % CO_2, 19% N_2). H_2 uptake and the product spectrum depend on the H_2/CO ratio (Jack et al., 2019) which was 1 in Oswald et al. (2016) and 0.54 in this study. CO is known to be a strong inhibitor of the hydrogenase activity (Devarapalli et al., 2016; Goldet et al., 2009; Jones and Woods, 1986), but CO utilization yields the formation of more reduced products (Jack et al., 2019). Moreover, acetate formation is favoured by increased H_2 consumption (Jack et al., 2019). Hence, the ratio of H_2/CO affects the product portfolio strongly.

Intracellular metabolites pattern during the process reveals a clear depletion of pyruvate accompanied by a strong accumulation of alanine in the second growth phase. Pyruvate serves as key precursor for 2,3-butanediol and lactate, which are mainly formed in the second phase of the process. In this regard, pyruvate depletion may limit the formation of 2.3-butanediol and isobutanol. Notably, the decreasing L-serine pool might hint to *C. ljungdahlii's* capacity converting L-serine to pyruvate via L-serine dehydratase to refill the pyruvate pool (Köpke et al., 2010).

Alanine may be synthesized by decarboxylation of aspartate and by transamination of valine, glutamate, and pyruvate (Parker and Pratt, 2010). Accordingly, it may serve as carbon and nitrogen storage that could be easily converted to pyruvate. The product formation of *C. ljungdahlii* is driven by its energy and redox management (Hermann et al., 2020). To counteract a surplus of reducing equivalents caused by continuous uptake of CO, *C. ljungdahlii* needs to produce more ethanol and 2.3-butanediol during the phase of retarded growth (Hermann et al., 2020; Richter et al., 2016). In addition, Richter et al. (2016) postulated that the metabolic shift from acidogenesis to solventogenesis of *C. ljungdahlii* is not regulated at the proteome level but rather by thermodynamics. Therefore, we hypothesize that the intracellular accumulation of alanine, valine, and glutamate enables *C. ljungdahlii* to react flexibly on increasing demands for pyruvate, the 'doorman' metabolite for getting rid of 'surplus' electrons.

This hypothesis is supported by the intracellular AEC and AXP patterns. Despite a reduction of AEC and the ATP concentration in the first growth phase, both values remained constant in the following period.

The initial decrease of the ATP pools may be associated with anabolic ATP needs considering that acetogens are living at the edge of thermodynamic feasibility. Retarded growth, consumption of acetate, and enhanced formation of reducing products enable *C. ljungdahlii* to keep its ATP pool constant during the second period. This may be advantageous for the recombinant production of isobutanol. Schatschneider et al. (2018) measured 0.1 $\mu molg_{CDW}^{-1}$ ATP, 0.09 $\mu molg_{CDW}^{-1}$ ADP, and 0.95 $\mu molg_{CDW}^{-1}$ AMP in CO-consuming, steadily growing *Clostridium autoethanogenum*, a close relative of *C. ljungdahlii*. Those values lead to the AEC of 0.13 which fit to the observations of this study. Interestingly, AXP levels and AEC are much lower than the so-called 'physiological' levels that range from 0.80 to 0.95 (Chapman et al., 1971). However, the latter rather mirror heterotrophic growth under aerobic conditions with ATP/C ratios of 6.3 – 2.3 (assuming catabolism of glucose with P/O ratios of 2.0 – 1.1). Instead, anaerobic ATP/C gain under autotrophic growth is an order of magnitude lower (Hermann et al., 2020).

Recombinant isobutanol formation

Syngas-based recombinant isobutanol formation by CLJU[KAIA] was successfully achieved, although at a low level, still. Given that the total free Gibbs reaction energy ΔG_R was even lower than in reference process (**Table 3.10**), no energy limitation was anticipated. Remarkably higher levels of valine compared to the wildtype cultivation together with the very low pyruvate levels suggested to block valine synthesis for increasing isobutanol formation. By this, a 6.5-fold increase of isobutanol titer compared to CLJU[KAIA] was achieved which supports the findings of Weitz et al. (2021). Energetically, the process should have been well equilibrated (**Table 3.10**) although intermediary shortcomings of reducing equivalents may not be ruled out completely. However, FBA revealed a limitation of NADPH at the end of the process, while NADH availabilities almost remained constant. Consequently, further improvements of isobutanol formation using CLJU[KAIA]::*ilvE* should be achievable by replacing the cofactor dependency on NADPH by NADH. Using a NADH-dependent

variant of the ketol-acid reductoisomerase Weitz (2020) demonstrated increased isobutanol formation (18%). Ethanol and 2,3-butanediol are the main products during syngas-based batch fermentation of *C. ljungdahlii* applying a H_2/CO ratio of approximately 0.5 (**Table 3.8**). Further strain optimization may aim to detour said reductive power into isobutanol formation. In case of ethanol this goal is very challenging as ethanol may be considered as a vital by-product of the acetaldehyde:ferredoxin oxidoreductase (AOR) which links its formation with ATP synthesis (Hermann et al., 2020; Liew et al., 2017; Liu et al., 2020; Mock et al., 2015; Zhu et al., 2020). However, elimination of 2,3-butanediol production may increase isobutanol formation as both products originate from the precursor pyruvate requiring NADPH as electron donor. Unfortunately, a first attempt to eliminate 2,3-butanediol formation in *C. ljungdahlii* was not successful. Thus, further approaches need to be performed (Weitz et al., 2021). Additionally, improved supply of H_2 may also increase the isobutanol formation. To check the hypothesis processes with higher H_2/CO ratios and/or higher reactor pressures during the solventogenic phase could be performed.

CONCLUSION

C. ljungdahlii is well equipped to convert syngas mixtures with H_2:CO ratios of 0.5 into reduced products. 30% of totally consumed carbon were used to produce mostly ethanol and 2.3-butanediol. Predominately, reducing equivalents originate from CO. However, the additional H_2 uptake, even if low, enables *C. ljungdahlii* to adapt simultaneous CO_2 reduction flexibly to NADPH needs. Intracellular pyruvate availability turned out to be a carbon bottleneck of alcohol formation. The implementation of the Ehrlich-pathway partly alleviated the carbon shortage. However, only the additional block of valine formation enabled to harvest the available carbon which resulted in a 6.5-fold increase of isobutanol formation. Analyzing the redox condition in CLJU[KAIA]::*ilvE* gives rise to the conclusion that a novel metabolic engineering target should be addressed next: The increased supply of NADPH. Targeting this goal should be in the focus of future autotrophic isobutanol formation with engineering *C. ljungdahlii*.

DATA AVAILABILITY STATEMENT

The raw data supporting the conclusions of this article will be made available by the authors, without undue reservation.

AUTHOR CONTRIBUTIONS

MH designed the study, conducted the bioreactor experiments, reconstructed the stoichiometric model, performed flux balance analyses, analyzed the datasets and drafted the manuscript. AT and MH designed and performed the metabolomics analysis. AF designed and set up the laboratory for the performance of synthesis gas bioreactor studies. MH supported this laboratory conversion. AN advised the network reconstruction and flux balance analysis. SW constructed the recombinant strains CLJU[KAIA] and CLJU[KAIA]::*ilvE*. FB and PD supervised the strain reconstruction and advised the study. RT conceived the study and corrected the manuscript. MH, AT, SW, FB, PD, and RT read and approved the final manuscript.

FUNDING

This work was funded by the Federal Ministry of Education and Research (BMBF, Grant Number: 031A468).

ACKNOWLEDGEMENTS

The authors thank Salaheddine Laghrami for excellent support with bioreactor fermentations and Mira Lenfers-Lücker for assistance with the HPLC analyses. We also thank Flora Siebler for her support and advice during this study. Furthermore, we thank all members of the project “Gase als neue Kohlenstoffquelle für biotechnologische Fermentationen (Gas-Fermentation)“ for a great cooperation. The

authors further gratefully acknowledge the funding of this work by the Federal Ministry of Education and Research (BMBF, Grant Number: 031A468).

SUPPLEMENTARY MATERIAL

The Supplementary Material for this article can be found online at: https://www.frontiersin.org/articles/10.3389/fbioe.2021.647853/full#supplementary-material and in chapter **7.3** of this document.

REFERENCES

See 6 references.

Conflict of Interest: The authors declare that the research was conducted in the absence of any commercial or financial relationships that could be construed as a potential conflict of interest.

3.5 Manuscript IV: The impact of CO gradients on *C. ljungdahlii* in a 125 m^3 bubble column: Mass transfer, circulation time and lifeline analysis

Flora Siebler, [1] Alexey Lapin, [2] Maria Hermann [1] and Ralf Takors [1,*]

[1]Institute of Biochemical Engineering, University of Stuttgart, Allmandring 31, 70569 Stuttgart, Germany

[2] Stuttgart Research Centre Systems Biology, University of Stuttgart, Nobelstraße 15, 70569 Stuttgart, Germany

*Corresponding author. Prof. Dr.-Ing. Ralf Takors

takors@ibvt.uni-stuttgart.de

KEYWORDS

pseudo-stationary gas gradient; two-phase Euler-Euler simulation; Lagrange trajectories; bubble column reactor, computational fluid dynamics (CFD)

ABSTRACT

Successful scale-up of biological fermentations requires the prevention of any performance losses from lab to production scale. Modelling large-scale conditions, in particular so-called lifeline analysis, is a proper approach to unravel potential risks and to guide the way for preventing non-wanted under-performance. This study focuses on synthesis gas fermentations in bubble columns which are particularly challenging because of poor carbon (C)-source solubility and low bacterial energy availability under such anaerobic conditions. As a model case, *Clostridium ljungdahlii* DSM 13528 is studied in a 125 m^3 bubble column reactor investigating bacterial motion patterns, circulation time, short- and long-term responses. A pseudo-stationary gas gradient was conducted with computational fluid dynamics in an Euler-Euler approach while the movement of the microorganism were simulated as Lagrangian massless particles. Cells were assigned uptake and product formation kinetics. Statistical lifeline analysis revealed that 97% of all cells experienced substrate limitations, whereas 84% were likely to undergo transcriptional changes after exposure in stress inducing zone longer than 70 s. Bacteria movements predominately occurred between low and moderate product biomass yield regions with longer residence times in the latter. The circulation time derived from mixing time analysis can be confirmed by regime transition strategy studies with about 10 s. Maximum residence times over 100 s as minimum regime crossing times of 10 s could also be identified. These findings show the high potential of Lagrange trajectories analysis in bubble column gas gradients which can be used for performance prediction and therefore risk minimization in scale-up.

INTRODUCTION

Supported by worldwide agreed resolutions such as the Paris Climate Agreement 2015, politicians and decision-makers in the industry more and more evaluate possibilities for establishing a CO_2 neutral bioeconomy (Philp, 2018). Accordingly, the use of synthesis gas (also called syngas) as a CO_2, CO and H_2 containing substrate gets in the focus to supply bacterial fermentations. Via syngas fermentations, said substrates can be converted through microbial routes to high-grade hydrocarbons (Daniell et al., 2012; Köpke et al., 2010) finally representing drop-in chemicals for the existing industrial infrastructure (Takors et al., 2018). From the engineering perspective, the main issue of this process is the poor mass transfer and equally low solubility of the gas components, since only dissolved carbon monoxide, carbon dioxide and hydrogen can be utilized by the acetogenic bacteria. Several reactor concepts have been investigated to overcome this challenge (Abubackar et al., 2011). As syngas fermentations typically yield commodities, i.e., low value, large volume products with small margins of economic benefit, large-scale gas fermentations should run with low operation costs. Furthermore, any loss of microbial production performance in large-scale should be prevented which is a challenging task (Takors, 2012). To minimize energy input and expenses, bubble columns are typically preferred. Compared to the conventional biotechnical set-up using stirred tanks they offer low operating costs and show high gas solubility because of their slim design and consequently high hydrostatic pressure.

However, the set-up or more precisely the competition between mixing and bioreaction creates gradients of dissolved substrates. In return, gradients impact the microbial activity as they impose fluctuating concentration in the cell environment. Various formulation of the same idea is to be found in Enfors et al; Lapin et al; Morchain et al; Schmalzriedt et al. (2003). This study will investigate related consequences focusing on the impact of a pseudo-stationary carbon monoxide gas gradient that will serve as the background of fluctuating bacteria. Pseudo-stationary gas gradient means that only a time point respectively ‘snap-shot’ of a large-scale bioreactor is simulated with a fixed biomass concentration. In this case, the gas holdup, as well as the liquid gas gradient, is stationary which does not account for the locally changing flow field. CO has been

chosen as a model case because of the growth inhibition that is created by high levels (Mohammadi et al., 2014). Concentration changes that cells experience while flowing along the so-called ‘lifelines’ will be recorded. Apparently, (i) a sound large-scale gas gradient in a bubble column with representative flow structures in form of a motion ‘snap-shot’ and (ii) the translation of nutrient availability into product and biomass formation are essential prerequisites of such simulations.

The latter (ii) requires a thorough understanding of the intracellular metabolic network which interacts with the cellular environment. A comprehensive genome-scale stoichiometric model of *Clostridium ljungdahlii* has been published by Nagarajan et al. (2013). Chen et al. (2015) succeeded to apply the genome-scale model with the dynamic flux balancing technique of Gomez et al. (2014) to resolve the spatiotemporal distributions of *C. ljungdahlii* fluxes in a bubble column reactor. For minimizing computational efforts, the bioreactor was discretized in a set of compartments each assuming homogenous conditions. In general, compartment-based bioreactor simulations are quite common (Heins et al., 2015; Pigou and Morchain, 2015; Vrábel et al., 2001) because they inherently offer high simulation speed even in combination with complex kinetics (Henson, 2003; Mantzaris et al., 1999). Challenging flow patterns may be well approximated. However, important bubble characteristics such as coalescence and breakup are rarely (Nauha et al., 2018) or not at all considered which have a great impact on mass transfer especially in large scales (Akita and Yoshida, 1973).

To fulfil the constraint (i) compartment-based approaches need to be replaced by improved spatial resolution applying computational fluid dynamics (CFD). For gas–liquid multiphase flows, either the Euler-Euler or the Euler-Lagrange approach can be used (Larsson et al., 1996; Noorman, H., Morud, K., Hjertager, B. H., Traegaardh, C., Larsson, G., & Enfors, S. O., 1993; Schmalzriedt et al., 2003). The latter allows more detailed bubble simulation but is not recommended for large-scale simulations with gas hold-ups higher than 10%. Solving the Euler-Euler approach combined with a population balance model (PBM) enables the implementation of important bubble physics such as bubble expansion, breakage and coalescence. Gas hold-up and mass transfer get more realistic as well as the simulation of a pseudo-stationary gas gradient.

This study aims to predict the impacts of large-scale bubble column fermentations through the 'eyes' of *C. ljungdahlii* DSM 13528 (Tanner et al., 1993) which was chosen as a promising acetogenic strain of industrial interest. So-called 'lifelines' will be calculated, i.e., fluctuation profiles of individual cells recording extracellular impacts of biological relevance. To fulfil the constraints (i) and (ii) Euler-Lagrange multi-phase simulations will be linked to metabolic models. Accordingly, the study follows the original approach of Lapin et al. (2004) which is gaining momentum by numerous continuing works (Haringa et al., 2017a; Haringa et al., 2017b; Haringa et al., 2016; Kuschel et al., 2017). The statistical interpretation of bacterial lifelines was initially shown by Haringa et al. (2016) and will also be applied in this study. The framework will be used to investigate the challenging design of large-scale bubble columns as a prerequisite of successful syngas fermentations. Conclusions will be drawn not only with respect to mass transfer and hydrodynamics but particularly regarding the expected impact of time-varying concentrations on the metabolic behaviour of *C. ljungdahlii* in a 125 m^3 bubble column.

MATERIALS AND METHODS

Geometry, reactor set-up and biological system

For the computational investigation of a large-scale synthesis gas gradient, a bubble column reactor of 25 m in height and 2.5 m in diameter has been chosen. *Clostridium ljungdahlii* DSM 13528 (Tanner et al., 1993) serves as a model organism using as carbon (C) source carbon monoxide provided by synthesis gas. The gas inflow was set to 0.15 vvm at the whole bottom surface area of the reactor (A_R = 5 m^2) and contained a CO/N_2-mixture of 55/45 vol-%. The initial bubble diameter was 4 mm. Media viscosity η_L, density ρ_L and surface tension σ_L was assumed to be similar to the properties of water with η_L = 0.001 Pa s^{-1}, ρ_L = 1000 kg m^{-3} and surface tension σ_L = 0.072 N m^{-1}. The process was assumed to be isotherm with an operating temperature of 310.15 K. No additional pressure was applied beside the ambient pressure of 1 atm and the hydrostatic pressure due to the column height. All values can also be found in **Table 3.12**.

Mathematical method and computational set-up

The multiphase approach was conducted by an Euler-Euler simulation and solved with the commercial computational fluid dynamics (CFD) program ANSYS Fluent 18.0. The reactor volume of 125 m^3 was discretised into 125,000 numerical cells (see also Appendix A of the original publication: Mesh). By solving the Reynolds-averaged Navier-Stokes equations (RANS) combined with the RNG (Re-Normalization Group) *k*-*ε*-model the gas gradient was approximated. The flow field in a bubble column is only developed when the liquid and dispersed phase are coupled and a bubbly flow reproduced. Coupling is achieved through the pressure and interphase exchange coefficients set by the chosen phase interaction correlations. The ideal gas law was applied. All other settings are listed in **Table 3.12**.

The flow equations were solved every 10 ms and the maximum iterations per time step were set to 25. However, only ten or fewer iterations per time step were needed. After 1,000 s a constant gas hold-up was reached which corresponds to approximately 10 simulation days with four cores and double precision. Likewise, the mass balance of gas in- and outflow converged in a steady state and the second modelling set-up was started.

In general, it should be stated that the *k*-*ε*-model represents a promising, commonly applied approach for estimating turbulent flow. However, because of its basic nature, non-accuracies of turbulence predictions may propagate further, e.g., affecting bubble breakage when applying the Luo model (Luo, 1995; Luo and Svendsen, 1996). Furthermore, Haringa et al. (2018) indicated that 1st order upwind has the tendency of underestimating turbulence quantities which may further affect the discrepancy between e.g. power input estimations using superficial gas velocity measurements and *k*-*ε*-derived predictions.

Table 3.12: Computational fluid dynamics simulation set-up for pseudo-stationary gas gradient. Listed are boundary conditions, physical properties, phase set-up and solution methods. Details on the mesh can be found in the Appendix A of the original publication.

	Boundary condition	**Units**
Inlet	Velocity inlet with 0.0625 m s^{-1} (ε_G = 1)	m s^{-1}
Outlet	Degassing	
Wall	Non-slip conditions	
Initial bubble size	4	mm

	Physical properties	**Units**
Column diameter D_R	2.5	m
Column height H_R	25	m
Media viscosity η_L	0.001	Pa s^{-1}
Media surface tension σ_L	0.072	N m^{-1}
Media density ρ_L	1,000	kg m^{-3}
Temperature T	310.15	K
CO/N_2 composition	55/45	vol-%

	Models and phase set-up	**Source**
Multiphase	Euler-Euler (implicit)	
Population balance model	discrete with 16 bins and a diameter range of 0.001 ≤ d_B ≤0.032 m	
Turbulence	RNG *k*-ε-model + differential viscosity model	
Phase interactions	Drag	Grace drag force or universal drag law (Clift et al., 2013)
	Lift	(Tomiyama et al., 2002)
	Wall Lubrication	(Antal et al., 1991)
	Turbulent Dispersion (c_d = 0.8)	(Burns et al., 2004)
	Turbulent Interaction	(Sato and Sekoguchi, 1975)
	Surface tension coefficient	Specified

	Solution methods	
Pressure-velocity coupling	Phase coupled SIMPLE	
Spatial discretization	Gradient	Least square cell based
	Momentum	QUICK
	Volume fraction	QUICK
	Turbulent kinetic energy	First order upwind
	Turbulent dissipation rate	First order upwind
	Phase 1 (liquid) and 2 (gas) species	First order upwind
	Phase 2 bin	First order upwind
Transient formulation	Bounded second order implicit	
Under-relaxation factors	between 0.3 and 1 (mostly default)	
Transient regime	Time step size	0.01 s
	Iterations per time step	maximum 25 (usually >10)
Simulation time	flow field	1,000 s
	gradient	500 s
	Lagrange trajectories	500 s

***Pseudo-stationary gas gradient*:** The next step to reach a pseudo-stationary gas gradient is to include breakage, coalescence and bubble expansion. Therefore, different bubble sizes were introduced by the population balance model (PBM) also available in ANSYS Fluent 18.0. All in all, 16 bubble classes with a diameter range of 0.001 m < d_B < 0.032 m were chosen and for both - breakage and coalescence - the Luo-model (Luo, 1995; Luo and Svendsen, 1996) was applied. In addition, two user defined functions (UDF) for mass transfer and the dissolved carbon monoxide uptake were included. For the simulation of mass transfer from gas to the liquid phase in non-agitated bubble column reactors the conform Higbie correlation for the mass transfer rate k_L was chosen and solved in each numerical cell (Higbie, 1935).

$$k_L = \frac{2}{\sqrt{\pi}} \sqrt{\frac{D_L v_{rel}}{d_B}} \tag{11}$$

The correlation depends only on the Sauter mean bubble diameter d_{32}, the diffusion coefficient of CO $D_{L,CO}$ = 2 e^{-9} m^2 s^{-1} and relative bubble velocity v_{rel} of the numerical cell. While the Sauter mean bubble diameter is applied, the effects of PBM bubble distribution is neglected in this case. Henry's law was used to estimate solubility with the coefficient $k_{H,cp}$ = 7.7 e^{-4} mol L^{-1} atm^{-1}. The pressure gradient was also accounted for in this UDF, giving the equilibrium concentration of carbon monoxide $c^*_{L,CO}$. The interfacial area concentration *a* is calculated assuming a spherical bubble shape which finally leads to the expression in Eq. ((12) for the mass transfer $\dot{m_{GL}}$ solved at each time step in each discretisation volume.

$$\dot{m_{GL}} = k_L(c^*_{L,CO} - c_{L,CO})\frac{6\varepsilon_G}{d_{32}} \tag{12}$$

The Higbie correlation for the mass transfer and spherical bubble shapes are rough simplifications. The reader should be aware that dimensionless numbers for the bubbles, such as Eötvös (~60), Morton (log(Mo) = -10) and Reynolds number (~5000) rather pinpoint to transient wobbling to spherical cap geometries (Grace, 1973). Additionally, gas hold-up and superficial gas velocity also indicate the transition between homogeneous bubbly flow to heterogeneous churn-turbulent flow (Deckwer et al., 1980; Kantarci et al., 2005; Krishna et al., 2001). Nevertheless, the Higbie correlation was used, not only for the sake of simplicity but also because profound mass transfer studies with the said biological matrix would have been needed which are far beyond the scope of this lifeline analysis.

The second UDF was written to describe the CO uptake kinetic q_c of *C. ljungdahlii* published by Mohammadi et al. (2014). With a maximum uptake of $q_{c,max}$ = 34.36 mmol g_{CDW}^{-1} h^{-1} and a Monod constant of K_M = 0.02 mmol g_{CDW}^{-1} the equation also includes a substrate ($c_{L,CO}$) inhibition modification by Andrews with an inhibition coefficient K_I = 0.55 mmol g_{CDW}^{-1}.

$$\mathrm{q_c} = \frac{\mathrm{q_{c,max}} c_{L,CO}}{c_{L,CO} + K_M + \frac{c^2_{L,CO}}{K_I}} \tag{13}$$

The dissolved carbon monoxide uptake takes place in each numerical cell at each time step. After another 500 s a new steady state for the gas hold-up and dissolved CO concentration was reached which does not account for the constantly changing periodic flow field. Pseudo-stationary gradient means that only a time point respectively ‘snap-shot’ of a real large-scale simulation is chosen with a temporary constant biomass concentration of 10 g L^{-1} and no cell multiplication. This assumption can be made since mixing and mass transfer time scales are much smaller than time scales for bacterial growth. The second simulation part lasted more than ten simulation days since 16 bubble classes instead of one, breakage, coalescence, bubble expansion, mass transfer and a reaction needed to be solved as well. Detailed changes in the volumetric mass transfer rate after 1000 s and 1500 s can be found in Appendix E of the original publication.

Lagrange trajectories: The final CFD simulation uses the generated pseudo-stationary gas gradient and flow field to analyse cell lifelines, movement patterns and circulation time. Therefore, besides the Euler-Euler phases a third phase, the bacteria were introduced as massless Lagrange particles as well as the discrete random walk (DRW) model was enabled. The gradient and flow field were set as frozen and not further calculated. With another user defined function every 30 ms the particle ID, the corresponding CO concentration and position were recorded. In total, 120,000 bacteria were tracked for 500 s. The trajectories were checked for ergodicity which can be found in Appendix B of the original publication: Statistical relevance. Further evaluations of the lifelines were conducted with the program MATLAB®.

Uptake kinetic and product formation correlation

C. ljungdahlii prefers CO over CO_2 because the substrate equally serves as a carbon and electron source. However, the consumption of CO_2 requires additional electrons originating from the crucial co-uptake of H_2. For the sake of simplicity, this case is omitted in the current study which focuses on the impact of CO gradients only. The growth of *C. ljungdahlii* coincides with the formation of the by-products acetate, ethanol, 2,3-butanediol and maybe even carbon dioxide (under distinct conditions). Clearly, the latter may only be produced under ample CO conditions when the carbon

drain to targeted products such as ethanol and 2,3-butanediol is limited (e.g., because of non-optimum strain engineering). Linking metabolic modelling with large-scale CFD represents a trade-off between crucial metabolic complexity and computational efforts necessary to solve the large-scale simulation problem. Because the use of genome-scale network models is computationally expensive a minimum stoichiometry model was formulated mirroring the essentials of *C. ljungdahlii* metabolism. With the help of a simple net Eq. (**14**) and the element balances for carbon C, hydrogen H and oxygen O (Eq.(**15**)) the correlation can be derived.

$$\underbrace{1\,CO}_{q_c} + \underbrace{Y_{H^+,CO}H^+}_{q_{h^+}} \rightleftharpoons \underbrace{Y_{X,CO}CH_{1.8}O_{0.5}}_{q_x} + \underbrace{Y_{Ac,CO}CH_{1.5}O}_{q_a} + \underbrace{Y_{EtOH,CO}CH_3o_{0.5}}_{q_e} \\ \underbrace{Y_{2,3But,CO}CH_{2.5}O_{0.5}}_{q_b} + \underbrace{Y_{CO_2,CO}CO_2}_{q_{c2}} + \underbrace{Y_{H_2O,CO}H_2O}_{q_b} \tag{14}$$

The net reaction includes all relevant products such as biomass (x), acetate (a), ethanol (e), 2,3-butanediol (b) and carbon dioxide (c2). Water (w) and hydroxide ion (h+) are needed for H- and O-balance. Analogous to the yields Y per C-mol CO the uptake and production rates *q* are indicated at the bottom in Eq.(**14**).

$$\begin{matrix} C: \\ H: \\ O: \end{matrix} \begin{pmatrix} 1 & 0 & 1 & 0 & 1 & 1 & 1 & 1 \\ 0 & 1 & 0 & 2 & 1.8 & 1.5 & 3 & 2.5 \\ 1 & 0 & 2 & 1 & 0.5 & 1 & 0.5 & 0.5 \end{pmatrix} \begin{pmatrix} q_c \\ q_{h^+} \\ q_{c2} \\ q_w \\ q_x \\ q_a \\ q_e \\ q_b \end{pmatrix} = \bar{0} \tag{15}$$

Eq. ((14) can also be transformed into Eq. ((15) which is five times under-determined. Therefore, the resulting solution space is restricted by lower (lb) and upper bounds (ub) as described in Eq. ((16). The ratio $q_c/1.7$ is motivated by own experimental observations (data not shown) studying the by-product formation of *C. ljungdahlli* wildtype under ample CO conditions.

$$\begin{matrix} lb \\ ub \end{matrix} = \begin{matrix} (q_c & -100 & q_c/1.7 & -100 & 0 & 0 & 0 & 0) \\ (q_c & 100 & q_c/1.7 & 100 & 2.5 & 100 & 100 & 100) \end{matrix} \tag{16}$$

Maximum growth for *C. ljungdahlii* is set to μ_{max} = 0.06 h^{-1}. H_2O and H^+ can either be consumed or produced and the by-products only produced.

$$f(q_c) = \max(q_x + q_a + q_e + q_b) \tag{17}$$

The optimal result can be derived by maximizing the sum of all production rates (Eq.(**17**)) which is graphically shown in **Figure 3.22 (A)** for different possible uptake rates. In each case, the element balances are not violated.

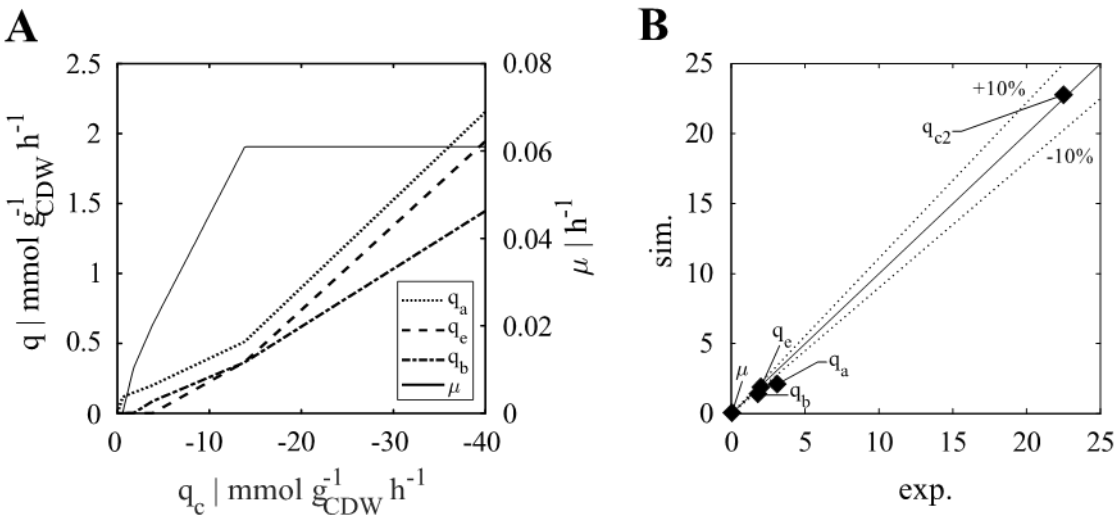

Figure 3.22: Optimization results for kinetic correlation (**A**) and comparison with experimental data (**B**). In (**A**) the maximization for product formation results are graphically shown for several possible CO uptake rates q_c. The production rates for acetate q_a, ethanol q_e and 2,3-butanediol q_b are shown as well as the growth rate μ on the left side. The simulation outcome was compared with experimental data in (**B**). The experimental rates in mmol g_{CDW}^{-1} h^{-1} were provided by M. Hermann (ongoing studies, IBVT) who performed synthesis gas fermentations with a gas composition of 55/30/5/10% for $CO/H_2/CO_2$/Ar.

Figure 3.22 (B) compares experimental findings with the simulation results. How the experiment was conducted can be found in Appendix D of the original publication: Experimental values. As the predictions are the result of elementary flux balance analysis, instantaneous 'pseudo-steady-state' transitions are intrinsically assumed which translate local q_c to growth and production rates. Accordingly, time-resolved metabolic or transcriptional dynamics as seen in Chen et al. (2015) and Löffler et al. (2016) are not covered by the simple modelling approach.

Statistical evaluation

Evaluation of regime transition events: For the statistical evaluation, the Lagrange trajectories were sorted and the CO concentration profiles filtered as described in Kuschel et al. (2017). The filtered concentration is translated into uptake kinetics and total product-biomass yields. The latter can be derived from the optimization results of the element balances which leads to Eq. (**(**18)) also shown in **Figure 3.23 (A)**. The total product-biomass yield describes the carbon share between all products and biomass as a function of the carbon uptake rate. High $Y_{P,X}$ values indicate that more carbon flows in the formation of the desired by-product. Accordingly, high $Y_{P,X}$ values can be considered as a proxy for strong metabolism in growing cells. The aim of this translation is to investigate how the cells move. From which gradient segment they come, where they go and for how long they stay in a certain environment defined by the surrounding dissolved CO concentration. Therefore, conditions have to be classified in high and low total product-biomass yields and in a transition phase between both regimes.

$$\mathrm{Y_{P,X}(q_c)} = \begin{cases} \dfrac{1.51\mathrm{q_c}}{\mathrm{q_c} - 2.29} & -14 < \mathrm{q_c} \leq 0 \\ -\dfrac{\mathrm{q_c}}{6} - 1 & \mathrm{q_c} \leq -14 \end{cases} \tag{18}$$

The first functional segment ranging from q_c = 0 to q_c < - 14 mmol g_{CDW}^{-1} h^{-1} shows Monod-type kinetics with a half-maximum yield at $K_{Yp,x}$ = 2.29 mmol g_{CDW}^{-1} h^{-1}. This value was also used to mark the beginning regime transition from low to higher yields. Translating the yield limits into CO concentration transfers the yield regime into a CO regime, respectively. When q_c ≤ – 14 mmol g_{CDW}^{-1} h^{-1} the function turns into a linear correlation. The maximum of CO conversion into biomass formation is achieved. Additional uptake directly fuels by-product formation. This switch was used as the second regime transition criterion indicating the high yield zone. Thus, three regimes can be specified: **L** for low yields from zero to - 2.29 mmol g_{CDW}^{-1} h^{-1} (0 ≤ $Y_{P,X}$ < 0.75), **T** for transition area between - 2.29 and - 14 mmol g_{CDW}^{-1} h^{-1} (0.75 ≤ $Y_{P,X}$ < 1.33) and **H** for high yields starting at - 14 mmol g_{CDW}^{-1} h^{-1}.

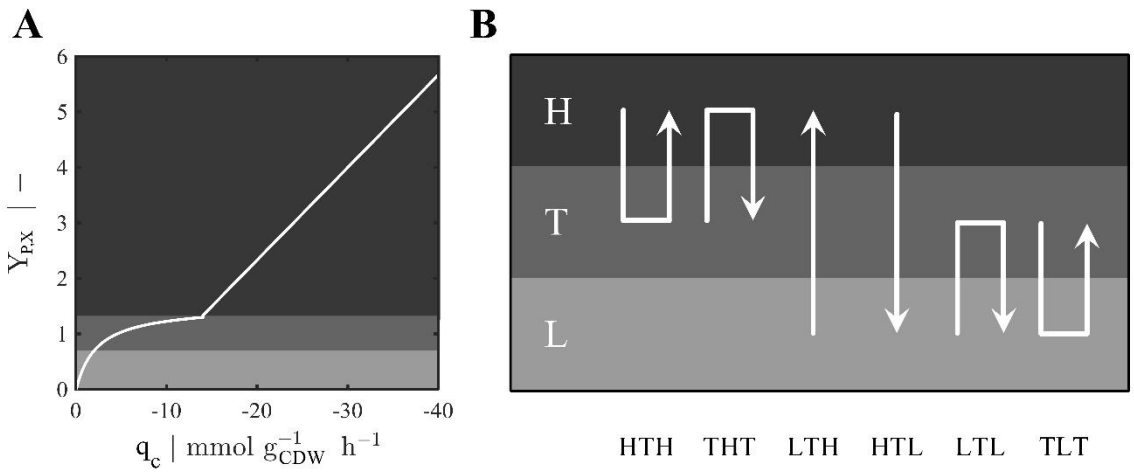

Figure 3.23: Regime classification as function of productivity. In (**A**) the product biomass yield $Y_{P,X}$ is given in C-mol per C-mol as a function of CO uptake rate (see also equation (**18**)). From q_c of zero to - 14 mmol g_{CDW}^{-1} h^{-1} the $Y_{P,X}$ function shows Monod-tyke trends with a half-maximum value of - 2.29 mmol g_{CDW}^{-1} h^{-1} which is also the threshold for entering the transition regime. The upper limit of transition is indicated by - 14 mmol g_{CDW}^{-1} h^{-1} when the $Y_{P,X}$ start ascending linearly. All six regime transition strategies are illustrated in (**B**).

The classification into three regimes is also graphically implied in **Figure 3.23**. The regime classification represents the number of smallest encoding units characterizing the shift between three gradient zones which the bacteria do transverse. Lifelines are characterized by a sequence of regime changes thereby integrating all extracellular stimuli exposed on the cell. Three gradient areas lead to six regime transition events which are schematically shown in **Figure 3.23 (B)** and are additionally described in the following list.

- **HTH**: Event from high to transition and back to high product per biomass yield areas.
- **THT**: Reverse movement starting from the transition area with retention in the high yield area and back to transition.
- **LTH:** Crossing all regimes from low to high and with dwelling in the transition area.
- **HTL**: Reverse event from low to high product biomass yields.
- **LTL**: Analogous to HTH but from low to higher and back to low yield areas with residence time in the transition domain.

- **TLT**: Same regimes but with a stay in the lower domain with little product biomass yields and start in the transition class.

The residence time is referred to as τ and accounts for the 'sandwich' regime always. The frequency of each regime transition event was counted and the duration recorded.

Evaluation of short- and long-term responses: For qualifying the stress impact of the cells biological criteria are necessary. To distinguish between short- and long-term responses, two sensitive thresholds are needed. The occurrence of critical CO concentrations flags the start of a short-term stress stimulus. The length of the exposure of this stimulus flags the putative triggering of long-term transcriptional responses. The longer a bacterium lingers in an area with the critical concentration the more severe the internal changes and therefore energy costs for the cell will be. Usually, short- and long-term responses can be examined with scale-down approaches such as plug-flow experiments (Löffler et al., 2016).

In the case of *C. ljungdahlii*, no comparable experimental studies are available. Accordingly, related threshold values were estimated taking the well-investigated *Escherichia coli* as reference. Taymaz-Nikerel et al. (2010) and Michalowski et al. (2017) estimated the maintenance demands and the maximum glucose uptake of *E. coli* as m_s = 0.057 $g_{gluc}\ g_{CDW}^{-1}$ and q_{max} = 1.8 $g_{gluc}\ g_{CDW}^{-1}\ h^{-1}$, respectively. Consequently, 3.2% of the maximum uptake are needed for maintenance demands under optimum growth conditions. In the case of *C. ljungdahlii*, the optimum CO uptake rate can be derived from the Andrew inhibition kinetic as $q_{c,max}^{real} = q_c\left(\sqrt{K_M K_I}\right)$ = 24.87 $g_c\ g_{CDW}^{-1}\ h^{-1}$ (0.1 mmol L^{-1}). Assuming that maintenance needs of *E. coli* and *C. ljungdahlii* are somewhat comparable the 3.2% fraction corresponds to $c_{L,CO}^{crit}$ = 0.003 mmol L^{-1}. This concentration is expected to be a good indicator for a biological regime shift as it marks the likely initiation of regulatory programs to adapt metabolic activities to the limiting CO supply.

Translating the metabolic stress stimulus into a transcriptional and translational response takes time. In the case of *E. coli*, early transcriptional responses were found after 30 – 40 s whereas the bulk of transcriptional activation occurred after 70 s (Löffler et al., 2016). Accordingly, minimum critical residence times in stress-inducing zones

were chosen as τ^{crit} = 10 s, τ^{crit} = 40 s and τ^{crit} = 70 s. Because related measurements are missing for *C. ljungdahlii* and because similar findings were found for other microbes (not yet published), the same criteria were set for *C. ljungdahlii* in this study. Further information on the evaluation of the short- and long-term response can be found in Appendix F of the original publication: Detailed short- and long-term responses evaluation.

RESULTS AND DISCUSSION

Flow field and pseudo-stationary gas gradient

To reach a pseudo-stationary gas gradient in an industrial-scale bubble column reactor two simulation set-ups have been chosen. The flow field was developed by solving the Euler-Euler multiphase approach with one entering bubble class of 4 mm and all phase interactions described in **Table 3.12**. As steady-state indicator the average gas hold-up ε_G was tracked for 1000 s until it stayed constant at 0.34. Then, the population balance model (bubble classes with breakage, coalescence, and expansion) was additionally enabled considering CO mass transfer with respect to the bacterial needs. After 1500 s the final CO gradient was reached (ε_G = 0.21). **Figure 3.24** shows the mean gas hold-up history in (**A**) as well as the changes in bubble size distribution (BSD) for the second simulation approach from 1000 s (start, dark grey) to 1500 s (end, red) in (**B**).

BSDs are indicated as a function of number density η_G in **Figure 3.24** (**B**). They reveal that both bubble breakage and coalescence occur, although the bubbles the tendency of coalescence is dominating. Since the initial bubble size is 4 mm (bin 7) this class is represented the most followed by bubble classes with larger diameters (first picture in **Figure 3.24** (**B**), distribution colored in red). The composition of the final BSD is similar to observations with water–air experiments of Lehr et al. (2002). However, the bubble column of this study is six times larger than the set-up of Lehr et al. (2002) creating longer bubble residence times and thus higher probability for coalescence finally leading to larger bubbles classes up to 3.2 cm (bin 16). Consequently, a lower average

gas hold-up was calculated after 1500 s compared to 1000 when coalescence was not yet considered.

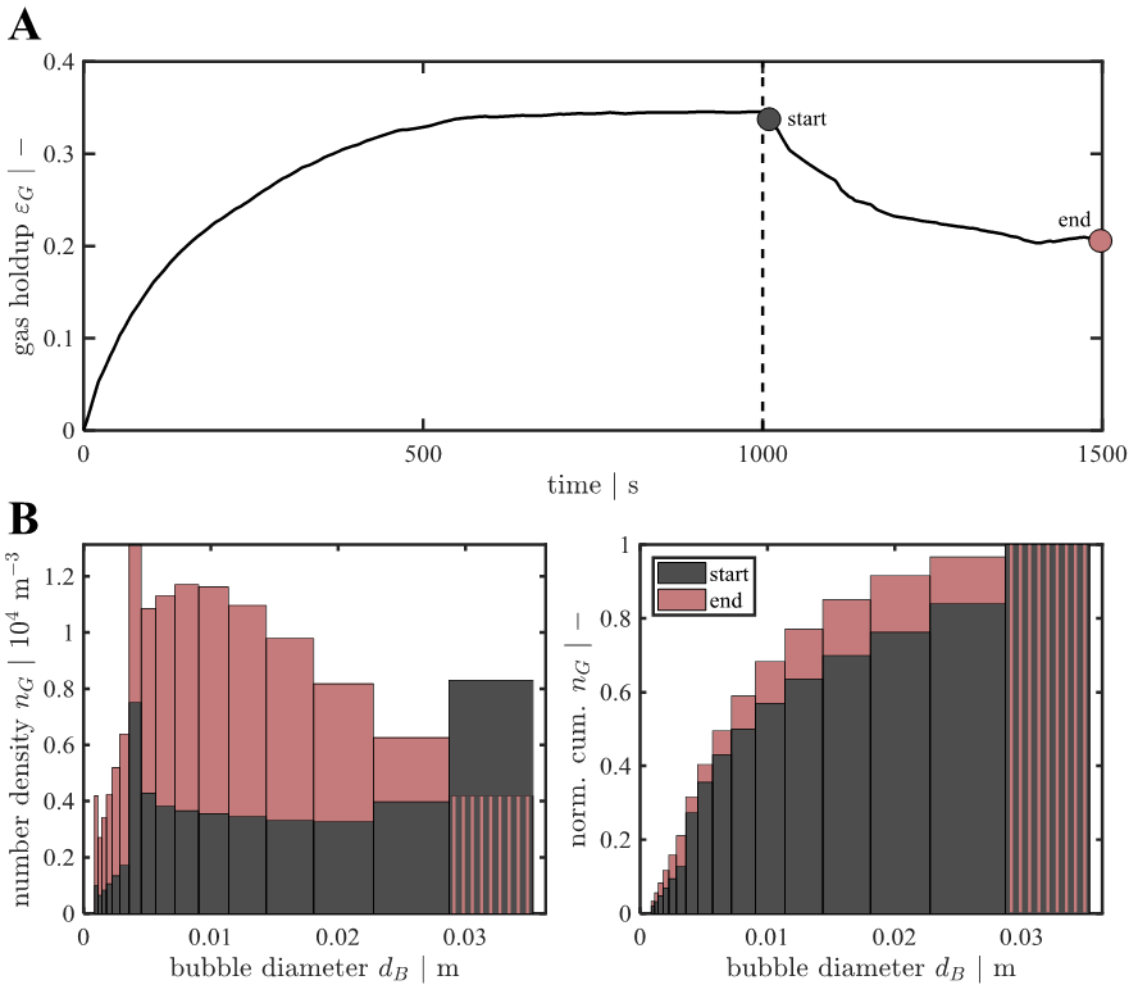

Figure 3.24: Simulation development to reach pseudo-stationary gas gradient. In (**A**) the average gas hold-up in the bubble column reactor is plotted versus time. During the first 1,000 s the flow field was developed with one bubble size and no mass transfer from gas to liquid. From 1,000 to 1,500 s breakage and coalescence and effects of hydrostatic pressure are enabled by including the population balanced model. The average bubble size distribution for start (dark grey) and end point (red) are shown in (**B**). The number density over diameter bin is given as normal and cumulative distribution. Similar to compartment approach the start parameter is always 4 mm (bin 7).

The flow field, gas hold-up, and concentration profiles of the CFD simulation are graphically displayed in **Figure 3.25** (**A**) to (**C**) after 1500 s simulation time. Whereas graphic (**B**) and (**C**) show similar gradient profiles with maximum values at the bottom

and reducing values towards the top, the flow field in (**A**) is different. By trend, high velocities are observed in the upper reactor region close to the wall and low to moderate flow patterns are dominating in the low part of the bubble column. The spatially distributed flow pattern reflects the impact of changing bubble size distribution very well. To be precise, the more proximate to the outer top regions the larger the average bubble size and the faster the bubble rising velocity is. Accordingly, faster bubble rise creates broader bubble size distributions (data not shown).

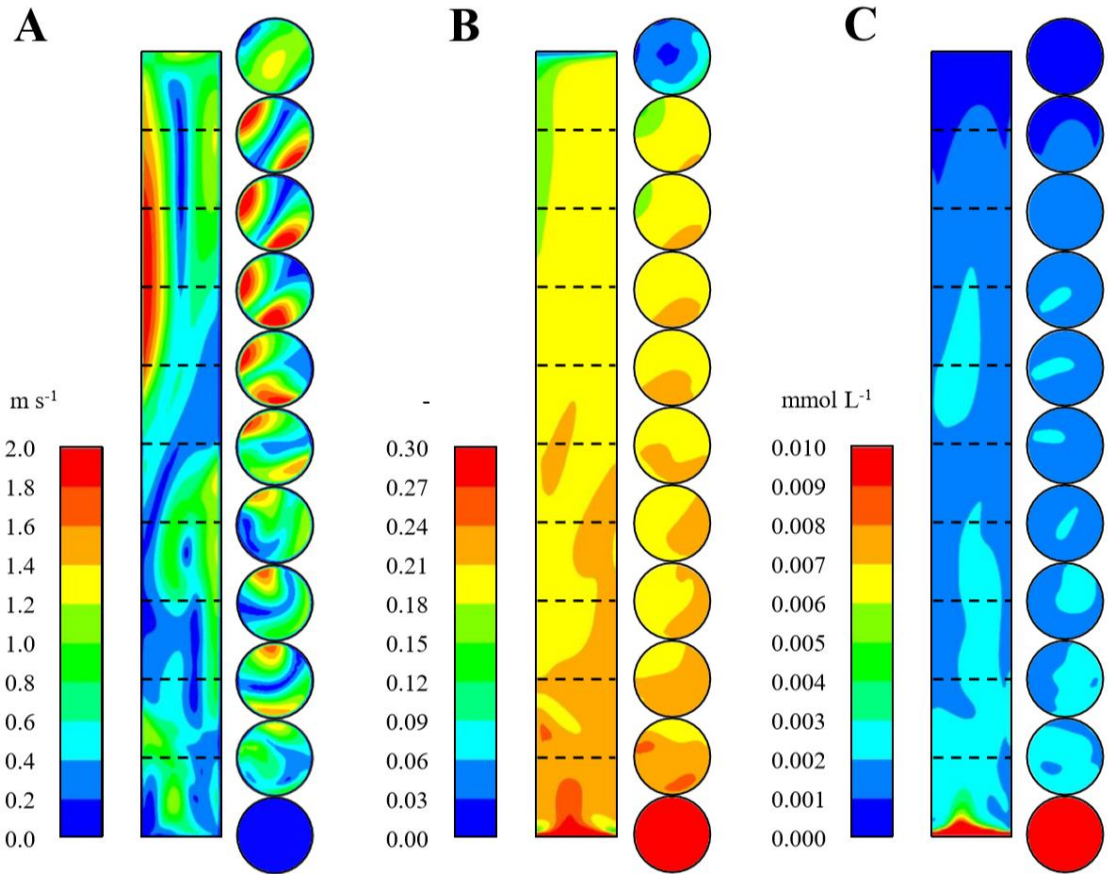

Figure 3.25: Flow field (**A**), gas hold-up (**B**) and CO concentration profile (**C**) of the CFD simulation. Colour scale and unit is given on the left side. Shown are side profiles and eleven section planes indicated by the dashed lines as well as reactor top and bottom. In (**A)** the velocity magnitude is depict.

As mentioned in the materials and methods section, the flow field has a cyclic behaviour. The distributions of **Figure 3.25** are 'snapshots' that re-occur frequently whereas the total hydrodynamic scenario is in steady-state with respect to the gas hold-up (see **Figure 3.24**). To investigate the impact of the gradients on the cells, the condition of **Figure 3.25** has been 'frozen' serving as a background for further studies.

Accordingly, the CO gas gradient was used to investigate the bacterial lifelines with respect to productivity, circulation time and long- and short-term responses. As such, the observations should be interpreted as a trend for qualifying the bacterial lifelines and for discussing putative impacts on cellular performance.

Bacterial lifelines and frequency of regime transition events

To assess statistically the bacterial movements through the gradients in the bubble column, regime shifts (introduced in the Material and Method section) were evaluated. The analysis focusses on the flow pattern qualifying the beginning, residence time and end of the bacterial flows (see **Figure 3.23** (**B**)). The stay in the transient interim regime is particularly of interest since information about possible performance changes of the microbe can be deduced. The threshold criteria defined in the Material and Method section basically mirror the assumption that the longer a bacterium stays in one regime the more likely it adapts to its surroundings. As a consequence, energetically demanding adaptations of the regulatory programs are initiated that may deteriorate the production capacity of the cells (Löffler et al., 2016).

Figure 3.26 (**A**) shows the regime-specific zones inside the bubble column. The regime classification H encoding high product biomass yields is depicted in dark grey and is located in the lowest column zone (zoomed detail). In contrast to H, the transition regime T (in lighter grey) spreads along the majority of the column height whereas the low product biomass yield regime L is located predominately at the top of the reactor. Moreover, the 30 s lasting courses of the two lifelines, L1 and L2, are depicted in **Figure 3.26** (**B**) to (**D**) together with their translation in product biomass yield profiles (**C**) and regime classifications (**D**). While the first lifeline L1 passes through all three regimes the second lingers in the transition regime for the time span of 30 s. For L1 two movement patterns can be recognized, the LTH and the THT regime transition events with dwell times of τ_{LTH} = 18.3 s and τ_{THT} = 2.1 s, respectively. However, L2 always stays in the T zone.

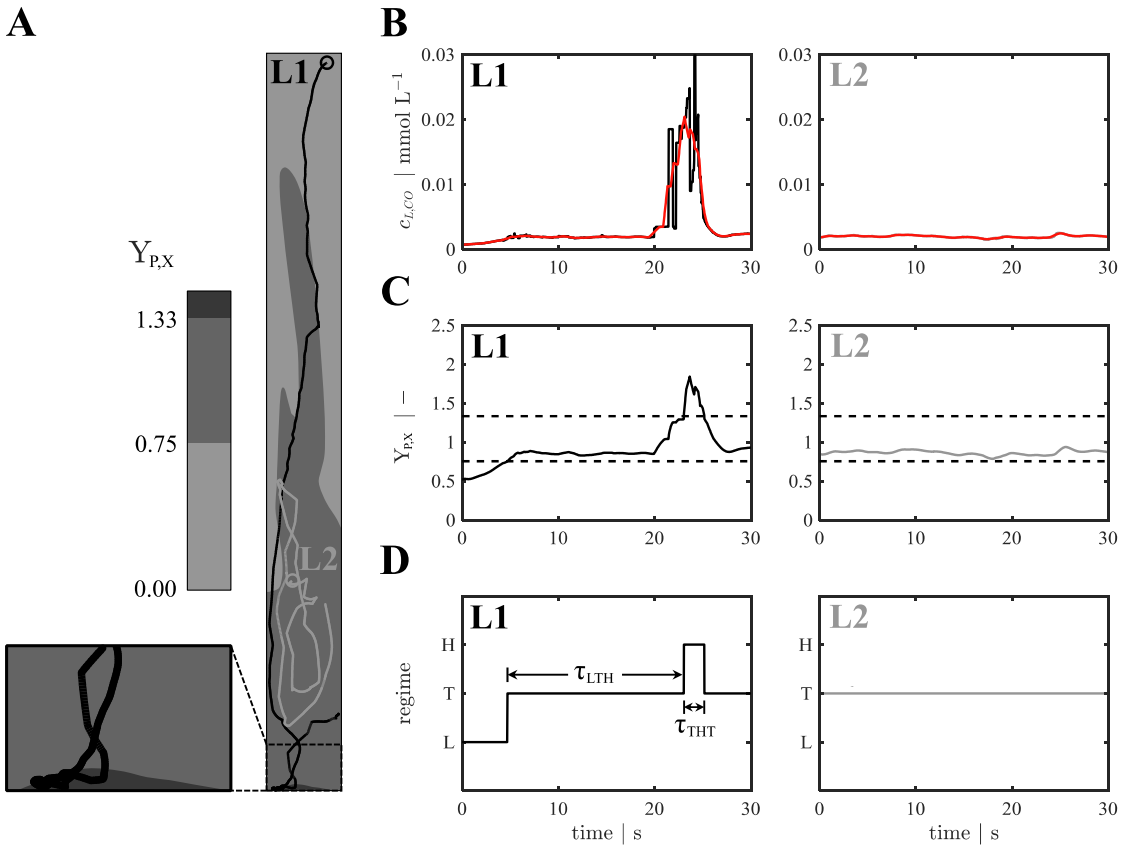

Figure 3.26: Exemplary two 30 s lasting bacterial lifelines L1 (black) and L2 (grey) are shown in spatial resolution in (**A**). The related CO concentration profiles are given in (**B**) also indicating the results of the moving-average filter (red line) (see also Kuschel et al., 2017). Concentrations are translated in uptake rates q_c finally yielding the total product-biomass yield $Y_{P,X}$ presented in (**C**). The black dashed lines indicate the regime transition boundaries which are used to translate the lifelines into regime switch diagrams with transient stays τ of each regime switching event (**D**). The regimes are divided into high (H), transition (T) and low (L) product biomass yields. For lifeline L1 two strategies are shown (LTH and THT) with different durations of stay τ.

Further lifeline processing comprises counting of transition events and grouping with respect to the residence time in the transient regime (**Figure 3.27**). Related values indicating maximum and average time of stays were calculated and listed in **Table 3.13**.

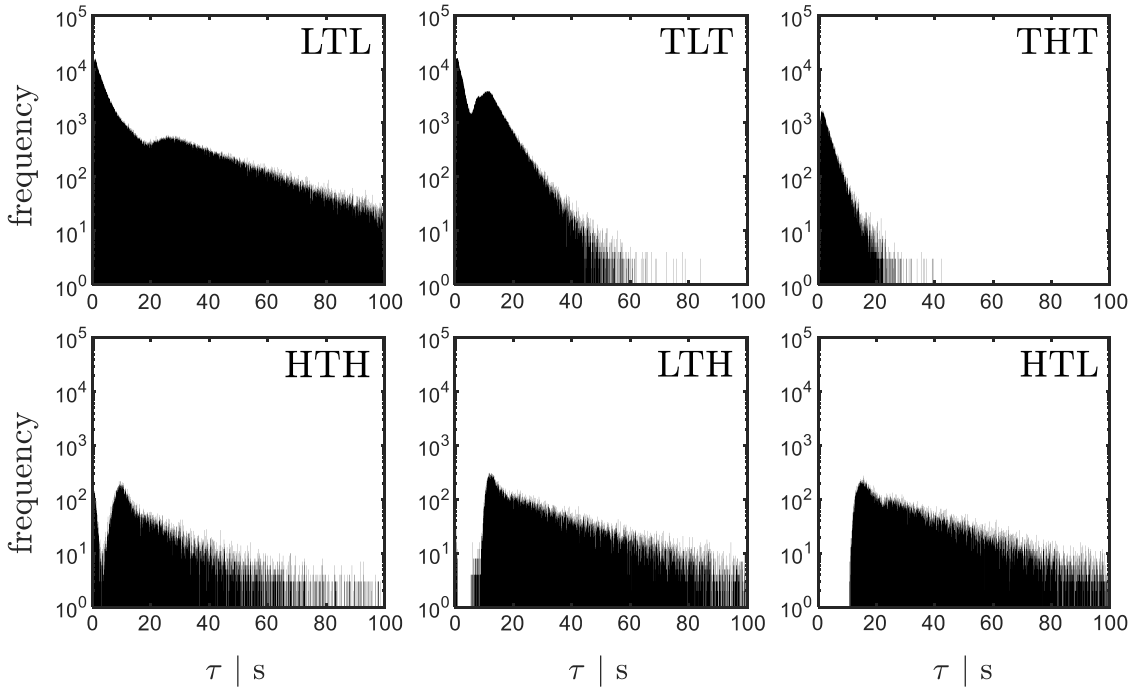

Figure 3.27: The frequency of all six regime transition events are given (log-scale) and plotted against their duration of stay τ in the second (transient) regime. For each histogram 600 bins have been chosen.

Movement patterns from the transition area to low product biomass yields and back (TLT) are the most common transitions with an overall probability of 46.0%. However, the second most likely regime transition LTL happens almost as often with 44.6% (see also **Table 3.13**). All other events have probabilities lower than 4%. As for the average and maximum residence times, very different results can be stated. While the mean dwell times $\bar{\tau}$ ranges from 3.4 s up to 32.8 s the maximum time spans can reach over 100 s for the LTH and HTL pattern. Movements starting in the transition regime and circling back to it (THT and TLT) show the lowest τ_{max} with 15.3 s for THT and 28.4 s for TLT. Movement patterns passing all regimes (LTH and HTL) reveal not only the longest but also a minimum residence time of about 10 s.

Table 3.13: Total frequency, average and maximum retention time. For each regime transition event the total frequency, mean $\bar{\tau}$ and τ_{max} is listed. For τ_{max} a confidence level of 99% was chosen.

Regime transition event	Total frequency in %	$\bar{\tau}$ in s	τ_{max} in s
LTL	44.6	12.1	86.6
TLT	46.0	7.2	28.4
THT	3.6	3.4	15.3
HTH	1.2	17.4	80.4
LTH	2.4	29.6	107.5
HTL	2.2	32.8	109.8

Whereas the total event frequency reflects the volumes encompassed by the related regimes the duration of a stay and how often a transition event occurs depends strongly on the gradient profile and on the flow field. Comparing the most likely events LTL and TLT differences in $\bar{\tau}$ and τ_{max} can be detected revealing relatively low values of $\bar{\tau}$ and τ_{max} for TLT. This can be explained by comparing **Figure 3.25** (**A**) with **Figure 3.26** (**A**), i.e., the flow field with the gradients divided in regimes. The finding that TLT and τ_{max} values are lower than LTL counterparts is in agreement with the higher velocities at the top of the reactor, in particular, close to the wall. They coincide with the low product biomass yield regime anticipating a high turnover of cells passing this zone. Accordingly, the TLT events reveal shorter time spans compared to the LTL although total event frequencies are similar.

The low event frequency of LTH and HTL regime transitions can be explained with the far distance between the high and the low zones (see **Figure 3.26** (**A**)). The bulk of the T compartment has to be passed either to reach the H area at the bottom or to enter the L zone travelling from the bottom. Regarding the flow pattern, such travels require 10 s at least. Hence, transitions are dominated by moderate regime shifts exposing cells from one adjacent regime to the other – and back. ‘Extreme’ shifts are relatively rare summing up to about 5% of all events (LTH + HTL). This finding is in agreement with similar observations of Haringa et al. (2017a) who investigated stirred tanks equipped with Rushton turbines under production-like conditions.

Additionally, the small volume of the H zone is worth noticing. The compartment represents less than 1% of the total bubble column, only. In other words, physical

properties of CO solubility are such poor that only a ‘tiny’ fraction of the bubble column is operating with maximum CO transfer. The majority of the bioreactor works with moderate or even limiting CO supply. Accordingly, putative CO inhibition is only an issue for a small compartment of the bubble column located at the bottom.

Besides the statistical evaluation of regime transitions, also the average circulation time of a bacterium can be estimated by weighting the average residence time of each regime transition event with its overall probability. Accordingly, the average circulation time in the bubble column is estimated as 10.5 s. The value reflects fairly good the estimation of 14.7 s which is derived from the mixing time (see Appendix C: Circulation time). Interesting enough, this is a remarkably low value for industrial type settings of this size. Often, stirred tank bioreactors reveal average circulation times of about 20 s (Haringa et al., 2017a; Kuschel et al., 2017). Noteworthy, such circulation times are found for power inputs of 4185 W/m^3 which is higher than 613 W/m^3 invested in bubble columns. This trend is independent weather simulated or observed power input is used. As a fundamental characteristic, bubble column reactors show good mixing properties due to long axial flow patterns. While stirred tank reactors with Rushton blades predominately reveal radial velocities with typical Eddy formations along the stirrer and hard transitions zones between the vortices. These vortex rolls can cause longer dwelling and therefore equally longer average circulation times.

Investigation of short- and long-term responses

The statistical evaluation of the Lagrange trajectories offers insight about the possible short- and long-term responses bacterial cells may show after proper induction. For this reason, two critical values have been chosen with respect to the concentration threshold and duration. Taking findings of *E. coli* as a reference, the short-term metabolic responses of *C. ljungdahlii* is expected to be triggered as soon as a critical CO value, namely the equivalence of starting maintenance demands, will be reached. In other words, when the dissolved CO concentration falls below 0.003 mmol L^{-1} the short-term response is assumed to be switched ‘on’. Because its translation in transcriptional and translational reprogramming requires time, different residence times of continuing stimulus were investigated: τ^{crit} = 10 s, τ^{crit} = 40 s and τ^{crit} = 70 s.

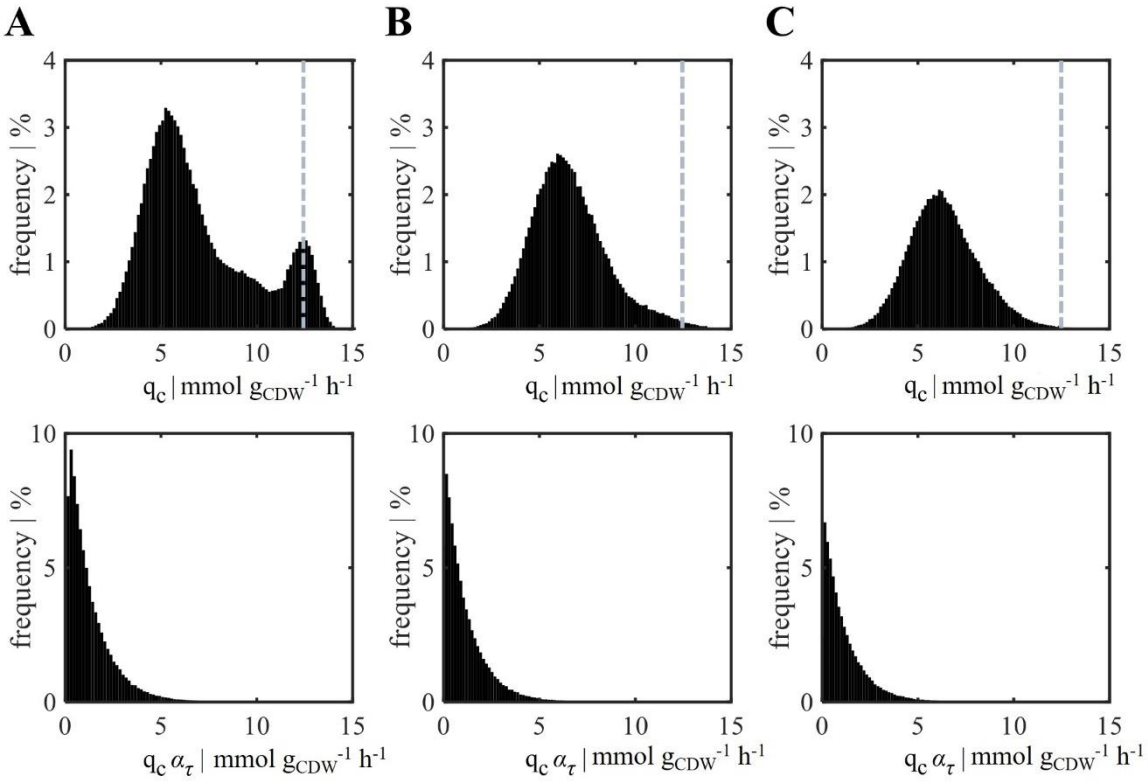

Figure 3.28: Expected bacterial responses while experiencing limitation for different exposure periods. Three critical periods τ^{crit} = 10 s in (**A**), τ^{crit}= 40 s in (**B**) and τ^{crit}= 70 s in (**C**) have been chosen to show the distribution of uptake rates (first row) and the weighted distribution by actual duration τ_i indicated by the case-specific weighting factor $\alpha_{\tau i}$ (second row). Histograms are normalized to the highest total percentage of the average occurrence (τ^{crit}= 10 s) and divided into 100 bins**.** The average uptake rate q_c = 12.26 mmol g_{CDW}^{-1} h^{-1} is indicated as a grey dotted line.

Figure 3.28 (**A**) to (**B**) depicts the results of the three stress exposure periods and **Figure 3.29** shows the distribution of cell fractions which are exposed to the CO stress stimulus for different residence times. The statistics of τ^{crit} = 10 s include τ^{crit} = 40 s and τ^{crit}= 70 s which is indicated in **Figure 3.28** and more clearly illustrated in **Figure 3.29**.

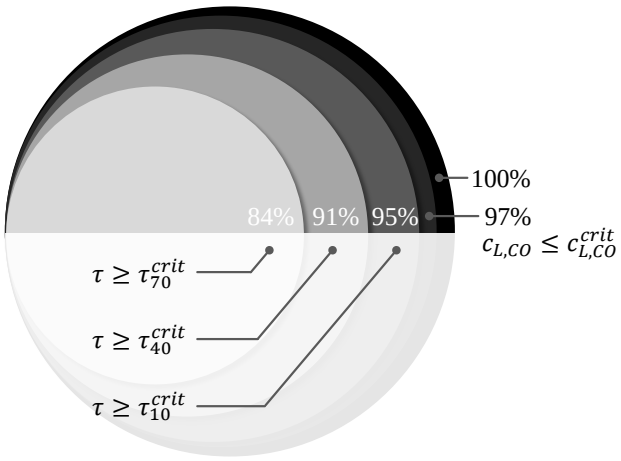

Figure 3.29: Distribution of cells exposed to CO stimuli with respect to different resting periods. Black indicates all cell of which (in dark grey) 97% experienced the critical value $\boldsymbol{c_{L,CO}^{crit}}$ = 0.003 mmol L^{-1}. The other grey colours indicate the cell fractions thereof which stayed in the stress zones with the exposure times as indicated.

According to **Figure 3.28**, the cellular population in the bubble column is not homogenous but heterogeneous instead. Short residence times of 10 s show a bimodal distribution (**Figure 3.28** (**A**)). Because carbon uptake rates directly correlate with product formation a bimodal distribution of production zones can be expected in this area, too. Additionally, the normalization by residence time indicates very short retention in high concentration areas which concludes with the finding for the THT event (**Table 3.13** with $\bar{\tau}_{THT}$= 3.4 s). However, longer exposure periods are somewhat homogenous, revealing unimodal distribution (**Figure 3.28** (**B**) and (**C**)). All three critical time periods statistics deviate strongly from the average uptake rate q_c = 12.26 mmol g_{CDW}^{-1} h^{-1} (**Figure 3.28** grey dotted line) which indicates that substrate limitation and time-dependent bacterial adaption will have a major negative effect on the overall production of this fermentation process.

From the biological perspective, the most striking observation is that about 97% of all bacteria experienced severe CO limitation at least once ($c_{L,CO}$< $c_{L,CO}^{crit}$). As indicated in **Figure 3.29**, 95% are likely to show immediate metabolic changes (exposure time 10 s) and even 84% stay in the CO limitation zone longer than 70 s. Taking the *E. coli* case as a reference, 70 s exposure time marks the beginning of transcriptional changes (Löffler et al., 2016). Cells are expected to react on external CO limitation by inducing starvation programs which coincide with severe up- and down-regulation of

related genes. In *E. coli*, such transcriptional adaptations could be quantified with respect to additional ATP demands revealing add-on maintenance needs of 15% – 50% depending on the stimulus. By analogy, similar add-on maintenance demands should be expected for *C. ljungdahlii* as well. Reductions of the product biomass yields and the growth rate are fairly probable. Nevertheless, it needs to be stressed that related experimental scale-up studies with *C. ljungdahlii* are simply missing. These are essential to proof the simulation results of the current work.

CONCLUSION

Lagrangian trajectories for *Clostridium ljungdahlii* have been successfully calculated enabling the lifeline analysis in an anaerobic, synthesis gas operated bubble column. Through the eyes of *C. ljungdahlii* the impacts of a pseudo-stationary carbon monoxide gas gradient were recorded with respect to short- and long-term CO stimuli.

Hydrodynamic analysis reveals a well-mixed bubble column showing average circulation times of about 10 s. The value is comparable to conventional stirred tank bioreactors but achieved with less power input. Defining CO-induced thresholds for triggering the short- and long-term response of the cells enabled the bubble column division into the H, T and L zones and – most important – the identification of related transition events. Although most of the transitions may be qualified as ‘moderate’, because they only consider shifts between adjacent regimes, they indicate transitions under already CO limiting conditions. In other words, most of the bioreactor is suffering CO supply which outlines the need to improve CO mass transfer and/or to engineer strains that cope with the conditions with the least add-on ATP demand. Given that calculated gradients will be much more pronounced with higher biomass concentrations and more active cells, the need to perform such engineering studies is apparent for further process intensification.

The lifeline analysis depends on the proper prediction of physical and biological impacts. The first requires accurate models for simulating e.g. local energy dissipation rates, mass transfer and flow fields. In particular, multiphase conditions are still very challenging requiring ongoing improvements for accurately predicting local energy

dissipation and for providing good estimations of bubble size distributions, breakage and coalescence. Fundamental research is necessary to derive related models also considering particularities of biotechnical application (e.g., media compositions). Intrinsically, said studies provide ‘snap-shots’ on fermentation performance. Thorough experimental and simulation studies are necessary for statistically evaluating their reliability further.

From the biological perspective, the study depends on the real stress response of *C. ljungdahlii* which – unfortunately – has not been investigated experimentally so far. Related results will surely improve our understanding of large-scale processes using the tool of lifeline analysis as a very promising design and optimization approach.

ACKNOWLEDGMENTS

At this point, we want to thank Maike Kuschel, Andreas Ulmer and Julia Zieringer for their inspiring discussion and support during the simulation process. This work was supported by the Federal Ministry of Education and Research (BMBF; FKZ031A468B).

AUTHOR CONTRIBUTIONS

Prof. Dr.-Ing. Ralf Takors and Dr. Alexei Lapin advised the study while Maria Hermann provided the experimental uptake and production rates. Simulation, evaluation, and writing of the manuscript was conducted by Flora Siebler.

DECLARATION OF COMPETING INTEREST

The authors have declared no conflicts of interest.

APPENDIX

The Supplementary Material for this article can be found in the original publication.

REFERENCES

See 6 references.

4 Discussion and Outlook

For the engineering of recombinant *C. ljungdahlii* strains that are autotrophically able to produce high-value biocommodities, it is necessary to quantitively characterize its metabolic pathways and energy conservation system. Therefore, in the framework of this thesis, combined approaches between controlled bioreactor experiments, metabolic engineering strategies, metabolic modelling and modelling tools for large-scale reactors systems were applied.

First, growth, product formation as well as energy and redox metabolism of the *C. ljungdahlii* wildtype strain, was analysed in dependence on different substrate conditions. Secondly, recombinant autotrophic isobutanol formation was investigated and realized. Finally, it was demonstrated how scale-up risks may be reduced by the combination between experimental results and mathematical modelling of large-scale bioreactors.

In the following sections, the main findings of this thesis are discussed across the single manuscripts and provided with a scientific outlook.

4.1 Substrate-defined product formation in *C. ljungdahlii* during autotrophic cultivation

Autotrophic product formation of *C. ljungdahlii* may significantly differ depending on the cultivation conditions. Relevant influence factors are cultivation mode, pH value, pressure and substrate composition as summarized in **2.1.3.** Under autotrophic conditions *C. ljungdahlii* mainly produces acetate and ethanol (see **Table 2.1**). However, it is also natively endowed to produce 2,3-butanediol (2,3-BD) and lactate. To shift the product pattern towards the reduced products ethanol and 2,3-BD different strategies were investigated. For one thing, alcohol formation may be favoured by introducing solventogenesis through a pH-shift or due to nutrient limitations (Abubackar et al., 2012; Martin et al., 2016; Richter et al., 2016; Richter et al., 2013). A further important influencing factor is the substrate gas composition, especially the choice of the electron source (CO or H_2). Phillips et al. (1994) compared autotrophic growth and product formation of *C. ljungdahlii* grown on CO or a mixture of CO_2 and

H_2, demonstrating a doubled growth rate and a higher ethanol-to-acetate ratio using CO. These results were further confirmed by Zhu et al. (2020). They showed superior growth rates and the formation of more electron-dense products with CO compared to H_2 and CO_2. In this context, we further analysed autotrophic product formation, intracellular carbon fluxes and energy metabolism of *C. ljungdahlii* under varying substrate conditions during controlled batch cultivations (see manuscript I, **3.2**). It was demonstrated that the energy source (H_2 or CO) is the key determinant for the product spectrum of autotrophically grown *C. ljungdahlii.* Applying CO as the sole substrate doubled growth rate, highest ATP formation rate and highest amounts of more-reduced products were realized. Whereas cultivation of *C. ljungdahlii* on H_2/CO_2 yielded almost exclusively the production of acetate (approx. 9 g L^{-1}), with CO mainly ethanol (approx. 5 g L^{-1}) and 2,3-BD (approx. 2 g L^{-1}) were produced. This is because, for one thing, CO is characterized by a superior gas-liquid mass transfer with Henry's law constants of 7.40 – 9.90 mM atm^{-1} compared to 0.78 mM atm^{-1} in case of H_2 (Sander, 1999). In addition, CO is thermodynamically favourable as its oxidation provide more Gibbs free energy to the cell compared to H_2. Furthermore, we identified electron availability realized by Fd_{red} provision as a crucial key parameter for the autotrophic product spectrum of *C. ljungdahlii*, due to the interplay between its redox metabolism, ATP synthesis, growth, and by-product formation. Applying CO, Fd_{red} metabolism by CODH, Rnf and Nfn complexes lead to NADH and NADPH provision that cannot be solely balanced by biomass and acetate formation. The resulting surplus of reducing equivalents yield the increased formation of ethanol and 2,3-BD. In contrast, Fd_{red} metabolism with H_2 via Hyd, formate dehydrogenase (FDH) and Nfn complex results in a redox phenotype that is fully equilibrated by biomass formation and the methyl branch activity with final acetate production (see manuscript I, **3.2**).

A further refinement of the product spectrum is possible through a mixed utilisation of H_2 and CO as energy sources. As demonstrated in manuscripts I and III (**3.2** and **3.4**), clearly more 2,3-BD (approx. 4 g L^{-1}) and ethanol (approx. 6 g L^{-1}) is produced by *C. ljungdahlii* culturing on syngas compared to the sole usage of CO as an energy source. This is due to the combined provision of Fd_{red} by Hyd and CODH yielding more reducing power for anabolic reactions and product formation (see manuscript I, **3.2**).

In addition, the H_2 supply enables *C. ljungdahlii* to adapt simultaneous CO_2 reduction flexibly to NADPH needs (see manuscript III, **3.4**). In our study, we have only seen a very low H_2 consumption besides a predominantly CO uptake. Numerous publications report a simultaneous and more equilibrated utilisation of H_2 and CO by acetogens that cause a clearly different product pattern compared to our results (Jack et al., 2019; Martin et al., 2016; Oswald et al., 2016; Richter et al., 2016; Richter et al., 2013; Valgepea et al., 2018; Valgepea et al., 2017b). Here, cultivation mode and the applied H_2/CO ratio represent important control variables.

Batch processes are often characterized by CO-excess and therefore only allow for a limited co-utilisation of H_2 and CO due to the CO-inhibition of acetogenic hydrogenases (Bertsch and Müller, 2015; Goldet et al., 2009; Wang et al., 2013; Younesi et al., 2005). Nevertheless, it applies to batch processes that increasing H_2/CO ratios lead to an increasing shift to acetate formation. Whereas with decreasing H_2/CO ratios the formation of more electron-dense products is favoured (Jack et al., 2019). We applied the H_2/CO ratio of 0.54 yielding acetate/ethanol/2,3 – BD ratios of 1.0/15.6/11.7 (see manuscript 1, **3.2**) and 1.0/15.5/9.1 (see manuscript III, **3.4**). Comparable to our cultivation mode, Oswald et al. (2016) performed controlled bioreactor batch processes with continuous syngas supply characterized by the H_2/CO ratio of 1.0. They reported a product spectrum containing acetate and ethanol in a ratio of 1.0/0.1 with no 2,3-BD production.

In contrast, H_2 supplementation to CO-limited continuous syngas cultivations improves the efficiency of ethanol production with the decreased loss of carbon into by-products. Using additional H_2 supply, the acetate/ethanol ratio of syngas-grown *C. autoethanogenum* was shifted from approx. 1 to approx. 0.2. However, in this study, H_2 supplementation did not result in 2,3-BD formation (Valgepea et al., 2018).

Therefore, CO-rich syngas batch fermentation with a low H_2/CO ratio should be applied for optimized 2,3-BD formation. Pressured-systems should be further investigated i to increase H_2-uptake despite low H_2/CO ratios and therefore provide more reducing power for alcohol formation.

In addition, CO_2 may influence H_2 and CO uptake - and thus electron provision during gas fermentations - as it is a reactant in both the hydrogenase-formate dehydrogenase

(Hyd-FDH) complex as well as the CODH reaction. Hence, studies on different CO_2 portions in syngas blends could provide further valuable results regarding autotrophic product formation of *C. ljungdahlii.*

4.2 Recombinant autotrophic isobutanol formation with *C. ljungdahlii*

According to our knowledge, the first reported syngas-based recombinant isobutanol formation with *C. ljungdahlii* was achieved applying a combined approach between metabolic engineering, lab-scale and bioreactor experiments as well as modelling-based intracellular carbon flux investigation via FBA (see manuscript II and III, **3.3** and **3.4**). In this context, plasmid-based amplification of the native carbon flux from pyruvate to KIV and additional recombinant incorporation of KivD from *Lactococcus lactis* and Adh from *Corynebacterium glutamicum* was proved to be a suitable metabolic engineering approach. This was realized in the recombinant strain *C. ljungdahlii* [pKAIA]. Since the Ehrlich pathway is based on valine biosynthesis, heterologous isobutanol formation employing this pathway was already achieved in several other microorganisms (Atsumi et al., 2008; Blombach et al., 2011; Li et al., 2012). However, carbohydrates were predominantly used as carbon sources. *C. ljungdahlii* [pKAIA] produced autotrophically low amounts of isobutanol both during batch cultivation in serum bottles (7 mg L^{-1}) and during controlled batch cultivation in a stirred tank bioreactor with continuous syngas supply (20 mg L^{-1}). Compared to the wildtype, isobutanol production goes along with a slightly increased H_2 uptake allowing higher intracellular NADPH provision through flexible adaptation of CO_2 reduction by the interplay of FDH, Hyd and the Nfn and Rnf complex (see manuscript III, **3.4**). However, besides recombinant isobutanol formation, *C. ljungdahlii* [pKAIA] showed faster growth and strongly enhanced native valine production compared to the wildtype. In addition, pyruvate and KIV were identified as limiting precursors for isobutanol formation due to very low intracellular pools and additional strong depletion during cultivation. Hence, a further mutant with blocked valine biosynthesis was generated (*C. ljungdahlii::ilvE* [pKAIA]) to increase carbon flux from KIV and pyruvate to isobutanol instead of valine.

Thus, isobutanol formation was increased 6.5-fold (130 mg L^{-1}). Based on FBA applying the respective experimentally derived reaction rates, energy limitation in isobutanol producing *C. ljungdahlii* strains did not prevail. However, an NADPH limitation was identified. Aklujkar et al. (2017) also demonstrated a potential limitation of NADPH during the lithotrophic growth of *C. ljungdahlii*. Since isobutanol formation in *C. ljungdahlii* [pKAIA] and *C. ljungdahlii::ilvE* [pKAIA] depends on NADPH, a further recombinant strain was generated (*C. ljungdahlii:ilvE* [pKAI$_{NADH}$A]). In contrast to the previous strains, *C. ljungdahlii:ilvE* [pKAI$_{NADH}$A] is characterized by an NADH-dependent ketol-acid reductoisomerase (IlvC) reaction. This genetic modification yields an 18 % increase in isobutanol formation during heterotrophic growth with KIV supplementation compared to the respective cultivation of *C. ljungdahlii::ilvE* [pKAIA] (Weitz, 2020). However, by means of autotrophic lab-scale experiments in serum bottles, that were characterized by changing pH value during the cultivation and an H_2/CO ratio of 0.9, no increase of isobutanol production could be shown. Nevertheless, further analysis of this strain in controlled, continuously gassed stirred-tank bioreactor studies with constant pH and an H_2/CO of 0.54 should be performed. In this manner, product formation of *C. ljungdahlii:ilvE* [pKAI$_{NADH}$A]) would be tested with identical conditions as the previous recombinant strains. Changes in pH-value may be crucial due to the pH-sensitivity of KivD activity. The pH optimum of KivD is 6.5, at a pH value of 5.7, the enzyme shows 50 % activity and only approx. 10% at a pH value below 5 (de la Plaza et al., 2004). Moreover, bioreactor studies would allow modelling-based subsequent interpretation of the experimentally derived rates by FBA and thus give additional hints on further metabolic engineering targets. In this context, the metabolic model rSMM should be extended by an NADH-dependent alcohol dehydrogenase reaction for the conversion of isobutyraldehyde to isobutanol to better reflect the real physiological conditions. So far, isobutanol formation in rSMM is modelled via a NADPH dependent alcohol dehydrogenase reaction. However, cofactor dependency of alcohol dehydrogenases may strongly vary in different organisms (Atsumi et al., 2010; Smith et al., 2010).

In addition, the autotrophic isobutanol formation of *C. ljungdahlii* may be improved by the elimination of other by-products to reduce carbon flux to non-wanted metabolites.

Atsumi et al. (2008) and Blombach et al. (2011) substantially increased heterologous isobutanol production by blocking multiple by-product routes. In *C. ljungdahlii,* 2,3-BD represents a promising target for by-product elimination, as it relies on pyruvate as a precursor as well as isobutanol. A recombinant *C. ljungdahlii* strain with blocked acetolactate decarboxylase activity, representing the first step in 2,3-BD formation, could be successfully generated. However, it was not possible to transform this strain with pKAIA using ClosTron^{TM}. In this regard, CRISPR-Cas systems for strain engineering should be tested (Huang et al., 2016; Woolston et al., 2018; Zhao et al., 2019).

4.3 Modelling-supported bioprocess development

Regarding bioprocess development with *C. ljungdahlii* for the syngas-based production of reduced high-value biocommodities, this thesis aimed to investigate its energy and redox management. For this purpose, bioreactor experiments were complementarily supplemented by a metabolic model containing 117 intracellular and 46 transport reactions, thereby balancing 180 metabolites (see manuscript I, **3.2**). By grouping biosynthetic pathways for the synthesis of glycerophospholipids, cell wall, DNA, and nucleotides, we succeeded in creating a reduced stoichiometric metabolic model (rSMM), that was nevertheless capable of reflecting experimentally results very well. The comparison between simulated growth rates μ_{sim} with experimentally observed growth rates μ_{exp} by linear regression revealed a high correlation coefficient $R^2 \geq 0.9944$ (see manuscript I, **3.2**). However, previously described stoichiometric metabolic models of acetogenic bacteria contain a significantly larger number of reactions to balance a clearly higher number of metabolites (see **Table 2.2**). By means of flux balance analysis (FBA), using experimentally derived substrate uptake and product formation rates, we identified intracellular Fd_{red} provision influencing electron availability as the key determinant for variable extracellular phenotypes on different substrate conditions. Consuming CO, Fd_{red} is provided by the CODH reaction and subsequently used to convert NAD^+ to NADH via the Rnf complex. NADH combined with Fd_{red} is then needed to regenerate NADPH via the Nfn complex. The consequent

use of NADPH and NADH enables *C. ljungdahlii,* in this case, to mainly produce ethanol and 2,3-BD, as well as small amounts of acetate and lactate. In the H_2 case, Fd_{red} is provided by means of the hydrogenase (Hyd) reaction with the simultaneous conversion of $NADP^+$ to NADPH. Fd_{red} is again used for NADH regeneration by the Rnf complex. In this case, applying the methyl branch combined with the Nfn complex as the consumption route for NADPH and NADH, *C. ljungdahlii* is metabolically driven to only produce acetate.

Thus far, our rSMM allows to interpret experimental results and predict intracellular carbon flux, ATP synthesis, and the link between redox balance and product formation when specifying substrate uptake and product secretion rates. Unfortunately, it is not yet possible to predict growth phenotypes with realistic product formation by only defining substrate uptake rates. This is because our model is strongly underdetermined. Its degree of freedom clearly exceeds quantifiable substrate uptake rates (see manuscript 1, **3.2**). Confining the solution space can be realized by coupling of the carbon and redox metabolisms as hypothesized by Valgepea et al. (2017b). In addition, different omics data can be overlaid on rSMM to enable a more accurate prediction of real phenotypes. Dash et al. (2016) summarizes numerous methods that can be used for this purpose. Furthermore, rSMM can be linked to mechanistic kinetic models that employ enzyme kinetics to describe biochemical reactions. By this, dynamic simulation of substrate utilisation as well as metabolite formations in the course of the fermentation could be performed (Dash et al., 2016).

Moreover, ATP maintenance costs in rSMM are described by a constant growth-associated value (GAM) of 46.7 $mmol_{ATP}$ $(g_{CDW})^{-1}$ (Nagarajan et al., 2013) as well as a non-growth-associated maintenance (NGAM) set to 5 $mmol_{ATP}$ $(g_{CDW}*h)^{-1}$. The latter value reflects well the mean maintenance cost identified for the closely related acetogen *C. autoethanogenum* on CO, syngas, and CO_2 + H_2 (Heffernan et al., 2020; Valgepea et al., 2018). However, Valgepea et al. (2017b) demonstrated that ATP maintenance costs in *C. autoethanogenum* are not constant. Applying FBA with ATP dissipation fluxes, used as an objective function, they showed increasing cellular maintenance with increasing biomass concentration. In addition, ATP maintenance

costs of *C. autoethanogenum* are substrate specific (Valgepea et al., 2018; Valgepea et al., 2017a; Valgepea et al., 2017b).

For a more accurate representation of the metabolism, rSMM could be expanded by species- and substrate-specific NGAM and GAM values. Therefore, continuous culture experiments must be employed, as demonstrated by Norman et al. (2019) for CO-grown *C. autoethanogenum*. However, this represents a time- and cost-consuming solution, in particular due to very low growth rates of acetogens compared to aerobic bacteria. Alternatively, a two-step FBA approach could be used by first optimizing the ATP dissipation flux prior to predicting 'maximum growth' phenotypes (Valgepea et al., 2017b).

In the context of a successful bioprocess development, process transfer into large-scale reactors (scale-up) also plays a crucial role. In particular, possible microbial performance losses due to large-scale production conditions must be taken into account (Takors, 2012). Pressure differences between the bottom and head regions of large-scale bioreactors yield variable gas solubilities in the bioreactor, and consequently, vertical gas substrate gradients occur in the case of syngas fermentation. This inhomogeneous distribution of substrate components in the bioreactor is reinforced by microbial substrate consumption resulting in additional radial gradients. Through this, cells fluctuating in large-scale bioreactors experience micro changes in substrate conditions that can affect cellular growth and product formation. For risk minimization, to prevent unwanted performance losses, large-scale substrate profiles as well as affected cell behaviour can be predicted before scale-up activities, applying different modelling tools (Takors, 2012).
In this regard, genome-scale metabolic models can be combined with a mathematical representation of large-scale bioreactors to gain valuable insight into bacterial behaviour when exposed to large-scale conditions (Chen et al., 2015; Gomez et al., 2014). For the same purpose, kinetic correlations in combination with computational fluid dynamics (CFD) can be used (Siebler, 2020). Based on the experimental results described in manuscript I (**3.2**), a kinetic correlation model was formulated that, in turn, was integrated into a 1-dimensional (1D) model characterizing a 125 m^3 bubble column reactor. In combination with CFD, the effect of large-scale bubble column CO

fermentation on *C. ljungdahlii*'s behaviour was finally analysed (see manuscript IV, **3.5**). Prior to this, bubble column reactors were assessed as one of the most suitable reactor designs for syngas fermentations based on a ranking system evaluating reactor performance and scale-up costs (Siebler, 2020). This reactor type implies low operation costs and yet enables high gas solubility due to its slim design yielding high hydrostatic pressure. Statistical lifeline analysis revealed that 97% of all cells faced CO limitations probably leading to transcriptional changes in 84% of the cells. Consequently, for example, CO mass transfer should be improved by applying elevated operating pressure or elongated gas-liquid contact times. The latter could be achieved by partially recycling the unconsumed gas (Chen et al., 2015).

So far, the approach described in manuscript IV (**3.5**) is only limited to CO conversion. In future works, the underlying kinetic correlation could be adapted for H_2 and CO_2 conversion and even extended to a multi-substrate kinetic for syngas cultivations. Applying these different substrate conditions and further process alterations (e.g. substrate recycling) could be simulated, investigated, and evaluated for scale-up purposes

5 Conclusion

With respect to gas fermentation bioprocesses with *C. ljungdahlii*, feed gas composition represents a crucial parameter for autotrophic growth and by-product formation. Applying CO as an energy source, high growth rates, ATP provision, and reduced by-product formation can be reached. On the contrary, feed gases containing H_2 as energy and CO_2 as a carbon source, mainly yield acetate production with lower growth and ATP formation rates. Using H_2 supplementation during CO-rich syngas cultivation, the formation of NADPH-dense products can be further increased. However, cultivation mode and CO/H_2-ratio are important control variables here. Applying a batch process with CO excess and a low H_2/CO ratio highest 2,3-BD formation can be realized.

The first recombinant autotrophic isobutanol formation with *C. ljungdahlii* was demonstrated with the same cultivation setup. In this context, intracellular availability of pyruvate and KIV were identified as carbon bottlenecks for high-value alcohol formation. Subsequently, strengthening the carbon flux through the recombinant pathway and eliminating the competitive valine formation yield a 6.5-fold increase in isobutanol production. Furthermore, an increase in intracellular NADPH availability and the elimination of the competitive 2,3-BD- formation should be investigated for superior syngas-based isobutanol formation with *C. ljungdahlii*.

Moreover, it was shown that mathematical modelling provides a suitable complementary tool to experimentation for understanding, predicting, and optimizing syngas fermentation processes. On the one hand, FBA, based on experimentally derived data, confirmed the interplay between ATP synthesis, redox metabolism, and carbon balance. In addition, important intracellular key-determinants, and bottlenecks for electron availability, as well as reduced by-product formation were identified. On the other hand, combining a kinetic correlation model with CFD allowed the prediction of *C. ljungdahlii*'s CO metabolism in a 125 m^3 bubble column reactor. Through this, it was revealed that 97% of all cells would face CO limitations, probably leading to transcriptional changes in most of the cells. This points to CO mass transfer as a key parameter in large-scale bioreactors.

6 References

Abubackar, H.N., Veiga, M.C., Kennes, C., 2011. Biological conversion of carbon monoxide: rich syngas or waste gases to bioethanol. Biofuels, Bioprod. Bioref. 5, 93–114. https://doi.org/10.1002/bbb.256.

Abubackar, H.N., Veiga, M.C., Kennes, C., 2012. Biological conversion of carbon monoxide to ethanol: effect of pH, gas pressure, reducing agent and yeast extract. Bioresource technology 114, 518–522. https://doi.org/10.1016/j.biortech.2012.03.027.

Akita, K., Yoshida, F., 1973. Gas Holdup and Volumetric Mass Transfer Coefficient in Bubble Columns. Effects of Liquid Properties. Ind. Eng. Chem. Proc. Des. Dev. 12, 76–80. https://doi.org/10.1021/i260045a015.

Aklujkar, M., Leang, C., Shrestha, P.M., Shrestha, M., Lovley, D.R., 2017. Transcriptomic profiles of Clostridium ljungdahlii during lithotrophic growth with syngas or H2 and CO2 compared to organotrophic growth with fructose. Scientific reports 7, 13135. https://doi.org/10.1038/s41598-017-12712-w.

Al-Bassam, M.M., Kim, J.-N., Zaramela, L.S., Kellman, B.P., Zuniga, C., Wozniak, J.M., Gonzalez, D.J., Zengler, K., 2018. Optimization of carbon and energy utilization through differential translational efficiency. Nature communications 9, 4474. https://doi.org/10.1038/s41467-018-06993-6.

Alberty, R.A., 1998. Calculation of standard transformed Gibbs energies and standard transformed enthalpies of biochemical reactants. Archives of biochemistry and biophysics 353, 116–130. https://doi.org/10.1006/abbi.1998.0638.

Alves, S.S., Maia, C.I., Vasconcelos, J., 2004. Gas-liquid mass transfer coefficient in stirred tanks interpreted through bubble contamination kinetics. Chemical Engineering and Processing: Process Intensification 43, 823–830. https://doi.org/10.1016/S0255-2701(03)00100-4.

Antal, S.P., Lahey, R.T., Flaherty, J.E., 1991. Analysis of phase distribution in fully developed laminar bubbly two-phase flow. International Journal of Multiphase Flow 17, 635–652. https://doi.org/10.1016/0301-9322(91)90029-3.

Atsumi, S., Hanai, T., Liao, J.C., 2008. Non-fermentative pathways for synthesis of branched-chain higher alcohols as biofuels. Nature 451, 86–89. https://doi.org/10.1038/nature06450.

Atsumi, S., Wu, T.-Y., Eckl, E.-M., Hawkins, S.D., Buelter, T., Liao, J.C., 2010. Engineering the isobutanol biosynthetic pathway in Escherichia coli by comparison of three aldehyde

reductase/alcohol dehydrogenase genes. Appl Microbiol Biotechnol 85, 651–657. https://doi.org/10.1007/s00253-009-2085-6.

Balch, W.E., Schobert, S., Tanner, R.S., WOLFE, R.S., 1977. Acetobacterium, a New Genus of Hydrogen-Oxidizing, Carbon Dioxide-Reducing, Anaerobic Bacteria. International Journal of Systematic Bacteriology 27, 355–361.

Banerjee, A., Leang, C., Ueki, T., Nevin, K.P., Lovley, D.R., 2014. Lactose-inducible system for metabolic engineering of Clostridium ljungdahlii. Appl. Environ. Microbiol. 80, 2410–2416. https://doi.org/10.1128/AEM.03666-13.

Barik, S., Prieto, S., Harrison, S.B., Clausen, E.C., Gaddy, J.L., 1988. Biological production of alcohols from coal through indirect liquefaction. Appl Biochem Biotechnol 18, 363–378. https://doi.org/10.1007/BF02930840.

Benevenuti, C., Amaral, P., Ferreira, T., Seidl, P., 2021. Impacts of Syngas Composition on Anaerobic Fermentation. Reactions 2, 391–407. https://doi.org/10.3390/reactions2040025.

Bengelsdorf, F.R., Dürre, P., 2017. Gas fermentation for commodity chemicals and fuels. Microbial biotechnology 10, 1167–1170. https://doi.org/10.1111/1751-7915.12763.

Bengelsdorf, F.R., Poehlein, A., Linder, S., Erz, C., Hummel, T., Hoffmeister, S., Daniel, R., Dürre, P., 2016. Industrial Acetogenic Biocatalysts: A Comparative Metabolic and Genomic Analysis. Frontiers in microbiology 7, 1036. https://doi.org/10.3389/fmicb.2016.01036.

Bertsch, J., Müller, V., 2015. Bioenergetic constraints for conversion of syngas to biofuels in acetogenic bacteria. Biotechnology for biofuels 8, 210. https://doi.org/10.1186/s13068-015-0393-x.

Black, W.B., Zhang, L., Kamoku, C., Liao, J.C., Li, H., 2018. Rearrangement of Coenzyme A-Acylated Carbon Chain Enables Synthesis of Isobutanol via a Novel Pathway in Ralstonia eutropha. ACS synthetic biology 7, 794–800. https://doi.org/10.1021/acssynbio.7b00409.

Blombach, B., Riester, T., Wieschalka, S., Ziert, C., Youn, J.-W., Wendisch, V.F., Eikmanns, B.J., 2011. Corynebacterium glutamicum tailored for efficient isobutanol production. Appl. Environ. Microbiol. 77, 3300–3310. https://doi.org/10.1128/AEM.02972-10.

Brigham, C., 2019. Perspectives for the biotechnological production of biofuels from CO2 and H2 using Ralstonia eutropha and other 'Knallgas' bacteria. Appl Microbiol Biotechnol 103, 2113–2120. https://doi.org/10.1007/s00253-019-09636-y.

Brinkmann-Chen, S., Flock, T., Cahn, J.K.B., Snow, C.D., Brustad, E.M., McIntosh, J.A., Meinhold, P., Zhang, L., Arnold, F.H., 2013. General approach to reversing ketol-acid reductoisomerase cofactor dependence from NADPH to NADH. Proceedings of the

National Academy of Sciences 110, 10946–10951. https://doi.org/10.1073/pnas.1306073110.

Buckel, W., Thauer, R.K., 2013. Energy conservation via electron bifurcating ferredoxin reduction and proton/Na(+) translocating ferredoxin oxidation. Biochimica et biophysica acta 1827, 94–113. https://doi.org/10.1016/j.bbabio.2012.07.002.

Burns, A.D., Frank, T., Hamill, I. Shi, J.M. (Eds.), 2004. The Favre averaged drag model for turbulent dispersion in Eulerian multi-phase flows. ICMF, 1-17.

Chapman, A.G., Fall, L., Atkinson, D.E., 1971. Adenylate energy charge in Escherichia coli during growth and starvation. J. Bacteriol. 108, 1072–1086.

Chen, C.-T., Liao, J.C., 2016. Frontiers in microbial 1-butanol and isobutanol production. FEMS microbiology letters 363, fnw020. https://doi.org/10.1093/femsle/fnw020.

Chen, J., Gomez, J.A., Höffner, K., Barton, P.I., Henson, M.A., 2015. Metabolic modeling of synthesis gas fermentation in bubble column reactors. Biotechnology for biofuels 8, 89. https://doi.org/10.1186/s13068-015-0272-5.

Clift, R., Grace, J.R., Weber, M.E., 2013. Bubbles, drops, and particles. Dover Publ, Mineola, NY, 381 pp.

Cotter, J.L., Chinn, M.S., Grunden, A.M., 2009. Ethanol and acetate production by Clostridium ljungdahlii and Clostridium autoethanogenum using resting cells. Bioprocess and biosystems engineering 32, 369–380. https://doi.org/10.1007/s00449-008-0256-y.

Daniell, J., Köpke, M., Simpson, S., 2012. Commercial Biomass Syngas Fermentation. Energies 5, 5372–5417. https://doi.org/10.3390/en5125372.

Daniell, J., Nagaraju, S., Burton, F., Köpke, M., Simpson, S.D., 2016. Low-Carbon Fuel and Chemical Production by Anaerobic Gas Fermentation. Advances in biochemical engineering/biotechnology 156, 293–321. https://doi.org/10.1007/10_2015_5005.

Dash, S., Ng, C.Y., Maranas, C.D., 2016. Metabolic modeling of clostridia: current developments and applications. FEMS microbiology letters 363. https://doi.org/10.1093/femsle/fnw004.

de la Plaza, M., Fernández de Palencia, P., Peláez, C., Requena, T., 2004. Biochemical and molecular characterization of Î±-ketoisovalerate decarboxylase, an enzyme involved in the formation of aldehydes from amino acids by Lactococcus lactis. FEMS microbiology letters 238, 367–374. https://doi.org/10.1111/j.1574-6968.2004.tb09778.x.

Deckwer, W.-D., Louisi, Y., Zaidi, A., Ralek, M., 1980. Hydrodynamic properties of the Fischer-Tropsch slurry process. Ind. Eng. Chem. Proc. Des. Dev. 19, 699–708.

Devarapalli, M., Atiyeh, H.K., Phillips, J.R., Lewis, R.S., Huhnke, R.L., 2016. Ethanol production during semi-continuous syngas fermentation in a trickle bed reactor using Clostridium ragsdalei. Bioresource technology 209, 56–65. https://doi.org/10.1016/j.biortech.2016.02.086.

Diender, M., Stams, A.J.M., Sousa, D.Z., 2015. Pathways and Bioenergetics of Anaerobic Carbon Monoxide Fermentation. Frontiers in microbiology 6, 1275. https://doi.org/10.3389/fmicb.2015.01275.

Diner, B.A., Fan, J., Scotcher, M.C., Wells, D.H., Whited, G.M., 2018. Synthesis of Heterologous Mevalonic Acid Pathway Enzymes in Clostridium ljungdahlii for the Conversion of Fructose and of Syngas to Mevalonate and Isoprene. Appl. Environ. Microbiol. 84. https://doi.org/10.1128/AEM.01723-17.

Drake, H.L., Daniel, S.L., Gößner Anita S., 2008. "Old Acetogens, New Light". Annals of the New York Academy of Sciences.

Enfors, S.-O., Jahic, M., Rozkov, A., Xu, B., Hecker, M., Jürgen, B., Krüger, E., Schweder, T., Hamer, G., O'Beirne, D., Noisommit-Rizzi, N., Reuss, M., Boone, L., Hewitt, C., McFarlane, C., Nienow, A., Kovacs, T., Trägårdh, C., Fuchs, L., Revstedt, J., Friberg, P.C., Hjertager, B., Blomsten, G., Skogman, H., Hjort, S., Hoeks, F., Lin, H.-Y., Neubauer, P., van der Lans, R., Luyben, K., Vrabel, P., Manelius, Å., 2001. Physiological responses to mixing in large scale bioreactors. Journal of Biotechnology 85, 175–185. https://doi.org/10.1016/S0168-1656(00)00365-5.

Feith, A., Teleki, A., Graf, M., Favilli, L., Takors, R., 2019. HILIC-Enabled 13C Metabolomics Strategies: Comparing Quantitative Precision and Spectral Accuracy of QTOF High- and QQQ Low-Resolution Mass Spectrometry. Metabolites 9. https://doi.org/10.3390/metabo9040063.

Fiehn, O., 2001. Combining genomics, metabolome analysis, and biochemical modelling to understand metabolic networks. Comparative and functional genomics 2, 155–168. https://doi.org/10.1002/cfg.82.

Flüchter, S., Follonier, S., Schiel-Bengelsdorf, B., Bengelsdorf, F.R., Zinn, M., Dürre, P., 2019. Anaerobic Production of Poly(3-hydroxybutyrate) and Its Precursor 3-Hydroxybutyrate from Synthesis Gas by Autotrophic Clostridia. Biomacromolecules 20, 3271–3282. https://doi.org/10.1021/acs.biomac.9b00342.

Fuhrer, T., Sauer, U., 2009. Different biochemical mechanisms ensure network-wide balancing of reducing equivalents in microbial metabolism. J. Bacteriol. 191, 2112–2121. https://doi.org/10.1128/jb.01523-08.

Furdui, C., Ragsdale, S.W., 2000. The role of pyruvate ferredoxin oxidoreductase in pyruvate synthesis during autotrophic growth by the Wood-Ljungdahl pathway. The Journal of biological chemistry 275, 28494–28499. https://doi.org/10.1074/jbc.M003291200.

Goldet, G., Brandmayr, C., Stripp, S.T., Happe, T., Cavazza, C., Fontecilla-Camps, J.C., Armstrong, F.A., 2009. Electrochemical kinetic investigations of the reactions of FeFe-hydrogenases with carbon monoxide and oxygen: comparing the importance of gas tunnels and active-site electronic/redox effects. Journal of the American Chemical Society 131, 14979–14989. https://doi.org/10.1021/ja905388j.

Gomez, J.A., Höffner, K., Barton, P.I., 2014. DFBAlab: a fast and reliable MATLAB code for dynamic flux balance analysis. BMC bioinformatics 15, 409. https://doi.org/10.1186/s12859-014-0409-8.

Grace, J., 1973. Shapes and velocities of bubbles rising in infinite liquid. Transactions of the Institution of Chemical Engineers 51, 116–120.

Graf, M., Zieringer, J., Haas, T., Nieß, A., Blombach, B., Takors, R., 2018. Physiological Response of Corynebacterium glutamicum to Increasingly Nutrient-Rich Growth Conditions. Frontiers in microbiology 9, 2058. https://doi.org/10.3389/fmicb.2018.02058.

Grand View Research, 2016. Isobutanol Market Size To Reach $1.18 Billion By 2022. https://www.grandviewresearch.com/press-release/global-isobutanol-market (accessed 12 October 2020).

Green, M.R., Sambrook, J., 2012. Molecular cloning: a laboratory manual. Cold Spring Harbor, NY: Cold Spring Harbor Laboratory Press.

Gunes, B., 2021. A critical review on biofilm-based reactor systems for enhanced syngas fermentation processes. Renewable and Sustainable Energy Reviews 143, 110950. https://doi.org/10.1016/j.rser.2021.110950.

Hamilton, J.J., Reed, J.L., 2014. Software platforms to facilitate reconstructing genome-scale metabolic networks. Environmental microbiology 16, 49–59. https://doi.org/10.1111/1462-2920.12312.

Haringa, C., Deshmukh, A.T., Mudde, R.F., Noorman, H.J., 2017a. Euler-Lagrange analysis towards representative down-scaling of a 22 m 3 aerobic S. cerevisiae fermentation. Chemical Engineering Science 170, 653–669. https://doi.org/10.1016/j.ces.2017.01.014.

Haringa, C., Noorman, H.J., Mudde, R.F., 2017b. Lagrangian modeling of hydrodynamic–kinetic interactions in (bio)chemical reactors: Practical implementation and setup guidelines. Chemical Engineering Science 157, 159–168. https://doi.org/10.1016/j.ces.2016.07.031.

Haringa, C., Tang, W., Deshmukh, A.T., Xia, J., Reuss, M., Heijnen, J.J., Mudde, R.F., Noorman, H.J., 2016. Euler-Lagrange computational fluid dynamics for (bio)reactor scale down: An analysis of organism lifelines. Eng. Life Sci. 16, 652–663. https://doi.org/10.1002/elsc.201600061.

Haringa, C., Vandewijer, R., Mudde, R.F., 2018. Inter-compartment interaction in multi-impeller mixing. Part II. Experiments, sliding mesh and large Eddy simulations. Chemical Engineering Research and Design 136, 886–899. https://doi.org/10.1016/j.cherd.2018.06.007.

Heap, J.T., Kuehne, S.A., Ehsaan, M., Cartman, S.T., Cooksley, C.M., Scott, J.C., Minton, N.P., 2010. The ClosTron: Mutagenesis in Clostridium refined and streamlined. Journal of microbiological methods 80, 49–55. https://doi.org/10.1016/j.mimet.2009.10.018.

Heap, J.T., Pennington, O.J., Cartman, S.T., Carter, G.P., Minton, N.P., 2007. The ClosTron: a universal gene knock-out system for the genus Clostridium. Journal of microbiological methods 70, 452–464. https://doi.org/10.1016/j.mimet.2007.05.021.

Heap, J.T., Pennington, O.J., Cartman, S.T., Minton, N.P., 2009. A modular system for Clostridium shuttle plasmids. Journal of microbiological methods 78, 79–85. https://doi.org/10.1016/j.mimet.2009.05.004.

Heffernan, J.K., Valgepea, K., Souza Pinto Lemgruber, R. de, Casini, I., Plan, M., Tappel, R., Simpson, S.D., Köpke, M., Nielsen, L.K., Marcellin, E., 2020. Enhancing CO 2 -valorization using Clostridium autoethanogenum for sustainable fuel and chemicals production 59. https://doi.org/10.1101/2020.01.23.917666.

Heider, J., Mai, X., Adams, M.W., 1996. Characterization of 2-ketoisovalerate ferredoxin oxidoreductase, a new and reversible coenzyme A-dependent enzyme involved in peptide fermentation by hyperthermophilic archaea. J. Bacteriol. 178, 780–787. https://doi.org/10.1128/jb.178.3.780-787.1996.

Heins, A.-L., Lencastre Fernandes, R., Gernaey, K.V., Lantz, A.E., 2015. Experimental and in silico investigation of population heterogeneity in continuous Sachharomyces cerevisiae scale-down fermentation in a two-compartment setup. J. Chem. Technol. Biotechnol. 90, 324–340. https://doi.org/10.1002/jctb.4532.

Henson, M.A., 2003. Dynamic modeling of microbial cell populations. Current opinion in biotechnology 14, 460–467. https://doi.org/10.1016/S0958-1669(03)00104-6.

Hepburn, C., Adlen, E., Beddington, J., Carter, E.A., Fuss, S., Mac Dowell, N., Minx, J.C., Smith, P., Williams, C.K., 2019. The technological and economic prospects for CO2 utilization and removal. Nature 575, 87–97. https://doi.org/10.1038/s41586-019-1681-6.

Hermann, M., Teleki, A., Weitz, S., Niess, A., Freund, A., Bengelsdorf, F.R., Dürre, P., Takors, R., 2021. Identifying and Engineering Bottlenecks of Autotrophic Isobutanol Formation in Recombinant C. ljungdahlii by Systemic Analysis. Frontiers in bioengineering and biotechnology 9, 647853. https://doi.org/10.3389/fbioe.2021.647853.

Hermann, M., Teleki, A., Weitz, S., Niess, A., Freund, A., Bengelsdorf, F.R., Takors, R., 2020. Electron availability in CO2 , CO and H2 mixtures constrains flux distribution, energy management and product formation in Clostridium ljungdahlii. Microbial biotechnology, 6, 1831–1846. https://doi.org/10.1111/1751-7915.13625.

Hess, V., Gallegos, R., Jones, J.A., Barquera, B., Malamy, M.H., Müller, V., 2016. Occurrence of ferredoxin:NAD(+) oxidoreductase activity and its ion specificity in several Gram-positive and Gram-negative bacteria. PeerJ 4, e1515. https://doi.org/10.7717/peerj.1515.

Higbie, R., 1935. The rate of absorption of a pure gas into a still liquid during short periods of exposure. Trans. AIChE 31, 365–389.

Huang, H., Chai, C., Li, N., Rowe, P., Minton, N.P., Yang, S., Jiang, W., Gu, Y., 2016. CRISPR/Cas9-Based Efficient Genome Editing in Clostridium ljungdahlii, an Autotrophic Gas-Fermenting Bacterium. ACS synthetic biology 5, 1355–1361. https://doi.org/10.1021/acssynbio.6b00044.

Huang, H., Chai, C., Yang, S., Jiang, W., Gu, Y., 2019. Phage serine integrase-mediated genome engineering for efficient expression of chemical biosynthetic pathway in gas-fermenting Clostridium ljungdahlii. Metabolic engineering 52, 293–302. https://doi.org/10.1016/j.ymben.2019.01.005.

Hungate, R.E., 1976. Chapter IV A Roll Tube Method for Cultivation of Strict Anaerobes, in: Norris, J.R. (Ed.), Methods in microbiology, vol. 3, 3rd ed. Academic Press, London, pp. 117–132.

Inoue, H., Nojima, H., Okayama, H., 1990. High efficiency transformation of Escherichia coli with plasmids. Gene 96, 23–28. https://doi.org/10.1016/0378-1119(90)90336-P.

Islam, M.A., Zengler, K., Edwards, E.A., Mahadevan, R., Stephanopoulos, G., 2015. Investigating Moorella thermoacetica metabolism with a genome-scale constraint-based metabolic model. Integrative biology : quantitative biosciences from nano to macro 7, 869–882. https://doi.org/10.1039/c5ib00095e.

Jack, J., Lo, J., Maness, P.-C., Ren, Z.J., 2019. Directing Clostridium ljungdahlii fermentation products via hydrogen to carbon monoxide ratio in syngas. Biomass and Bioenergy 124, 95–101. https://doi.org/10.1016/j.biombioe.2019.03.011.

Jin, S., Bae, J., Song, Y., Pearcy, N., Shin, J., Kang, S., Minton, N.P., Soucaille, P., Cho, B.-K., 2020. Synthetic Biology on Acetogenic Bacteria for Highly Efficient Conversion of C1 Gases to Biochemicals. International journal of molecular sciences 21. https://doi.org/10.3390/ijms21207639.

Jones, D.T., Woods, D.R., 1986. Acetone-Butanol Fermentation Revisited. Microbiological Reviews, 484–524.

Junghans, L., Teleki, A., Wijaya, A.W., Becker, M., Schweikert, M., Takors, R., 2019. From nutritional wealth to autophagy: In vivo metabolic dynamics in the cytosol, mitochondrion and shuttles of IgG producing CHO cells. Metabolic engineering 54, 145–159. https://doi.org/10.1016/j.ymben.2019.02.005.

Kantarci, N., Borak, F., Ulgen, K.O., 2005. Bubble column reactors. Process Biochemistry 40, 2263–2283. https://doi.org/10.1016/j.procbio.2004.10.004.

Karabektas, M., Hosoz, M., 2009. Performance and emission characteristics of a diesel engine using isobutanol–diesel fuel blends. Renewable Energy, 34(6), 1554-1559. Renewable Energy 34, 1554–1559. https://doi.org/10.1016/J.RENENE.2008.11.003.

Koning, W. de, van Dam, K., 1992. A method for the determination of changes of glycolytic metabolites in yeast on a subsecond time scale using extraction at neutral pH. Analytical Biochemistry 204, 118–123. https://doi.org/10.1016/0003-2697(92)90149-2.

Köpke, M., Gerth, M.L., Maddock, D.J., Mueller, A.P., Liew, F., Simpson, S.D., Patrick, W.M., 2014. Reconstruction of an acetogenic 2,3-butanediol pathway involving a novel NADPH-dependent primary-secondary alcohol dehydrogenase. Appl. Environ. Microbiol. 80, 3394–3403. https://doi.org/10.1128/AEM.00301-14.

Köpke, M., Held, C., Hujer, S., Liesegang, H., Wiezer, A., Wollherr, A., Ehrenreich, A., Liebl, W., Gottschalk, G., Dürre, P., 2010. Clostridium ljungdahlii represents a microbial production platform based on syngas. Proceedings of the National Academy of Sciences 107, 13087–13092. https://doi.org/10.1073/pnas.1004716107.

Köpke, M., Mihalcea, C., Bromley, J.C., Simpson, S.D., 2011a. Fermentative production of ethanol from carbon monoxide. Current opinion in biotechnology 22, 320–325. https://doi.org/10.1016/j.copbio.2011.01.005.

Köpke, M., Mihalcea, C., Liew, F., Tizard, J.H., Ali, M.S., Conolly, J.J., Al-Sinawi, B., Simpson, S.D., 2011b. 2,3-Butanediol Production by Acetogenic Bacteria, an Alternative Route to Chemical Synthesis, Using Industrial Waste Gas. Appl. Environ. Microbiol. 77, 5467–5475. https://doi.org/10.1128/AEM.00355-11.

Krishna, R., van Baten, J.M., Urseanu, M.I., Ellenberger, J., 2001. Design and scale up of a bubble column slurry reactor for Fischer–Tropsch synthesis. Chemical Engineering Science 56, 537–545. https://doi.org/10.1016/S0009-2509(00)00258-X.

Kuschel, M., Siebler, F., Takors, R., 2017. Lagrangian Trajectories to Predict the Formation of Population Heterogeneity in Large-Scale Bioreactors. Bioengineering (Basel, Switzerland) 4. https://doi.org/10.3390/bioengineering4020027.

LanzaTech Press release, 2018. World's First Commercial Waste Gas to Ethanol Plant Starts Up. https://www.lanzatech.com/2018/06/08/worlds-first-commercial-waste-gas-ethanol-plant-starts/ (accessed 18 September 2021).

Lapin, A., Müller, D., Reuss, M., 2004. Dynamic Behavior of Microbial Populations in Stirred Bioreactors Simulated with Euler−Lagrange Methods: Traveling along the Lifelines of Single Cells. Ind. Eng. Chem. Res. 43, 4647–4656. https://doi.org/10.1021/ie030786k.

Lapin, A., Schmid, J., Reuss, M., 2006. Modeling the dynamics of E. coli populations in the three-dimensional turbulent field of a stirred-tank bioreactor—A structured–segregated approach. Chemical Engineering Science 61, 4783–4797. https://doi.org/10.1016/j.ces.2006.03.003.

Larsson, G., Trnkvist, M., Wernersson, E.S., Trgrdh, C., Noorman, H., Enfors, S.-O., 1996. Substrate gradients in bioreactors: origin and consequences. Bioprocess Engineering 14, 281–289. https://doi.org/10.1007/BF00369471.

Latif, H., Zeidan, A.A., Nielsen, A.T., Zengler, K., 2014. Trash to treasure: production of biofuels and commodity chemicals via syngas fermenting microorganisms. Current opinion in biotechnology 27, 79–87. https://doi.org/10.1016/j.copbio.2013.12.001.

Leang, C., Ueki, T., Nevin, K.P., Lovley, D.R., 2013. A genetic system for Clostridium ljungdahlii: a chassis for autotrophic production of biocommodities and a model homoacetogen. Appl. Environ. Microbiol. 79, 1102–1109. https://doi.org/10.1128/AEM.02891-12.

Lehr, F., Millies, M., Mewes, D., 2002. Bubble-Size distributions and flow fields in bubble columns. AIChE J. 48, 2426–2443. https://doi.org/10.1002/aic.690481103.

Li, H., Opgenorth, P.H., Wernick, D.G., Rogers, S., Wu, T.-Y., Higashide, W., Malati, P., Huo, Y.-X., Cho, K.M., Liao, J.C., 2012. Integrated electromicrobial conversion of CO2 to higher alcohols. Science (New York, N.Y.) 335, 1596. https://doi.org/10.1126/science.1217643.

Liang, J., Huang, H., Wang, S., 2019. Distribution, Evolution, Catalytic Mechanism, and Physiological Functions of the Flavin-Based Electron-Bifurcating NADH-Dependent

Reduced Ferredoxin: NADP+ Oxidoreductase. Frontiers in microbiology 10, 373. https://doi.org/10.3389/fmicb.2019.00373.

Liew, F., Henstra, A.M., Köpke, M., Winzer, K., Simpson, S.D., Minton, N.P., 2017. Metabolic engineering of Clostridium autoethanogenum for selective alcohol production. Metabolic engineering 40, 104–114. https://doi.org/10.1016/j.ymben.2017.01.007.

Liew, F., Martin, M.E., Tappel, R.C., Heijstra, B.D., Mihalcea, C., Köpke, M., 2016. Gas Fermentation-A Flexible Platform for Commercial Scale Production of Low-Carbon-Fuels and Chemicals from Waste and Renewable Feedstocks. Frontiers in microbiology 7, 694. https://doi.org/10.3389/fmicb.2016.00694.

Lin, P.P., Mi, L., Morioka, A.H., Yoshino, K.M., Konishi, S., Xu, S.C., Papanek, B.A., Riley, L.A., Guss, A.M., Liao, J.C., 2015. Consolidated bioprocessing of cellulose to isobutanol using Clostridium thermocellum. Metabolic engineering 31, 44–52. https://doi.org/10.1016/j.ymben.2015.07.001.

Lin, P.P., Rabe, K.S., Takasumi, J.L., Kadisch, M., Arnold, F.H., Liao, J.C., 2014. Isobutanol production at elevated temperatures in thermophilic Geobacillus thermoglucosidasius. Metabolic engineering 24, 1–8. https://doi.org/10.1016/j.ymben.2014.03.006.

Liu, J., Guo, T., Wang, D., Shen, X., Liu, D., Niu, H., Liang, L., Ying, H., 2016. Enhanced butanol production by increasing NADH and ATP levels in Clostridium beijerinckii NCIMB 8052 by insertional inactivation of Cbei_4110. Applied microbiology and biotechnology 100, 4985–4996. https://doi.org/10.1007/s00253-016-7299-9.

Liu, Z.-Y., Jia, D.-C., Zhang, K.-D., Zhu, H.-F., Zhang, Q., Jiang, W.-H., Gu, Y., Li, F.-L., 2020. Ethanol Metabolism Dynamics in Clostridium ljungdahlii Grown on Carbon Monoxide. Appl. Environ. Microbiol. 86. https://doi.org/10.1128/AEM.00730-20.

Ljungdahl, L.G., 1986. The autotrophic pathway of acetate synthesis in acetogenic bacteria. Annual review of microbiology 40, 415–450. https://doi.org/10.1146/annurev.mi.40.100186.002215.

Löffler, M., Simen, J.D., Jäger, G., Schäferhoff, K., Freund, A., Takors, R., 2016. Engineering E. coli for large-scale production - Strategies considering ATP expenses and transcriptional responses. Metabolic engineering 38, 73–85. https://doi.org/10.1016/j.ymben.2016.06.008.

Luo, H., 1995. Coalescence, breakup and liquid circulation in bubble column reactors.

Luo, H., Svendsen, H.F., 1996. Theoretical model for drop and bubble breakup in turbulent dispersions. AIChE J. 42, 1225–1233. https://doi.org/10.1002/aic.690420505.

Mantzaris, N.V., Liou, J.-J., Daoutidis, P., Srienc, F., 1999. Numerical solution of a mass structured cell population balance model in an environment of changing substrate concentration. Journal of Biotechnology 71, 157–174. https://doi.org/10.1016/S0168-1656(99)00020-6.

Marcellin, E., Behrendorff, J.B., Nagaraju, S., DeTissera, S., Segovia, S., Palfreyman, R.W., Daniell, J., Licona-Cassani, C., Quek, L., Speight, R., Hodson, M.P., Simpson, S.D., Mitchell, W.P., Köpke, M., Nielsen, L.K., 2016. Low carbon fuels and commodity chemicals from waste gases – systematic approach to understand energy metabolism in a model acetogen. Green Chem. 18, 3020–3028. https://doi.org/10.1039/C5GC02708J.

Martin, M.E., Richter, H., Saha, S., Angenent, L.T., 2016. Traits of selected Clostridium strains for syngas fermentation to ethanol. Biotechnology and bioengineering 113, 531–539. https://doi.org/10.1002/bit.25827.

Mayer, A., Weuster-Botz, D., 2017. Reaction engineering analysis of the autotrophic energy metabolism of Clostridium aceticum. FEMS microbiology letters 364. https://doi.org/10.1093/femsle/fnx219.

Meyer, C., Papoutsakis, E., 1989. Increased levels of ATP and NADH are associated with increased solvent production in continuous cultures of Clostridium acetobutylicum. Appl Microbiol Biotechnol 30. https://doi.org/10.1007/BF00263849.

Miao, R., Xie, H., Lindblad, P., 2018. Enhancement of photosynthetic isobutanol production in engineered cells of Synechocystis PCC 6803. Biotechnology for biofuels 11, 267. https://doi.org/10.1186/s13068-018-1268-8.

Michalowski, A., Siemann-Herzberg, M., Takors, R., 2017. Escherichia coli HGT: Engineered for high glucose throughput even under slowly growing or resting conditions. Metabolic engineering 40, 93–103. https://doi.org/10.1016/j.ymben.2017.01.005.

Mock, J., Zheng, Y., Mueller, A.P., Ly, S., Tran, L., Segovia, S., Nagaraju, S., Köpke, M., Dürre, P., Thauer, R.K., 2015. Energy Conservation Associated with Ethanol Formation from H 2 and CO 2 in Clostridium autoethanogenum Involving Electron Bifurcation. J. Bacteriol. 197, 2965–2980. https://doi.org/10.1128/JB.00399-15.

Mohammadi, M., Mohamed, A.R., Najafpour, G.D., Younesi, H., Uzir, M.H., 2014. Kinetic studies on fermentative production of biofuel from synthesis gas using Clostridium ljungdahlii. TheScientificWorldJournal 2014, 910590. https://doi.org/10.1155/2014/910590.

Molitor, B., Marcellin, E., Angenent, L.T., 2017. Overcoming the energetic limitations of syngas fermentation. Current opinion in chemical biology 41, 84–92. https://doi.org/10.1016/j.cbpa.2017.10.003.

Monod, J., 1949. The growth of bacterial cultures. Annual review of microbiology 3, 371–394.

Morchain, J., Gabelle, J.-C., Cockx, A., 2014. A coupled population balance model and CFD approach for the simulation of mixing issues in lab-scale and industrial bioreactors. AIChE J. 60, 27–40. https://doi.org/10.1002/aic.14238.

Müller, V., 2003. Energy conservation in acetogenic bacteria. Appl. Environ. Microbiol. 69, 6345–6353. https://doi.org/10.1128/AEM.69.11.6345–6353.2003.

Müller, V., Imkamp, F., Biegel, E., Schmidt, S., Dilling, S., 2008. Discovery of a ferredoxin:NAD+-oxidoreductase (Rnf) in Acetobacterium woodii: a novel potential coupling site in acetogens. Annals of the New York Academy of Sciences 1125, 137–146. https://doi.org/10.1196/annals.1419.011.

Nagarajan, H., Sahin, M., Nogales, J., Latif, H., Lovley, D.R., Ebrahim, A., Zengler, K., 2013. Characterizing acetogenic metabolism using a genome-scale metabolic reconstruction of Clostridium ljungdahlii. Microbial cell factories 12, 118.

Nauha, E.K., Kálal, Z., Ali, J.M., Alopaeus, V., 2018. Compartmental modeling of large stirred tank bioreactors with high gas volume fractions. Chemical Engineering Journal 334, 2319–2334. https://doi.org/10.1016/j.cej.2017.11.182.

Noorman, H., Morud, K., Hjertager, B. H., Traegaardh, C., Larsson, G., & Enfors, S. O. (Ed.), 1993. CFD modeling and verification of flow and conversion in a 1 m3 bioreactor, 241-258.

Norman, R.O., Millat, T., Schatschneider, S., Henstra, A.M., Breitkopf, R., Pander, B., Annan, F.J., Piatek, P., Hartman, H.B., Poolman, M.G., Fell, D.A., Winzer, K., Minton, N.P., Hodgman, C., 2019. Genome-scale model of C. autoethanogenum reveals optimal bioprocess conditions for high-value chemical production from carbon monoxide. Engineering Biology 3, 32–40. https://doi.org/10.1049/enb.2018.5003.

O'Brien, E.J., Monk, J.M., Palsson, B.O., 2015. Using Genome-scale Models to Predict Biological Capabilities. Cell 161, 971–987. https://doi.org/10.1016/j.cell.2015.05.019.

Öppinger, C., Kremp, F., Müller, V., 2021. Is reduced ferredoxin the physiological electron donor for MetVF-type methylenetetrahydrofolate reductases in acetogenesis? A hypothesis. International microbiology : the official journal of the Spanish Society for Microbiology. https://doi.org/10.1007/s10123-021-00190-0.

Orth, J.D., Thiele, I., Palsson, B.Ø., 2010. What is flux balance analysis? Nature biotechnology 28, 245–248. https://doi.org/10.1038/nbt.1614.

Oswald, F., Dörsam, S., Veith, N., Zwick, M., Neumann, A., Ochsenreither, K., Syldatk, C., 2016. Sequential Mixed Cultures: From Syngas to Malic Acid. Frontiers in microbiology 7, 891. https://doi.org/10.3389/fmicb.2016.00891.

Oswald, F., Stoll, I.K., Zwick, M., Herbig, S., Sauer, J., Boukis, N., Neumann, A., 2018. Formic Acid Formation by Clostridium ljungdahlii at Elevated Pressures of Carbon Dioxide and Hydrogen. Frontiers in bioengineering and biotechnology 6, 6. https://doi.org/10.3389/fbioe.2018.00006.

Parker, E.J., Pratt, A.J., 2010. Amino Acid Biosynthesis, in: Hughes, A.B. (Ed.), Amino Acids, Peptides and Proteins in Organic Chemistry. Wiley-VCH Verlag GmbH & Co. KGaA, Weinheim, Germany, pp. 1–82.

Pavan, M., 2022. The New Biorefineries: Integration with New Technologies for Carbon Capture and Utilization to Produce Bioethanol, in: Soccol, C.R., Amarante Guimarães Pereira, G., Dussap, C.-G., Porto de Souza Vandenberghe, L. (Eds.), Liquid Biofuels: Bioethanol, vol. 12. Springer International Publishing, Cham, pp. 457–487.

Perez, J.M., Richter, H., Loftus, S.E., Angenent, L.T., 2013. Biocatalytic reduction of short-chain carboxylic acids into their corresponding alcohols with syngas fermentation. Biotechnology and bioengineering 110, 1066–1077. https://doi.org/10.1002/bit.24786.

Perutka, J., Wang, W., Goerlitz, D., Lambowitz, A.M., 2004. Use of computer-designed group II introns to disrupt Escherichia coli DExH/D-box protein and DNA helicase genes. Journal of molecular biology 336, 421–439. https://doi.org/10.1016/j.jmb.2003.12.009.

Philipps, G., Vries, S. de, Jennewein, S., 2019. Development of a metabolic pathway transfer and genomic integration system for the syngas-fermenting bacterium Clostridium ljungdahlii. Biotechnology for biofuels 12, 112. https://doi.org/10.1186/s13068-019-1448-1.

Phillips, J.R., Clausen, E.C., Gaddy, J.L., 1994. Synthesis gas as substrate for the biological production of fuels and chemicals. Appl Biochem Biotechnol 45-46, 145–157. https://doi.org/10.1007/BF02941794.

Phillips, J.R., Klasson, K.T., Clausen, E.C., Gaddy, J.L., 1993. Biological production of ethanol from coal synthesis gas. Appl Biochem Biotechnol 39-40, 559–571. https://doi.org/10.1007/BF02919018.

Philp, J., 2018. The bioeconomy, the challenge of the century for policy makers. New biotechnology 40, 11–19. https://doi.org/10.1016/j.nbt.2017.04.004.

Pigou, M., Morchain, J., 2015. Investigating the interactions between physical and biological heterogeneities in bioreactors using compartment, population balance and metabolic models. Chemical Engineering Science 126, 267–282. https://doi.org/10.1016/j.ces.2014.11.035.

Plassmeier, J., Barsch, A., Persicke, M., Niehaus, K., Kalinowski, J., 2007. Investigation of central carbon metabolism and the 2-methylcitrate cycle in Corynebacterium glutamicum

by metabolic profiling using gas chromatography-mass spectrometry. Journal of Biotechnology 130, 354–363. https://doi.org/10.1016/j.jbiotec.2007.04.026.

Ragsdale, S.W., 2008. Enzymology of the wood-Ljungdahl pathway of acetogenesis. Annals of the New York Academy of Sciences 1125, 129–136. https://doi.org/10.1196/annals.1419.015.

Ragsdale, S.W., Pierce, E., 2008. Acetogenesis and the Wood-Ljungdahl pathway of CO(2) fixation. Biochimica et biophysica acta 1784, 1873–1898. https://doi.org/10.1016/j.bbapap.2008.08.012.

Richter, H., Martin, M., Angenent, L., 2013. A Two-Stage Continuous Fermentation System for Conversion of Syngas into Ethanol. Energies 6, 3987–4000. https://doi.org/10.3390/en6083987.

Richter, H., Molitor, B., Wei, H., Chen, W., Aristilde, L., Angenent, L.T., 2016. Ethanol production in syngas-fermenting Clostridium ljungdahlii is controlled by thermodynamics rather than by enzyme expression. Energy Environ. Sci. 9, 2392–2399. https://doi.org/10.1039/C6EE01108J.

Sander, R., 1999. Compilation of Henry's law constants for inorganic and organic species of potential importance in environmental chemistry. Citeseer.

Sato, Y., Sekoguchi, K., 1975. Liquid velocity distribution in two-phase bubble flow. International Journal of Multiphase Flow 2, 79–95. https://doi.org/10.1016/0301-9322(75)90030-0.

Schatschneider, S., Abdelrazig, S., Safo, L., Henstra, A.M., Millat, T., Kim, D.-H., Winzer, K., Minton, N.P., Barrett, D.A., 2018. Quantitative Isotope-Dilution High-Resolution-Mass-Spectrometry Analysis of Multiple Intracellular Metabolites in Clostridium autoethanogenum with Uniformly 13C-Labeled Standards Derived from Spirulina. Analytical chemistry 90, 4470–4477. https://doi.org/10.1021/acs.analchem.7b04758.

Schilling, C.H., Edwards, J.S., Letscher, D., Palsson, B.Ø., 2000. Combining pathway analysis with flux balance analysis for the comprehensive study of metabolic systems. Biotechnol. Bioeng. 71, 286–306. https://doi.org/10.1002/1097-0290(2000)71:4<286:AID-BIT1018>3.0.CO;2-R.

Schmalzriedt, S., Jenne, M., Mauch, K., Reuss, M., 2003. Integration of physiology and fluid dynamics. Advances in biochemical engineering/biotechnology 80, 19–68. https://doi.org/10.1007/3-540-36782-9_2.

Schuchmann, K., Müller, V., 2012. A bacterial electron-bifurcating hydrogenase. The Journal of biological chemistry 287, 31165–31171. https://doi.org/10.1074/jbc.m112.395038.

Schuchmann, K., Müller, V., 2014. Autotrophy at the thermodynamic limit of life: a model for energy conservation in acetogenic bacteria. Nature reviews. Microbiology 12, 809–821. https://doi.org/10.1038/nrmicro3365.

Senger, R.S., Papoutsakis, E.T., 2008. Genome-scale model for Clostridium acetobutylicum: Part I. Metabolic network resolution and analysis. Biotechnol. Bioeng. 101, 1036–1052. https://doi.org/10.1002/bit.22010.

Siebler, F., 2020. Scale-up of gas fermentations: Modelling tools for risk minimisation. Universitätsbibliothek der Universität Stuttgart, Stuttgart, Online-Ressource.

Siebler, F., Lapin, A., Hermann, M., Takors, R., 2019. The impact of CO gradients on C. ljungdahlii in a 125 m3 bubble column: Mass transfer, circulation time and lifeline analysis. Chemical Engineering Science 207, 410–423. https://doi.org/10.1016/j.ces.2019.06.018.

Smith, K.M., Cho, K.-M., Liao, J.C., 2010. Engineering Corynebacterium glutamicum for isobutanol production. Appl Microbiol Biotechnol 87, 1045–1055. https://doi.org/10.1007/s00253-010-2522-6.

Sun, X., Atiyeh, H.K., Huhnke, R.L., Tanner, R.S., 2019. Syngas fermentation process development for production of biofuels and chemicals: A review. Bioresource Technology Reports 7, 100279. https://doi.org/10.1016/j.biteb.2019.100279.

Takors, R., 2012. Scale-up of microbial processes: impacts, tools and open questions. Journal of Biotechnology 160, 3–9. https://doi.org/10.1016/j.jbiotec.2011.12.010.

Takors, R., Bathe, B., Rieping, M., Hans, S., Kelle, R., Huthmacher, K., 2007. Systems biology for industrial strains and fermentation processes--example: amino acids. Journal of Biotechnology 129, 181–190. https://doi.org/10.1016/j.jbiotec.2007.01.031.

Takors, R., Kopf, M., Mampel, J., Bluemke, W., Blombach, B., Eikmanns, B., Bengelsdorf, F.R., Weuster-Botz, D., Dürre, P., 2018. Using gas mixtures of CO, CO2 and H2 as microbial substrates: the do's and don'ts of successful technology transfer from laboratory to production scale. Microbial biotechnology 11, 606–625. https://doi.org/10.1111/1751-7915.13270.

Tan, Y., Liu, J., Chen, X., Zheng, H., Li, F., 2013. RNA-seq-based comparative transcriptome analysis of the syngas-utilizing bacterium Clostridium ljungdahlii DSM 13528 grown autotrophically and heterotrophically. Molecular bioSystems 9, 2775–2784. https://doi.org/10.1039/C3MB70232D.

Tanner, R.S., Miller, L.M., Yang, D., 1993. Clostridium ljungdahlii sp. nov., an Acetogenic Species in Clostridial rRNA Homology Group I. International Journal of Systematic Bacteriology 43, 232–236. https://doi.org/10.1099/00207713-43-2-232.

Taymaz-Nikerel, H., Borujeni, A.E., Verheijen, P.J.T., Heijnen, J.J., van Gulik, W.M., 2010. Genome-derived minimal metabolic models for Escherichia coli MG1655 with estimated in vivo respiratory ATP stoichiometry. Biotechnol. Bioeng. 107, 369–381. https://doi.org/10.1002/bit.22802.

Teleki, A., Sánchez-Kopper, A., Takors, R., 2015. Alkaline conditions in hydrophilic interaction liquid chromatography for intracellular metabolite quantification using tandem mass spectrometry. Analytical Biochemistry 475, 4–13. https://doi.org/10.1016/j.ab.2015.01.002.

Thiele, I., Palsson, B.Ø., 2010. A protocol for generating a high-quality genome-scale metabolic reconstruction. Nature protocols 5, 93–121. https://doi.org/10.1038/nprot.2009.203.

Tomiyama, A., Tamai, H., Zun, I., Hosokawa, S., 2002. Transverse migration of single bubbles in simple shear flows. Chemical Engineering Science 57, 1849–1858. https://doi.org/10.1016/S0009-2509(02)00085-4.

Tremblay, P.-L., Zhang, T., Dar, S.A., Leang, C., Lovley, D.R., 2012. The Rnf complex of Clostridium ljungdahlii is a proton-translocating ferredoxin:NAD+ oxidoreductase essential for autotrophic growth. mBio 4, e00406-12. https://doi.org/10.1128/mBio.00406-12.

Ueki, T., Nevin, K.P., Woodard, T.L., Lovley, D.R., 2014. Converting carbon dioxide to butyrate with an engineered strain of Clostridium ljungdahlii. mBio 5, e01636-14. https://doi.org/10.1128/mBio.01636-14.

Valgepea, K., Loi, K.Q., Behrendorff, J.B., Lemgruber, R.d.S.P., Plan, M., Hodson, M.P., Köpke, M., Nielsen, L.K., Marcellin, E., 2017a. Arginine deiminase pathway provides ATP and boosts growth of the gas-fermenting acetogen Clostridium autoethanogenum. Metabolic engineering 41, 202–211. https://doi.org/10.1016/j.ymben.2017.04.007.

Valgepea, K., Souza Pinto Lemgruber, R. de, Abdalla, T., Binos, S., Takemori, N., Takemori, A., Tanaka, Y., Tappel, R., Köpke, M., Simpson, S.D., Nielsen, L.K., Marcellin, E., 2018. H2 drives metabolic rearrangements in gas-fermenting Clostridium autoethanogenum. Biotechnology for biofuels 11, 55. https://doi.org/10.1186/s13068-018-1052-9.

Valgepea, K., Souza Pinto Lemgruber, R. de, Meaghan, K., Palfreyman, R.W., Abdalla, T., Heijstra, B.D., Behrendorff, J.B., Tappel, R., Köpke, M., Simpson, S.D., Nielsen, L.K., Marcellin, E., 2017b. Maintenance of ATP Homeostasis Triggers Metabolic Shifts in Gas-Fermenting Acetogens. Cell systems 4, 505-515.e5. https://doi.org/10.1016/j.cels.2017.04.008.

Villadsen, J., Nielsen, J., Lidén, G., 2011. Bioreaction engineering principles, 3rd ed. Springer Science & Business Media.

Vrábel, P., van der Lans, R.G., van der Schot, F.N., Luyben, K.C., Xu, B., Enfors, S.-O., 2001. CMA: integration of fluid dynamics and microbial kinetics in modelling of large-scale fermentations. Chemical Engineering Journal 84, 463–474. https://doi.org/10.1016/S1385-8947(00)00271-0.

Wang, S., Huang, H., Kahnt, J., Mueller, A.P., Köpke, M., Thauer, R.K., 2013. NADP-specific electron-bifurcating FeFe-hydrogenase in a functional complex with formate dehydrogenase in Clostridium autoethanogenum grown on CO. J. Bacteriol. 195, 4373–4386. https://doi.org/10.1128/JB.00678-13.

Weitz, S., 2020. Konstruktion und Analyse isobutanolbildender autotropher acetogener Bakterien.

Weitz, S., Hermann, M., Linder, S., Bengelsdorf, F.R., Takors, R., Dürre, P., 2021. Isobutanol Production by Autotrophic Acetogenic Bacteria. Frontiers in bioengineering and biotechnology 9, 657253. https://doi.org/10.3389/fbioe.2021.657253.

Wess, J., Brinek, M., Boles, E., 2019. Improving isobutanol production with the yeast Saccharomyces cerevisiae by successively blocking competing metabolic pathways as well as ethanol and glycerol formation. Biotechnology for biofuels 12, 173. https://doi.org/10.1186/s13068-019-1486-8.

Whitham, J.M., Tirado-Acevedo, O., Chinn, M.S., Pawlak, J.J., Grunden, A.M., 2015. Metabolic response of Clostridium ljungdahlii to oxygen exposure. Appl. Environ. Microbiol. 81, 8379–8391. https://doi.org/10.1128/AEM.02491-15.

Wood, H.G., 1991. Life with CO or CO2 and H2 as a source of carbon and energy. The FASEB journal 5, 156–163.

Woolston, B.M., Emerson, D.F., Currie, D.H., Stephanopoulos, G., 2018. Rediverting carbon flux in Clostridium ljungdahlii using CRISPR interference (CRISPRi). Metabolic engineering 48, 243–253. https://doi.org/10.1016/j.ymben.2018.06.006.

Xie, B.-T., Liu, Z.-Y., Tian, L., Li, F.-L., Chen, X.-H., 2015. Physiological response of Clostridium ljungdahlii DSM 13528 of ethanol production under different fermentation conditions. Bioresource technology 177, 302–307. https://doi.org/10.1016/j.biortech.2014.11.101.

Xiong, W., Lin, P.P., Magnusson, L., Warner, L., Liao, J.C., Maness, P.-C., Chou, K.J., 2016. CO2-fixing one-carbon metabolism in a cellulose-degrading bacterium Clostridium thermocellum. Proceedings of the National Academy of Sciences 113, 13180–13185. https://doi.org/10.1073/pnas.1605482113.

Yang, X., Tsao, G.T., 1994. Mathematical modeling of inhibition kinetics in acetone-butanol fermentation by Clostridium acetobutylicum. Biotechnol. Prog. 10, 532–538. https://doi.org/10.1021/bp00029a012.

Yi, J., Huang, H., Liang, J., Wang, R., Liu, Z., Li, F., Wang, S., 2021. A Heterodimeric Reduced-Ferredoxin-Dependent Methylenetetrahydrofolate Reductase from Syngas-Fermenting Clostridium ljungdahlii. Microbiology spectrum 9, e0095821. https://doi.org/10.1128/Spectrum.00958-21.

Younesi, H., Najafpour, G., Mohamed, A.R., 2005. Ethanol and acetate production from synthesis gas via fermentation processes using anaerobic bacterium, Clostridium ljungdahlii. Biochemical Engineering Journal 27, 110–119. https://doi.org/10.1016/j.bej.2005.08.015.

Zhao, R., Liu, Y., Zhang, H., Chai, C., Wang, J., Jiang, W., Gu, Y., 2019. CRISPR-Cas12a-Mediated Gene Deletion and Regulation in Clostridium ljungdahlii and Its Application in Carbon Flux Redirection in Synthesis Gas Fermentation. ACS synthetic biology 8, 2270–2279. https://doi.org/10.1021/acssynbio.9b00033.

Zhu, H.-F., Liu, Z.-Y., Zhou, X., Yi, J.-H., Lun, Z.-M., Wang, S.-N., Tang, W.-Z., Li, F.-L., 2020. Energy Conservation and Carbon Flux Distribution During Fermentation of CO or H2/CO2 by Clostridium ljungdahlii. Frontiers in microbiology 11, 416. https://doi.org/10.3389/fmicb.2020.00416.

Zimmermann, M., Sauer, U., Zamboni, N., 2014. Quantification and mass isotopomer profiling of α-keto acids in central carbon metabolism. Analytical chemistry 86, 3232–3237. https://doi.org/10.1021/ac500472c.

7 Appendix

7.1 Supplementary Material to Manuscript I

Table 7.1: Compounds of the reduced stoichiometric metabolic model (rSMM)

Identifier	Description
10fthf	10-Formyltetrahydrofolate
13dpg	3-Phospho-D-glyceroyl phosphate
26dap_M	meso-2,6-Diaminoheptanedioate
2obut	2-Oxobutanoate
2pg	D-Glycerate 2-phosphate
3mob	3-Methyl-2-oxobutanoate
3pg	3-Phospho-D-glycerate
4abut	4-Aminobutanoate
5mthf	5-Methyltetrahydrofolate
Accoa	Acetyl-CoA
BMB	Biomass elemental balance compensation
Biomass	Biomass
Cellwall	Cellwall
H	H^+
H_ex	H^+
Lipid	Lipide
ac	Acetate
acald	Acetaldehyde
accoa	Acetyl-CoA
actn_R	M__R__Acetoin
actp	Acetyl phosphate
adocbl	Adenosylcobalamin
adp	ADP
aicar	5-Amino-1-(5-Phospho-D-ribosyl)imidazole-4-carboxamide
akg	2-Oxoglutarate
ala_L	L-Alanine
alac_S	(S)-2-Acetolactate
amet	S-Adenosyl-L-methionine
amp	AMP
arab_L	L-Arabinose
arg_L	L-Arginine
asn_L	L-Asparagine
asp_L	L-Aspartate
aspsa	L-Aspartate 4-semialdehyde
atp	ADP
btd_RR	(R,R)-2,3-Butanediol

btn	Biotin
ca2	Calcium
cdp	CDP
chor	chorismate
cit	Citrate
cl	Chloride
cmp	CMP
co	Carbon monoxide
co2	Carbon dioxide
coa	Coenzyme A
cobalt2	Co^{2+}
ctp	CTP
cu2	Cu^{2+}
cys_L	L-Cysteine
datp	dATP
dctp	dCTP
dgtp	dGTP
dhap	Dihydroxyacetone phosphate
dhf	7,8-Dihydrofolate
dttp	dTTP
e4p	D-Erythrose 4-phosphate
etoh	Ethanol
f1p	D-Fructose 1-phosphate
f6p	D-Fructose 6-phosphate
fad	Flavin adenine dinucleotide oxidized
fdp	D-Fructose 1,6-bisphosphate
fdox_4_2	oxidized ferredoxin
fdxr_4_2	reduced ferredoxin
fe2	Fe^{2+}
fol	Folate
for	Formate
fum	Fumarate
g3p	Glyceraldehyde 3-phosphate
gdp	GDP
gln_L	L-Glutamine
glu_L	L-Glutamate
gly	Glycine
glyc	Glycerol
gmp	GMP
gtp	GTP
h	H^+
h2	Hydrogen
h2o	H_2O
h2s	Hydrogen sulfide

hco3	Bicarbonate
his_L	L-Histidine
hom_L	L-Homoserine
icit	Isocitrate
ile_L	L-Isoleucine
imp	IMP
isobut	Isobutyl alcohol
k	Potassium
lac_D	D-Lactate
leu_L	L-Leucine
lys_L	L-Lysine
mal_L	L-Malate
malcoa	Malonyl-CoA
met_L	L-Methionine
mg2	Mg^{2+}
mlthf	5,10-Methylenetetrahydrofolate
mn2	Mn^{2+}
mobd	Molybdate
nad	Nicotinamide adenine dinucleotide
nadh	reduced Nicotinamide adenine dinucleotide
nadp	Nicotinamide adenine dinucleotide phosphate
nadph	reduced Nicotinamide adenine dinucleotide phosphate
nh4	Ammonium
ni2	Ni^{2+}
no2	Nitrite
no3	Nitrate
oaa	Oxaloacetate
pep	Phosphoenolpyruvate
phe_L	L-Phenylalanine
pi	Phosphate
pnto	(R)-Pantothenate
ppi	Diphosphate
pro_L	L-Proline
prpp	5-Phospho-alpha-D-ribose 1-diphosphate
pydx5p	Pyridoxal 5'-phosphate
pyr	Pyruvate
r5p	alpha-D-Ribose 5-phosphate
ribflv	Riboflavin
ru5p_D	D-Ribulose 5-phosphate
s7p	Sedoheptulose 7-phosphate
ser_L	L-Serine
so3	Sulfite
so4	Sulfate
succ	Succinate

teca_CL	glycerol teichoic acid
thf	5,6,7,8-Tetrahydrofolate
thm	Thiamin
thmpp	Thiamine diphosphate
thr_L	L-Threonine
trp_L	L-Tryptophan
tyr_L	L-Tyrosine
udcpdp	Undecaprenyl diphosphate
udp	UDP
ump	UMP
urea	Urea
utp	UTP
val_L	L-Valine
xu5p_D	D-Xylulose 5-phosphate
zn2	Zn^{2+}

Table 7.2: Reactions of the reduced stoichiometric metabolic model (rSMM)

Identifier	Reaction
ACALD	acald + coa + nad = Accoa + h + nadh
ACCOAL	accoa = Accoa
ACCOAS	co + coa + 5mthf = accoa + thf
ACKr	ac + atp = actp + adp + h
ACLDC	alac__S + h = actn__R + co2
ACLS	h + 2*pyr => alac__S + co2
ACONT	cit = icit
ADK1	amp + atp = 2*adp + 2*h
AICARS	prpp + 2*gln__L + 2*h2o + 4*atp + gly + 10fthf + co2 + asp__L => aicar + fum + 4*adp + 11*h + 4*pi + 2*glu__L + thf + ppi
ALCD2x	etoh + nad = acald + h + nadh
AMPS	imp + asp__L + gtp => pi + amp + fum + h + gdp
AOR_CL	ac + 3*h + fdxr_4_2 = acald + h2o + fdxo_4_2
ARA	2*arab__L + 2*atp => xu5p__D + r5p + 2*adp + 4*h
ARGS	accoa + 2*glu__L + nadph + 3*atp + co2 + nh4 + asp__L + h2o => coa + 6*h + 2*adp + nadp + 2*pi + akg + ac + amp + ppi + arg__L + fum
ASNS1	asp__L + atp + gln__L + h2o => amp + asn__L + glu__L + h + ppi
ASP4DC	asp__L + h => ala__L + co2
ASPSAS	asp__L + atp + nadph + h = aspsa + adp + nadp + pi + h
ASPT	asp__L => fum + nh4
ASPTA	akg + asp__L = glu__L + oaa
ATPM	atp + h2o => adp + pi + 2*h
ATPS4r	adp + pi + 3.66*H_ex + 2*h = atp + 3.66*H + h2o
BTDD_RR	btd_RR + nad => actn__R + h + nadh

Biomass	BMB + 0.000223*10fthf + 0.000223*5mthf + 0.000279*accoa + 0.000223*adocbl + 0.38513*ala__L + 0.000223*amet + 0.22177*arg__L + 0.18073*asn__L + 0.18073*asp__L + 46.719*atp + 2e-06*btn + 0.005098*ca2 + 0.000223*chor + 0.005098*cl + 0.000167*coa + 2.5e-05*cobalt2 + 0.000694*cu2 + 0.040484*ctp + 0.068661*cys__L + 0.029167*datp + 0.013104*dctp + 0.013104*dgtp + 0.029167*dttp + 0.000223*fad + 0.013822*fe2 + 0.1973*gln__L + 0.1973*glu__L + 0.45932*gly + 0.065225*gtp + 42.656*h2o + 0.071028*his__L + 0.21782*ile__L + 0.19118*k + 0.33778*leu__L + 0.25728*lys__L + 3.1e-05*malcoa + 0.11522*met__L + 0.008496*mg2 + 0.000223*mlthf + 0.000677*mn2 + 7e-06*mobd + 4.5e-05*nadh + 0.000335*nadph + 0.012745*nh4 + 0.000316*ni2 + 0.1389*phe__L + 0.16573*pro__L + 0.000223*pydx5p + 0.000223*ribflv + 0.16179*ser__L + 0.004248*so4 + 0.015433*teca_CL + 0.000223*thf + 0.000223*thmpp + 0.1902*thr__L + 0.042617*trp__L + 0.10339*tyr__L + 5.5e-05*udcpdp + 0.043698*utp + 0.31726*val__L + 0.000333*zn2 + 0.00961*Lipid + 0.0041*Cellwall => Biomass + 46.666*adp + 46.666*h + 46.6618*pi + 0.28697*ppi + 4.5e-05*nad + 0.000335*nadp
CDPS	atp + cmp = adp + cdp + h
CELLWALLSYNTHESIS	14*f6p + 14*accoa + 14*utp + 7*pep + 7*ala__L + 14*gln__L + 7*26dap__M + 7*ala__L + 6*nadph + 35*atp + 11*h2o => Cellwall + 14*coa + 14*ppi + 49*pi + 7*glu__L + 6*nadp + 35*adp + 7*ump + 7*udp + 97*h
CHORS_2	e4p + 2*pep + nadph + atp => 4*pi + nadp + adp + chor + 2*h
CODH4_1	co + fdxo_4_2 + h2o = co2 + fdxr_4_2 + 2*h
CS	accoa + h2o + oaa => cit + coa + h
CTPS	atp + gln__L + h2o + utp => adp + ctp + glu__L + 3*h + pi
CTPS1	atp + nh4 + utp => adp + ctp + 3*h + pi
CTPS2	cdp + atp = adp + ctp + h
CYS_LS	accoa + ser__L + h2s => ac + cys__L + 2*h + coa
CoASYNTHASE	pnto + 3*atp + ctp + cys__L = coa + 2*adp + cmp + 2*ppi + co2 + 2*h
DAPDC	26dap__M + h => co2 + lys__L
DHFR	fol + nadh = dhf + nad
Dihydrofolatereductase	dhf + nadph + h = thf + nadp
ENO	2pg = h2o + pep + h
FBA	fdp + h = dhap + g3p
FBP	fdp + h2o = f6p + pi
FDH	2*co2 + fdxr_4_2 + nadph + h = fdxo_4_2 + 2*for + nadp
FRD1	fum + nadh + h = succ + nad
FRNDPR2r_1	fdxr_4_2 + h + nadh + 2*nadp = fdxo_4_2 + nad + 2*nadph
FRUK	atp + f1p => adp + fdp + 2*h
FTHFLi	atp + for + thf = 10fthf + adp + pi
FUM	fum + h2o = mal__L
GABAS	arg__L + 2*h2o + akg + nad => urea + co2 + glu__L + 4abut + h + nadh
GAPD	g3p + nad + pi = 13dpg + h + nadh
GDPS	gmp + atp = adp + gdp + h
GLNS	atp + glu__L + nh4 => adp + gln__L + 2*h + pi
GLUDy	glu__L + h2o + nadp = akg + h + nadph + nh4
GLUS	akg + gln__L + h + nadph => 2*glu__L + nadp

GMPS	imp + 2*h2o + nad + atp + gln__L => 2*h + nadh + amp + glu__L + gmp + ppi
GTPS	atp + gdp = adp + gtp + h
Glycerolo xidase	glyc + atp + nad => dhap + adp + nadh + 2*h
HCO3E	co2 + h2o = h + hco3
HISS	atp + prpp + 3*h2o + gln__L + 2*nad => 2*ppi + 5*h + aicar +akg + pi + his__L + 2*nadh
HSDy	hom__L + nadp = aspsa + h + nadph
HYDFDN 2r	fdxo_4_2 + 2*h2 + nadp = fdxr_4_2 + 3*h + nadph
IBS	3mob + nadph + 2*h = isobut + co2 + nadp +
ICDHx	icit + nad = akg + co2 + nadh
ILEUS	2obut + 2*h + pyr + nadph + glu__L => co2 + nadp + h2o + akg + ile__L
IMPS	aicar + 10fthf => thf + imp + h2o + 2*h
LDH_D	lac__D + nad => h + nadh + pyr
LEUS	3mob + accoa + 2*h2o + nad + glu__L => coa + h + h2o + nadh + co2 + akg + leu__L
LIPIDSY NTHESIS	28*dhap + 256*accoa + 224*atp + 460*nadph + 16*ctp + 12*h2o + 4*ser__L => Lipid + 256*coa + 224*adp + 236*pi + 460*nadp + 016*cmp + 16*ppi + 4*co2 + 4*glyc + 12*h
LYSSII	aspsa + pyr + nadph + glu__L + h => nadp + akg + 26dap__M + h2o
MDH	mal__L + nad = h + nadh + oaa
ME1	mal__L + nad => co2 + nadh + pyr
ME2	mal__L + nadp => co2 + nadph + pyr
MET_LSII	hom__L + accoa + h2s + 5mthf => coa + h + ac + met__L + thf
MTHFR5	fdxo_4_2 + mlthf + 2*nadh = 5mthf + fdxr_4_2 + 2*nad
NO2R	2*fdxr_4_2 + no2 + 7*h + nadh => 2*fdxo_4_2 + 2*h2o + nad + nh4
NO3R	fdxr_4_2 + 2*h + no3 => fdxo_4_2 + h2o + no2
OIVS	2*pyr + nadph + 2*h => co2 + nadp + 3mob + h2o
PC	atp + hco3 + pyr => adp + 2*h + oaa + pi
PGK	3pg + atp = 13dpg + adp + 2*h
PGM	2pg = 3pg
PHES	chor + h + glu__L => co2 + h2o + akg + phe__L
POR_2	coa + fdxo_4_2 + pyr = accoa + co2+ fdxr_4_2 + h
PPA	h2o + ppi => h + 2*pi
PPCK	atp + oaa => adp + co2 + pep + h
PPDK	atp + pi + pyr => amp + pep + ppi + h
PROS	atp + glu__L + h + 2*nadph => adp + 2*nadp + pi+ h2o + pro__L
PRPPS	atp + r5p => amp + h + prpp
PTAr	Accoa + pi = actp + coa
PYK	adp + 2*h + pep => atp + pyr
RNF	fdxr_4_2 + H + nad + h = fdxo_4_2 + nadh + H_ex
RPE	ru5p__D = xu5p__D
RPI	r5p = ru5p__D
SERS	3pg + nad + glu__L + h2o => 2*h + nadh + akg + pi + ser__L
SHMT	mlthf + gly + h2o = thf + ser__L
SO3R	3*fdxr_4_2 + 8*h + so3 => 3*fdxo_4_2 + 3*h2o + h2s
SO4R	atp + gtp + h2o + so4 + nadph = so3 + amp + gdp + pi + ppi + nadp + h

TALA	g3p + s7p + h = e4p + f6p
THRAi	thr__L => acald + gly
THRD_L	thr__L => 2obut + nh4
THR_LS	atp + hom__L + h2o => adp + 2*h + pi + thr__L
TKT1	r5p + xu5p__D = g3p + s7p
TKT2	e4p + xu5p__D = f6p + g3p + h
TPI	dhap = g3p + h
TRP_LS	chor + gln__L + prpp + ser__L => glu__L + pyr + ppi + co2 + 2*h2o+ trp__L + g3p
TS_MTHFC_MTHFD	10fthf + nadph = h2o + mlthf + nadp
TYRS	chor + nad + glu__L => co2 + nadh + akg + tyr__L
UDCPDPSYNTHASE	11*g3p + 11*pyr + 33*nadph + 11*ctp + 11*atp + 22*h => udcpdp + 33*nadp + 11*cmp + 11*adp + 21*ppi + 22*h2o + 11*co2
UDPS	ump + atp = adp + udp + h
UMPS	2*atp + gln__L + hco3 + asp__L + prpp + nad => 2*adp + glu__L + 2*pi + ppi + co2 + ump + 4*h + nadh
UTPS	udp + atp = adp + utp
VALTA	akg + val__L = 3mob + glu__L
ametSYNTHASE	met__L + atp + h2o => amet + ppi + pi + h
dATPS	atp + 2*h + fdxr_4_2 => datp + fdxo_4_2 + h2o
dCTPS	ctp + 2*h + fdxr_4_2 => dctp + fdxo_4_2 + h2o
dGTPS	gtp + 2*h + fdxr_4_2 => dgtp + fdxo_4_2 + h2o
dTTPS	2*atp + ump + mlthf + fdxr_4_2 + h => 2*adp + h2o + fdxo_4_2 + dhf + dttp
fadSYNTHASE	ribflv + 2*atp => fad + adp + ppi + 2*h
malcoaSYNTHASE	accoa + atp + hco3 => malcoa + adp + pi + 2*h
pydx5pSYNTHASE	g3p + gln__L + r5p => pydx5p + glu__L + 3*h2o + pi + h
teca_CL_SYNTHASE	25*ala__L + 25*atp + 25*dhap + 25*nadph + 25*ctp + f6p + gln__L + accoa + utp => teca_CL + 25*nadp + 25*ppi + glu__L + coa + 25*amp + 25*cmp + 2*h + 26*ppi + udp
thmppSYNTHASE	thm + 2*atp => thmpp + 2*adp + 3*h
ARBabc	atp_external + h2o_external + arab__L_external => adp_C + arab__L_C + 2*h_C + pi_C
ARBt2r	h_external + arab__L_external
D_LACt2	h_external + lac__D_external
EX_BMB	BMB_C=BMB_external
EX_ac	ac_C = ac_external
EX_btd_RR	btd_RR_C=btd_RR_external
EX_btn	btn_external = btn_C
EX_co	co_external = co_C
EX_co2	co2_external = co2_C

EX_etoh	etoh_C = etoh_external
EX_h2	h2_external = h2_C
EX_h2s	h2s_C=h2s_external
EX_lac_D	lac__D_C=lac__D_external
EX_nh4	nh4_external = nh4_C
EX_pyr	pyr_C=pyr_external
EX_so3	so3_C=so3_external
Ex_arab_ _L	arab__L_C=arab__L_external
FRUpts	pep_C + fru_external => f1p_C + pyr_C
NO2t2r	h_external + no2_external = h_C + no2_C
NO3t2r	h_external + no3_external = h_C + no3_C
PYRt2	h_external + pyr_external
Pantothenate transport	pnto_external => pnto_C
Ribflv transport	ribflv_external => ribflv_C
T.h	h_C=h_external
T.h2o	h2o_C=h2o_external
T.hco3	hco3_C=hco3_external
T_4abut	4abut_C=4abut_external
T_Biomass	Biomass_C=Biomass_external
T_H	H_C=H_external
T_H_ex	H_ex_C=H_ex_external
T_KIV	3mob_C=3mob_external
accoa	for_C=for_external
T_isobut	isobut_C=isobut_external
T_succ	succ_C=succ_external
T_urea	urea_C=urea_external
T_val	val__L_C=val__L_external
adocbl transport	adocbl_external => adocbl_C
ca2 transport	ca2_external => ca2_C
cl transport	cl_external => cl_C
cobalt2 transport	cobalt2_C = cobalt2_external
cu2 transport	cu2_C = cu2_external
fe2 transport	fe2_external => fe2_C
fol transport	fol_external => fol_C
k transport	k_external => k_C
mg2 transport	mg2_external => mg2_C

mn2 transport	mn2_external => mn2_C
mobd transport	mobd_external => mobd_C
ni2 transport	ni2_external => ni2_C
phosphate transport	pi_C = pi_external
so4 transport	so4_external => so4_C
thm transport	thm_external => thm_C
zn2 transport	zn2_external => zn2_C

Table 7.3: Additional reaction in the modified reduced stoichiometric metabolic model (modified_rSMM)

Identifier	Reaction
FHL	for + h = co2 + h2

Table 7.4: Simulated average reaction rates for each condition applying FBA based on the rSMM. Simulated reaction rates for every experiment and corresponding standard deviations can be found online at (Excel tab: Flux simulations): https://sfamjournals.onlinelibrary.wiley.com/action/downloadSupplement?doi=10.1111%2F1751-7915.13625&file=mbt213625-sup-0002-Tables.xlsx

	Simulated average reaction rates, mmol $(g*h)^{-1}$				
Identifier	**CO Phase I**	**CO Phase II**	**CO_2/H_2**	**SG Phase I**	**SG Phase II**
ACALD	0.052	-0.030	-0.002	0.000	-0.006
ACCOAL	4.367	2.330	11.158	6.814	2.596
ACCOAS	6.194	3.447	11.446	8.764	3.831
ACKr	-4.310	-2.340	-11.160	-6.810	-2.590
ACLDC	0.550	0.462	0.000	0.675	0.506
ACLS	0.550	0.462	0.000	0.675	0.506
ACONT	0.046	0.009	0.019	0.034	0.011
ADK1	0.081	0.054	0.090	0.060	0.024
AICARS	0.009	0.002	0.004	0.007	0.002
ALCD2x	-4.100	-2.570	0.000	-4.780	-2.800
AMPS	0.009	0.002	0.004	0.006	0.002
AOR_CL	4.043	2.580	-0.020	4.737	2.794
ARA	0.000	0.000	0.000	0.000	0.000
ARGS	0.013	0.003	0.005	0.009	0.003
ASNS1	0.010	0.002	0.004	0.008	0.002
ASP4DC	0.047	0.009	0.020	0.035	0.011
ASPSAS	0.046	0.009	0.041	0.073	0.011
ASPT	0.000	0.000	0.000	0.000	0.000

ASPTA	-0.152	-0.031	-0.085	-0.152	-0.036
ATPM	5.000	5.000	5.000	5.000	5.000
ATPS4r	12.082	6.897	10.974	15.341	7.686
BTDD_RR	-0.550	-0.462	0.000	-0.675	-0.506
Biomass	0.057	0.011	0.024	0.042	0.014
CDPS	0.031	0.006	0.013	0.023	0.007
CELLWALLSYNTHESIS	0.000	0.000	0.000	0.000	0.000
CHORS_2	0.016	0.003	0.007	0.012	0.004
CODH4_1	29.684	17.223	-11.446	31.366	19.329
CS	0.046	0.009	0.019	0.034	0.011
CTPS	0.000	0.000	0.000	0.002	0.001
CTPS1	0.003	0.001	0.001	0.000	0.000
CTPS2	0.031	0.006	0.013	0.023	0.007
CYS_LS	0.004	0.001	0.002	0.003	0.001
CoASYNTHASE	0.000	0.000	0.000	0.000	0.000
DAPDC	0.015	0.003	0.006	0.011	0.003
DHFR	0.000	0.000	0.000	0.000	0.000
Dihydrofolatreductase	0.002	0.000	0.001	0.001	0.000
ENO	-0.154	-0.031	-0.042	-0.075	-0.037
FBA	-0.025	-0.005	-0.010	-0.018	-0.006
FBP	0.025	0.005	0.010	0.018	0.006
FDH	3.095	1.723	5.733	4.400	1.915
FRD1	0.000	0.000	0.000	0.000	0.000
FRNDPR2r_1	5.038	2.664	-2.804	5.002	3.047
FRUK	0.000	0.000	0.000	0.000	0.000
FTHFLi	6.190	3.446	11.466	8.800	3.830
FUM	0.031	0.006	0.013	0.023	0.007
GABAS	0.000	0.000	0.000	0.000	0.000
GAPD	-0.101	-0.020	-0.042	-0.075	-0.024
GDPS	0.004	0.001	0.002	0.003	0.001
GLNS	1.332	0.013	4.032	5.448	0.525
GLUDy	0.923	-0.070	3.861	5.142	0.426
GLUS	1.270	0.000	4.006	5.399	0.509
GMPS	0.004	0.001	0.002	0.003	0.001
GTPS	0.013	0.003	0.005	0.010	0.003
Glyceroloxidase	0.002	0.000	0.001	0.002	0.001
HCO3E	1.598	-0.782	-0.266	-3.290	-1.616
HISS	0.004	0.001	0.002	0.003	0.001
HSDy	-0.030	-0.006	-0.035	-0.061	-0.007
HYDFDN2r	0.000	0.000	23.180	3.860	-0.160
IBS	0.000	0.000	0.000	0.000	0.000
ICDHx	0.046	0.009	0.019	0.034	0.011
ILEUS	0.012	0.002	0.005	0.009	0.003
IMPS	0.013	0.003	0.006	0.010	0.003
LDH_D	-0.039	-0.054	0.000	-0.091	-0.060

LEUS	0.019	0.004	0.008	0.014	0.005
LIPIDSYNTHESIS	0.001	0.000	0.000	0.000	0.000
LYSSII	0.016	0.003	0.007	0.012	0.004
MDH	0.031	0.006	0.013	0.023	0.007
ME1	0.000	0.000	0.000	0.000	0.000
ME2	0.000	0.000	0.000	0.000	0.000
MET_LSII	0.007	0.001	0.003	0.005	0.002
MTHFR5	6.201	3.448	11.448	8.769	3.833
NO2R	0.000	0.000	0.000	0.000	0.000
NO3R	0.000	0.000	0.000	0.000	0.000
OIVS	0.037	0.008	0.016	0.028	0.009
PC	0.355	0.034	0.092	0.263	0.080
PGK	0.101	0.020	0.042	0.075	0.024
PGM	0.154	0.031	0.042	0.075	0.037
PHES	0.008	0.002	0.003	0.006	0.002
POR_2	-1.595	-1.070	-0.190	-1.779	-1.180
PPA	0.127	0.063	0.109	0.094	0.035
PPCK	0.188	0.000	0.000	0.100	0.040
PPDK	0.000	0.038	0.056	0.000	0.005
PROS	0.009	0.002	0.004	0.007	0.002
PRPPS	0.023	0.005	0.010	0.017	0.005
PTAr	4.310	2.340	11.160	6.810	2.590
PYK	0.000	0.000	0.000	0.000	0.000
RNF	22.109	12.622	20.082	28.073	14.065
RPE	-0.021	-0.004	-0.009	-0.015	-0.005
RPI	-0.021	-0.004	-0.009	-0.015	-0.005
SERS	0.053	0.011	0.000	0.000	0.013
SHMT	-0.035	-0.007	0.007	0.013	-0.008
SO3R	0.000	0.004	0.000	0.000	0.000
SO4R	0.000	0.000	0.000	0.000	0.000
TALA	-0.002	0.000	-0.001	-0.002	-0.001
THRAi	0.000	0.000	0.022	0.039	0.000
THRD_L	0.012	0.002	0.005	0.009	0.003
THR_LS	0.023	0.005	0.032	0.056	0.006
TKT1	-0.002	0.000	-0.001	-0.002	-0.001
TKT2	-0.018	-0.004	-0.008	-0.014	-0.004
TPI	-0.060	-0.012	-0.025	-0.044	-0.014
TRP_LS	0.002	0.000	0.001	0.002	0.001
TS_MTHFC_MTHFD	6.167	3.442	11.456	8.784	3.825
TYRS	0.006	0.001	0.002	0.004	0.001
UDCPDPSYNTHASE	0.000	0.000	0.000	0.000	0.000
UDPS	0.007	0.001	0.003	0.005	0.002
UMPS	0.007	0.001	0.003	0.005	0.002
UTPS	0.010	0.002	0.004	0.007	0.002
VALTA	-0.018	-0.004	-0.008	-0.013	-0.004

ametSYNTHASE	0.000	0.000	0.000	0.000	0.000
dATPS	0.002	0.000	0.001	0.001	0.000
dCTPS	0.001	0.000	0.000	0.001	0.000
dGTPS	0.001	0.000	0.000	0.001	0.000
dTTPS	0.002	0.000	0.001	0.001	0.000
fadSYNTHASE	0.000	0.000	0.000	0.000	0.000
malcoaSYNTHASE	0.000	0.000	0.000	0.000	0.000
pydx5pSYNTHASE	0.000	0.000	0.000	0.000	0.000
teca_CL_SYNTHASE	0.001	0.000	0.000	0.001	0.000
thmppSYNTHASE	0.000	0.000	0.000	0.000	0.000
ARBabc	0.000	0.000	0.000	0.000	0.000
ARBt2r	0.000	0.000	0.000	0.000	0.000
D_LACt2	0.000	0.000	0.000	0.000	0.000
EX_BMB	-0.057	-0.011	-0.024	-0.042	-0.014
EX_ac	0.290	-0.235	11.190	2.090	-0.199
EX_btd_RR	0.550	0.462	0.000	0.675	0.506
EX_btn	0.000	0.000	0.000	0.000	0.000
EX_co	35.878	20.670	0.000	40.130	23.160
EX_co2	-21.770	-14.450	22.760	-25.660	-17.030
EX_etoh	4.100	2.570	0.000	4.780	2.800
EX_h2	0.000	0.000	46.360	7.720	-0.320
EX_h2s	-0.011	0.002	-0.004	-0.008	-0.003
EX_lac_D	0.039	0.054	0.000	0.091	0.060
EX_nh4	0.414	0.083	0.172	0.306	0.098
EX_pyr	0.000	0.000	0.000	0.000	0.000
EX_so3	0.000	-0.004	0.000	0.000	0.000
Ex_arab__L	0.000	0.000	0.000	0.000	0.000
FRUpts	0.000	0.000	0.000	0.000	0.000
NO2t2r	0.000	0.000	0.000	0.000	0.000
NO3t2r	0.000	0.000	0.000	0.000	0.000
PYRt2	0.000	0.000	0.000	0.000	0.000
Pantothenate transport	0.000	0.000	0.000	0.000	0.000
Ribflv transport	0.000	0.000	0.000	0.000	0.000
T,h	-0.767	-1.476	9.857	-3.102	-2.392
T,h2o	-17.749	-9.049	24.021	-11.459	-9.515
T,hco3	1.236	-0.817	-0.361	-3.558	-1.698
T_4abut	0.000	0.000	0.000	0.000	0.000
T_Biomass	0.057	0.011	0.024	0.042	0.014
T_H	0.000	0.000	0.000	0.000	0.000
T_H_ex	0.000	0.000	0.000	0.000	0.000
T_KIV	0.000	0.000	0.000	0.000	0.000
T_for	0.000	0.000	0.000	0.000	0.000
T_isobut	0.000	0.000	0.000	0.000	0.000
T_succ	0.000	0.000	0.000	0.000	0.000
T_urea	0.000	0.000	0.000	0.000	0.000

T_val	0.000	0.000	0.000	0.000	0.000
adocbl transport	0.000	0.000	0.000	0.000	0.000
ca2 transport	0.000	0.000	0.000	0.000	0.000
cl transport	0.000	0.000	0.000	0.000	0.000
cobalt2 transport	0.000	0.000	0.000	0.000	0.000
cu2 transport	0.000	0.000	0.000	0.000	0.000
fe2 transport	0.001	0.000	0.000	0.001	0.000
fol transport	0.000	0.000	0.000	0.000	0.000
k transport	0.011	0.002	0.005	0.008	0.003
mg2 transport	0.000	0.000	0.000	0.000	0.000
mn2 transport	0.000	0.000	0.000	0.000	0.000
mobd transport	0.000	0.000	0.000	0.000	0.000
ni2 transport	0.000	0.000	0.000	0.000	0.000
phosphate transport	-0.047	-0.010	-0.020	-0.035	-0.011
so4 transport	0.000	0.000	0.000	0.000	0.000
thm transport	0.000	0.000	0.000	0.000	0.000
zn2 transport	0.000	0.000	0.000	0.000	0.000

Assumptions: (Villadsen et al. 2011)	
1. Balanced stoichiometry of the overall reaction	
2. Average elemental composition of biomass:	$CH_{1.81}O_{0.52}N_{0.21}$
3. Molecular weight of Biomass:	24.6 g (C-mole biomass)$^{-1}$
4. Formula:	

$$\Delta G_R = (\sum_i Y_{Pi/S} * \Delta G_{c,i})_{products} - (\sum_i Y_{Si/S} * \Delta G_{c,i})_{substrates}$$

$$-\Delta G_{Ci} = 94.4\kappa_i^* + 86.6\ kJ(C-mole)^{-1};\ \kappa_i^* > 0$$

5. Degrees of reduction (κ*) per carbon	
Compound	**κ***
Biomass	4.77
Acetic acid	4
Ethanol	6
2,3-Butanediol	5.50
Lactate	3.70
CO_2	0
CO	2
H_2	2
NH_3	0
H^+	0
H_2O	0

This assumption was made based on the fully oxidized status of a proton, as no reference in the literature could be found

Compound	ΔG_{ci}	experimentally determined Yields $Y_{i/Carbon\ Source}$, C-mole (C-mole)$^{-1}$					
		CO I	CO II	CO2/H2 I	CO2/H2 II	SG I	SG II
Biomass	-536.888	0.032	0.032	0.036	0.040	0.026	0.028
Acetic acid	-464.2	0.037	0.013	0.962	0.931	0.007	0.009
Ethanol	-653	0.203	0.236	0.011	0.019	0.231	0.232
2,3-Butanediol	-605.8	0.092	0.076	0.000	0.000	0.095	0.107
Lactate	-435.88	0.013	0.009	0.000	0.000	0.009	0.011
CO_2	0	0.679	0.654	-1.000	-1.000	0.712	0.716
CO	-275.4	-1.000	-1.000	0.000	0.000	-1.000	-1.000
H_2	-275.4	0.000	0.000	-1.844	-1.802	0.003	0.007
NH_3	0	-0.007	-0.007	-0.008	-0.008	-0.005	-0.006
H^+	0	0.157	0.002	0.104	-0.016	0.213	0.201
H_2O	0	-0.556	-0.485	1.033	1.059	-0.603	-0.622

calculated ΔG_R					
CO I	CO II	CO2/H2 I	CO2/H2 II	SG I	SG II
-46.75	-48.41	-34.66	-29.94	-45.03	-32.72

Figure 7.1: Determination of ΔG_R. The calculation can also be reproduced online at (Excel tab: delta GR determination): https://sfamjournals.onlinelibrary.wiley.com/action/downloadSupplement?doi=10.1111%2F1751-7915.13625&file=mbt213625-sup-0002-Tables.xlsx

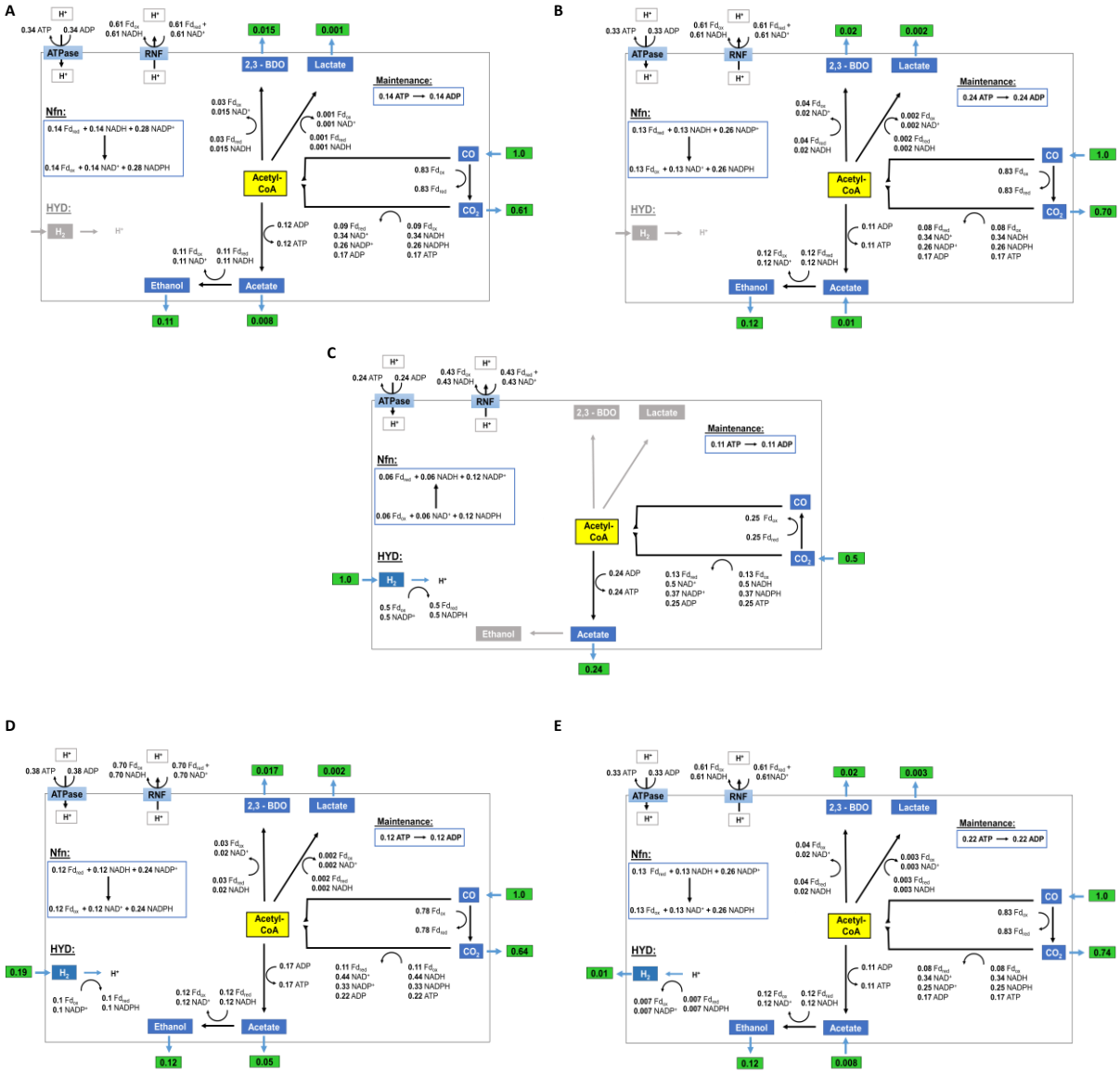

Figure 7.2: Metabolic fluxes of reducing equivalents and ATP formation for growth of *C. ljungdahlii* based on the conversion of CO in the first (A) and second growth Phase (B), on CO_2+H_2 (C) or syngas in the first (D) and second growth Phase (E). The simulated rates were normalized to the respective uptake rate of the energy source (CO or H_2). For each substrate condition two independent steadily gassed batch cultivations in stirred-tank bioreactors were performed (T = 37°C; pH = 5.9; V_R = 3 L; v = 500 rpm). Please see the figure in original size at: https://sfamjournals.onlinelibrary.wiley.com/action/downloadSupplement?doi=10.1111%2F1751-7915.13625&file=mbt213625-sup-0001-FigS1.png

Table 7.5: Determination of the exponential growth rate for each data set and growth phase observed using regression fitting. Summarized are the determined growth rates μ and the corresponding coefficients of determination R^2 for the cultivation experiments with the three substrate gases CO (39% CO, 4% CO_2, 57% Ar), CO_2+H_2 (47.5% H_2, 47.5% CO_2, 5% Ar) and syngas (55% CO, 30% H_2, 5% CO_2, 10% Ar) performed in duplicates

Results	CO I Phase 1	CO I Phase 2	CO II Phase 1	CO II Phase 2	CO_2+H_2 I	CO_2+H_2 II	Syngas I Phase 1	Syngas I Phase 2	Syngas II Phase 1	Syngas II Phase 2
μ. h^{-1}	0.055	0.013	0.057	0.010	0.025	0.026	0.038	0.014	0.048	0.013
R^2. -	0.998	0.97	0.991	0.974	0.999	0.996	0.992	0.998	0.996	0.912

Table 7.6: Experimentally determination of the substrate uptake and product formation rates rate for each data set and growth phase detected.Summarized are the biomass substrate and biomass product yields $Y_{x/s}$ and $Y_{X/P}$, the corresponding coefficients of determination R^2 as well as the subsequently determined substrate uptake and product formation rates for the cultivation experiments with the three substrate gases **CO** (39% CO, 4% CO_2, 57% Ar), **CO_2+H_2** (47.5% H_2, 47.5% CO_2, 5% Ar) **and syngas** (55% CO, 30% H_2, 5% CO_2, 10% Ar) performed in duplicates. Negative values reflect uptake rates, whereas positive rates represent formation rates.

Meta-bolite i	Results	CO I Phase 1	CO I Phase 2	CO II Phase 1	CO II Phase 2	CO_2+ H_2 I	CO_2+ H_2 II	Syn-gas I Phase 1	Syn-gas I Phase 2	Syn-gas II Phase 1	Syn-gas II Phase 2
CO	Yx/i. mol $gCDW^{-1}$	-1.44	-0.61	1.69	-0.52	/	/	-0.97	-0.68	-1.25	-0.53
	R^2, -	0.995	0.966	0.999	0.983	/	/	0.999	0.999	0.989	0.916
	q_i, mmol $(g_{CDW}*h)^{-1}$	-38.24	-21.20	-33.51	-20.14	/	/	-38.88	-20.87	-41.38	-25.46
H_2	$Y_{x/i}$, mol g_{CDW}^{-1}	/	/	/	/	-0.51	-0.53	-4.71	43.37	-6.99	42.13
	R^2, -	/	/	/	/	0.997	0.984	0.916	0.979	0.988	0.999
	q_i, mmol $(g_{CDW}*h)^{-1}$	/	/	/	/	-43.38	-49.34	-8.04	0.32	-7.41	-0.318
Acetate	$Y_{x/i}$, mol g_{CDW}^{-1}	264.0	-91.8	133.8	-31.7	2.2	2.2	15.1	-108.1	31.4	-49.7
	R^2, -	0.933	0.858	0.587	0.996	0.993	0.989	0.985	0.901	0.999	0.833
	q_i, mmol $(g_{CDW}*h)^{-1}$	0.21	-0.14	0.38	-0.33	10.49	11.89	2.52	-0.13	1.65	-0.27
Ethanol	$Y_{x/i}$, mol g_{CDW}^{-1}	11.87	5.08	15.87	4.02	/	/	7.95	5.95	10.78	4.08
	R^2, -	0.993	0.958	0.909	0.96	/	/	0.966	0.999	0.982	0.939
	q_i, mmol $(g_{CDW}*h)^{-1}$	4.634	2.559	3.566	2.584	/	/	4.760	2.321	4.807	3.283
2,3-Butane-diol	$Y_{x/i}$, mol g_{CDW}^{-1}	102.3	27.31	100.4	23.26	/	/	73.82	25.78	61.80	19.23
	R^2, -	0.983	0.958	0.986	0.982	/	/	0.962	0.997	0.983	0.885
	q_i, mmol $(g_{CDW}*h)^{-1}$	0.537	0.476	0.564	0.447	/	/	0.512	0.535	0.838	0.476

Lactate	$Y_{x/i}$, mol g_{CDW}^{-1}	1389	229	1507	200	/	/	398	289	636	185
	R^2, -	0.999	0.996	0.854	0.981	/	/	0.999	0.975	0.979	0.964
	q_i, mmol $(g_{CDW}*h)^{-1}$	0.040	0.057	0.037	0.051	/	/	0.095	0.048	0.081	0.072
CO_2	$Y_{x/i}$, mol g_{CDW}^{-1}	2.435	0.920	2.701	0.704	-1.049	-1.084	1.963	0.909	1.616	0.710
	R^2, -	0.992	0.967	0.99	0.983	0.983	0.996	0.991	0.999	0.990	0.916
	q_i, mmol $(g_{CDW}*h)^{-1}$	22.582	14.131	20.956	14.771	-21.258	-24.271	19.270	15.183	32.049	18.876

Table 7.7: Mean values of the uptake and secretion fluxes used as constraints for FBA and the corresponding standard deviations for the cultivation experiments with the three substrate gases **CO** (39% CO, 4% CO_2, 57% Ar), **CO_2+H_2** (47.5% H_2, 47.5% CO_2, 5% Ar) **and syngas** (55% CO, 30% H_2, 5% CO_2, 10% Ar) performed in duplicates.

Metabolite i	Results	CO Phase 1	CO Phase 2	CO_2+H_2	Syngas Phase 1	Syngas Phase 2
CO	mean rate q_i, mmol $(g_{CDW}*h)^{-1}$	-35.878	-20.668	/	-40.132	-23.164
	standard deviation, mmol $(g_{CDW}*h)^{-1}$	3.344	0.753	/	1.766	3.242
H_2	mean rate q_i, mmol $(g_{CDW}*h)^{-1}$	/	/	-46.360	-7.724	0.318
	standard deviation, mmol $(g_{CDW}*h)^{-1}$	/	/	4.219	0.44	0.9*10*-5
Acetate	mean rate q_i, mmol $(g_{CDW}*h)^{-1}$	0.292	-0.235	11.189	2.086	-0.199
	standard deviation, mmol $(g_{CDW}*h)^{-1}$	0.119	0.132	0.987	0.614	0.1
Ethanol	mean rate q_i, mmol $(g_{CDW}*h)^{-1}$	4.1	2.571	/	4.784	2.802
	standard deviation, mmol $(g_{CDW}*h)^{-1}$	0.756	0.018	/	0.033	0.68
2,3-Butanediol	mean rate q_i, mmol $(g_{CDW}*h)^{-1}$	0.55	0.462	/	0.675	0.506
	standard deviation, mmol $(g_{CDW}*h)^{-1}$	0.019	0.02	/	0.23	0.042
Lactate	mean rate q_i, mmol $(g_{CDW}*h)^{-1}$	0.039	0.054	/	0.091	0.06
	standard deviation, mmol $(g_{CDW}*h)^{-1}$	1,4*10*-3	0.003	/	0.0131	0.017
CO_2	mean rate q_i, mmol $(g_{CDW}*h)^{-1}$	21.769	14.451	-22.765	25.659	17.03
	standard deviation, mmol $(g_{CDW}*h)^{-1}$	1.15	0.452	2.13	9.036	2.611

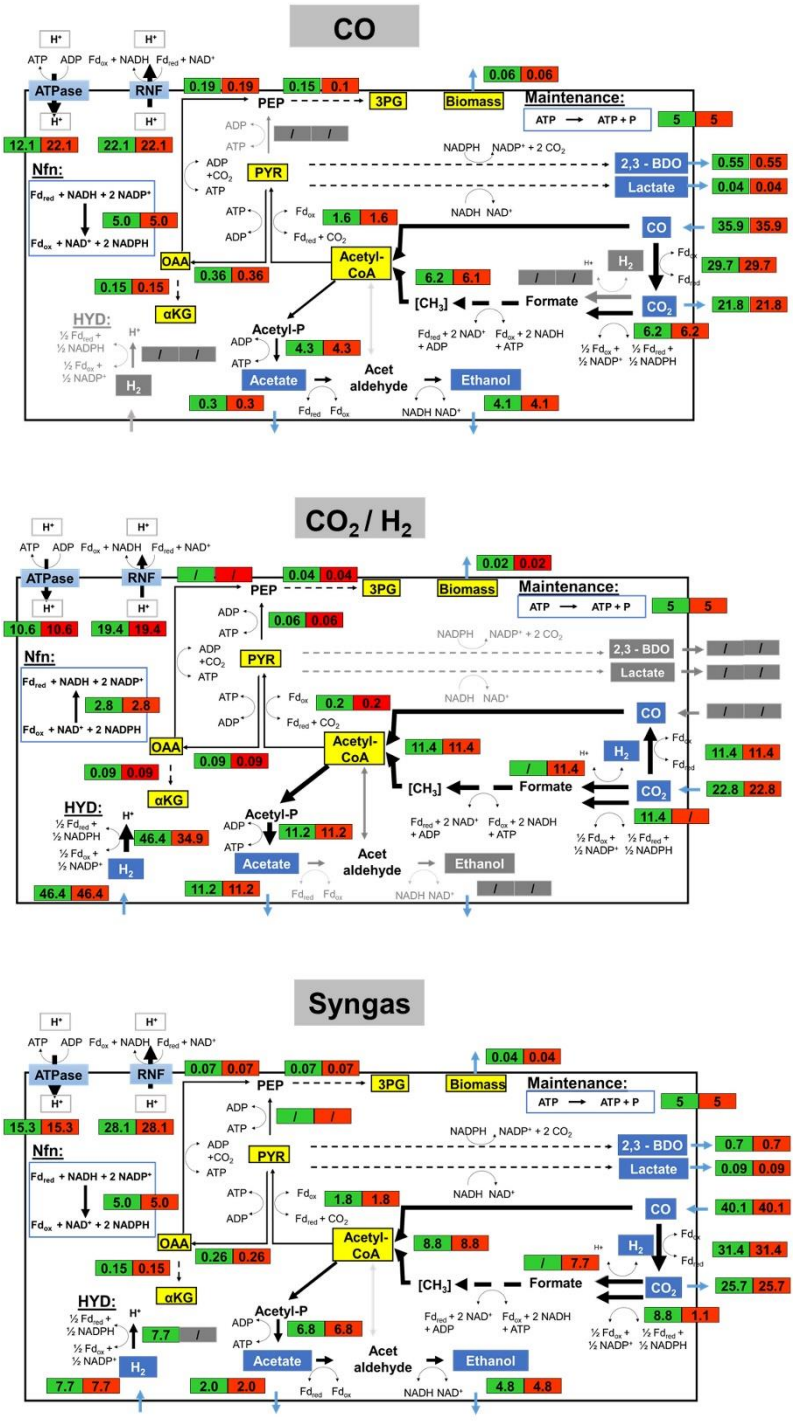

Figure 7.3: Comparison of the simulated fluxes using the models rSMM and modified rSMM. Illustrated are the metabolic flux distributions of *C. ljungdahlii* based on the conversion of CO, CO_2 + H_2 and syngas in steadily gassed batch cultivations in stirred-tank bioreactors, performed in duplicates. Illustrated are the simulated fluxes in mmol $(g_{CDW}*h)^{-1}$ for the first growth phase using the models rSMM (■) and modified rSMM (■). A tabular listing of the associated fluxes can be found online at: (Excel tab: Comparison rSMM_modified rSMM)
https://sfamjournals.onlinelibrary.wiley.com/action/downloadSupplement?doi=10.1111%2F1751-7915.13625&file=mbt213625-sup-0002-Tables.xlsx

Table 7.8: ATP, Fd_{red} and NAD^+ yields derived from flux balance analysis using the models rSMM and modified rSMM considering exponentially growing *C. ljungdahlii* based on CO, CO_2+H_2 or syngas as substrates. The illustrated ATP yields refer to the ATPase activity coupled to the Rnf complex.

	rSMM	modified rSMM	rSMM	modified rSMM	rSMM	modified rSMM	rSMM	modified rSMM
Substrate	**ATP, mole $mole_{(CO+H2)}^{-1}$**	**ATP, mole $mole_{(CO+H2)}^{-1}$**	**Fd_{red}, mole $mole_{(CO+H2)}^{-1}$**	**Fd_{red}, mole $mole_{(CO+H2)}^{-1}$**	**NAD^+, mole $mole_{(CO+H2)}^{-1}$**	**NAD^+, mole $mole_{(CO+H2)}^{-1}$**	**NADPH, mole $mole_{(CO+H2)}^{-1}$**	**NADPH, mole $mole_{(CO+H2)}^{-1}$**
CO	0.34	0.34	0.77	0.77	0.49	0.49	0.02	0.02
CO_2+H_2	0.24	0.24	0.44	0.44	0.43	0.43	0.008	0.008
Syngas	0.32	0.32	0.72	0.72	0.47	0.47	0.014	0.014

Table 7.9: Percentage provision of NAD^+ and Fd_{red} and consumption of NADH and NADPH in the methyl branch derived from flux balance analysis using the models rSMM and modified rSMM considering exponentially growing cells of *C. ljungdahlii* based on CO, CO_2+H_2 or syngas as substrates.

	rSMM	modified rSMM	rSMM	modified rSMM	rSMM	modified rSMM	rSMM	modified rSMM
Substrate	**NAD^+, %**	**NAD^+, %**	**Fd_{red}, %**	**Fd_{red}, %**	**NADH, %**	**NADH, %**	**NADPH, %**	**NADPH, %**
CO	56.10	56	8.66	8.66	56.10	56.10	92.16	92.16
CO_2/H_2	100	100	16.54	39.64	100	100	74.16	65.67
Syngas	62.70	62.63	9.95	20.52	62.70	62.63	95.09	93.20

7.2 Supplementary Material to Manuscript II

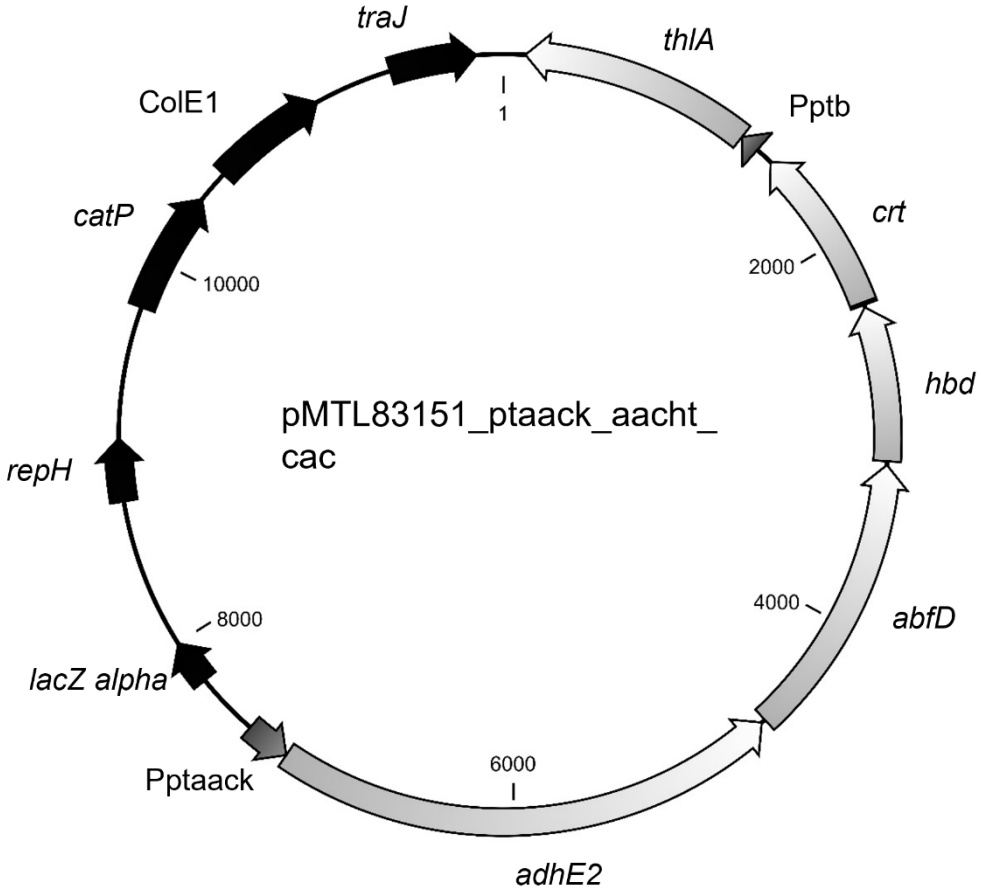

Figure 7.4: Schematic representation of plasmid pMTL83151_ptaack_aacht_cac. *adhE2*, bifunctional aldehyde/alcohol dehydrogenase gene (*C. acetobutylicum*); *abfD*, 4-hydroxybutyryl-CoA dehydratase gene (*Clostridium scatologenes*); *crt*, crotonase gene (*C. acetobutylicum*); *hbd*, 3-hydroxybutyryl-CoA dehydrogenase gene (*C. acetobutylicum*); *thlA*, acetyl-CoA acetyltransferase gene (*C. acetobutylicum*); *catP*, chloramphenicol resistance gene; ColE1, origin of replication for Gram-negative bacteria; *repH*, origin of replication for Gram-positive bacteria; *lacZ* alpha, truncated b-galactosidase gene (*E. coli*); *traJ*, gene for DNA transfer by conjugation.

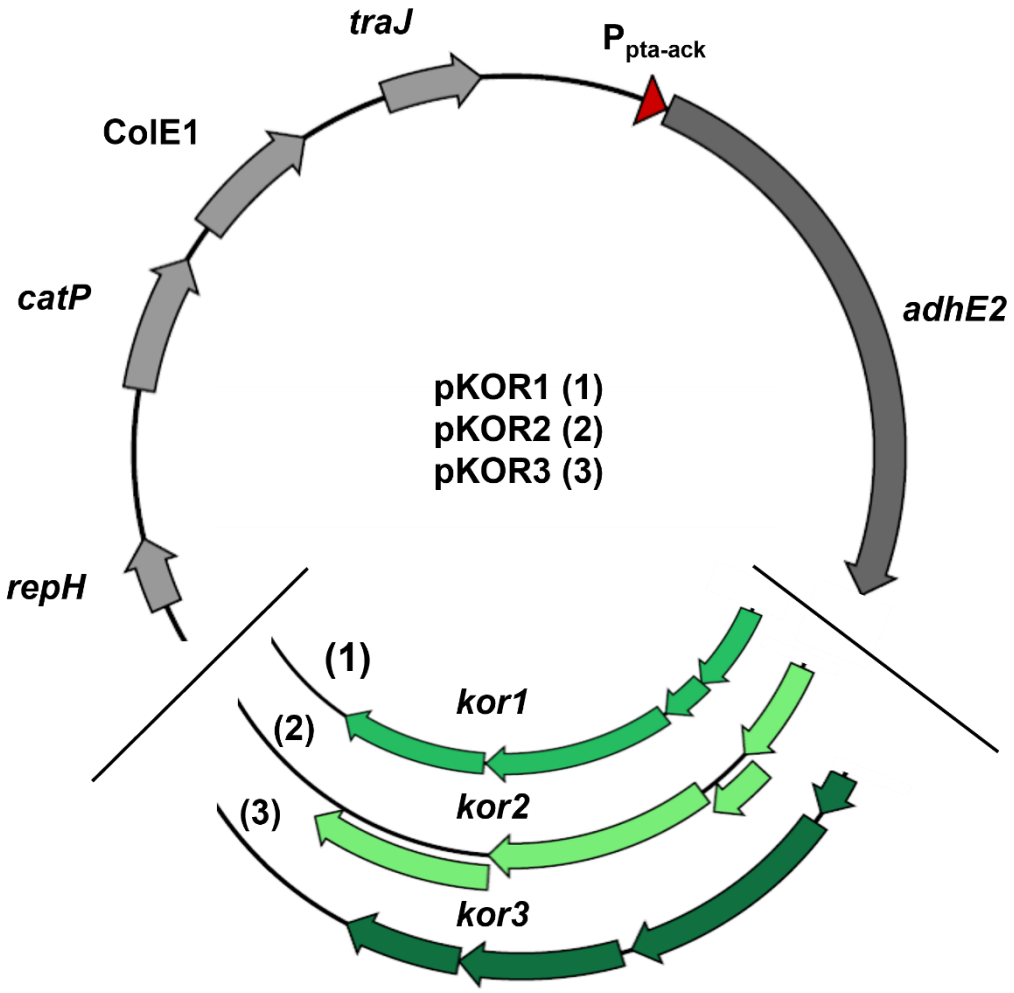

Figure 7.5: Schematic representation of plasmids pKOR1, pKOR2 and pKOR3. *kor1*, *kor2*, *kor3*, potential ketoisovalerate ferredoxin oxidoreductases gene clusters (*C. thermocellum*); *adhE2* bifunctional aldehyde/alcohol dehydrogenase gene (*C. acetobutylicum*); $P_{pta\text{-}ack}$, promoter upstream of *pta-ack* genes *(C. ljungdahlii*); *catP*, chloramphenicol resistance gene; ColE1, origin of replication for Gram-negative bacteria; *repH*, origin of replication for Gram-positive bacteria; *traJ*, gene for DNA transfer by conjugation.

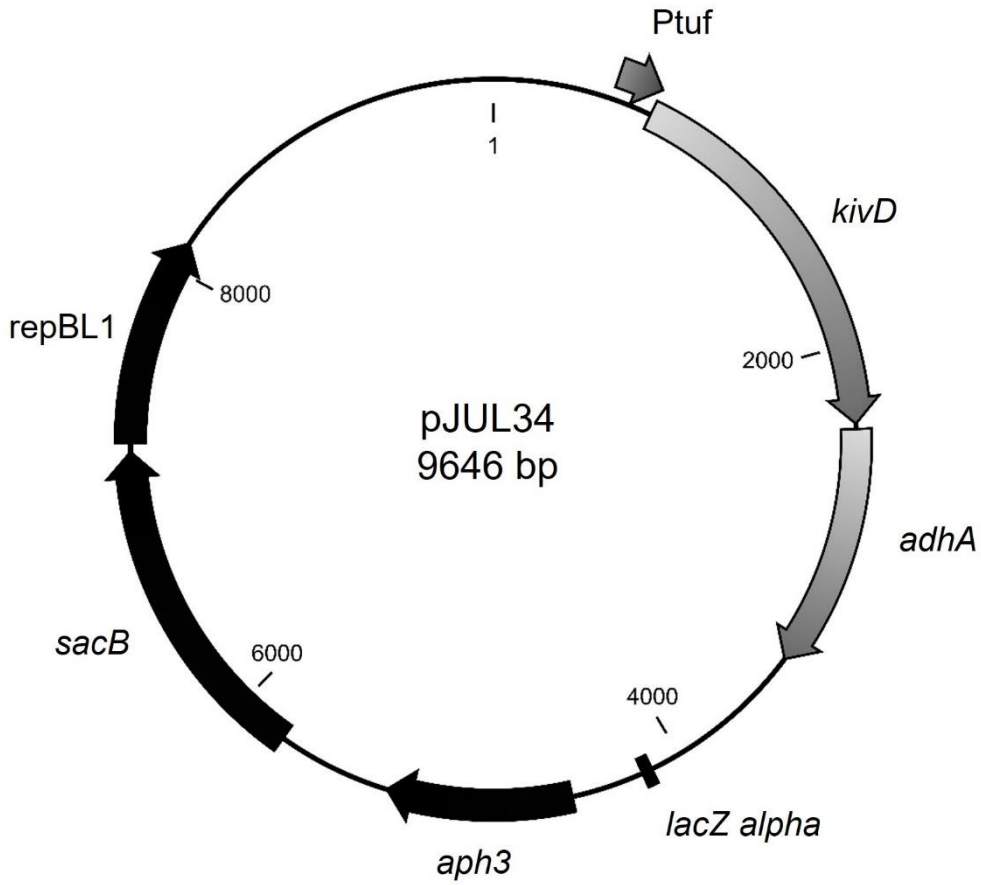

Figure 7.6: Schematic representation of plasmid pJUL34. P_{tuf}, promoter upstream of EF-Tu gene (*L. lactis*); *kivD*, ketoisovalerate decarboxylase gene (*L. lactis*); *adhA*, alcohol dehydrogenase gene (*Corynebacterium glutamicum*); *lacZ alpha*, truncated b-galacosidase gene (*E. coli*); *aph3,* kanamycin resistance gene; *sacB,* levansucrase gene; repBL1, origin of replication for *Corynebacterium*.

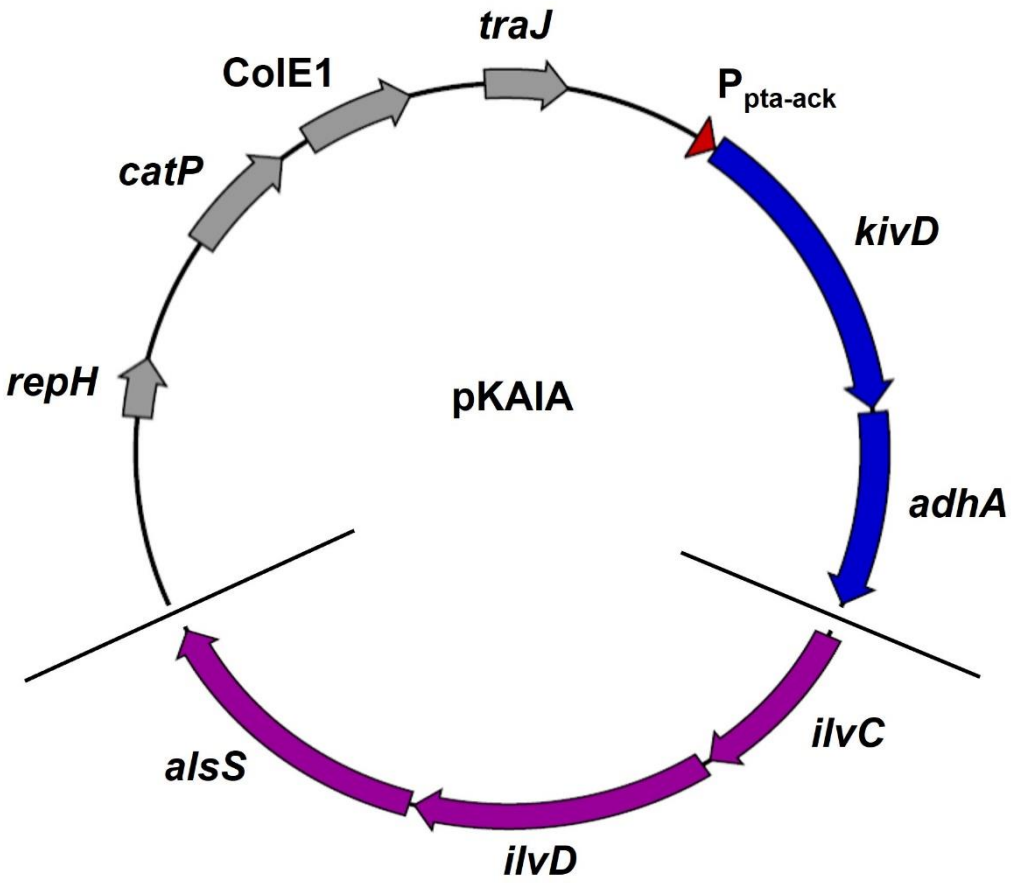

Figure 7.7: Schematic representation of plasmid pKAIA. *kivD*, ketoisovalerate decarboxylase gene (*L. lactis*); *adhA*, alcohol dehydrogenase gene (*C. glutamicum*); *ilvC*, ketol-acid reductoisomerase gene (*C. ljungdahlii*); *ilvD*, dihydroxy-acid dehydratase gene (*C. ljungdahlii*); *alsS*, acetolactate synthase gene (*C. ljungdahlii*); $P_{pta\text{-}ack}$, promoter upstream of *pta-ack* genes (*C. ljungdahlii*); *catP*, chloramphenicol resistance gene; ColE1, origin of replication for Gram-negative bacteria; *repH*, origin of replication for Gram-positive bacteria; *traJ*, gene for DNA transfer by conjugation.

ATGGCAAATTATTTTAATACACTTAATCTTAGACAACAACTTGCACAACTTGGAAAATGTAGATTTATGGGAAGAGATGAATTTGC
AGATGGTGCAAGTTATCTTCAGGGAAAAAAAGTTGTTATAGTTGGATGTGGTGCACAAGGACTTAATCAGGGACTTAATATGAGA
GATAGTGGACTTGATATAAGTTATGCACTTAGAAAAGAAAGTATAGCAGAAAAAGATGCAGATTGGAGAAAAGCAACAGAAAAT
GGATTTAAAGTTGGAACATATGAAGAATTAATACCTCAAGCAGATCTTGTTATAAATCTTACACCTGATAAAGTTCATTCAGATGTT
GTTAGAACAGTTCAACCTCTTATGAAAGATGGTGCTGCACTTGGATATAGTCATGGTTTTAATATAGTTGAAGTTGGAGAACAAAT
AAGAAAGGGAATAACAGTTGTAATGGTTGCACCTAAATGTCCTGGAACAGAAGTTAGAGAAGAGTATAAGAGAGGATTTGGAG
TTCCTACACTTATAGCAGTTCATCCTGAAAATGATCCTAAAAGAGAAGGTATGGCAATAGCAAAAGCATGGGCAGCAGCAACAGG
TGGACATAGAGCTGGTGTTTTAGAAAGTAGTTTTGTTGCAGAAGTTAAATCAGATCTTATGGGAGAACAGACAATACTTTGTGGA
ATGCTTCAAGCAGGATCACTTCTTTGCTTTGATAAGCTTGTTGAAGAGGGAACTGATCCAGCATATGCAGAAAAGCTTATACAGT
TTGGATGGGAAACAATAACAGAAGCACTTAAACAAGGTGGAATAACACTTATGATGGATAGACTTAGCAATCCTGCAAAGTTAAG
AGCTTATGCTCTTTCAGAGCAACTTAAAGAAATAATGGCACCTCTTTTTCAAAAACATATGGATGATATAATAAGCGGAGAATTTA
GTAGTGGAATGATGGCAGATTGGGCAAATGATGATAAAAAACTTCTTACTTGGAGAGAAGAAACTGGAAAAACAGCATTTGAA
ACAGCACCTCAATATGAGGGAAAGATAGGTGAGCAAGAATATTTTGATAAAGGTGTTCTTATGATAGCAATGGTTAAGGCTGGTG
TTGAACTTGCATTTGAGACAATGGTTGATAGTGGAATAATAGAAGAAAGTGCATATTATGAATCACTTCATGAATTACCTCTTATAG
CAAATACAATTGCAAGAAAAAGACTTTATGAAATGAATGTTGTTATAAGTGATACAGCAGAATATGGAAATTATCTTTTTAGTTATG
CATGTGTTCCTTTACTTGAACCTTTTATGGCAGAACTTCAACCTGGTGATCTTGGAAAAGCAATACCTGAAGGTGCAGTTGATAAT
GGACAACTTAGAGATGTTAATGAAGCAATAAGAAGTCATGCAATAGAACAAGTTGGAAAAAAGCTTAGAGGATATATGACAGAT
ATGAAAAGAATAGCAGTTGCAGGATAA

Figure 7.8: Sequence of the commercially synthesized and codon-optimized *ilvC*^{NADH} gene.

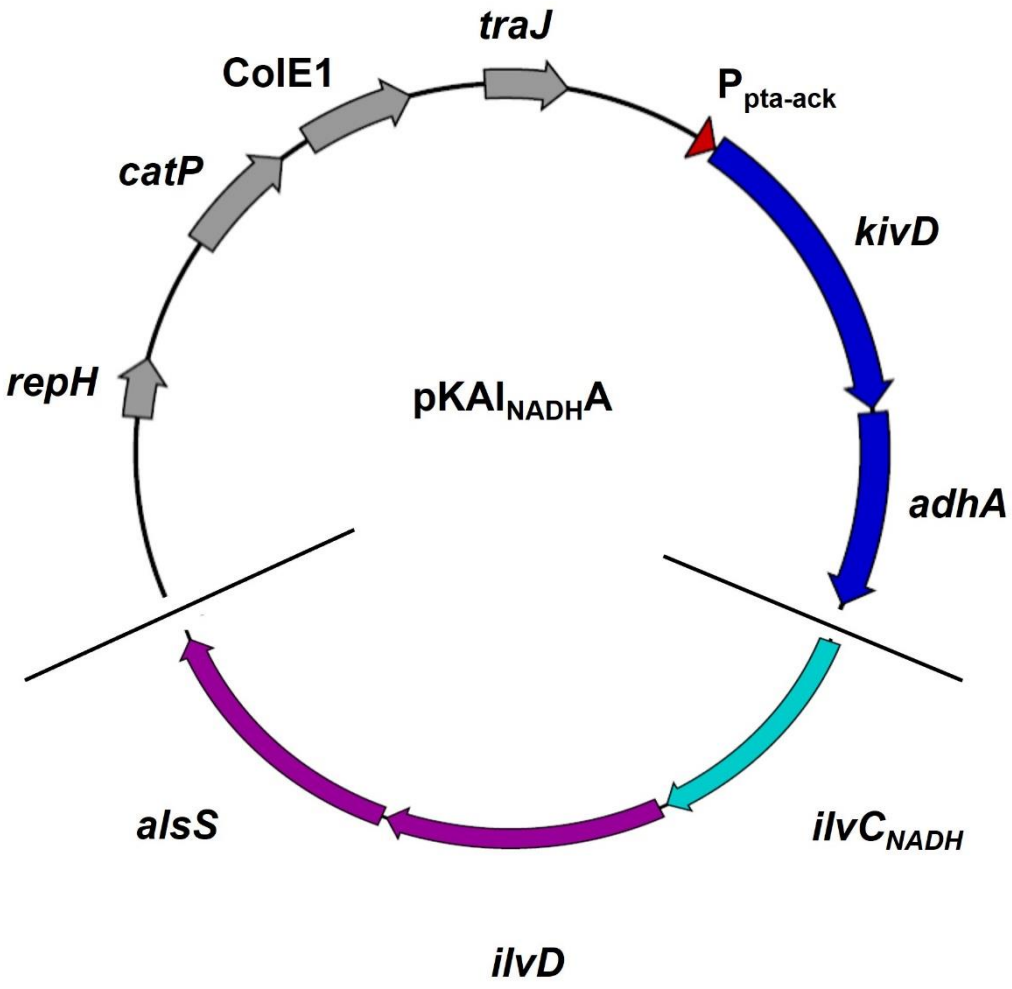

Figure 7.9: Schematic representation of plasmid pKAI$_{NADH}$A. *kivD*, ketoisovalerate decarboxylase gene (*L. lactis*); *adhA*, alcohol dehydrogenase gene (*Corynebacterium glutamicum*); *ilvC*, ketol-acid reductoisomerase gene (*C. ljungdahlii*); i*lvC*^{NADH}, NADH-dependent ketol-acid reductoisomerase gene (Ec_IlvCP2D1-A1 from *E. coli*, codon-optimized for clostridia); *ilvD*, dihydroxy-acid dehydratase gene (*C. ljungdahlii*); *alsS*, acetolactate synthase gene (*C. ljungdahlii*); P$_{pta-ack}$, promoter upstream of *pta-ack* genes (*C. ljungdahlii*); *catP*, chloramphenicol resistance gene; ColE1, origin of replication for Gram-negative bacteria; *repH*, origin of replication for Gram-positive bacteria; *traJ*, gene for DNA transfer by conjugation.

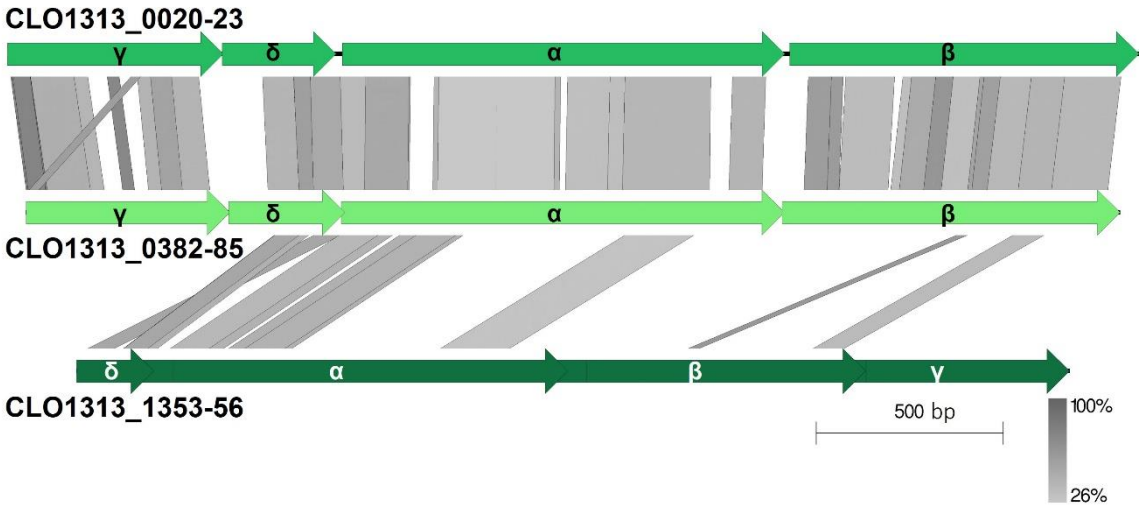

Figure 7.10: tBLASTx comparison of gene clusters Clo1313_0020-0023 [*kor1*], Clo1313_0382-0385 [*kor2*], and Clo1313_1353-1356 [*kor3*] from *C. thermocellum*.

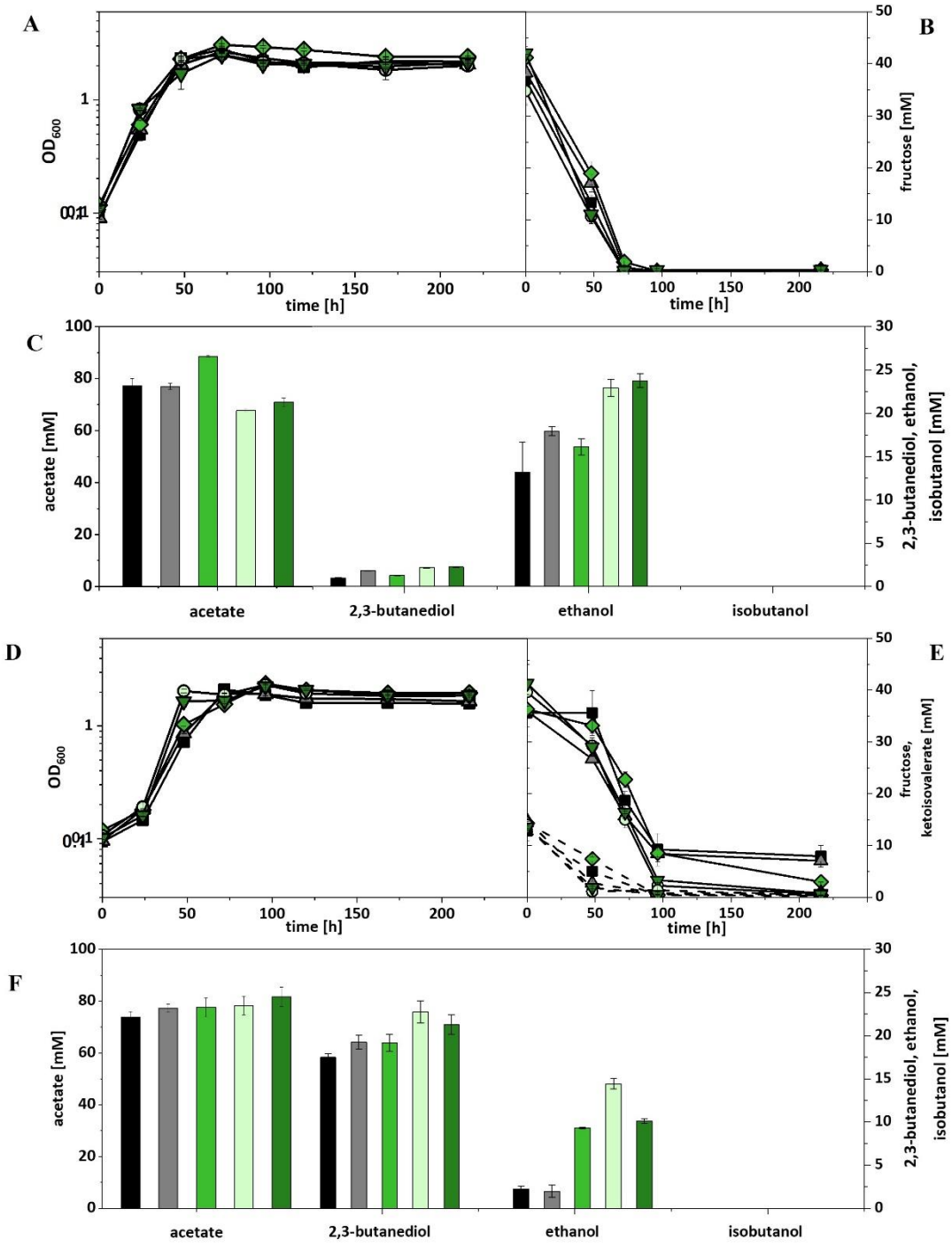

Figure 7.11: Heterotrophic isobutanol production with recombinant *C. ljungdahlii* strains by the Kor pathway. Growth behavior (**A,D**); fructose consumption (**B,E**); ketoisovalerate consumption (E); product pattern (C,F). *C. ljungdahlii* [WT], black, squares; *C. ljungdahlii* [pM83], gray, triangles; *C. ljungdahlii* [pKOR1], green, diamonds; *C. ljungdahlii* [pKOR2], light green, circles; *C. ljungdahlii* [pKOR3], dark green, triangle pointing downward. Panels (**A–C**) without ketoisovalerate supplementation; Panels (**D–F**) with ketoisovalerate supplementation. Each strain was analyzed in biological triplicates(*n = 3*).

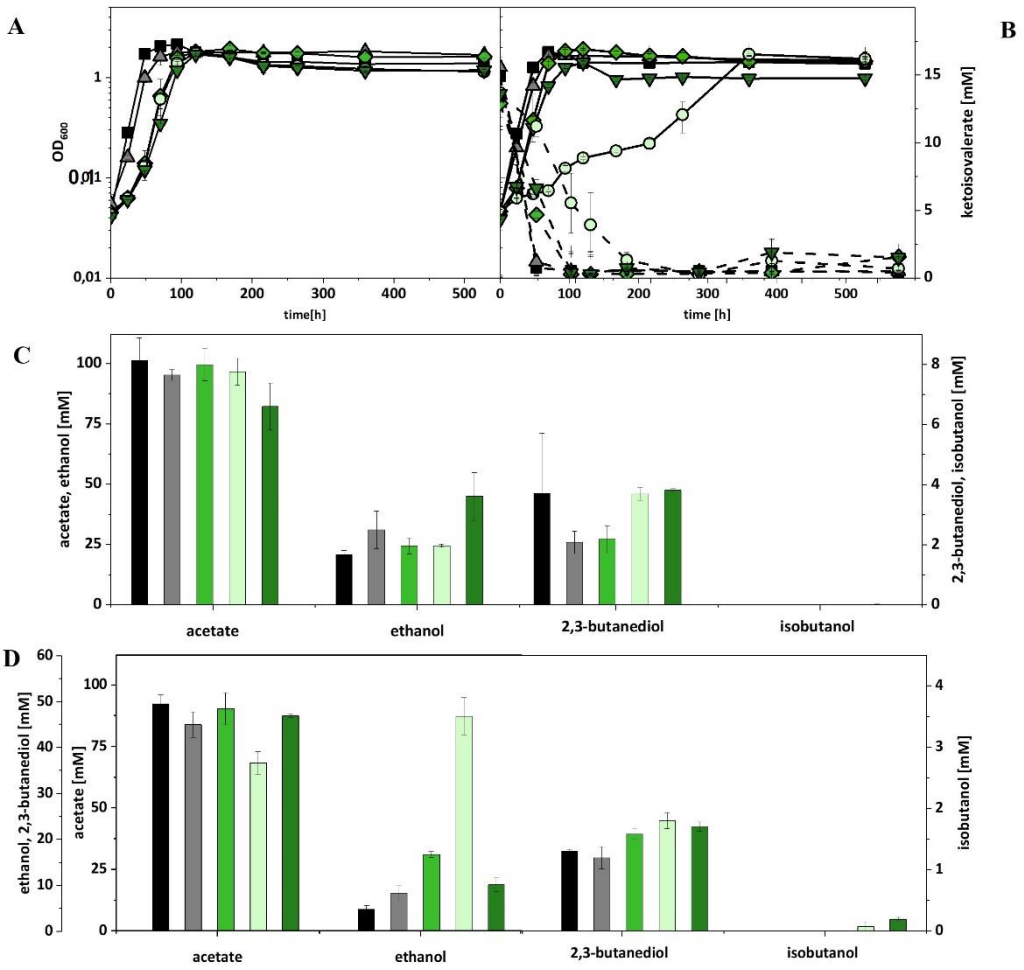

Figure 7.12: Autotrophic isobutanol production with recombinant *C. ljungdahlii* strains by the Kor pathway. Growth behavior (**A,B**); ketoisovalerate consumption (**B**); product pattern (C,D). *C. ljungdahlii* [WT], black, squares; *C. ljungdahlii* [pM83], gray, triangles; *C. ljungdahlii* [pKOR1], green, diamonds; *C. ljungdahlii* [pKOR2], light green, circles; *C. ljungdahlii* [pKOR3], dark green, triangle pointing downward. Panels **(A,C**) without ketoisovalerate supplementation; Panels (**B,D**) with ketoisovalerate supplementation. Each strain was analyzed in biological triplicates (*n = 3*).

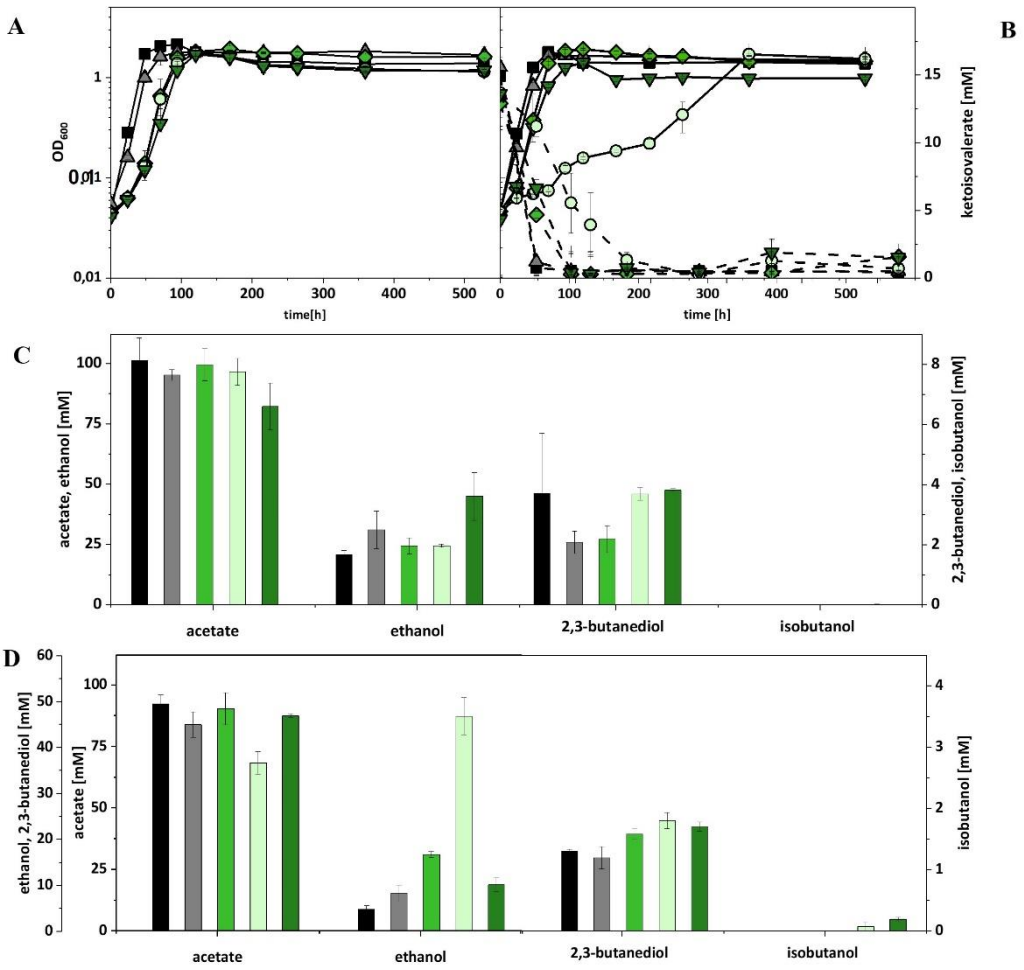

Figure 7.13: Heterotrophic isobutanol production with recombinant *A. woodii* strains by the KivD pathway. Growth behavior (A,D); fructose consumption (**B,E**); ketoisovalerate consumption (**E**); product pattern (**C,F**). *A. woodii* [WT], black, squares*; A. woodii* [pM83], gray, triangles; *A. woodii* [pKAIA], blue, diamonds. Panels (**A–C**) without ketoisovalerate supplementation; Panels (**D–F**), with ketoisovalerate supplementation. Each strain was analyzed in biological triplicates (*n* = *3*).

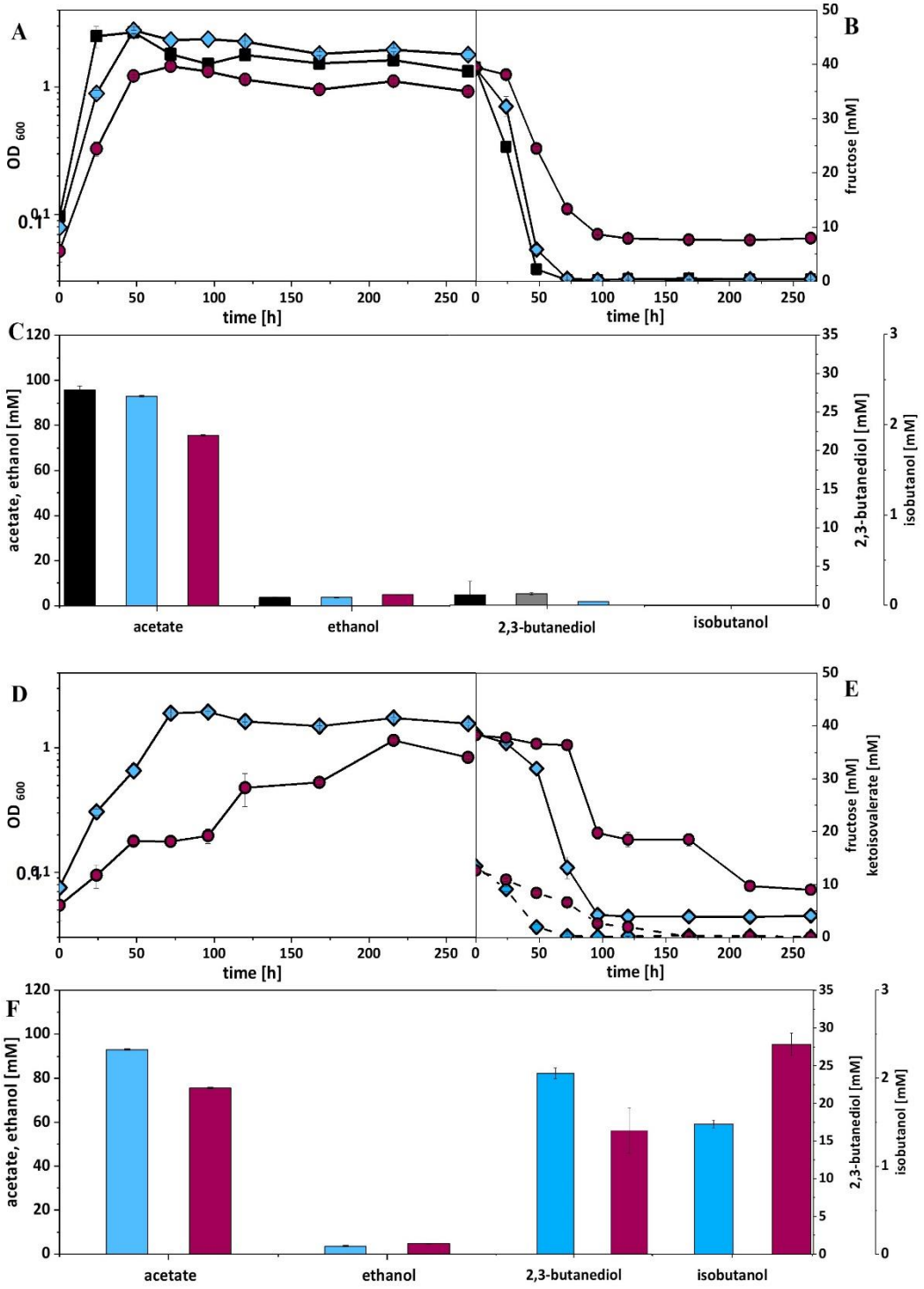

Figure 7.14: Heterotrophic isobutanol production with recombinant *C. ljungdahlii* strains by the KivD pathway. Growth behavior (**A,D**); fructose consumption (**B,E**); ketoisovalerate consumption (E); product range (C,F). *C. ljungdahlii* [WT], black, squares; *C. ljungdahlii* [pKAIA], blue, diamonds; *C. ljungdahlii:ilvE* [pKAIA], purple, circles. Panels (**A–C**) without ketoisovalerate supplementation; Panels (**D–F**) with ketoisovalerate supplementation. Each strain was analyzed in biological triplicates (*n = 3*).

7.3 Supplementary Material to Manuscript III

Table 7.10: Determination of the exponential growth rate for each data set and growth phase observed using regression fitting. Summarized are the determined growth rates μ and the corresponding coefficients of determination R^2 for the cultivation experiments with the three strains CLJU[WT, REF], CLJU[KAIA] and CLJU[KAIA]::*ilvE*

Results	CLJU [WT] I Phase 1	CLJU [WT] I Phase 2	CLJU [WT] II Phase 1	CLJU [WT] II Phase 2	CLJU [KAIA] Phase 1	CLJU [KAIA] Phase 2	CLJU[KAIA] ::ilve[KAIA] Phase 1	CLJU[KAIA] ::ilve[KAIA] Phase 2
μ. h-1	0.044	0.012	0.052	0.013	0.072	0.020	0.055	0.011
R^2. -	0.998	0.969	0.992	0.993	0.996	0.994	0.999	0.945

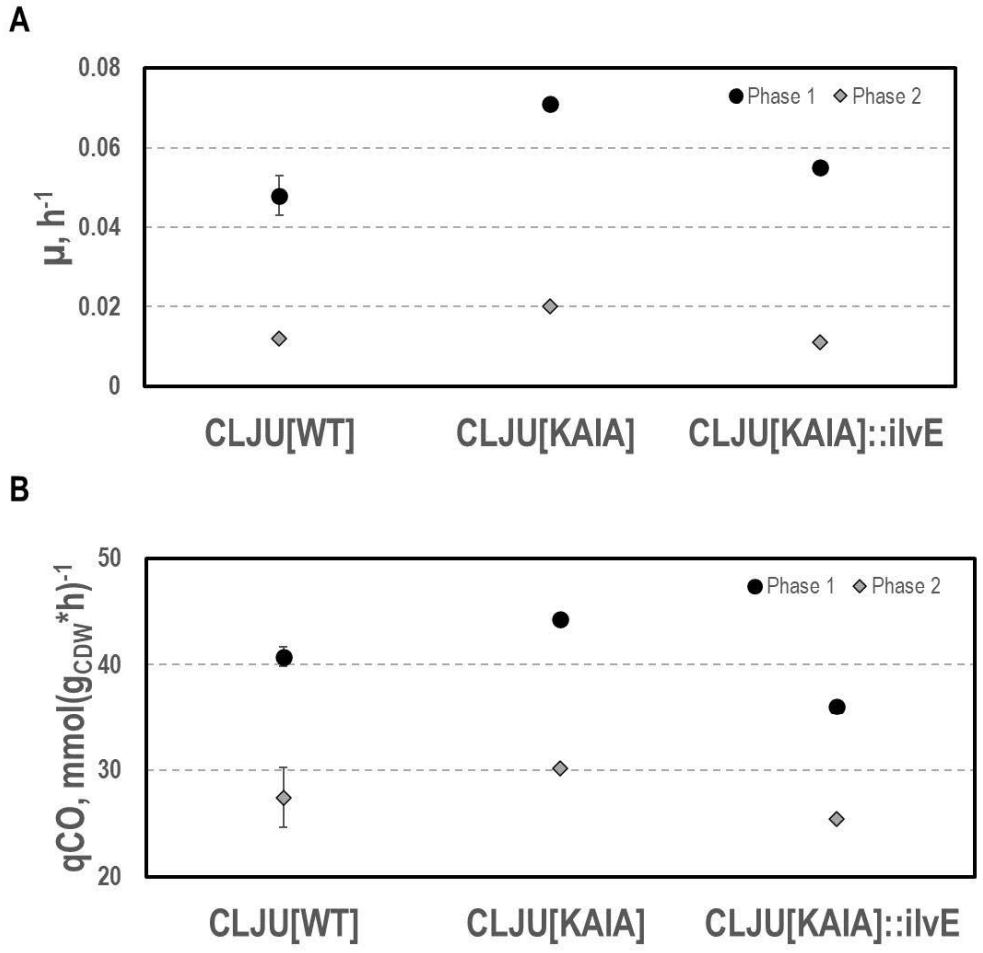

Figure 7.15: Comparative analysis of growth rates μ (**A**) and CO uptake rates qCO (**B**) for the syngas-based batch cultivation of CLJU[WT, REF], CLJU[KAIA] and CLJU[KAIA]::*ilvE* in a stirred tank bioreactor with a continuous gas supply. Error bars are derived from biological duplicates for the cultivation of CLJU[WT, REF].

Table 7.11: Simulated average reaction rates for each condition applying FBA based on the modified_rSMM. Simulated reaction rates for every experiment of the wildtype cultivation and corresponding standard deviations can be found online at (Excel tab: Flux simulations): https://www.frontiersin.org/articles/10.3389/fbioe.2021.647853/full#supplementary-material

Identifier	CLJU[WT] Phase 1	CLJU[WT] Phase 2	CLJU[KAIA] Phase 1	CLJU[KAIA] Phase 2	CLJU[KAIA]::ilvE Phase 1	CLJU[KAIA]::ilvE Phase 2
ACALD	0.017	-0.004	1.379	0.01	0.00	0.00
ACCOAL	5.717	2.499	5.081	3.31	4.47	2.37
ACCOAS	8.266	4.107	8.125	5.15	6.76	3.78
ACKr	-5.734	-2.495	-6.460	-3.32	-4.47	-2.37
ACLDC	0.935	0.702	0.970	0.77	0.77	0.59
ACLS	0.935	0.702	0.970	0.77	0.77	0.59
ACONT	0.041	0.010	0.065	0.02	0.05	0.01
ADK1	0.072	0.035	0.113	0.03	0.22	0.05
AICARS	0.008	0.002	0.013	0.00	0.01	0.00
ALCD2x	-3.925	-2.780	-4.558	-3.64	-3.19	-2.07
AMPS	0.008	0.002	0.012	0.00	0.01	0.00
AOR_CL	3.895	2.776	4.482	3.63	3.13	2.07
ARA	0.000	0.000	0.000	0.00	0.00	0.00
ARGS	0.011	0.003	0.018	0.00	0.01	0.00
ASNS1	0.009	0.002	0.014	0.00	0.01	0.00
ASP4DC	0.042	0.010	0.066	0.02	0.05	0.01
ASPSAS	0.088	0.010	0.139	0.03	0.10	0.01
ASPT	0.000	0.000	0.000	0.00	0.00	0.00
ASPTA	-0.182	-0.032	-0.286	-0.07	-0.21	-0.03
ATPM	5.000	5.000	5.000	5.00	5.00	5.00
ATPS4r	14.744	8.136	14.575	10.19	12.44	7.14
BTDD_RR	-0.935	-0.702	-0.970	-0.77	-0.77	-0.59
Biomass	0.051	0.012	0.080	0.02	0.06	0.01
CDPS	0.027	0.007	0.043	0.01	0.03	0.01
CELLWALLSYNTHESIS	0.000	0.000	0.000	0.00	0.00	0.00
CHORS_2	0.014	0.003	0.023	0.01	0.02	0.00
CODH4_1	32.489	23.325	36.120	25.02	29.27	21.66
CS	0.041	0.010	0.065	0.02	0.05	0.01
CTPS	0.003	0.000	0.004	0.00	0.00	0.00
CTPS1	0.000	0.001	0.000	0.00	0.00	0.00
CTPS2	0.027	0.007	0.043	0.01	0.03	0.01
CYS_LS	0.004	0.001	0.006	0.00	0.00	0.00
CoASYNTHASE	0.000	0.000	0.000	0.00	0.00	0.00
DAPDC	0.013	0.003	0.020	0.00	0.02	0.00
DHFR	0.000	0.000	0.000	0.00	0.00	0.00
Dihydrofolatreductase	0.002	0.000	0.002	0.00	0.00	0.00

ENO	-0.090	-0.033	-0.141	-0.03	-0.10	-0.03
FBA	-0.022	-0.005	-0.035	-0.01	-0.03	0.00
FBP	0.022	0.005	0.035	0.01	0.03	0.00
FDH	1.990	2.014	2.847	2.27	2.81	1.69
FHL	-4.329	-0.079	-2.498	-0.64	-1.19	-0.39
FRD1	0.000	0.000	0.000	0.00	0.00	0.00
FRNDPR2r_1	5.550	3.143	6.147	3.87	5.27	2.85
FRUK	0.000	0.000	0.000	0.00	0.00	0.00
FTHFLi	8.309	4.106	8.193	5.17	6.81	3.77
FUM	0.027	0.006	0.043	0.01	0.03	0.01
GABAS	0.000	0.000	0.000	0.00	0.00	0.00
GAPD	-0.090	-0.021	-0.141	-0.03	-0.10	-0.02
GDPS	0.004	0.001	0.006	0.00	0.00	0.00
GLNS	3.673	0.706	2.357	2.00	1.03	0.01
GLUDy	3.305	0.619	1.780	1.86	0.60	-0.06
GLUS	3.615	0.693	2.266	1.98	0.96	0.00
GMPS	0.004	0.001	0.006	0.00	0.00	0.00
GTPS	0.012	0.003	0.018	0.00	0.01	0.00
Glyceroloxidase	0.002	0.000	0.003	0.00	0.00	0.00
HCO3E	-9.027	-0.106	-4.628	-3.05	-2.50	0.26
HISS	0.004	0.001	0.006	0.00	0.00	0.00
HSDy	-0.074	-0.006	-0.116	-0.03	-0.09	-0.01
HYDFDN2r	0.000	0.000	0.000	0.00	0.00	0.00
IBS	0.000	0.000	0.000	0.00	0.00	0.04
ICDHx	0.041	0.010	0.065	0.02	0.05	0.01
ILEUS	0.011	0.003	0.017	0.00	0.01	0.00
IMPS	0.012	0.003	0.019	0.00	0.01	0.00
LDH_D	-0.065	-0.059	-0.140	-0.07	-0.03	-0.02
LEUS	0.017	0.004	0.027	0.01	0.02	0.00
LIPIDSYNTHESIS	0.000	0.000	0.001	0.00	0.00	0.00
LYSSII	0.015	0.003	0.023	0.01	0.02	0.00
MDH	0.027	0.006	0.043	0.01	0.03	0.01
ME1	0.000	0.000	0.000	0.00	0.00	0.00
ME2	0.000	0.000	0.000	0.00	0.00	0.00
MET_LSII	0.006	0.001	0.009	0.00	0.01	0.00
MTHFR5	8.272	4.108	8.134	5.16	6.76	3.78
NO2R	0.000	0.000	0.000	0.00	0.00	0.00
NO3R	0.000	0.000	0.000	0.00	0.00	0.00
OIVS	0.033	0.008	0.052	0.01	0.04	0.05
PC	0.317	0.057	0.497	0.12	0.23	0.03
PGK	0.090	0.021	0.141	0.03	0.10	0.02
PGM	0.090	0.033	0.141	0.03	0.10	0.03
PHES	0.007	0.002	0.011	0.00	0.01	0.00

POR_2	-2.341	-1.559	-2.718	-1.77	-2.04	-1.36
PPA	0.113	0.045	0.178	0.04	0.27	0.06
PPCK	0.120	0.021	0.189	0.05	0.00	0.00
PPDK	0.000	0.018	0.000	0.00	0.14	0.04
PROS	0.008	0.002	0.013	0.00	0.01	0.00
PRPPS	0.020	0.005	0.032	0.01	0.02	0.00
PTAr	5.734	2.495	6.460	3.32	4.47	2.37
PYK	0.000	0.000	0.000	0.00	0.00	0.00
RNF	26.981	14.888	26.673	18.64	22.77	13.06
RPE	-0.018	-0.004	-0.029	-0.01	-0.02	0.00
RPI	-0.018	-0.004	-0.029	-0.01	-0.02	0.00
SERS	0.000	0.011	0.000	0.00	0.00	0.01
SHMT	0.016	-0.007	0.025	0.01	0.02	-0.01
SO3R	0.000	1.017	0.000	0.00	0.00	1.47
SO4R	0.000	0.000	0.000	0.00	0.00	0.00
TALA	-0.002	0.000	-0.003	0.00	0.00	0.00
THRAi	0.047	0.000	0.074	0.02	0.06	0.00
THRD_L	0.011	0.003	0.017	0.00	0.01	0.00
THR_LS	0.068	0.005	0.107	0.03	0.08	0.00
TKT1	-0.002	0.000	-0.003	0.00	0.00	0.00
TKT2	-0.016	-0.004	-0.026	-0.01	-0.02	0.00
TPI	-0.053	-0.013	-0.084	-0.02	-0.06	-0.01
TRP_LS	0.002	0.001	0.003	0.00	0.00	0.00
TS_MTHFC_MTHFD	8.289	4.101	8.161	5.16	6.78	3.77
TYRS	0.005	0.001	0.008	0.00	0.01	0.00
UDCPDPSYNTHASE	0.000	0.000	0.000	0.00	0.00	0.00
UDPS	0.006	0.002	0.010	0.00	0.01	0.00
UMPS	0.006	0.002	0.010	0.00	0.01	0.00
UTPS	0.009	0.002	0.014	0.00	0.01	0.00
VALTA	-0.016	-0.004	-0.025	-0.01	-0.02	0.00
ametSYNTHASE	0.000	0.000	0.000	0.00	0.00	0.00
dATPS	0.001	0.000	0.002	0.00	0.00	0.00
dCTPS	0.001	0.000	0.001	0.00	0.00	0.00
dGTPS	0.001	0.000	0.001	0.00	0.00	0.00
dTTPS	0.001	0.000	0.002	0.00	0.00	0.00
fadSYNTHASE	0.000	0.000	0.000	0.00	0.00	0.00
malcoaSYNTHASE	0.000	0.000	0.000	0.00	0.00	0.00
pydx5pSYNTHASE	0.000	0.000	0.000	0.00	0.00	0.00
teca_CL_SYNTHASE	0.001	0.000	0.001	0.00	0.00	0.00
thmppSYNTHASE	0.000	0.000	0.000	0.00	0.00	0.00

ARBabc	0.000	0.000	0.000	0.00	0.00	0.00
ARBt2r	0.000	0.000	0.000	0.00	0.00	0.00
D_LACt2	0.000	0.000	0.000	0.00	0.00	0.00
EX_BMB	-0.051	-0.012	-0.080	-0.02	-0.06	-0.01
EX_ac	1.860	-0.277	0.630	-0.30	1.36	0.31
EX_btd_RR	0.935	0.702	0.970	0.77	0.77	0.59
EX_btn	0.000	0.000	0.000	0.00	0.00	0.00
EX_co	40.755	27.432	44.245	30.18	36.03	25.44
EX_co2	-33.017	-19.230	-32.220	-22.78	-24.65	-17.56
EX_etoh	3.925	2.780	4.558	3.64	3.19	2.07
EX_h2	4.329	0.079	2.498	0.64	1.19	0.39
EX_h2s	-0.009	1.015	-0.015	0.00	-0.01	1.47
EX_lac_D	0.065	0.059	0.140	0.07	0.03	0.02
EX_nh4	0.369	0.088	0.578	0.14	0.43	0.08
EX_pyr	0.000	0.000	0.000	0.00	0.00	0.00
EX_so3	0.000	-1.017	0.000	0.00	0.00	-1.47
Ex_arab__L	0.000	0.000	0.000	0.00	0.00	0.00
FRUpts	0.000	0.000	0.000	0.00	0.00	0.00
NO2t2r	0.000	0.000	0.000	0.00	0.00	0.00
NO3t2r	0.000	0.000	0.000	0.00	0.00	0.00
PYRt2	0.000	0.000	0.000	0.00	0.00	0.00
Pantothenate transport	0.000	0.000	0.000	0.00	0.00	0.00
Ribflv transport	0.000	0.000	0.000	0.00	0.00	0.00
T.h	-9.502	-2.910	-7.625	-4.19	-3.77	-2.82
T.h2o	-7.371	-11.392	-13.645	-10.82	-13.10	-10.00
T.hco3	-9.350	-0.164	-5.135	-3.17	-2.74	0.23
T_4abut	0.000	0.000	0.000	0.00	0.00	0.00
T_Biomass	0.051	0.012	0.080	0.02	0.06	0.01
T_H	0.000	0.000	0.000	0.00	0.00	0.00
T_H_ex	0.000	0.000	0.000	0.00	0.00	0.00
T_KIV	0.000	0.000	0.000	0.00	0.00	0.00
accoa	0.000	0.000	0.000	0.00	0.00	0.00
T_isobut	0.000	0.000	0.000	0.00	0.00	0.04
T_succ	0.000	0.000	0.000	0.00	0.00	0.00
T_urea	0.000	0.000	0.000	0.00	0.00	0.00
T_val	0.000	0.000	0.000	0.00	0.00	0.00
adocbl transport	0.000	0.000	0.000	0.00	0.00	0.00
ca2 transport	0.000	0.000	0.000	0.00	0.00	0.00
cl transport	0.000	0.000	0.000	0.00	0.00	0.00
cobalt2 transport	0.000	0.000	0.000	0.00	0.00	0.00
cu2 transport	0.000	0.000	0.000	0.00	0.00	0.00
fe2 transport	0.001	0.000	0.001	0.00	0.00	0.00

fol transport	0.000	0.000	0.000	0.00	0.00	0.00
k transport	0.010	0.002	0.015	0.00	0.01	0.00
mg2 transport	0.000	0.000	0.001	0.00	0.00	0.00
mn2 transport	0.000	0.000	0.000	0.00	0.00	0.00
mobd transport	0.000	0.000	0.000	0.00	0.00	0.00
ni2 transport	0.000	0.000	0.000	0.00	0.00	0.00
phosphate transport	-0.042	-0.010	-0.066	-0.02	-0.05	-0.01
so4 transport	0.000	0.000	0.000	0.00	0.00	0.00
thm transport	0.000	0.000	0.000	0.00	0.00	0.00
zn2 transport	0.000	0.000	0.000	0.00	0.00	0.00

Assumptions:	
1. Balanced stoichiometry of the overall reaction	
2. Average elemental composition of biomass:	$CH_{1.81}O_{0.52}N_{0.21}$
3. Molecular weight of Biomass:	24.6 g (C-mole biomass)$^{-1}$
4. Formula:	

$$\Delta G_R^0 = \left(\sum_i Y_{sp_i}\, G_{f,i}\right)_{products} - \left(\sum_i Y_{ss_j}\, G_{f,j}\right)_{substrates}$$

5. Degrees of reduction (κ*) per carbon	
Compound	**κ***
Biomass	4.8
Acetic acid	4
Ethanol	6
2,3-Butanediol	5.5
Lactate	3.7
Isobutanol	6.0
CO_2	0
CO	2
H_2	2
NH_3	0
H^+	0
H_2O	0

This assumption was made based on the fully oxidized status of a proton, as no reference in the literature could be found

6. Standard Gibbs free energy $\Delta G_{f,i}$ in kJ (C-mole)$^{-1}$	
Biomass	-74.36
Acetic acid	-131.69
Ethanol	-90.24
2,3-Butanediol	-85.11
Lactate	-119.90
Isobutanol	-41.87
CO_2	-394.39
CO	-137.16
H_2	0
NH_3	-26.57
H^+	0
H_2O	-237.14

This assumption was made based on the standard Gibbs free energy of H_2, as no reference in the literature could be found

Determination of ΔG_R								
Compound	**experimentally determined Yields $Y_{i/Carbon\ Source}$, C-mole (C-mole)$^{-1}$**				**calculated ΔG_R**			
	CLJU[WT] I	**CLJU[WT] II**	**CLJU[KAIA]**	**CLJU[KAIA]::ilvE**	**CLJU[WT] I**	**CLJU[WT] II**	**CLJU[KAIA]**	**CLJU[KAIA]::ilvE**
Biomass	0.028	0.023	0.026	0.027				
Acetic acid	0.009	0.011	0.006	0.024				
Ethanol	0.232	0.144	0.199	0.173				
2,3-Butanediol	0.107	0.110	0.092	0.107				
Lactate	0.011	0.009	0.010	0.002				
Isobutanol	0.000	0.000	0.001	0.003				
CO_2	0.716	0.709	0.690	0.650	-32.20	-34.91	-36.15	-37.89
CO	-1.000	-1.000	-1.000	-1.000				
H_2	0.007	0.017	0.029	0.024				
NH_3	-0.006	-0.005	-0.005	0.000				
H^+	0.201	0.331	0.142	0.058				
H_2O	-0.622	-0.566	-0.541	-0.471				

Figure 7.16: Determination of ΔG_R. The calculation can also be reproduced online at (Excel tab: delta GR determination): https://www.frontiersin.org/articles/10.3389/fbioe.2021.647853/full#supplementary-material